

# Principles of Rapid Machine Design

by

Eberhard Bamberg

M.Sc., Advanced Manufacturing Systems  
Brunel University, 1993

Dipl.-Ing, Maschinenbau  
Universität Stuttgart, 1996

SUBMITTED TO THE DEPARTMENT OF MECHANICAL ENGINEERING  
IN PARTIAL FULFILLMENT OF THE DEGREE OF

DOCTOR OF PHILOSOPHY

at the

MASSACHUSETTS INSTITUTE OF TECHNOLOGY

June 2000

© 2000 Massachusetts Institute of Technology  
All rights reserved

Signature of Author .....  
Department of Mechanical Engineering  
May 19, 2000

Certified by .....  
Professor Alexander H. Slocum  
Professor of Mechanical Engineering  
Thesis Supervisor

Accepted by .....  
Professor Ain A. Sonin  
Professor of Mechanical Engineering  
Chairman, Committee on Graduate Students



---

<b>Abstract</b> . . . . .	<b>7</b>
<b>Acknowledgments</b> . . . . .	<b>9</b>
<b>Chapter 1. Introduction</b> . . . . .	<b>11</b>
1.1 Overview . . . . .	11
1.2 Summary of Contributions . . . . .	13
<b>Chapter 2. Design Principles</b> . . . . .	<b>15</b>
2.1 Computer Aided Concept Generation . . . . .	16
2.1.1 Background . . . . .	16
2.1.2 Overview . . . . .	17
2.1.3 Concept Generation . . . . .	17
2.1.4 CAD Component Libraries . . . . .	20
2.2 Component Selection Process . . . . .	25
2.2.1 Stiffness Budget . . . . .	25
2.2.2 First Pass Selection . . . . .	27
2.2.3 Second Pass Selection . . . . .	28
2.2.4 Bearing Calculations . . . . .	30
2.2.5 Ballscrew and Drive Motor Calculations . . . . .	34
2.3 Concept Selection Process . . . . .	39
2.3.1 First Round Elimination - Fulfillment of Functional Requirements . . . . .	42
2.3.2 Second Round Elimination - Visual Inspection . . . . .	43
2.3.3 Third Round Elimination - Analytical Analysis . . . . .	44
2.3.4 Fourth Round Elimination - FEA Analysis . . . . .	48
2.4 Finite Element Modeling Techniques . . . . .	51
2.4.1 Basic Facts About FEA . . . . .	52
2.4.2 Basic FEA Elements . . . . .	53
2.4.3 Modeling Bearings . . . . .	56
2.4.4 Modeling Plates as Shells . . . . .	64
2.4.5 Constraints . . . . .	65
2.4.6 Performance and Accuracy . . . . .	66
2.5 Conclusion . . . . .	71
<b>Chapter 3. Manufacturing Principles</b> . . . . .	<b>73</b>
3.1 Fabricated Structures . . . . .	73
3.2 Kinematically Defined Machine Supports . . . . .	78
3.3 Standard Machine Elements . . . . .	79

---

3.3.1	Linear Rails	79
3.3.2	Ballscrews	81
3.4	Replication	82
3.4.1	Reference Edge	83
3.4.2	Replicated Joints	83
<b>Chapter 4.</b>	<b>Damping</b>	<b>85</b>
4.1	Mathematical Models	85
4.2	Material Damping	88
4.3	Damping in Bolted Joints and Bearings	89
4.4	Active Damping	89
4.5	Constrained Layer Damping	90
4.5.1	Background	90
4.5.2	Principle of Constrained Layer Damping	91
4.5.3	The Split Tube Design	94
4.5.4	Concrete Cast Damper	96
4.5.5	Reinforced Concrete Cast Damper Design	99
4.5.6	Round Core Concrete Cast with Multiple Reinforcement	103
4.5.7	Concrete Cast with Interlocking Constraining Layers	106
<b>Chapter 5.</b>	<b>Damping Experiments</b>	<b>109</b>
5.1	Building the Dampers	110
5.1.1	Split Tube	110
5.1.2	Concrete Core Damper	111
5.1.3	Concrete Core Cast with Reinforcement	113
5.1.4	Concrete Mixture	114
5.1.5	Material Cost	115
5.2	Experimental Setup	116
5.3	Damping Calculations	117
5.4	Experimental Data	119
5.5	Test Results	122
5.6	Conclusion	123
<b>Chapter 6.</b>	<b>Case Study - STG</b>	<b>125</b>
6.1	STG	127
6.1.1	Overall Machine Concepts	128
6.1.2	First Round Elimination - Fulfillment of Functional Requirements	131



---

6.1.3	Second Round Elimination - Visual Inspection	131
6.1.4	Result of First and Second Round Elimination	135
6.1.5	Third Round Elimination - FEA Analysis	135
6.1.6	Final Round Elimination - Team Discussion	139
6.2	STG Base	139
6.2.1	STG Base Concepts	139
6.2.2	Design Optimization	145
6.3	STG Gantry	149
6.3.1	STG Gantry Concepts	149
6.4	STG Modal Analysis	154
6.4.1	Rigid Body Modes	155
6.4.2	Actual Modes	157
6.4.3	Recommendations	162
<b>Chapter 7.</b>	<b>Case Study - TubeMill</b>	<b>163</b>
7.1	Error Budget	164
7.2	Overall Machine Concepts	167
7.3	Base Concepts	168
7.3.1	First Round Elimination - FEA Analysis	169
7.3.2	Second Pass Elimination - Global Sensitivity Study	173
7.4	TubeMill Gantry Concepts	175
7.5	Design Optimization of Gantry	181
<b>Nomenclature</b>		<b>183</b>
<b>References</b>		<b>185</b>



# **Principles of Rapid Machine Design**

by

Eberhard Bamberg

Submitted to the Department of Mechanical Engineering  
on May 19, 2000 in Partial Fulfillment of the  
Requirements for the Degree of Doctor of Philosophy  
at the Massachusetts Institute of Technology

## **ABSTRACT**

Following a continuing industry wide trend that began many years ago, design-to-manufacturing times for all kinds of products are getting increasingly shorter. The production equipment industry is no exception to this development and needs to respond accordingly.

This thesis presents a novel approach to conceptual design as part of a rapid machine design initiative. Solid model CAD systems and advanced engineering tools are used during the early design phase to generate realistic concepts of designs for manufacturing equipment. Concept evaluation is done very effectively through use of advanced analysis tools such as Finite Element Analysis. Core elements of this initiative are: create reasonably detailed concepts with 3D CAD systems, analyze concepts analytically if possible or through use of finite element methods if necessary, and build designs from fabricated structures so there are no tooling times or costs, resulting in short design-to-manufacture times. In addition, to enable this methodology to be realizable, a new design for structural damping is presented which helps to reduce design uncertainty caused by vibration. The novel constrained layer damping design achieves the same or better levels of damping at a fraction of the cost of existing designs.

Case studies of two fabricated machine tool structures are used to illustrate this new FEA based concept evaluation technique. The first study illustrates this design process in which the new approach to conceptual design led to a fundamentally new way of designing machine tool structures. A second study presents an optimization process where FEA is used to select, size and position structural members of a truss-like machine base.

Thesis Committee:

Prof. Alexander H. Slocum (Chair)

Prof. Sanjay Sarma

Prof. Samir Nayfeh

Dept. of Mechanical Engineering, Massachusetts Institute of Technology



# ACKNOWLEDGMENTS

This research was supported by Bill Silberhorn and Bud Webber of the Elk Rapids Engineering Corporation, a division of Star Cutter Company. I am grateful to Stan Ruskowski for his open mind towards new ideas and turning them into an actual machine tool.

My special thanks go to my friend and advisor Alex Slocum for his guidance and never ending inspiration. Snowboarding wouldn't be the same without him. Prof. Sanjay Sarma for his constructive criticism on writing this thesis and Prof. Samir Nayfeh for sharing his vast knowledge on machine dynamics with me as well as letting me use his modal analysis hard- and software.

I could not have completed this work without help from Kripa Varanasi who with great patience introduced me to modal analysis, its equipment, and the proper interpretation of the results. I would also like to express my gratefulness towards all my colleagues from the Precision Engineering Research Group for keeping me on my toes in the past and hopefully the future too.

And last but not least Stacy Morris for her understanding during the past months of intense writing - may the future provide more quality time.

And at last a word of wisdom from yet another source of inspiration to all those designers out there that still don't think analysis is necessary:

Do Or Do Not - There Is No Try

*Yoda*



# Chapter 1

## INTRODUCTION

### 1.1 Overview

The methodology of rapid machine design attempts to shorten design-to-manufacture time of production equipment by using advanced engineering tools such as Computer Aided Design systems (CAD) and Finite Element Analysis (FEA) during the conceptual design phase. It is hypothesized that by identifying the best of all available design concepts, overall development time can be shortened. Further time savings result from building machine components out of fabricated structures instead of casts. This eliminates the need for making molds and other specialized tooling systems, and provides a high degree of flexibility in terms of changing the design and/or making modifications to design specifications.

Special FEA modeling techniques and principles are being presented that allow designers to create models that are optimized for fast computing time at reasonable accuracy. Case studies of two fabricated machine tool structures are used to illustrate this new FEA based concept evaluation technique. The first study illustrates this design process, in which the new approach to conceptual design led to a fundamentally new way of designing machine tool structures. A second study presents an optimization process where FEA is used to select, size and position structural members of a truss-like machine base. These results assist the designer in the subsequent selection of the best concept.

Using solid models for concept generation has several tremendous advantages:

- The solid model makes it very easy to visualize the concept.
- Easy interfaces to mechanical analysis packages allow fast and accurate evaluation of the design.
- By combining existing concepts, new ideas can be quickly realized.
- Component libraries allow fast insertion of predefined, standard key components.
- Upon concept selection, existing models can be used for continuing design work.
- Through exchange of files, design teams can effectively communicate with each other outside meetings.
- Files are easy to output to rapid prototyping.

Welded machine tool structures provide easy scalability in terms of size and outstanding flexibility in terms of fast design and fabrication; however, damping of the structure is a very critical issue. Unlike cast iron or polymer concrete-based components, welded steel plates have virtually no internal damping and are therefore prone to unwanted vibrations. Filling the structure with concrete or sand adds damping but also a great deal of unwanted weight. A better approach is the use of constrained layer damping where a viscoelastic layer is squeezed between the structure and one or more constraining layers. Kinetic energy from relative motion between the structure and the constraining layer as it occurs during bending or twisting gets dissipated into heat by the viscoelastic layer. This mechanism introduces damping into the system, thereby limiting the structure's response to excitation frequencies near its modes. Unfortunately, existing shear layer damping designs tend to be costly to implement. A novel constrained layer design is presented which achieves the same or even better level of damping as existing designs at a fraction of the cost.



---

## 1.2 Summary of Contributions

1. Conceptual design specific component libraries: introduction to parametric CAD part files that simplify the use of computer aided design packages in the early stage of conceptual design.
2. Special FEA modeling techniques: introduction of equivalent Young's moduli for modeling bearings and similar components from solid finite elements to realistically simulate the behavior of these components.
3. Fundamentally new way of creating machine base structures: fabrication of the base of a machine from standard, large diameter tubes, resulting in development and implementation of a completely new base design.
4. Component selection tools: development of spreadsheets for rapid selection of machine components that assist designers to very quickly select components based on functional requirements.
5. Novel constrained layer damping design based on expanding concrete: design and testing of a concrete cast constrained layer damping system that combines the performance of viscoelastic damping with material damping provided by the concrete. Material costs are 70-80% lower compared to a conventional design and fabrication of the dampers has been significantly simplified. With comparable damping capability, the new design has an outstanding performance-to-cost ratio.



# Chapter 2

## DESIGN PRINCIPLES

Traditionally, design is done in a very sequential manner. First, concepts are created as sketches on paper and then qualitatively evaluated using common tools such as Pugh charts. The evaluation, which might be supported by some basic calculations that attempt to predict the performance of the design, is the basis for the selection of a small number of concepts. The second round concepts are developed in more detail and subject to a more thorough evaluation. Eventually the best concept is chosen and developed in full detail using computer aided design tools. During the detailing phase, design optimization might be done with the use of Finite Element Analysis software, and finally technical drawings are generated and released to manufacturing after a final review.

This traditional design approach has a few shortcomings and many of them are associated with the hand-sketching of concepts. The principles of rapid machine design aim to speed up the design process by using advanced engineering tools as early as the conceptual design phase. This involves the creation of concepts using a 3D solid modeler. At this point it is necessary to address the level of detail required at this phase of the design. In terms of evaluating a concept on the basis of performance and costs, all major components should be present. This includes the structure of the machine as well as all moving parts. While it may seem tedious to already include components such as ballscrews and linear bearings, having a modular component library at hand makes the inclusion of these parts actually rather painless. Of course, none of the components are shown in full detail. Bolt

holes, rail profiles, rounds and chamfers are all suppressed to minimize the computing time required to update the model.

## **2.1 Computer Aided Concept Generation**

### **2.1.1 Background**

Design theory and methodology is widely covered in literature and recent work has also examined the use of Computer Aided Design packages for conceptual design as well as concept selection tools. Bozzo et al (1999) have developed a qualitative structural analysis framework, suitable for the evaluation of conceptual designs as well as for tutoring systems. Harrington (1998) reports significant time savings from using software tools that assist in the conceptual design phase of a mechanical system. An overview of current research regarding Computer Aided Design tools for conceptual design has been compiled by Hsu and Woon (1998). Arai and Kazuaki (1992) analyzed conceptual design and identified a large amount of simple routine work included. They conclude that computers provide powerful support tools for these complex yet routine works. The findings of Bjarnemo et al (1995), on the other hand, identify shortcomings of CAD systems and conclude that these systems do not yet possess the necessary features to fully accommodate all of the activities of the conceptual design phase. Building a bridge between traditional, paper-based and computer-aided conceptual design is the subject of a study by Lipson et al (1995) which investigated tools that convert hand sketched line drawings into 2D objects. The system analyzes the input and then reconstructs a 3D model of the object most likely to be represented by the sketch. Sketches are used also in a study by van Dijk (1995), who had such a system evaluated by a team of professional industrial designers.

A concept for a finite element based design tool is outlined in a paper by Burman et al (1994). The work attempts to facilitate Finite Element Analysis in the early phases of the engineering design process, especially the conceptual design phase.

## 2.1.2 Overview

Evaluating reasonably detailed concept drawings rather than somewhat primitive hand sketches offers several key advantages:

- Better evaluation potential due to enhanced visualization. The ability to print or rotate the model on the screen gives the reviewers a chance to look at the concepts from different angles. Animating moving parts helps to identify critical design issues.
- Fast new concept generation through combination of existing concepts. By combining different aspects from various existing designs, new variations can rapidly be created.
- Easy documentation and archiving. Prints and pictures can easily be included in presentations and files archived in a database for future use.
- CAD models can readily be evaluated using advanced engineering tools such as Finite Element Analysis. Models of concepts that are stripped of irrelevant details may be analyzed in a very short amount of time, providing meaningful data for the concept selection.
- File sharing allows design teams to efficiently co-operate and communicate. The ability to exchange files is a great way to share ideas and stimulate new thoughts outside meetings.
- Concepts selected for further development can be based on initial model, avoiding duplicated work. By adding details to an existing conceptual model, the design can be refined and developed to full detail.

The new approach to conceptual design can be applied at any phase during the concept generation, whether it is the design as a whole or a component in particular. And because components are already part of the machine assembly, changes in their design are automatically updated in the entire realm. Too often conceptual design involves too little analysis of critical functions, such as dynamic stiffness. One of the contributions of this thesis is to show that detailed analysis can be critical in the conceptual phase, and that solid models and FEA are key enabling tools.

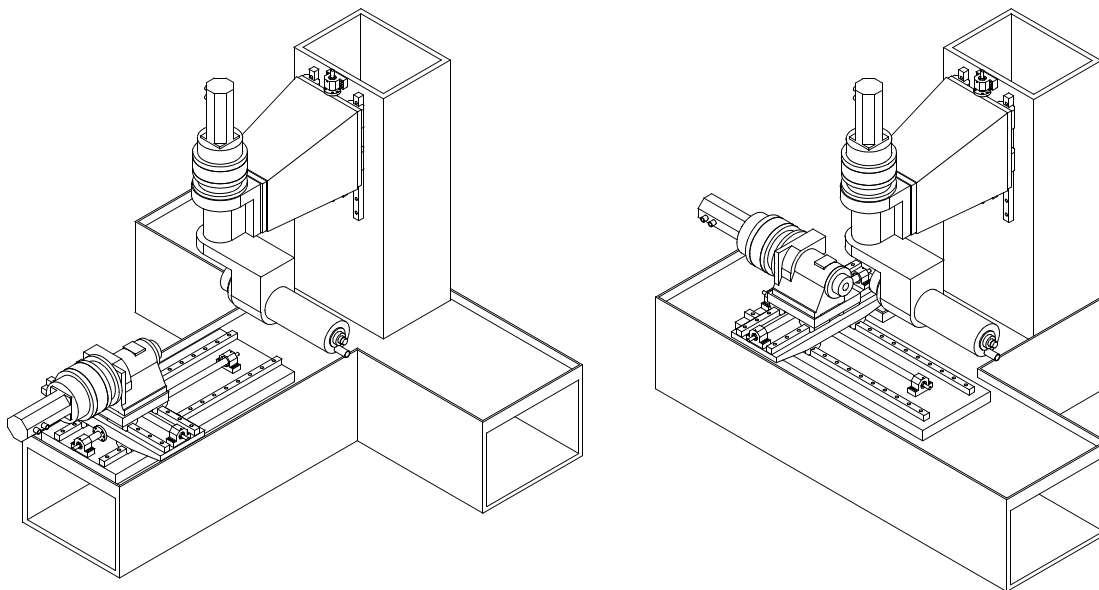
## 2.1.3 Concept Generation

In the following, concepts of the Star Technology Grinder (STG) five-axis tool and cutter grinder and the three-axis TubeMill are presented to illustrate this novel approach to con-

ceptual machine design. All models were created using a component library which contains standard engineering parts such as linear rails, motors, ballscrews, etc.

The Star STG is a five-axis tool and cutter grinder designed for the manufacturing of end mills and similar shaped workpieces. The complex geometry of the workpieces requires the machine to have three linear and two rotary axes. Though not listed as part of the functional requirements (FR's) (see Chapter 6), in order to follow the company's strategy, the new machine had to include a few components of the existing machine such as the numerical controllers and the traction drive systems used to spin the two rotary axes. Also, in accordance with the principles of rapid machine design, the STG had to be built from standard parts as much as possible. This includes the use of standard linear rails instead of labor intensive box ways. Because the machine's functional requirements do not demand extremely high speeds and accelerations for the axes, the design is equipped with ballscrews instead of highly dynamic but also very costly linear motor systems.

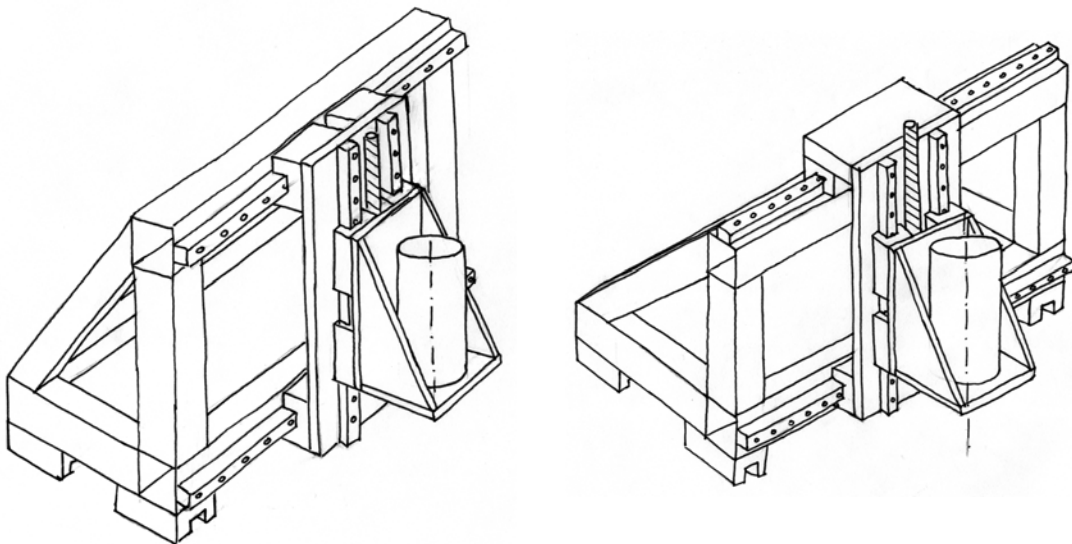
In Figure 2.1, two selected concepts of the STG are shown. By comparing the two designs, the evolution process that takes an existing design, and modifies parts of it to turn it into a new concept, can clearly be seen. It is worth noting that all STG concepts shown in Chap-



**Figure 2.1** CAD generated STG concepts 7 (a) and 8 (b)

ter 6 are basically derived from concept #1 (Figure 6.2a). This is achieved by successively rearranging components in such a way that they satisfy one of the main functional requirements: having three linear and two rotary axes. In the process of doing so, many different layouts can be generated with appropriate detail in a reasonable amount of time. At this point it is very important to not discard layouts that seemingly don't work. Though one may not conform to all functional requirements, a further iteration may produce new, viable design solutions or simply trigger new ideas. Concept selection should be done in the next phase of the design and not any sooner.

The concepts shown in Figure 2.1 have the following in common: each design has three linear and two rotary axes. What changes between designs is their arrangement, meaning the way they are stacked up on top of each other. Because every concept is built from the same standard components, creation of such a model is a matter of minutes only. In fact, new concepts are very often created by making modifications to an existing design. If done on paper, every new design variation will have to start from scratch (Figure 2.2) while solid modeler based concepts can be created by modifying a copy of the existing design. As a result of the details shown in every concept, evaluation is much more likely to be deterministic, as compared to hand sketches where most details are omitted.



**Figure 2.2** Hand sketched TubeMill gantry concepts

### **Evolutionary Design**

Up until now, no distinguishing between different types of design has been made. The question now is whether using a CAD system for conceptual design is applicable for both of the basic kinds of design that are practiced: evolutionary and revolutionary design. Evolutionary design is the most often practiced form of product development, and is based on existing designs that are further developed to better achieve a set of existing or newly defined functional requirements. These may include cost, safety, function, size, reliability, etc. Because the new design very often has strong ties to an existing design, it is also likely to reuse components or other already available elements. Clearly, in this case, it is of great advantage to use a CAD system because the reused components are already available as CAD files and ready to be included in the new designs.

### **Revolutionary Design**

Revolutionary design, on the other hand, has no legacy but starts with a clean sheet of paper, or, in the case of a CAD system, with an empty file. Most designers will probably find it easier to start such a task on paper rather than on a screen because unlike CAD, paper is free of any geometric constraints. What starts out as random lines and scribbles may eventually form some kind of a concept but at this point it is often too vague to be created in binary form. This is perfectly acceptable and does in no way contradict any previous statements. In a way, sketching out an idea on paper is merely an extension to formulating that very same idea as a thought and turning it into a three-dimensional CAD model.

#### **2.1.4 CAD Component Libraries**

In Section 2.1.3, machine concepts were created with an unprecedented level of detail to assist the selection process that follows the creation of these concepts. If each of the components shown would have to be set up every time they are needed, creating the concepts would be too time consuming to be justifiable. Instead, part and component libraries are used where standard machine elements are already defined. However, in order to be really



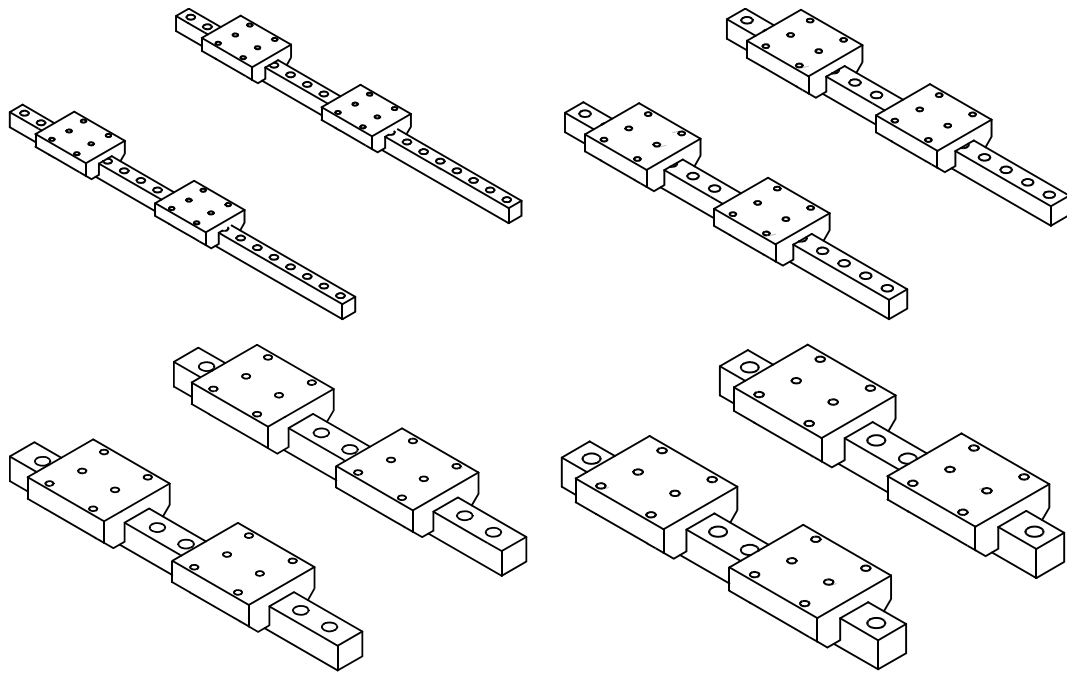
useful for conceptual design, ordinary part libraries are of limited use. This requirement is also discussed in a study by Horvath et al on morphological aspects of machine components that are used to derive skeletons through generic modeling of components. As discussed in Section 2.1.3, new concepts are often created by modifying existing one. This may require components to be updated to account for the new arrangement. With ordinary component libraries, this would require the deletion of the existing component and subsequent insertion of the new component. Furthermore, for the case that the updated component is referenced by other components, deleting this feature also affects the references, requiring to either re-route or recreate them. For a CAD system to be truly useful for conceptual design, any existing standard component must be updateable without the need for replacing it.

In Pro/ENGINEER<sup>TM</sup><sup>1</sup>, the existing way of defining a family of parts that maintain the shape but have their dimensions changed between sizes, is to use a family table. Only one part needs to be created and all dimensions, which change between sizes, are edited in the form of a table. Unfortunately, once such a family table driven component is added to an assembly, it can not be changed to a different member of that same family. Instead, the component has to be deleted and a new one will have to be added using that very same family table.

This shortcoming causes problems if features of the component are referenced by other assembly members, which is generally the case. Family tables, although very easy to set up, are therefore not useful for component libraries used in rapid machine design. The preferred library consists of components that can be updated without the need for deletion and re-insertion.

---

1. Pro/ENGINEER<sup>TM</sup> is registered trademark of Parametric Technology Corporation

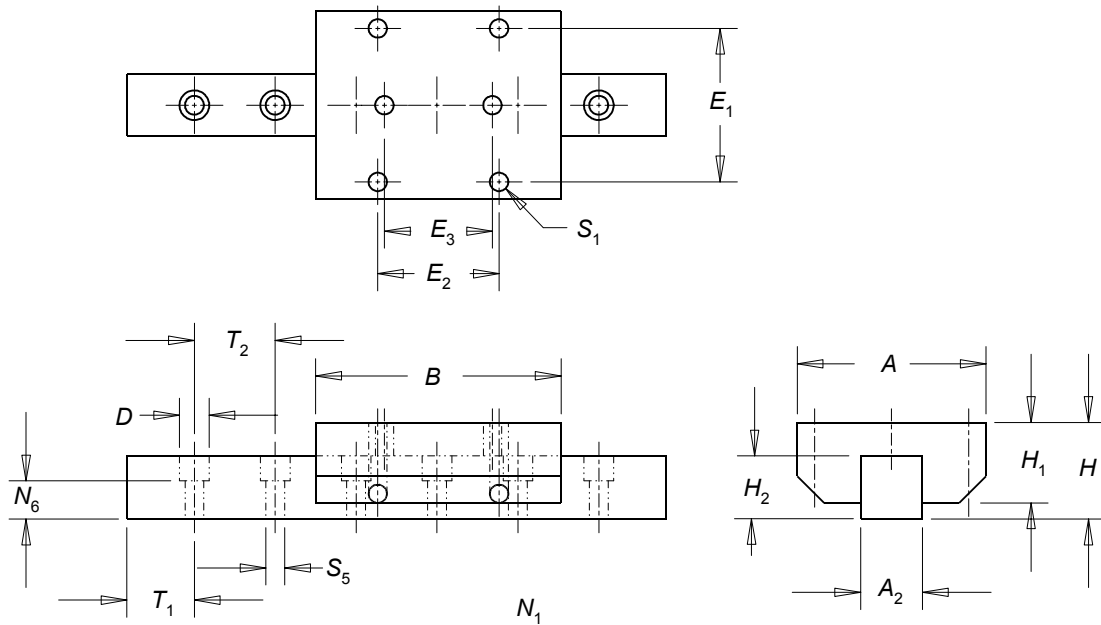


**Figure 2.3** Linear rail assembly - size 25, 35, 45, and size 55

### Linear Bearing Systems

In the following example, roller rails from Star Linear are used to illustrate the generation of a Pro/ENGINEER model of a linear rail assembly that satisfies the requirements set in Section 2.1.4. As discussed in Section 2.2.1, linear bearing systems are an integral part of rapidly designing and building production equipment. It is therefore imperative to have these systems available to the CAD system as a standard component. Fortunately, linear bearing systems maintain their shape between sizes, making it quite easy to define one single component that covers the entire available range of products.

Figure 2.3 shows an assembly of two linear rails and four runner blocks in the common sizes 25, 35, 45, and 55. Ordinarily, a library containing a size 25 rail and the appropriate runner block would be used to put together the assembly shown in Figure 2.3a, while the other assemblies in Figure 2.3 would be created from separate part files, each specific to the bearing size used. As mentioned earlier, changing the bearing size of such an assembly would require to delete the existing linear rail assembly and replace it with the updated



**Figure 2.4** Roller Rail dimensions

bearing size. Any references made to this assembly would have to be re-created in order to fully define the model. However, there is a much better way of addressing this issue which starts with the definition of the part files. In fact, updating the size 25 rail assembly in Figure 2.3a to any of the other sizes takes as few as two mouse clicks and an additional two key strokes. Instead of creating separate files for each individual bearing size, a generic set of files is created that contains all information necessary to create any of the bearing components in all available sizes. The dimensions required for setting up such universal part files for a rail are listed in Table 2.1 and those for the runner blocks can be found in Table 2.2. A sketch with the dimensions is also given in Figure 2.4.

These dimensions are added to the assembly file in form of relations that also contain *if* statements to accommodate the different types of rails available. A single parameter (rail size 25, 35, 45, or 55) is then used to determine what size bearings should be created and assembled. A slight complication in this model is the determination of the number of bolt holes and their position. Table 2.1 lists the parameter  $T_{1\min}$  as the minimum distance

between the center of the bolt hole and the starting edge of the rail. The actual position, however, is a function of the rail length and the resulting number of bolt holes.

**TABLE 2.1** Star Linear Roller Rail™<sup>a</sup> - rail dimensions [mm]

Size	$A_2$	$H_2$	$D$	$S_5$	$T_{1min}$	$T_2$
25	23	23.55	11.0	7.0	13.0	30.0
35	34	31.1	15.0	9.0	16.0	40.0
45	45	39.1	20.0	14.0	18.0	52.5
55	53	47.85	24.0	16.0	20.0	60.0
65	63	58.15	26.0	18.0	21.0	75.0

a. Roller Rail™ is a trademark of Deutsche Star GmbH, Germany

**TABLE 2.2** Star Linear Roller Rail™ systems - runner block dimensions [mm]

Size	$A$	$B$	$H$	$H_1$	$E_1$	$E_2$	$E_3$	$S_1$
25	70	91.0	36	30	57	45	40	6.8
35	100	114.0	48	41	82	62	52	8.6
45	120	140.0	60	51	100	80	60	10.5
55	140	166.5	70	58	116	95	70	12.5

Eq. 2.1 can be used to determine the number of bolt holes and Eq. 2.2 determines the position of the first bolt hole.

$$N = \text{floor}\left(\frac{L - 2T_{1min}}{T_2}\right) + 1 \quad (2.1)$$

$$T_1 = \frac{L - 2T_2}{2} \quad (2.2)$$

These equations are also implemented in the assembly file whose relations are given in Appendix A.

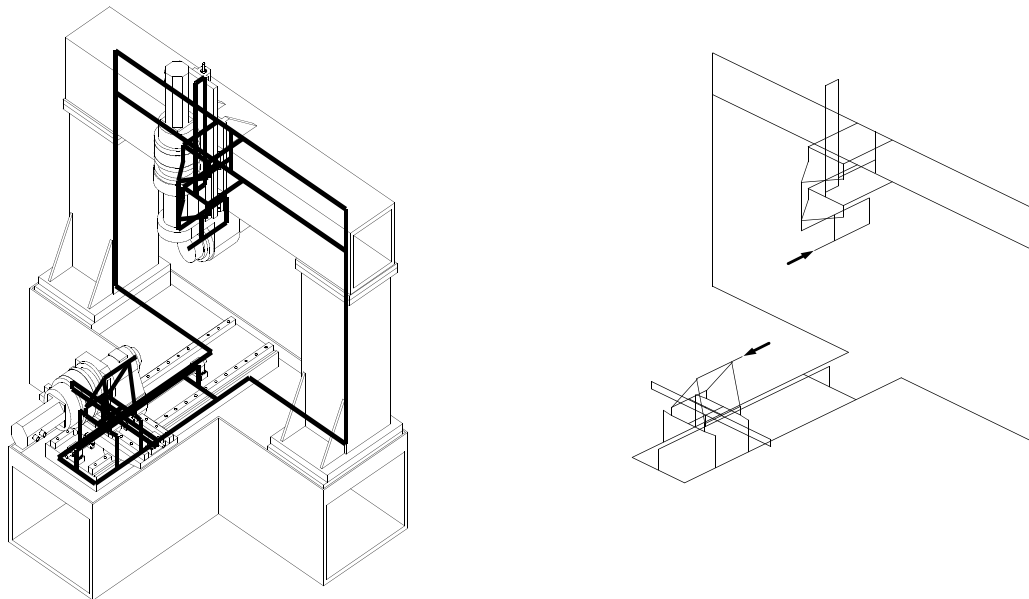
## 2.2 Component Selection Process

A machine tool is an assembly of many individual parts, each of which has a finite stiffness. Of particular interest are those components that are part of the structural loop (Figure 2.5), through which the action and reaction forces during machining travel. The stiffness of these components have a major impact on the accuracy of a machine tool. Hence, it is essential to consider the effects of such elements as early as possible to accurately predict the performance of machine concepts.

### 2.2.1 Stiffness Budget

As a first step in the design process, the machine is laid out as realistically as possible using real dimensions such as required axis travel, work volume, spindle size, etc. Next, a stick figure as shown in Figure 2.5b is created which represents the loop through which the cutting force pair (action and reaction) travels. Using the lengths and forces shown in this figure, loads onto all the other machine components can be quickly calculated.

When designing a machine tool for a certain performance/accuracy, one of the most important criteria is the effective stiffness of the tool/work piece interface. This value



**Figure 2.5** Structural loop of a gantry type machine tool

describes the magnitude of the force [N] required to push the tool away from the work piece by a unit length [ $\mu\text{m}$ ]. In general, values between 10 and 25 N/ $\mu\text{m}$  are considered to be adequate for machine tools. For the STG, the structural loop stiffness was targeted to be on the order of 50 N/ $\mu\text{m}$ , making this machine well suited for accurate machining.

As the next step, each major assembly of the machine (the 5 axes, spindle, base and bridge), a minimum stiffness is allocated. The principle behind this procedure is the assumption that each of the assemblies act like a spring of finite stiffness, and once arranged in series, compose the core of the machine. The total stiffness of an assembly of springs in series can then be calculated from:

$$k_{tot} = \left( \sum_{i=1}^n \frac{1}{k_i} \right)^{-1} \quad (2.3)$$

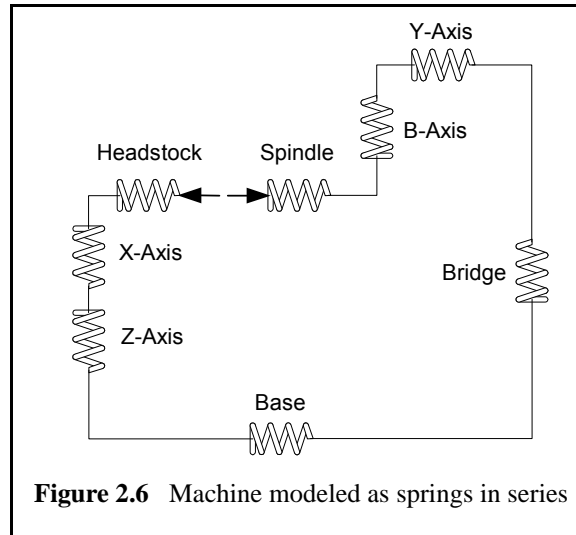
where  $k_i$  denotes the stiffness of each individual assembly. Once the appropriate amount of stiffness is allocated for each component, the above presented technique is also applied to each sub-component until every element of the structural loop is accounted for. In general, stiffness of elements is anisotropic, i.e. dependent on direction. To account for this non-uniformity, Eq. 2.3 is applied independently in all principal directions, normally defined by the machine axes. The allocated stiffness values are a key criteria for selecting or dimensioning structural and machine elements.

In attempting to achieve a targeted structural loop stiffness of 50 N/ $\mu\text{m}$ , a good starting point would be to calculate  $k_i$  with the assumption that all components are of equal stiffness. Next, using the above data and a spreadsheet created according to the stick figure shown in Figure 2.5, each component of each assembly becomes sized so as to fulfill the stiffness requirement calculated. Hence, with an assembly of eight components, the stiffness that each individual assembly needs to have in order to achieve a total rigidity of 50 N/ $\mu\text{m}$  comes out to be 400 N/ $\mu\text{m}$ . At an assumed cutting force of 1000 N in each direction, the deflection of the work spindle with respect to the grinding spindle will be no

more than 20  $\mu\text{m}$ . This requires each component to contribute no more than 2.5  $\mu\text{m}$  to the overall deflection of the machining interface.

### 2.2.2 First Pass Selection

The selection results for a design using linear ball bearing trucks is shown in Table 2.3. Of special interest are the Y-axis which would require no less than 8 bearing trucks of size 65, and the Z-axis with its massive 50 mm ballscrew. As mentioned before, roller-based bearings are considerably stiffer than ball-based bearings because of the way they make contact with the bearing surfaces. The line contact of a



**Figure 2.6** Machine modeled as springs in series

roller is inherently more rigid than the point contact of a ball and therefore more common in machine tool applications. In fact, some bearing manufacturers don't even offer linear bearing systems with balls. The results of the component selection based on roller systems is shown in Table 2.4. The number of trucks required for the Y-axis has dropped from eight to four and their size from 65 mm to 55 mm. The Z-axis ballscrew is still massive and would add heavily to the costs of the drive system.

As can be seen from the tables, only considering the bearings of the machine, the overall rigidity is already around the targeted value of 50 N/mm, which requires the rest of the machine to be virtually infinitely stiff. Realizing that this is impossible, especially when looking at the cantilevered structure of the Y-axis, the above bearing selection needs to be re-iterated starting with the components that contribute most to the overall compliance. This would be the grinding spindle, which unfortunately cannot be improved on. Next in line, considering that the X-direction appears to be the weak point, would be to look at the headstock, where the work spindle extends considerably past its bearings.

**TABLE 2.3** First pass component selection with ball rails

<b>Component</b>	<b>Machine Element</b>	<b><math>K_x</math> [N/<math>\mu\text{m}</math>]</b>	<b><math>K_y</math> [N/<math>\mu\text{m}</math>]</b>	<b><math>K_z</math> [N/<math>\mu\text{m}</math>]</b>
X-axis	ballscrew 40x10Rx6-6, pre-stretched 4 trucks, size 35	377	3308	801
Y-axis	ballscrew 40x10Rx6-6, pre-stretched 8 trucks, size 65	217	435	372
Z-axis	ballscrew 50x10R6-6, pre-stretched, 4 trucks, size 35	620	3305	369
A-axis	YRT 200	372	3000	372
B-axis		470	470	298
Grinding Spindle	GMN HC 170G-10000/21	140	140	298
<b>Total</b>		<b>47.9</b>	<b>79.7</b>	<b>56.1</b>

**TABLE 2.4** First pass component selection with roller rails

<b>Component</b>	<b>Machine Element</b>	<b><math>K_x</math> [N/<math>\mu\text{m}</math>]</b>	<b><math>K_y</math> [N/<math>\mu\text{m}</math>]</b>	<b><math>K_z</math> [N/<math>\mu\text{m}</math>]</b>
X-axis	ballscrew 40x10Rx6-6, pre-stretched 4 trucks, size 25	381	3568	827
Y-axis	ballscrew 40x10Rx6-6, pre-stretched 4 trucks, size 55	296	441	539
Z-axis	ballscrew 50x10R6-6, pre-stretched, 4 trucks, size 25	647	3565	374
A-axis	YRT 200	372	3000	372
B-axis		470	470	298
Grinding Spindle	GMN HC 170G-10000/21	140	140	298
<b>Total</b>		<b>51.2</b>	<b>80.2</b>	<b>59.1</b>

### 2.2.3 Second Pass Selection

The preliminary selections in Table 2.3 and Table 2.4 are based on the assumptions that each component needs to have a pre-determined rigidity regardless of how easy or difficult it is to achieve. While this may be a good starting point, it is by no means practical.



Using roller bearings, for instance, would require four massive size 55 trucks for the Y-axis but only tiny size 25 for the other two axes. For economic reasons it is desirable to use one type of ballscrew and bearing blocks only and vary the number and location of these trucks instead. Reasons for standardizing components include:

- Smaller inventory.
- Larger purchase volume may lead to better pricing.
- Maintenance staff needs fewer replacement parts.
- Better modularity.
- Reduced complexity.

There are several reasons why it is an advantage to have more than four bearing trucks per axis, i.e more than two trucks per rail. The most obvious one is increased rigidity and better protection from accidental overloading such as machine crashes. It is also true that the smoothness of the axis travel increases with the number of trucks involved. This is a result of increased averaging between the individual bearing trucks as they are following the rails which are not perfectly straight [Slocum (b)]. Also, all calculations so far did not include the structure which is by no means infinitely stiff. Having more points of contact between the structure and the bearings shortens the free, unsupported lengths of structural members, noticeably decreasing their stiffness requirement. Table 2.5 shows the result of a component selection based on six bearing trucks per axis. After a few iterations, it was decided to standardize using size 35 roller rails because they offer a large enough safety against indentation from machine crashes. All three machine axes will receive 6 trucks for increased stiffness and better averaging, resulting in smoother axis travel. Also, a 40 mm ballscrew with a single nut and light pre-load was chosen.

**TABLE 2.5** Component selection with size 35 roller rails

<b>Component</b>	<b>Machine Element</b>	<b><math>K_x</math> [N/<math>\mu\text{m}</math>]</b>	<b><math>K_y</math> [N/<math>\mu\text{m}</math>]</b>	<b><math>K_z</math> [N/<math>\mu\text{m}</math>]</b>
X-axis	ballscrew 40x10Rx6-6, pre-stretched 6 trucks, size 35	401	8796	1989
Y-axis	ballscrew 40x10Rx6-6, pre-stretched 6 trucks, size 35	192	429	361
Z-axis	ballscrew 40x10R6-6, pre-stretched, 6 trucks, size 35	1564	8785	304
A-axis	YRT 200	372	3000	372
B-axis		470	470	298
Grinding Spindle	GMN HC 170G-10000/21	140	140	298
<b>Total</b>		<b>49.2</b>	<b>82.0</b>	<b>56.4</b>

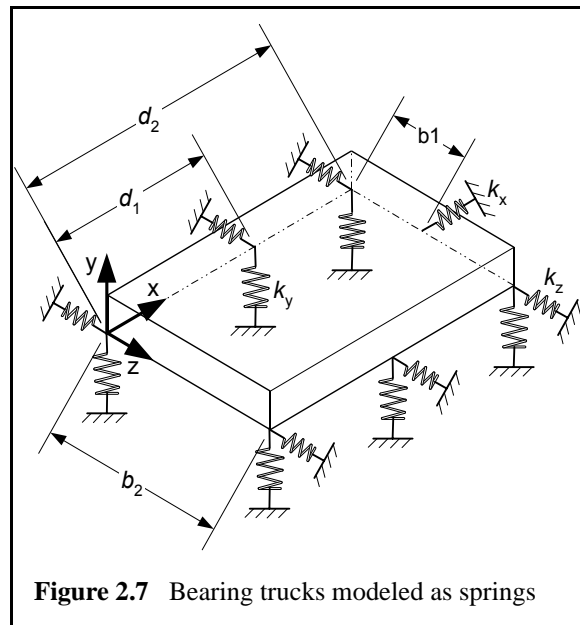
### 2.2.4 Bearing Calculations

Bearing systems are not infinitely stiff because their internal rolling elements are subject to Hertzian contact and elastic deformations, and as a result, will exhibit a certain amount of compliance. In a machine tool where cutting forces create substantial forces during operation, the compliance in the bearings is a substantial source of error which cannot be neglected. Often, bearings are selected on the basis of two characteristics: the life estimation and the rated accuracy. The life estimation depends on the load the bearing has to take, the duty cycle it is going through and the load capacity, a value which is quoted by the bearing manufacturer [Shigley et al]. The rated accuracy of a bearing is dependent on its design and how well it is manufactured. For a machine tool, selecting a bearing on the basis of these two criteria is generally not good enough. Bearings are an integral part of the structural loop and their rigidity needs to be considered as well.

Rolling element bearings are highly standardized machine elements available from a wide range of suppliers. The competitive market not only ensures aggressive pricing and dependable quality, it also forces the suppliers to provide the customers with detailed information on their products. Generally, bearings behave like elastic springs and their

stiffness in the principal directions is usually quoted in catalogs or data sheets. These values are the basis for a third, very important criteria on selecting bearings: the overall bearing rigidity.

For an assembly with 6 bearing trucks as shown in Figure 2.7, the vertical ( $k_y$ ) and lateral stiffness ( $k_z$ ) of each individual bearing is modeled from two springs, twelve springs altogether. The ballscrew is also modeled from a spring and denoted  $k_x$ . The equations of this overconstrained system are derived from Lagrange's equation of motion with the inertia terms set to zero in order to simulate a quasi-static system [Craig]. The bearing force and displacement calculations are performed with the



**Figure 2.7** Bearing trucks modeled as springs

assumption that the structure to which the bearings are mounted is significantly less compliant than the bearings itself. This allows the linear displacements of each bearing to be written in terms of the system displacement coordinates  $x$ ,  $y$ ,  $z$ ,  $\theta_x$ ,  $\theta_y$ ,  $\theta_z$ . For maximum flexibility, the coordinate system is located centered and on top of one of the corner bearings. This eliminates the need for having to locate the system center of stiffness, which can be difficult for a non-symmetric arrangement. However, for a symmetric design where the center of stiffness for the entire system can easily be located at the center between the bearings, it is of advantage to place the coordinate system at this point. The compliance matrix  $C$  then becomes a purely diagonal matrix, i.e. only the elements on the matrix diagonal are populated. All other elements of the matrix are zero, simplifying the calculations substantially. The derivation is given in Appendix A. The compliance matrix of the system pictured in Figure 2.7 is:

$$C = \frac{1}{d_1^2 + d_2^2 - d_1 d_2} \begin{bmatrix} \frac{4k_z(d_1^2 + d_2^2 - d_1 d_2) + 3k_x b_1^2}{4k_x k_z} & 0 & \frac{-(d_1 + d_2)b_1}{4k_z} & 0 & \frac{-3b_1}{4k_z} & 0 \\ 0 & \frac{5(d_1^2 + d_2^2) - 2d_1 d_2}{12k_y} & 0 & \frac{d_1^2 + d_2^2 - d_1 d_2}{3k_y b_2} & 0 & \frac{-(d_1 + d_2)}{4k_y} \\ \frac{-(d_1 + d_2)b_1}{4k_z} & 0 & \frac{d_1^2 + d_2^2}{4k_z} & 0 & \frac{d_1 + d_2}{4k_z} & 0 \\ 0 & \frac{d_1^2 + d_2^2 - d_1 d_2}{3k_y b_2} & 0 & \frac{2(d_1^2 + d_2^2 - d_1 d_2)}{3k_y b_2^2} & 0 & 0 \\ \frac{-3b_1}{4k_z} & 0 & \frac{d_1 + d_2}{4k_z} & 0 & \frac{3}{4k_z} & 0 \\ 0 & \frac{-(d_1 + d_2)}{4k_y} & 0 & 0 & 0 & \frac{3}{4k_y} \end{bmatrix} \quad (2.4)$$

To find the displacement of the system, the force and moment vector needs to be created:

$$\vec{Q}^T = \begin{bmatrix} F_x & F_y & F_z & M_x & M_y & M_z \end{bmatrix} \quad \text{with} \quad \vec{M} = -(\vec{F} \times \vec{r}_F) \quad (2.5)$$

where  $\vec{r}_F$  is the location of  $\vec{F}$   $\vec{r}_F^T = \begin{bmatrix} x_F & y_F & z_F \end{bmatrix}$

The linear and rotary displacements of the system are:

$$\vec{q} = \vec{C}\vec{Q} \quad \text{where} \quad \vec{q}^T = \begin{bmatrix} x & y & z & \theta_x & \theta_y & \theta_z \end{bmatrix} \quad (2.6)$$

To find the linear displacements at the location of the load use:

$$\begin{bmatrix} \Delta x_F \\ \Delta y_F \\ \Delta z_F \end{bmatrix} = \begin{bmatrix} x \\ y \\ z \end{bmatrix} + \begin{bmatrix} \theta_x \\ \theta_y \\ \theta_z \end{bmatrix} \times \vec{r}_F \quad (2.7)$$

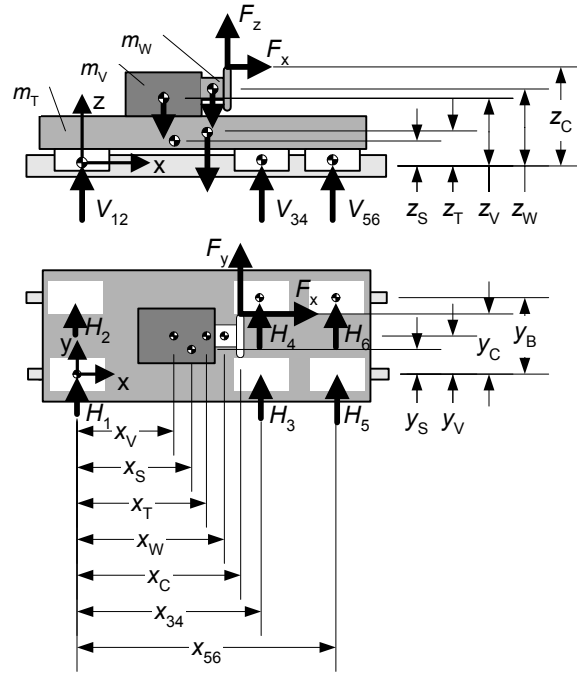
The effective stiffness at the load location is then defined as:

$$k_{F,x} = \frac{\sqrt{F_x^2 + F_y^2 + F_z^2}}{\Delta x_F} \quad k_{F,y} = \frac{\sqrt{F_x^2 + F_y^2 + F_z^2}}{\Delta y_F} \quad k_{F,z} = \frac{\sqrt{F_x^2 + F_y^2 + F_z^2}}{\Delta z_F} \quad (2.8)$$

The spreadsheet for an assembly with 6 trucks is shown in Figure 2.8 and is based on Eq. 2.4 to Eq. 2.8.

### Input Data

Parameter	Sym.	Value	Unit
<b>Machining</b>			
Cutting force x-direction	$F_x$	1	N
Cutting force y-direction	$F_y$	1	N
Cutting force z-direction	$F_z$	1000	N
Feed rate	$V_c$	5	m/min
Rapid motion	$V_{max}$	15.24	m/min
Acceleration time	$T_{ac}$	0.5	s
Rapid feed percent. of duty cycle	$q$	10	%
<b>Table</b>			
Mass of Table	$M_t$	150	kg
x-dist. table CG - CS	$X_t$	225	mm
y-dist. table CG - CS	$Y_t$	150	mm
z-dist. table CG - CS	$Z_t$	90	mm
Dist. betw. 1. and 2. pair of trucks	$X_{34}$	350	mm
Dist. betw. 1. and 3. pair of trucks	$X_{56}$	450	mm
Spacing between rails	$Y_b$	300	mm
<b>Ball screw</b>			
y-dist. center of ballscrew - CS	$Y_s$	150	mm
z-dist. center of ballscrew - CS	$Z_s$	0	mm
Stiffness of ballscrew assembly	$K_s$	462	N/ $\mu$ m
<b>Vice</b>			
Mass of Vice	$M_v$	100	kg
x-dist. vice CG - CS	$X_v$	200	mm
y-dist. vice CG - CS	$Y_v$	150	mm
z-dist. vice CG - CS	$Z_v$	200	mm
<b>Workpiece</b>			
Mass of Workpiece	$M_w$	2	kg
x-dist. workpiece CG - CS	$X_w$	300	mm
y-dist. workpiece CG - CS	$Y_w$	150	mm
z-dist. workpiece CG - CS	$Z_w$	300	mm
<b>Point of Cutting</b>			
x-dist point of cutting - CS	$X_c$	1052	mm
y-dist. point of cutting - CS	$Y_c$	250	mm
z-dist. point of cutting - CS	$Z_c$	225	mm
<b>General</b>			
Gravitational acceleration	$g$	9.81	m/s <sup>2</sup>
Required lifetime	life	40000	h



### Output Data

Part number	Size	C_dyn N	Nominal Life h	fulfill lifetime?	vertical rigidity N/ $\mu$ m	lateral rigidity N/ $\mu$ m	Kx N/ $\mu$ m	Ky N/ $\mu$ m	Kz N/ $\mu$ m
1651, 1622	15	6000	84513	OK	360	263	455	2212	120
standard	20	14500	1192819	OK	455	350	575	2792	152
flanged	25	17600	2133086	OK	581	416	735	3571	194
	30	24400	5683815	OK	679	441	859	4183	226
	35	32300	13184935	OK	827	555	1046	5091	276
	45	52400	56294282	OK	1125	737	1425	6929	375
	55	75600	169058033	OK	1369	847	1735	8444	456
	65	123000	728091163	OK	1640	1000	2079	10119	546
1851, 1821	25	26900	7616006	OK	892	533	1129	5507	297
standard	35	56300	69822535	OK	1466	823	1858	9066	488
flanged	45	92300	307663183	OK	2068	1136	2625	12797	689
	55	128900	837971364	OK	2666	1571	3390	16465	888
1853, 1824	25	33300	14447847	OK	892	533	1129	5507	297
long	35	68700	126864653	OK	1466	823	1858	9066	488
flanged	45	119200	662672872	OK	2068	1136	2625	12797	689
	55	165000	1757608962	OK	2666	1571	3390	16465	888
	65	265500	7322577923	OK	4285	3750	5476	26232	1428

Figure 2.8 Excel spreadsheet to calculate deflections and lifetime of machine table with 6 trucks

### 2.2.5 Ballscrew and Drive Motor Calculations

The rigidity of a ballscrew system is affected by a variety of parameters. The two obvious ones are the shaft diameter  $d_S$  and shaft length  $L_S$ . In order not to overconstrain the system, the end of the shaft to which the drive motor is attached is generally fixed, meaning a set bearings constrains all 3 linear degrees of freedom. The non-driven end of the shaft is typically supported by a floating bearing used to constrain two rotary degrees of freedom, allowing the shaft to rotate only around its axis of revolution. As the shaft heats up and begins to expand thermally, the supported end of the shaft is allowed to float inside the pillow block while the driven end is securely held in place. This is a standard design and is guaranteed to work. However, when the design calls for long axis travel and high rigidity, the compliance of the shaft and its critical speed become a major concern. In such a situation, the floating bearing can be replaced with a fixed bearing, adding a fourth linear constraint to the system. The allowable thrust load of a fixed-fixed shaft is four times that of a fix-supported bearing system and the increase in rigidity is of the same order. Because both ends are now fixed, thermal expansion of the shaft would cause it to buckle and the thrust bearings would have to take very high axial forces, wearing the bearings out very quickly. This problem can be solved by pre-stretching the ballscrew by an incremental length equivalent to the amount the screw will thermally expand during machining. Now, the thrust bearings have to take high loads during the warming-up phase of the machine, but once it has reached thermal equilibrium, both ends of the ballscrew are fixed with no excessive loads remaining on the bearings. The length the screw needs to be stretched can be calculated from:

$$\Delta L_S = L_S \alpha_S \Delta T \quad (2.9)$$

where  $L_S$  denotes the un-stretched length of the screw at ambient temperature. The thermal expansion coefficient is given as  $\alpha_S$  and is on the order of  $12 \times 10^{-6}$  1/K for steel.  $\Delta T$  is the average temperature increase of the shaft. The problem with using Eq. 2.9 is the determination of the increase in temperature. It can be predicted by developing a thermal model of the assembly from the frictional losses within the nut and the duty cycle of the machine.

Given that the ballscrew assembly has very little mass compared to the structure it is mounted to, a model with a constant temperature at the end of the shaft is appropriate, with very little heat loss due to convection but instead mostly through conduction into the base. A less deterministic approach would be to loosen the fixed bearing (works with face-to-face bearings only) and have it act as a floating bearing, then run the machine until it is thermally stable, i.e. all components have reached their final temperature. Now the fixed bearing can be tightened slightly and secured.

It should be noted that the force required to pre-stretch a ballscrew can be very substantial and needs to be considered when laying out the structure. The force required to stretch the screw by the amount  $\Delta L_s$  calculated in Eq. 2.9 is (see Section A.4 on page 194):

$$F_{PL} = \alpha_s EA_s \Delta T \quad (2.10)$$

For a 40 mm ballscrew with an average increase in temperature of 3°C, the preload force comes out to be 12 kN. This is a huge load that may cause the structure to warp.

The lead of a ballscrew affects three important parameters: the torque required at a given thrust load, the achievable positioning accuracy of the servo system and the maximum speed at which the axis can travel. Small leads achieve high accuracy and large thrust forces but have limited speeds. Large leads achieve the exact opposite and it is the designer's task to find the best compromise between the three parameters. The basic equations required for calculating the characteristics of ballscrew assemblies are given in Table 2.6 and an excerpt of the spreadsheet for selecting ballscrews is shown in Figure 2.10. The selection tool is build upon the Star Linear catalog and outputs the required ballscrew and motor size for a given axis, as well as rigidity values and allowable speeds for various shaft end conditions.

TABLE 2.6 Ballscrew calculation

Property	Equation
shaft cross section	$A_S = \frac{\pi}{4}(d_S - 0.71d_W)^2$
shaft moment of inertia	$I_S = \frac{\pi}{64}(d_S - 0.71d_W)^4$
thrust force	$F_{thrust} = F_c + mg(\mu \cos \alpha + \sin \alpha)$
acceleration force	$F_{ac} = m \frac{v_{max}}{t_{ac}} + mg(\mu \cos \alpha + \sin \alpha)$
maximum thrust force	$F_{ax} = F_{trust}$ if $(F_{thrust} > F_{ac})$ $F_{ax} = F_{ac}$ if $(F_{ac} > F_{thrust})$
average thrust force	$F_{av} = \sqrt[3]{F_{thrust}^3 q + F_{ac}^3 (1 - q)}$
buckling (fixed-free)	$0.25 \frac{\pi^2 EI_S}{L_a^2} > F_{ax}$
buckling (supported-supported)	$\frac{\pi^2 EI_S}{L_a^2} > F_{ax}$
buckling (fixed-supported)	$2 \frac{\pi^2 EI_S}{L_a^2} > F_{ax}$
buckling (fixed-fixed)	$4 \frac{\pi^2 EI_S}{L_a^2} > F_{ax}$
maximum shaft speed	$n_{max} = \frac{v_{max} N_1}{lead N_2}$
shaft speed during cutting	$n_f = \frac{v_f}{lead}$
average shaft speed	$n_{av} = n_f q + n_{max} (1 - q)$
lifetime	$Life = \left( \frac{C_{dyn}}{F_{av}} \right)^3 10^6$
polar moment of inertia, gear 1	$J_1 = \frac{\pi}{32} \rho b (d_{p1}^4 - d_{i1}^4)$
polar moment of inertia, gear 2	$J_2 = \frac{\pi}{32} \rho b (d_{p2}^4 - d_{i2}^4)$
polar moment of inertia, shaft	$J_S = \frac{\pi}{32} \rho L d_S^4$
moment of inertia acting on motor	$J_M = J_1 + (J_2 + J_S) \left( \frac{N_1}{N_2} \right)^2 + J_{Rotor} + m \left( \frac{N_1 lead}{N_2 2\pi} \right)^2$
pre-load force	$F_{A0} = C_{dyn} \frac{preload}{100}$
torque from thrust force	$T_{thrust} = \frac{F_{thrust} lead}{2\pi \eta}$
torque from pre-load	$T_P = \mu_N F_{A0} \frac{lead}{2\pi}$



**TABLE 2.6** Ballscrew calculation

Property	Equation
frictional torque from acceleration	$T_i = \frac{J_M 2\pi n_{max}}{t_{ac}}$
torque required for machining	$T_m = (T_{thrust} + T_P) \frac{N_1}{N_2}$
torque required for acceleration	$T_{ac} = T_i + T_P \frac{N_1}{N_2}$
DN value	$d_S n_{max} < 70000$
lifetime (cycles)	$Life = \left(\frac{C_{dyn}}{F_{av}}\right)^3 10^6$
lifetime (hours)	$Life_h = \frac{Life}{n_{av} 60}$
shaft stiffness, free end	$K_{S,free} = \frac{A_S E}{L_a}$
shaft stiffness, fixed end	$K_{S,fixed} = \frac{4A_S E}{L_a}$
ballscrew rigidity (free end)	$(K_{S,free}^{-1} + K_B^{-1} + K_N^{-1})^{-1}$
ballscrew rigidity (fixed end)	$(K_{S,fixed}^{-1} + K_B^{-1} + K_N^{-1})^{-1}$

**Input Data**

PARAMETER	VALUE	UNITS	SYMBOL	SI-Value	SI Unit
<b>Machining Data</b>					
Cutting force	1000	N	F_c	1000	N
Feed rate	1.2	m/min	v_f	0.02	m/s
percentage of duty cycle	90	percent	q	0.9	percent
Rapid Motion	15.24	m/min	v_max	0.254	m/s
Acceleration time	0.5	second	t_ac	0.5	s
<b>Table Data</b>					
Mass	650	kg	m	650	kg
Incline angle	0	degrees	alpha	0	degrees
Coefficient of friction	0.01		mu	0.01	
Gravity	9.81	m/s^2	g	9.81	m/s^2
Density	7.85E-06	kg/mm^3	rho	7.85E+03	kg/m^3
Youngs Modulus	2.10E+05	N/mm^2	E	2.10E+11	N/m^2
<b>Ball Screw Data</b>					
Ballscrew length	1300	mm	L_S	1.3	m
Mounting length	1200	mm	L_a	1.2	m
Mech. Efficiency	90	percent	eta	0.9	
Preload factor	13	percent	pre_factor	0.13	
Nut friction factor	0.1		mu_N	0.1	
Expected lifetime	40000	hours	life	40000	hours

**Figure 2.9** Input parameter for ballscrew selection

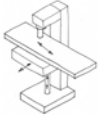
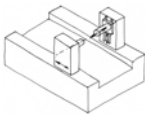
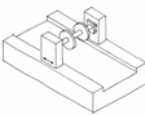
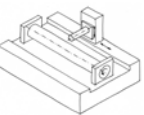
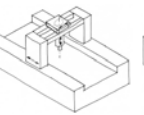
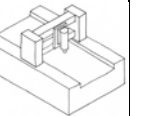
Single Nut Type	Symbol	Unit	8x2.5Rx1.588-3	12x5Rx2.5-3
<b>Motor</b>				
required speed	n_max	rpm	6096	3048
required torque during machining	T_M	N-m	0.5	1.0
required torque during acceleration	T_ac	N-m	0.8	0.7
<b>Ballscrew</b>				
Buckling load fixed-free < Fa?	P_fixed_free	N	No	No
Buckling load supp-supp < Fa?	P_supp_supp	N	No	No
Buckling load fixed-supp < Fa?	P_fixed_supp	N	No	OK
Buckling load fixed-fixed < Fa?	P_fixed_fixed	N	No	OK
DN value < 100000?	DN		OK	OK
Lifetime long enough?			No	No
Lifetime	Life_h	hours	358	8067
Rigidity of ballscrew (non-fixed end)	K_nonfixed	N/micron	6.0	12.6
Rigidity of ballscrew (fixed end)	K_fixed	N/micron	19.7	36.8
Gear 1: # of teeth	N_1		1	1
Gear 1: pitch circle dia	dp_1	mm	0	0
Gear 1: inside dia	di_1	mm	0	0
Gear 2: # of teeth	N_2		1	1
Gear 2: pitch circle dia	dp_2	mm	0	0
Gear 2: inside dia	di_2	mm	0	0
Gear width	B	mm	0	0
Motor moment of inertia	J_Rotor	kg-m <sup>2</sup>	0.0005	0.0005
Screw diameter	d_s	mm	8	12
Lead	lead	mm	2.5	5
Ball diameter	d_w	mm	1.588	2.5
Dynamic load rating	C_dyn	N	2900	6500
Nut Rigidity	K_N	N/micron	140	210
Support bearing rigidity	K_B	N/micron	200	200
Threaded shaft rigidity, non-fixed end	K_S_nonfixed	N/micron	6.491722618	14.36992705
Threaded shaft rigidity, fixed end	K_S_fixed	N/micron	25.96689047	57.4797082
Thrust load	F_thrust	N	1063.77	1063.77
Acceleration load	F_ac	N	393.97	393.97
Maximum axial load	F_ax	N	1063.77	1063.77
Average axial load	F_av	N	1028.98	1028.98
Machining speed	n_f	rpm	480.00	240.00
Average speed	n_av	rpm	1041.60	520.80
Lifetime	Life	revolutions	22385670	252067101
Cross sectional area	A_s	m <sup>2</sup>	3.70956E-05	8.21139E-05
2 nd Moment of inertia	I_s	m <sup>4</sup>	1.09505E-10	5.36566E-10
Moment of inertia of gear 1	J_1	kg-m <sup>2</sup>	0	0
Moment of inertia of gear 2	J_2	kg-m <sup>2</sup>	0	0
Mass moment of inertia of threaded shaft	J_S	kg-m <sup>2</sup>	4.10367E-06	2.07748E-05
Moment of inertia acting on motor	J_M	kg-m <sup>2</sup>	0.000607008	0.000932392
Preload	F_A0	N	377	845
Frictional torque due to ext. loads	T_thrust	N-m	0.470287383	0.940574767
Frictional torque due to preload	T_P	N-m	0.015000353	0.067242963
Frictional torque due to acceleration	T_j	N-m	0.774993371	0.595212699

Figure 2.10 Output data of ballscrew selection spreadsheet

### 2.3 Concept Selection Process

The traditional approach to concept selection usually involves some kind of chart where the advantages and disadvantages are listed for all concepts. Commonly used chart types are Pugh charts and its derivatives. The traditional Pugh chart is a table that lists strengths and weaknesses of designs relative to one specific design chosen to serve as a reference. An often used version uses zeros if designs are comparable, minus and double minus for designs that perform worse, and plus and double plus for designs that perform significantly better than the reference design. This comparison is done for the entire set of criteria relevant for the evaluation and at the end, the ratings for each design are simply added up. With this method, the design with the highest score is the best performing concept and the winner of the comparison. Table 2.7 is an example of such a Pugh chart and shows the evaluation of overall machine concepts for the TubeMill, which is presented in full detail as a case study in Chapter 7.

**TABLE 2.7** Pugh chart for TubeMill overall concept evaluation

						
Low cost	0	0	-	-	0	0
High accuracy	0	-	-	--	+	+
High stiffness	0	-	0	-	0	++
Good repeatability	0	--	++	--	0	+
Scalability	0	+	++	+	++	++
Good dynamics	0	+	+	++	+	+
Ease of workpiece setup	0	++	++	++	++	++
Easy chip removal	0	0	0	0	0	0
Ability to drill and tap	0	++	--	++	0	0
<b>Total</b>	<b>0</b>	<b>2</b>	<b>3</b>	<b>1</b>	<b>6</b>	<b>9</b>

In this example, six rather different machine concepts are evaluated using concept #1, a conventional Bridgeport type of milling machine, as the reference design by which the other designs are judged. However, using a Pugh chart in the above fashion can be treacherous because every criteria has equal weight within the decision matrix. This method does not take into account that some criteria are more important than others, and can therefore lead to wrong conclusions. It is generally advisable to use a modified version of a Pugh chart, whereby each criteria has an associated weight factor. The idea behind this method is to strengthen important characteristics while limiting the influence of less important criteria.

A designer must reliably assess criteria used to characterize designs and their predicted performance. The Standard Handbook of Machine Design lists the following basic decision making ingredients and their commonly practiced surrogates:

**TABLE 2.8** Basic decision making ingredients [Dieter]

<b>Ingredient</b>	<b>Surrogate</b>
Fact	Information
Knowledge	Advice
Experience	Ad hoc experimentation
Analysis	Intuition
Judgment	None

In practice, many designers rely heavily on the surrogates listed in Table 2.8 rather than the basic ingredients these surrogates are derived from. By doing so, some of the essence of the design is not captured because it eludes the simplified and sometimes even crude decision-making replacements. In times where fierce competition forces designers to rapidly converge on both performance and economics, “second hand” tools are no longer good enough for selecting the single best design concept. Therefore, one of the core elements of rapid machine design is to shift the focus away from non-deterministic towards fully deterministic methods for classifying design concepts. This is especially true for the

analysis part of the decision-making process which has all too often been replaced by intuition. This is not to say that designers must analyze every single concept, including those with design flaws or impossible challenges obvious enough to be detected right away. Such efforts would be futile and frustrating at times. However, successful detection of such challenges requires a fair amount of experience which is hard to quantify. In this thesis it is therefore stipulated that producing hard evidence by conducting scientific analyses is greatly preferable to using intuition as the basis for selecting design concepts. Reasons for doing so include:

- Reproducible results. Detailed calculations or finite element methods produce results that are easily reproducible at a later stage of the design and even long after the designer in charge has left. Intuition based decisions, on the other hand, are hard to re-derive by fellow peers.
- No ambiguity. A number, just like a picture, says more than a thousand words. Quantifying designs with meaningful numbers such as weight, stiffness, modal frequency, etc., rather than words helps avoiding ambiguity.
- Fair comparison between very different designs. Intuition may work reasonably well for design that are very similar but is likely to fail if designs are fundamentally different.
- Results point out design challenges. Analysis performed on concepts also points out design challenges, making this additional information available right away.

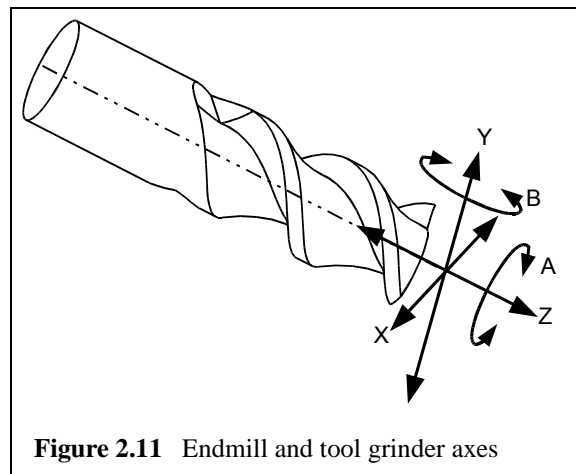
As said before, detailed analysis of concepts is a key enabling tool during the selection process but it is obviously not necessary to apply these tools on every single concept. A good designer does not reject a design during the creating phase, because though not viable, it may still aid in the creation of better designs. This leads to the following important conclusion: concept selection must have a structured hierarchy whereby selection happens at different levels of detail, starting with a coarse set of criteria which is subsequently refined until the best possible concept is identified. A good start has its roots in the table of functional requirements, and verifies whether all concepts actually fulfill the frame set herein.

### 2.3.1 First Round Elimination - Fulfillment of Functional Requirements

The most obvious criteria one would apply to evaluate a concept is the ability to perform the task for which it is designed. For the case of a machine tool, this is determined by the motion required for the generation of the workpiece's geometry. The exact data are usually listed as functional requirements, although additional information may occasionally be necessary and is illustrated with Figure 2.11. The picture shows a two-flute endmill, a typical workpiece for a tool and cutter grinder, and labels the axes for the machine. Although the functional requirements specify details about the machine's axes such as range of motion, their orientation with respect to each other isn't necessarily listed as well. In such a case it is crucial to examine a typical workpiece and judge the concepts accordingly.

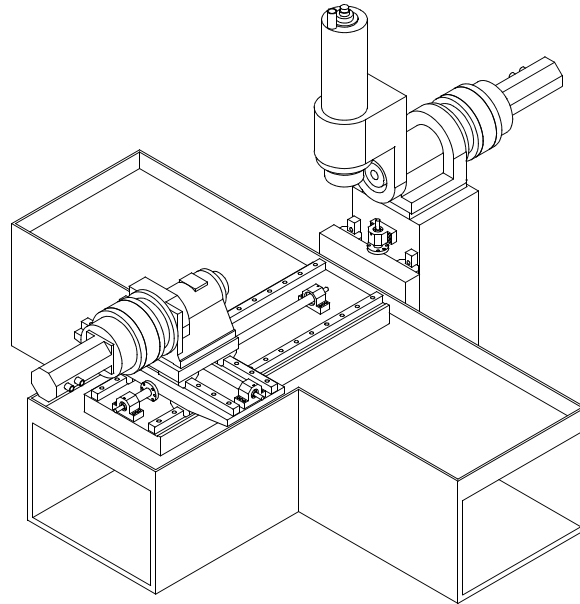
For the tool and cutter grinder that grinds endmills as shown in Figure 2.11, the two rotary axes and their orientation with respect to the endmill itself are of special importance. The rotation of the A-axis is used to grind the cylindrical surface of the workpiece and therefore has to be continuous and along the endmill's axis of rotation. The B-axis needs to have a rotation of

$\pm 120^\circ$  in order to grind the round cutting edges of a ball endmill and must be orientated normal to the endmill's axis of rotation.



**Figure 2.11** Endmill and tool grinder axes

The elimination of the STG machine concept #4 shown in Figure 2.12 is an example to illustrate this technique. Although the concept fulfills the basic requirement of having three linear and two rotary axes, one of which provides continuous rotation while the other one is limited to  $\pm 120^\circ$ , the machine fails to satisfy the required orientation of the axes to manufacture the endmill shown in Figure 2.11. As shown in the figure, the B-axis with a range of  $\pm 120^\circ$  needs to be normal to either the Y-axis or the X-axis in order to grind a ball

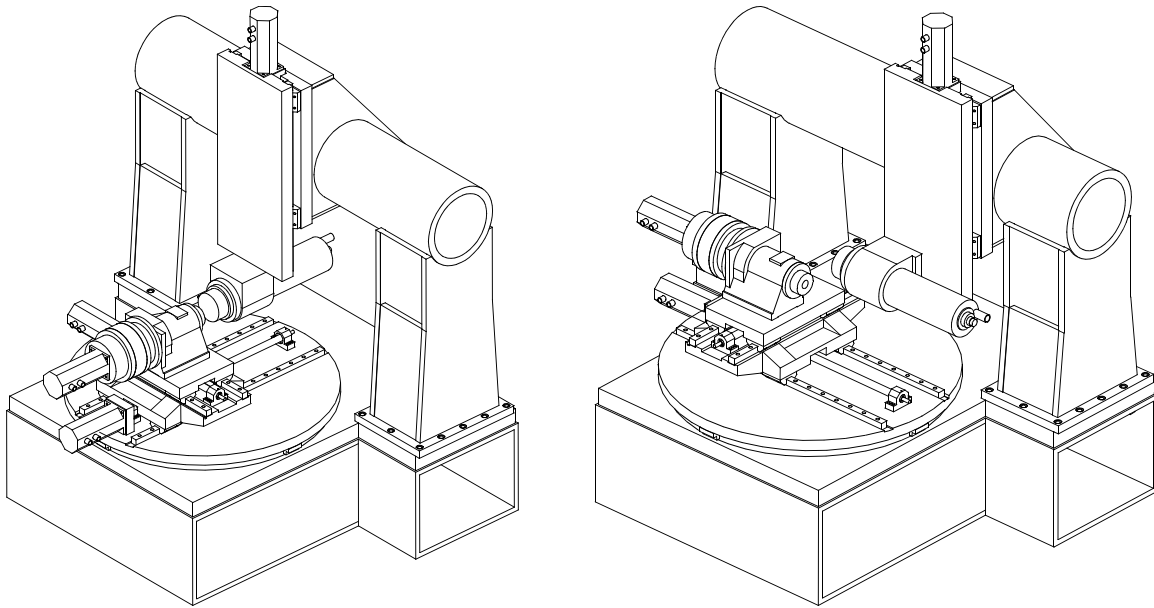


**Figure 2.12** STG machine concept #4

endmill. However, concept #4 has its B-axis normal to the Z-axis and therefore fails to satisfy the single most important functional requirement: the ability to manufacture the workpieces the machine is designed for.

### **2.3.2 Second Round Elimination - Visual Inspection**

Prior to detailed design evaluation, visual inspection of the concepts is another valuable tool to narrow down the number of variations. However, this tool can only reliably be applied to variations that are very similar and only differ in a very limited number of details, preferably one or two only. For designs that are very different, visual inspection is not deterministic enough, unless the design flaws are extremely obvious. This stage of the evaluation process can also be used to identify the most critical component of the design which will need special attention during the detailing phase. To illustrate this process, machine concepts where visual inspection is applicable are shown in Figure 2.13. The presented designs are very similar with all axes being identical. The only difference is the way the spindle is mounted to the Y-axis. For design concept #11, the spindle is rotated 90° which allows it to be mounted closer to the Y-axis bearings. The shorter lever arm



**Figure 2.13** STG concepts #10 and 11

reduces the loads on the bearings and the Abbe error which is a direct result of the Y-axis rotation. Furthermore, because the spindle mount is higher, the entire bridge can be lowered by using shorter uprights. This saves weight and also increases the stiffness of the bridge altogether. An increase of the dynamic stiffness is a direct result of these improvements. This example closely follows the rule that designs need to be very similar in order to reliably apply the technique of visual inspection.

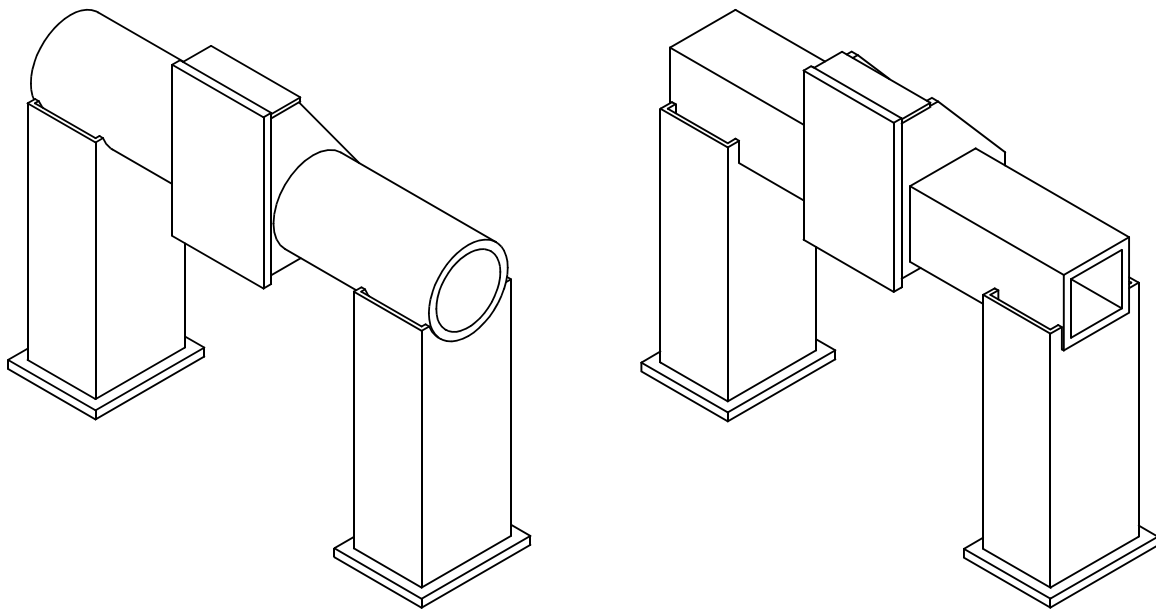
### **2.3.3 Third Round Elimination - Analytical Analysis**

The next step up in complexity and sophistication would be a selection of concepts based on an analytic solution to a given engineering problem. The STG gantry concepts shown in Figure 2.14 are a good example where only a deterministic evaluation will select the best concept. Both designs fulfill the functional requirements set for the machine and also conform to the geometric constraints set by the overall machine concept. At this point, it is necessary to include performance and economics in the selection process. Performance criteria mainly relate to characteristics such as stiffness, natural frequency and weight, all of which have an affect on how well the concept will perform the task it is designed for.



The best design would achieve the highest possible stiffness with the least possible weight, and have the highest possible natural frequency. Economical criteria, on the other hand, address issues related to costs. These are determined not only by the amount and type of materials used but also include issues related to the manufacturing process involved. As a rule of thumb, commonly used materials in standard sizes are more readily available and less expensive than exotic materials in non-standard sizes. Round tubes, for instance, are highly standardized and available in a wide range of sizes and wall thicknesses, while the range of available sizes for square tubes is noticeably smaller. Economics therefore suggest using a round structure as opposed to a structure built from a square tube.

The gantry in Figure 2.14, which has been chosen as an example for this section, is subject to bending and torsional loads which result from the fact that cutting forces at the spindle are transmitted into the gantry via a lever arm (the Y-axis). One concept is built with a square tube connecting the two uprights while the other design is realized with a round tube. Visual inspection suggests that both concepts are viable, although the square tube design might be preferable because of its native flat surfaces which make manufacturing easier compared to the rounded surfaces of the alternative design. Still, judging a concept



**Figure 2.14** STG gantry concepts

in this manner is highly subjective and often hard to follow by fellow peers. The better approach would be to have some hard evidence why one concept is better than the other, and such an approach will be developed in this section.

The tube connecting the two uprights is subject to bending and torsional loads and the resulting compliances are the selection criteria for this example. The formula for the polar moment of inertia for a thin walled cross section of arbitrary shape can be derived from Saint-Venant's principle [Young]:

$$I = \frac{4A_m^2 t}{U_m} \quad (2.11)$$

where  $A_m$  denotes the mean area enclosed by the outer and inner boundaries,  $U_m$  the length of the median, and  $t$  the constant wall thickness. The resulting equations for round and square cross sections together with the well known equations for the area moment of inertia are given in Table 2.9.

**TABLE 2.9** Moment of inertia for round and square cross section with thin wall thickness

	<b>Round Tube</b>	<b>Square Tube</b>
area moment of inertia	$I_{b,rd} = \frac{\pi}{64} (w_{rd}^4 - (w_{rd} - 2t)^4)$	$I_{b,sq} = \frac{1}{12} (w_{sq}^4 - (w_{sq} - 2t)^4)$
polar moment of inertia	$I_{t,rd} = \frac{\pi}{4} (w_{rd} - \frac{t}{2})^3 t$	$I_{t,rd} = \frac{(w_{rd} - \frac{t}{2})^4}{w_{rd} - t} t$

For the purpose of comparing the two cross sections analytically, the wall thickness  $t$  is assumed to be much smaller than the characteristic width  $w$ . Factoring out the equations given in Table 2.9 and cancelling all high order terms of  $t$  ( $t \ll w$ ) results in (see (A.1), page 189, (A.2), (A.5), and (A.4)):

$$\begin{aligned}
 I_{b,rd} &= \frac{\pi}{8} w_{rd}^3 t \quad \text{round cross section} \\
 I_{b,sq} &= \frac{2}{3} w_{sq}^3 t \quad \text{square cross section}
 \end{aligned} \tag{2.12}$$

$$\begin{aligned}
 I_{t,rd} &= \frac{\pi}{4} w_{rd}^3 t \quad \text{round cross section} \\
 I_{t,sq} &= w_{sq}^3 t \quad \text{square cross section}
 \end{aligned} \tag{2.13}$$

According to Eq. 2.12 and Eq. 2.13, at a given envelope size ( $w_{sq} = w_{rd}$ ) and identical wall thickness, the square tube's torsional stiffness is larger by a factor of  $4/\pi$  (27%) and a factor of  $16/3\pi$  (69%) for the bending stiffness. The square tube is about 27% heavier than the round tube and equally more expensive, assuming general availability and the fact that material costs scale fairly well with weight. In reality, square tubes are much harder find than round tubes, so the difference in cost is likely to be even larger.

Designing a system with equal weight and thus theoretically equal cost changes the difference in stiffness quite a bit. At a given width  $w_{sq}$  for a square tube, the diameter  $w_{rd}$  of a round tube with equal weight can be calculated to (see (A.5), page 190):

$$w_{rd} = \frac{4}{\pi} \left( w_{sq} + \left( \frac{\pi}{4} - 1 \right) t \right) \tag{2.14}$$

Plugging the diameter found in Eq. 2.14 into Eq. 2.13, the newly found polar moment of inertia for the round tube comes out to be:

$$I_{t,rd} = \frac{16}{\pi^2} \left( w_{sq} + \left( \frac{\pi}{4} - 1 \right) t \right)^3 t \tag{2.15}$$

Realizing that  $w_{sq} \gg \left( \frac{\pi}{4} - 1 \right) t$ , Eq. 2.15 can be further simplified to:

$$I_{t,rd} = \frac{16}{\pi^2} w_{sq}^3 t \tag{2.16}$$

Similarly, applying the result of Eq. 2.14 to the simplified area moment of inertia found in Eq. 2.12 results in:

$$I_{b,rd} = \frac{8}{\pi^2} w_{sq}^3 t \quad (2.17)$$

Now the factor by which the bending stiffness of the square tube is larger than that of the round tube can be found to be  $\pi^2/12$  (-18%) and the corresponding factor for the torsional would be  $\pi^2/16$  (-38%). In fact, a round tube having the same wall thickness and weight as a square tube is significantly stiffer than its square counterpart, especially in terms of torsional loads.

In order to find the best compromise between performance and cost, the round tube may be sized such that its bending stiffness is identical to that of a square tube with the same wall thickness. Using the first order findings of Eq. 2.12 and setting them equal results in:

$$w_{rd} = \sqrt[3]{\frac{16}{3\pi}} w_{sq} \quad (2.18)$$

Plugging the diameter  $w_{rd}$  found in Eq. 2.18 into Eq. 2.13, the torsional stiffness of a round tube can be found to be larger by a factor of  $4/3$  (33%) while being lighter by 7%. This performance advantage combined with the fact that round tubes are available in many more sizes and wall thicknesses than square tubes makes the round structure the preferred shape of choice. It is therefore concluded that the gantry built upon the round tube (Figure 2.14b) is the better concept.

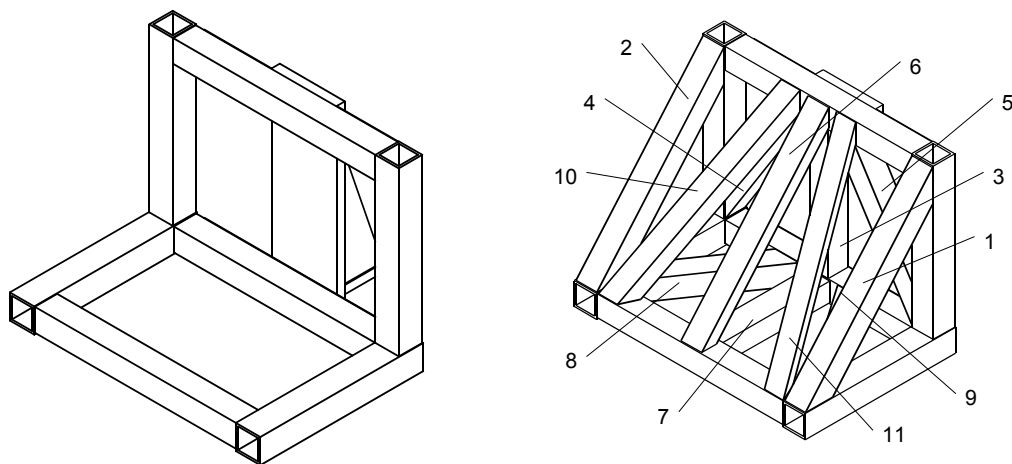
### 2.3.4 Fourth Round Elimination - FEA Analysis

In Section 2.3.3, an analytical model was developed to create hard evidence for the selection process of a component. Now, concepts of a gantry design are presented whose geometry is too complex to be solved in closed form. Visual inspection of the models might work for a few concepts but is most likely too subjective to identify the best concept. In traditional design methodology, where the concept selection process is rather basic, a non-

optimal concept might be picked which then becomes optimized with more effort than necessary in a later design phase. Applying the concept of rapid machine design ensures that the best possible concept is picked right from the start. Of course, the best concept can only be selected if it has been developed and is therefore available to be selected. Having a discriminating concept selection process at hand is no substitute for creative concept generation. Poor creation of concepts combined with a good selection process is no better or worse than having a creative mind generating great concepts combined with a poor selection scheme.

A series of concepts for a gantry were created by adding standard rectangular tubes to the basic frame shown in Figure 2.15a. Through different combinations, twelve concepts were created altogether (see Section 7.4). The numbering system for the Finite Element Analysis is shown Figure 2.15b. The tubes that form the basic frame of the gantry coincident with concept #1 are not numbered.

The model for this analysis is built from shell elements, an idealization which is perfectly appropriate for the materials and shapes used. The mounting surfaces for the linear bearing trucks are used to fully constrain the model and a cutting force of 1000 N in all three directions was applied to the mounting surface of the spindle (see Figure 2.16). For time efficient computation, the series of analyses was run in a batch mode. This mode allows



**Figure 2.15** Basic frame (concept #1) for TubeMill gantry (a) and fully featured concept (b)

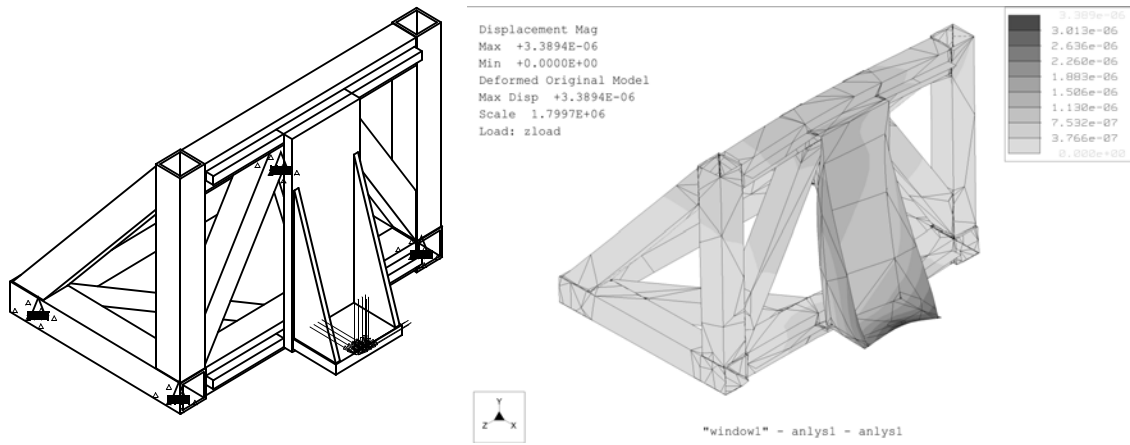


Figure 2.16 TubeMill Gantry: FEA model (a) and deformation fringe plot (b)

defining a series of analyses without starting the computation right away. Instead, all models are prepared off-line and their definitions are added to a batch file. Starting that file will run all analyses in the order they were defined which can conveniently be done overnight or on a weekend without taking up valuable computing time during regular hours.

The stiffness values shown in Figure 2.17 were calculated using the ratio between the vectors of the cutting force and the maximum displacement of the spindle mounting surface. The results for the stiffness are labeled in terms of the machine axes. The Z-axis is parallel

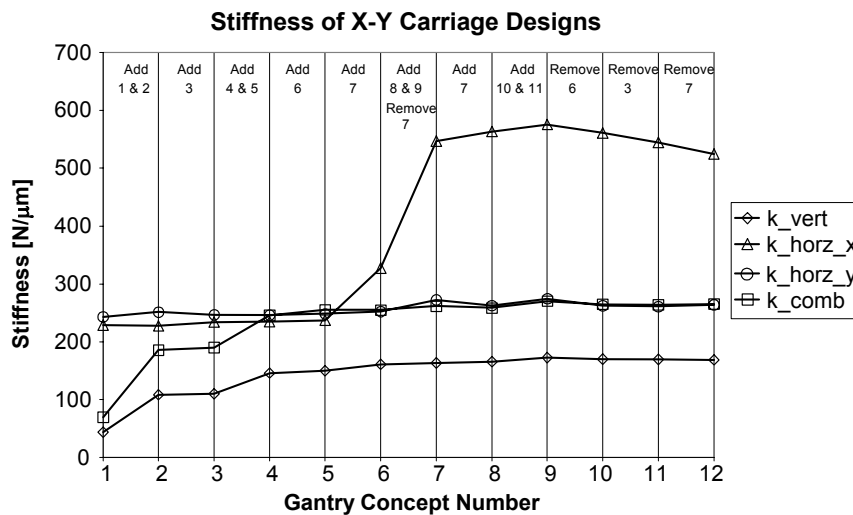
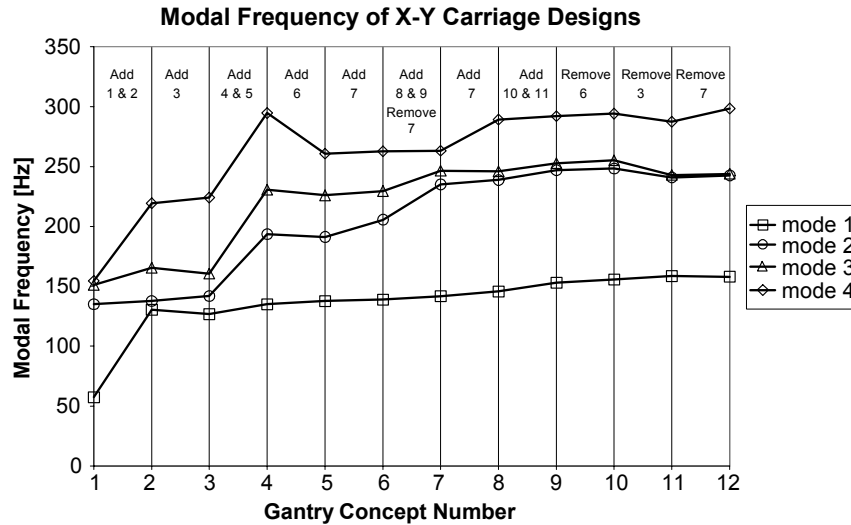


Figure 2.17 TubeMill gantry stiffness comparison



**Figure 2.18** TubeMill gantry modal frequency comparison

to the spindle axis and points from the tool towards the workpiece. The X-axis is oriented along the main gantry bearings and points from the workpiece towards the gantry. The orientation of the Y-axis is derived from the right-hand rule.

From Figure 2.17 and Figure 2.18 the following can be derived:

- Structural elements #1, #2, #4, #5, #8, #9, #10, and #11 are the beams with the most impact on the gantry's static and dynamic stiffness.
- Elements #3, #6, and #7 only play an insignificant role and will therefore not be used for the final design.
- Design #12 offers the best compromise between performance, weight, and manufacturing costs, and will therefore be used as the final design for the TubeMill's gantry.

## 2.4 Finite Element Modeling Techniques

Analyzing structures for their mechanical characteristics can be done in closed form only for very simple geometries. The deflection of a cantilevered beam, for instance, can be accurately predicted only for small displacements and well known boundary conditions using the beam equations as set up by Euler. If the cross section of the beams varies too

widely or the boundary conditions aren't defined well enough, those equations can no longer be used with an acceptable degree of accuracy. Structures such as the bed or bridge of a machine tool are frequently too complex for any closed form solutions. Their behavior under loads, such as cutting forces, can only be predicted using Finite Element Analysis techniques. Here, the geometry to be analyzed is represented by elements of finite size that share common points (nodes). Each node has a certain degree of freedom and all nodes together form a matrix that represents the stiffness matrix of this particular geometry.

### **2.4.1 Basic Facts About FEA**

Finite element methods are used to solve problems whose mathematical formulation would be too complex to be solved analytically. Instead, the problem is discretized and formulated using elements of finite size. As the size of these elements is decreased, the solution of the finite element analysis should approach the exact solution which is governed by the differential equations of motion of the actual model [Bathe]. This convergence is an important process of the analysis and the only means to quantify the result of an analysis and therefore cannot be neglected. The most widely used method to achieve convergence is referred to as h-method analysis. This scheme refines the mesh through decreasing the element size uniformly until the difference of a particular measure between two subsequent runs does not change more than a preset percentage (level of convergence).

Commonly used measures include strain energy and maximum nodal displacement. An alternative approach is taken by the p-method whereby the number of elements remains constant. Instead, the polynomial displacement expansions are increased gradually until the result has converged to within specified limits. For the case that a p-method analysis fails to converge, adding more elements by decreasing their size should help to achieve convergence. If refining the mesh does not produce the desired improvement, the mesh needs to be examined for the existence of a crack. This may occur if the automatic mesher fails to represent the actual geometry due to extreme geometric constraints such as very



small angles or radii. Failure to achieve convergence with a h-method tool can usually be traced to either the use of incompatible element types, the existence of a crack inside the mesh, or improper constraints of the model.

Commercially available finite element software is available from many different suppliers and while their appearance and interfaces may vary widely, all of them use either the h- or p-method or a combination (h/p-method) to achieve convergence of the finite element solution. For cases where the mesh has to be created manually, simply increasing the polynomial order is a very convenient and effective method of achieving higher quality results. However, automatic meshing tools have made the need for manual meshing all but obsolete and refining the mesh by decreasing the element size is a very reliable method to achieve high quality results. For this reason, most available software packages are based on the h-method.

### **2.4.2 Basic FEA Elements**

Elements are divided in three groups: one-, two- and three-dimensional elements. Three-dimensional elements are the most versatile elements available. It is very easy to assemble these elements to accurately reflect the real geometry but this ease of use comes with a big penalty: computing time is several times longer than a similar model using one- or two-dimensional elements. The idealized one- or two-dimensional elements, on the other hand, need more care during the creation but will run much faster than the more complex three-dimensional elements. Recent development in elements may make it possible to combine elements previously believed to be incompatible. Schorderet and Gmuer (1997) proposed solid to shell transition elements that allow a designer to combine these otherwise incompatible element types. This is of special importance to machine design where some components may be reliably approximated by shells while others can only be modeled from solids. In the end, it is the designer's responsibility to find the best compromise between accuracy of the results and time required for setup and to run the model.

## Beams

A beam is a one-dimensional element that:

- Represents a structure whose length is much greater than its other two dimensions.
- Has a constant cross section and thickness and thus a well known moment of inertia.

The basic approach in analytical beam bending analysis is to exclude deformations from shear and to assume that a line normal to the neutral axis of the beam remains straight during the deformation and that its rotation is equal to the slope of the beam midsurface [Bathe]. These assumptions lead to the well known Euler beam equations where the transverse displacement  $w$  is the only variable. Beam elements in Finite Element Analysis do not exclude the shear deformations. Instead, the formulation is based on the Timoshenko beam theory and does not require sections originally normal to the neutral axis to remain normal to the midsurface [Crandall et al].

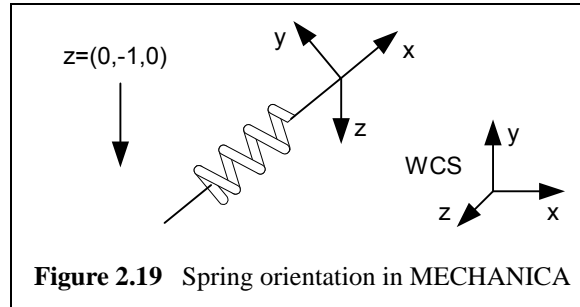
Beam representations work well where structural members already have the shape of beams. A bridge, for instance, which is built from a truss, can be very accurately modeled from beam elements. Such a model would run very quickly, several orders of magnitude faster than a comparable model built from three-dimensional elements. However, machine tools don't generally consist of beams or structural members that can easily be modeled from beam elements. For this reason, simple one-dimensional elements are very rarely used in the analysis of machine tools.

## Springs

A spring represents a linear elastic spring connection. In Pro/MECHANICA there are two types of springs available: point-to-point and point-to-ground.

### ***Point-to-point***

This type of spring is used to connect two components of an assembly to each other. A spring has three linear stiffnesses, the axial stiffness  $k_{xx}$  and two lateral stiffnesses  $k_{yy}$  and  $k_{zz}$ . It also has three rotational stiffnesses  $T_{xx}$ ,  $T_{yy}$  and  $T_{zz}$ . The element needs



**Figure 2.19** Spring orientation in MECHANICA

to be oriented in the model using the local X-axis which is along the length of the spring and the local Z-axis, whose orientation in the World Coordinate System (WCS) needs to be specified in the form of an orientation vector (see Figure 2.19). Pro/MECHANICA™<sup>1</sup> then uses the right-hand rule to determine the local Y-axis [PTC].

Point-to-point springs are extremely well suited to simulate the behavior of elastic components such as bearings and ballscrews, especially when combined with other simplified elements such as beams or shells. While it is possible, though not recommended, to connect springs to 3D elements by constraining the rotations of the connecting points, stress concentrations that result from point loads may cause the model to converge very slowly. Thus, most often, springs are used with 2D elements (shells).

### ***Point-to-Ground***

In some analyses it might be preferable to constrain a part or an assembly in a way that has some elasticity. Such a non-rigid support can be easily modeled using point-to-ground springs. Unlike point-to-point springs, grounded springs don't need to be oriented using a vector as shown in Figure 2.19. Their orientation is always with respect to the WCS.

### **Shells**

A shell element is a two-dimensional element that:

1. Pro/MECHANICA™ is registered trademark of Parametric Technology Corporation

- Represents a structure that is relatively thin compared to its length and width.
- Has a constant cross section and thickness.

The formulation of this element is based on the theory of plates with transverse shear deformations. This theory uses the assumptions that particles of the plate originally on a straight line that is normal to the undeformed middle surface remain on a straight line during deformation [Bathe]. Shell elements are created by compressing opposed surfaces to a common mid surface. Pro/MECHANICA places elements on the mid surface only, using the thickness associated with each portion of the shell to determine the depth of the elements [PTC]. If the model includes a meeting of more than two surface pairs, it is important to have the compressed mid surfaces all intersect at a common point or axis. If they do not, Pro/MECHANICA may fail to generate the proper geometry and either not run at all or produce unrealistic results. The basic elements used to create shells are fast running triangles or quadrilaterals. As with beam elements, spurious shear stresses are predicted with the displacement-based elements. These spurious shear stresses result in a strong artificial stiffening of the elements as the thickness-to-length decreases [Bathe].

## **Solids**

A solid element is a three-dimensional element that:

- Represents a structure that is as thick and wide as it is long.
- Has a cross section and thickness that can vary.

As such, three-dimensional elements like bricks, wedges or tetrahedras are the most versatile elements available. Computing time for these elements is several times longer compared to the idealized elements described earlier but set up times are shorter because no special care in creating the geometry needs to be exercised.

### **2.4.3 Modeling Bearings**

In an assembly, bearings generally represent a major source of compliance and need to be modeled accordingly. While in theory it should be possible to model a bearing with all its

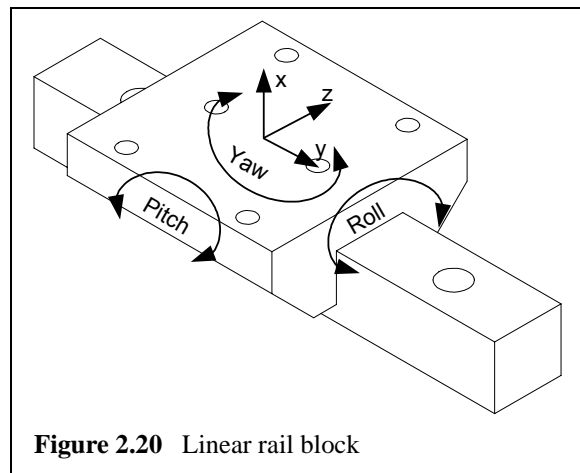
rolling elements and surfaces and then use a contact analysis to predict elastic deformation, such a model would not only take a very long time to set up but an even longer time to run. Fortunately, there is a much easier way of doing this: catalogs or data sheets provided by the bearing manufacturers have fairly detailed information on the stiffness of their products in all major directions. All the designer has to do is to incorporate this information into the FEA model. In the following, two methods of specifying bearing data are presented. The first method makes use of spring elements and the second introduces the concept of equivalent Young's moduli whereby bearings are modeled with their actual dimensions but have modified material properties that allow such a bearing to behave just like its real counterpart.

### Background

In literature, very few references on modeling techniques for bearings can be found. Among those is a study by Wang and Chang (1994) on the dynamic analysis of a spindle bearing modeled from springs and mass elements. Pitarresi and Haller (1997) use the same technique to model air bearings by using multiple springs to mimic a realistic behavior.

### Modeling Bearings Using Elastic Spring Elements

The simplest way of modeling a bearing would be to use a spring element. Such an element has three linear and three rotational stiffnesses. The first linear stiffness ( $k_{xx}$ ) is along the length of the axis and the other two ( $k_{yy}$  and  $k_{zz}$ ) are perpendicular to its axis. The rotational counterparts are  $T_{xx}$ ,  $T_{yy}$ , and  $T_{zz}$  respectively. While this is sufficient to model the vertical and lateral



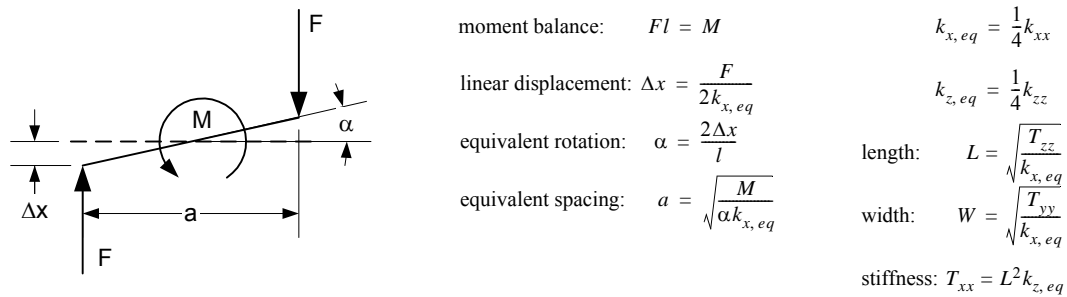
stiffness of a linear bearing block as well as its compliance in the roll, pitch and yaw direction, its single point of contact may cause the model to have difficulties converging. Also,

because solid elements have no rotations but translations only, single point contacts cannot be used to transmit moment loads from a spring into a FEA model built from solid elements. An alternative approach would be to model a bearing truck from four springs, one at each corner of the bearing. Now the loads are distributed over four points, thereby reducing stress concentrations considerably.

**TABLE 2.10** Linear and angular stiffness for selected Star Linear rail systems [Star Linear, Rasch]

Type	Size	Preload	Vertical	Lateral	Yaw	Roll	Pitch
			$k_{xx}$ [N/ $\mu$ m]	$k_{zz}$ [N/ $\mu$ m]	$T_{xx}$ [Nm/rad]	$T_{yy}$ [Nm/rad]	$T_{zz}$ [Nm/rad]
Ball	35	2%	690	531	-	3770	8550
Ball	45	2%	945	648	-	8850	20570
Ball	55	2%	1230	770	-	15930	33300
Roller	25	13%	890	490	-	1850	8000
Roller	35	8%	1466	800	-	6120	18750
Roller	45	13%	2070	1100	-	16000	60000
Roller	55	13%	2670	1540	-	25000	81800

The equivalent stiffness values for the four springs and distances between them need to be calculated such that they behave just like the real bearing. This can be achieved by following the first order approximation shown in Figure 2.21. The presented scheme relates the rotation of the bearing caused by a moment load to an equivalent load using vertical and horizontal force components only. As a result, four springs with equivalent stiffnesses



**Figure 2.21** Approximate equivalent spring stiffness and spacing

$k_{x,eq}$  and  $k_{z,eq}$  which form a rectangle of length  $L$  (Y-direction) and width  $W$  (Z-direction) can be used to represent a linear bearing block with acceptable accuracy while adding very little to the computing time required (Table 2.11).

**TABLE 2.11** Values for stiffness, length and width of linear bearing when modeled with 4 springs

Type	Size	Preload	Vertical $k_{x,eq}$ [N/ $\mu$ m]	Lateral $k_{z,eq}$ [N/ $\mu$ m]	Length L [mm]	Width W [mm]	Resulting Yaw [Nm/rad]
Ball	35	2%	173	133	7.0	4.7	6570
Ball	45	2%	236	162	9.3	6.1	14120
Ball	55	2%	308	193	10.4	7.2	20870
Roller	25	13%	223	123	6.0	2.9	4410
Roller	35	8%	367	200	7.1	4.1	10220
Roller	45	13%	518	275	10.8	5.6	31850
Roller	55	13%	668	385	11.1	6.1	47150

To verify the above approximation, the resulting compliance in the yaw direction can be calculated and compared to the angular deflection chart as measured by Star Linear. Using the equations in Figure 2.21, the yaw stiffness can be calculated to be 15660 Nm/rad. From the deflection chart given in Figure 2.22, a value of 15000 Nm/rad can be taken. The error between the predicted and measured value for the yaw stiffness comes out to be 4.4% which is reasonably good for a first order approximation.

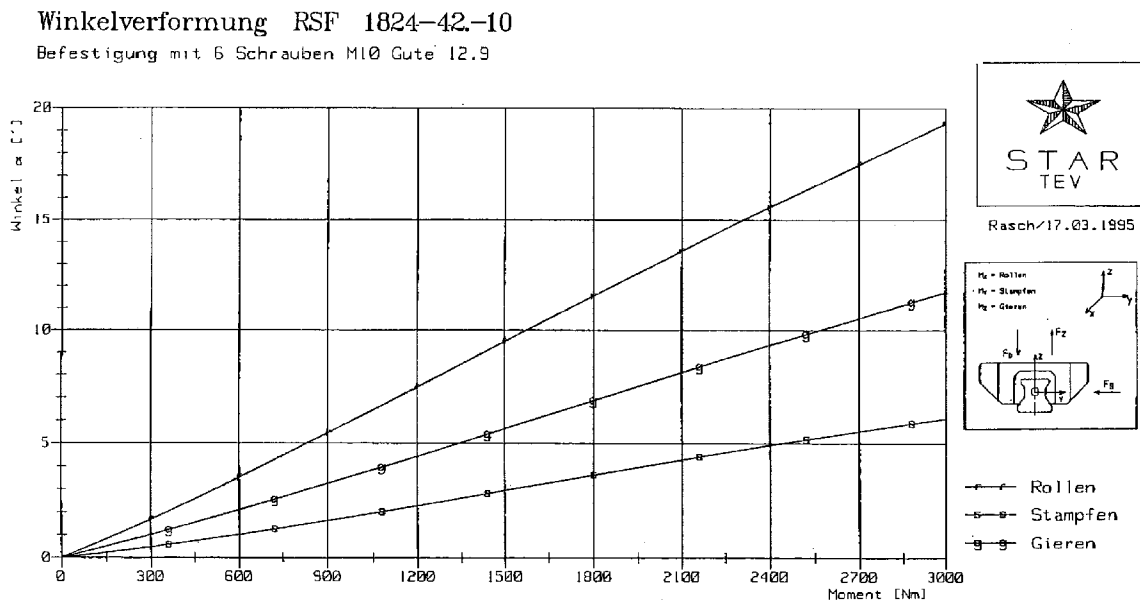


Figure 2.22 Angular deflection of Star Linear roller block size 45 (8% preload)

### Modeling Bearings Using Solids

During the conceptual phase of design, using idealizations such as shells and springs is a great way of achieving reasonably accurate results with very short computing time required. As the design evolves and more and more details are added, using such idealizations usually becomes increasingly painful because of the extra care necessary in creating these elements as well as the obvious discrepancy in appearance between the idealization and the real component. The designer is now left with two choices: to maintain two separate models, one idealized but fast running FEA model and a second, detailed CAD model for creating drawings, etc., or to prepare a realistic CAD model which can be used for the FEA as well. For the first approach, all tools required were presented in the previous sections but the second choice will need an extension.

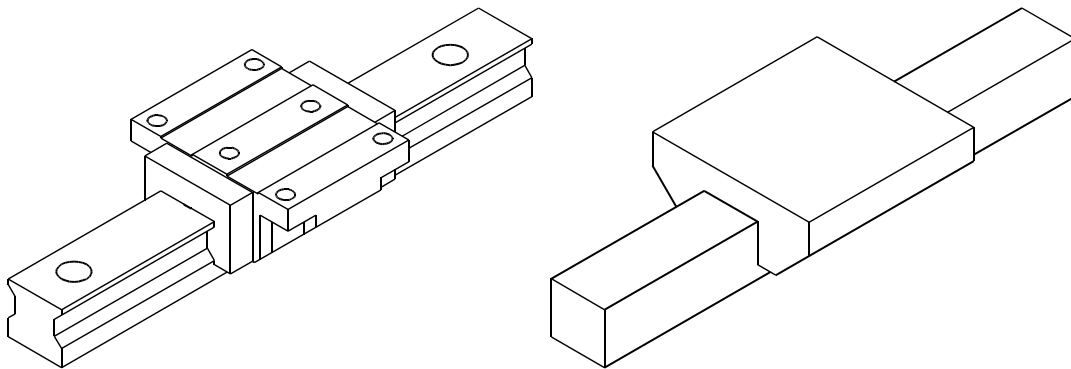
As said before, compliance of bearings is mostly a result of elastic deformation of the rolling elements. The housing of linear bearing block, for instance, is several orders of magnitude stiffer than its rolling elements. This has the following implication: a bearing block



modeled from a common material such as steel or even aluminum will appear much stiffer than it actually is. As a consequence, the result of such an FEA run will show significantly smaller displacements in the static analysis and much higher modal frequencies in the dynamic analysis than would occur in reality. In order to bring the analysis to an acceptable accuracy, two measures can be undertaken:

- Modify the geometry of the bearing model such that it will deflect as much as the real bearing.
- Modify the material properties of the modeled bearing such that it will deflect as much as the real bearing.

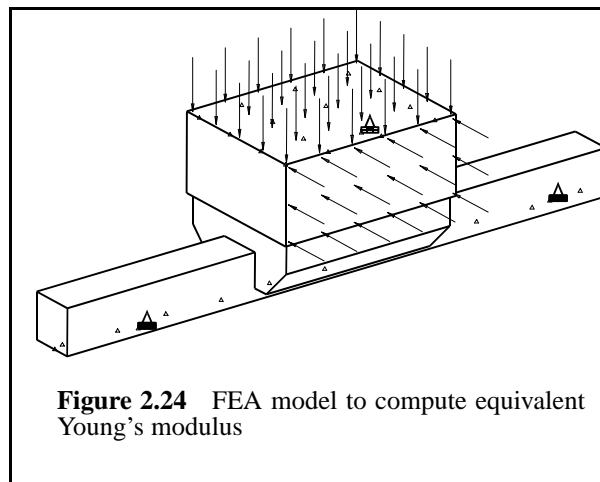
The first choice would defy the main objective for setting up an FEA model using solids: to closely resemble the appearance of the actual design. This leaves the second choice of modifying the bearing material. To preserve the mass of the bearing, the density of this new material will have to be very close to that of the actual material. What will be dramatically different is the Young's modulus of this idealized bearing material and will be referred to subsequently as the equivalent Young's modulus. It enables a bearing modeled with the actual dimensions to behave just like a real bearing even though none of the elements that cause this behavior (i.e. the rolling elements) are modeled. To speed up runtime of FEA analyses, it is crucial to suppress irrelevant details of the part or assembly to be examined. For a static analysis where displacements are to be investigated, rounds and chamfers can safely be eliminated. Bolt holes can also be neglected if they are small com-



**Figure 2.23** Linear Rail System, fully featured (a) and simplified for FEA purposes (b)

pared to the surrounding structure. Figure 2.23 shows a simplified linear rail system in comparison to an assembly that has all important features just like the real part.

In Table 2.12 the equivalent Young's moduli are given for a few representative linear rail blocks systems. The dimensions used accurately reflect the size of the actual part in order to preserve the overall shape. The equivalent Young's modulus for the trucks has been computed such that the modeled bearings have a compliance identical to their real



counterpart. The FEA model for this computation is shown in Figure 2.24. Linear rails often double as structural elements to stiffen the structure and therefore need to be modeled from steel to preserve this behavior in the model. The top plate is modeled from steel also to obtain realistic results. The bottom surface of the rail is fully constrained and the top plate has a constraint that prevents the bearing block from rolling when it is subject to the lateral load.

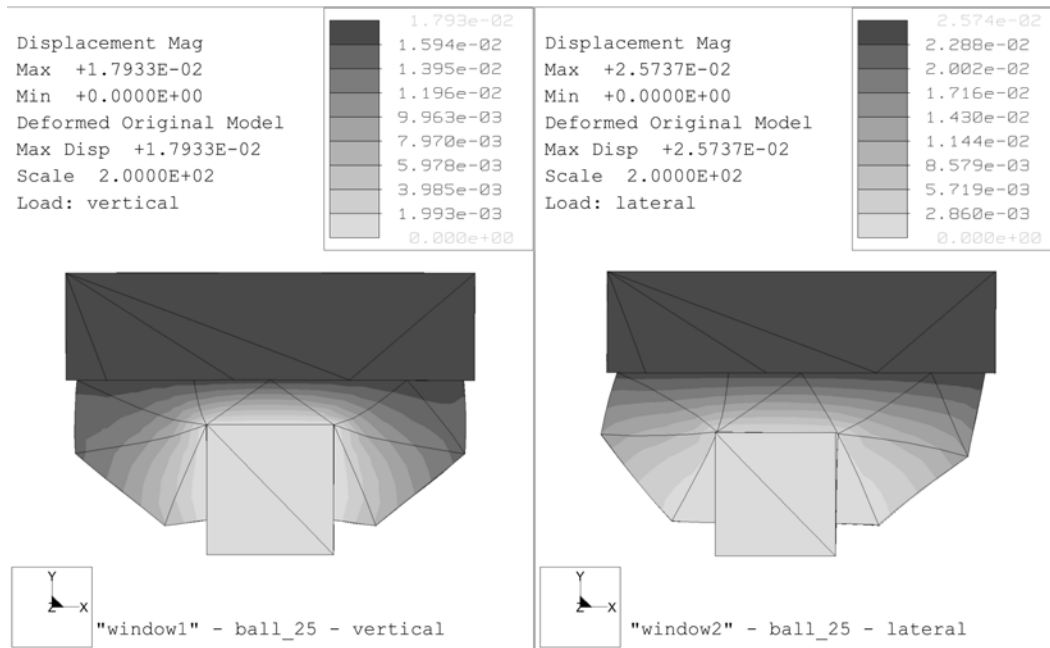
Figure 2.25 shows the fringe plot of the deformed linear bearing system under vertical and lateral loads. Because the equivalent Young's modulus of the bearing truck is much

**TABLE 2.12** Equivalent Young's Moduli and Dimensions for Selected Star Linear Rail Systems

Type	Size    Preload		Truck					Rail	
			Length [mm]	Width [mm]	Height [mm]	$E_x$ [N/mm <sup>2</sup> ]	$E_z$ [N/mm <sup>2</sup> ]	Width [mm]	Height [mm]
Ball	25	8%	81	70	29.5	3650	2040	23	24.25
Ball	35	8%	105	100	40	3560	2100	34	31.85
Ball	45	8%	133	120	50	3690	2180	45	39.85
Ball	55	8%	159	140	57	3505	2370	53	47.25
Roller	25	13%	91	70	30	5400	2920	23	23.55
Roller	35	13%	114	100	41	7060	3650	34	31.1
Roller	45	13%	140	120	51	8500	4060	45	39.1
Roller	55	13%	166.5	140	58	8800	4180	53	47.85

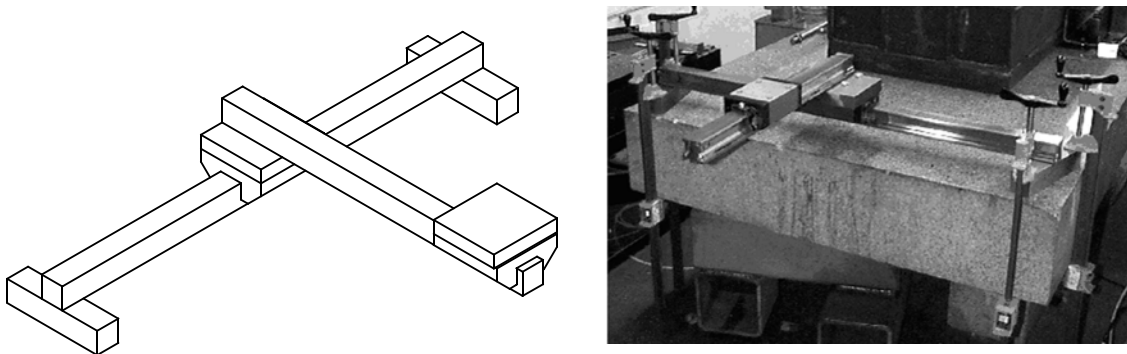
smaller than that of the rail, all deformations occur in the truck. Special care when specifying these material properties is required because the material properties are anisotropic, meaning they are not uniform in all directions. In Pro/MECHANICA, material properties are specified in the World Coordinate System, which means that depending on the bearing orientation, more than one material property set might be required. The Poisson's Ratio for these analyses was set to 0.3 and the shear modulus, which also has to be specified, can be calculated from the following constitutive equation:

$$G = \frac{E}{2(1 + \mu)} \quad (2.19)$$



**Figure 2.25** Fringe plot of size 25 linear bearing system (balls)

The technique of modeling bearings with an equivalent Young's modulus has been verified with a series of static and dynamic stiffness tests performed on an axis assembly designed for the next-generation JetMachining® Center<sup>1</sup> [Varela]. The FEA model and the actual test setup are shown in Figure 2.26. The static stiffness at the end of the cantilevered Y-axis was measured by adding weights to the end of the beams and measuring the deflection.



**Figure 2.26** JetMachining® Center axis: FEA model (a) and experimental setup (b)

1. JetMachining® Center is registered trademark of OMAX Corp.

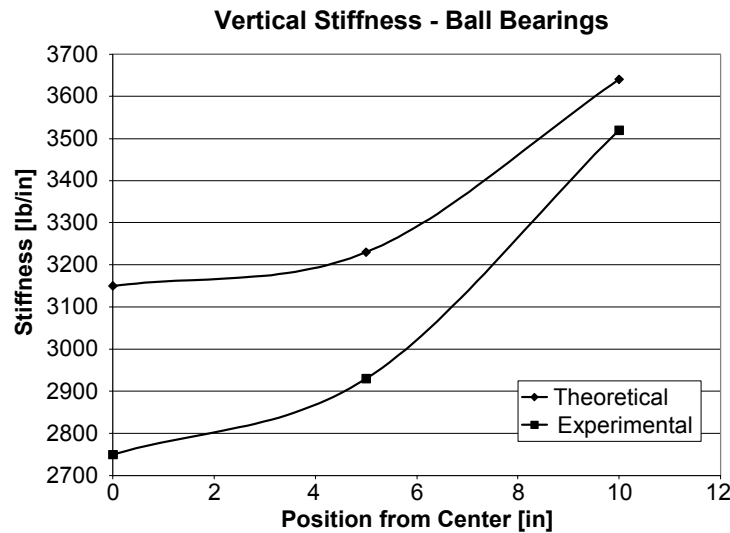


Figure 2.27 JetMachining® Center axis stiffness

tion using a 0.0005 inch resolution dial indicator. Stiffness measurements were taken with the Y-axis positioned on the middle of the X-axis, 5 inches from the middle, and 10 inches from the middle. The FEA results were off by 15%, 10% and 3% compared to the actual results. The stiffness results of the actual measurement and the theoretical stiffness predicted by the FEA are summarized in Figure 2.27. The first and second modal frequencies were predicted to be 37 Hz and 72 Hz. Using a frequency analyzer and an impact hammer, the actual modes were found to be 36 Hz and 75 Hz, an error of only 3% and 4% respectively.

#### 2.4.4 Modeling Plates as Shells

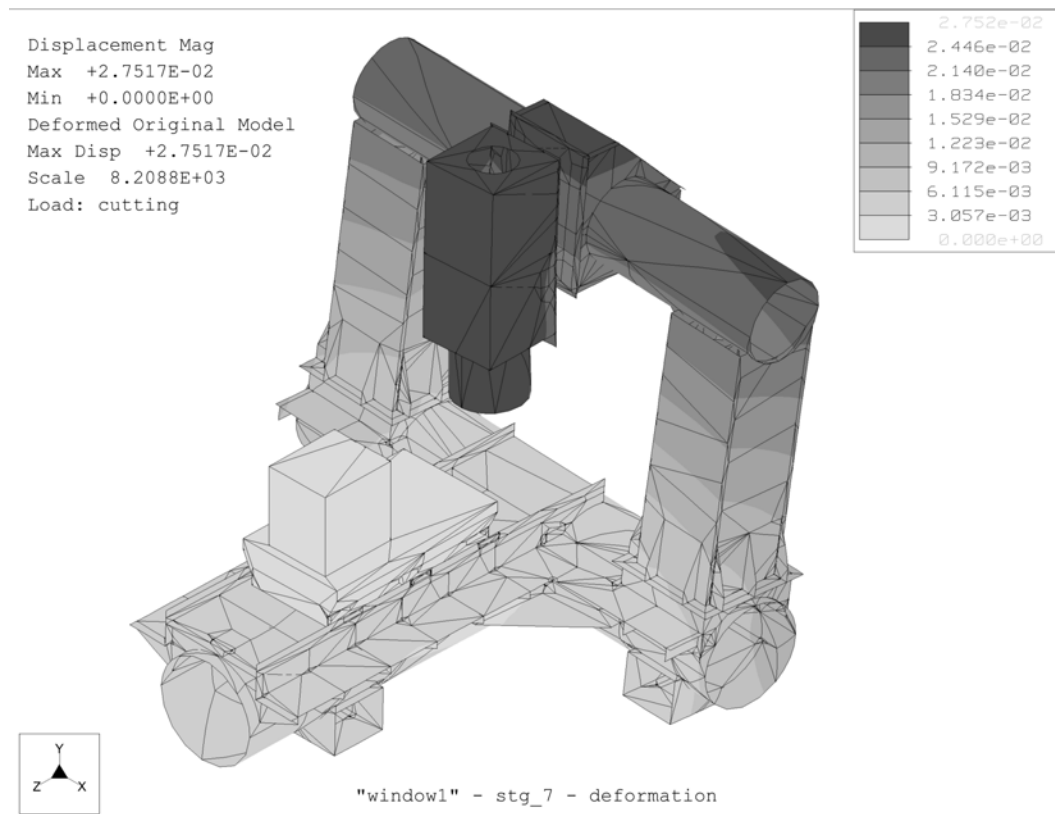
Fabricated machine tool structures are mostly welded together from steel plates. Because they are much longer and wider than they are thick, plates can be very accurately modeled as shells. Unlike using solids, the volume of such a plate does not need to be filled with computing intensive three-dimensional elements. Instead, fast running two-dimensional elements are used to span the length and width of a plate and each shell element has a constant thickness associated with it. Because shells are an idealization, several key constraints need to be obeyed when setting up a model.

- The thickness of a shell element is constant. Elements that have non-parallel surfaces cannot be modeled using shells.
- Shell elements need to be much longer and wider compared to the thickness. A minimum length-to-width ratio is around 20 to 1.
- Upon compression of the mid surfaces, no gaps can be tolerated. This becomes an especially tricky issue in assemblies where the location of the mid surface needs to be set manually.
- No loads or constraints can be specified using surfaces that are going to be compressed.
- Intersections are very critical because the compressed mid surfaces need to intersect at a common point or axis.

### 2.4.5 Constraints

For an FEA model to be set up properly, all six degrees of freedom of a rigid body need to be fully constrained. Mathematically, this is achieved by constraining 6 spatially distributed points, where no more than 2 points can be on a single line. In practice, constraining points causes a model to have stress concentrations, making the convergence of the analysis more difficult than necessary. Therefore, rather than using points or even edges, surface patches are the most practical means of constraining a model. For a machine base, for instance, those patches would have the size and location of the actual machine supports, which makes the analysis as realistic as possible. This is especially important for modal analyses where the constraints have a large influence on the mode shapes and their frequencies. In such a case, the model may remain unconstrained and a filter applied to get rid of the rigid body modes that are otherwise detected.

For structural stiffness analyses, where the displacements between two specific components are of interest, one of the components can be used to constrain the model while the other one applies the loads. An example of this technique, where the loop stiffness of a machine concept is investigated, is presented in Figure 2.28. Rather than constraining the base using its supports, the headstock is fully constrained. The loads to simulate machining forces are applied at the spindle.



**Figure 2.28** FEA analysis to predict loop stiffness

## 2.4.6 Performance and Accuracy

The previous sections indicated the basic differences between basic FEA elements and it is now time to go into more detail about the differences in performance and accuracy involved.

### Cantilevered Beam

First, two simple beams with one end fixed and the other one free are modeled with two-dimensional (shells) and three-dimensional elements. A load is attached to the free end of the beam and the displacement at the free end is computed. The runtime and predicted displacements at the free end of the beam depending on the convergence level of strain

energy and local displacement are presented together with the exact solution according to Euler [Avalone et al] in Table 2.13 and Table 2.14.

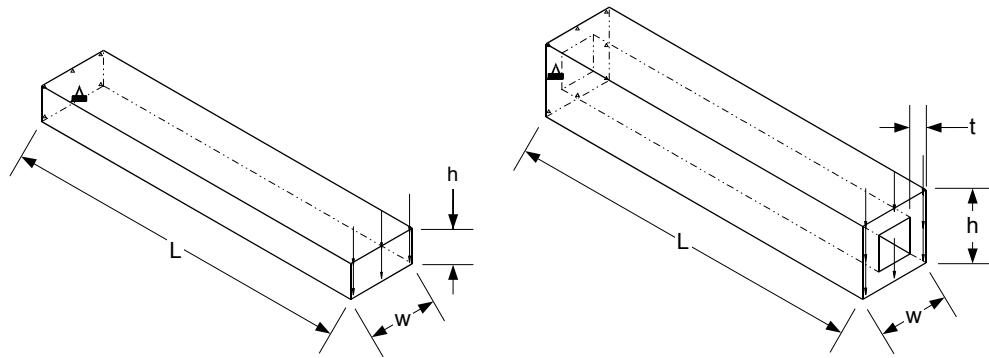
**TABLE 2.13** Solid beam, 100 mm long with load of 100 N attached to free end

Cross Section	Type	10% Convergence		5% Convergence		1% Convergence		Euler
		disp. [mm]	time [s]	disp. [mm]	time [s]	disp. [mm]	time [s]	
20x5	Solid	7.794E-1	6	7.862E-1	8	7.896E-1	20	7.980E-1
	Shell	7.823E-1	4	7.823E-1	3	7.823E-1	3	
20x10	Solid	9.852E-2	5	9.910E-2	8	9.943E-2	19	1.0E-1
	Shell	9.889E-2	4	9.889E-2	3	9.889E-2	4	
20x20	Solid	1.242E-2	5	1.267E-2	5	1.268E-2	20	1.250E-2
	Shell	1.271E-2	3	1.271E-	3	1.271E-	4	

**TABLE 2.14** Thin walled beam, 100 mm long with load of 100 N attached to free end

Cross Section	Type	10% Convergence		5% Convergence		1% Convergence		Euler
		disp. [mm]	time [s]	disp. [mm]	time [s]	disp. [mm]	time [s]	
20x20x2	Solid	2.367E-2	38	2.388E-2	59	2.399E-2	173	2.117E-2
	Shell	2.319E-2	8	2.319E-2	4	2.396E-2	5	
20x20x5	Solid	1.388E-2	13	1.390E-2	24	1.396E-2	37	1.333E-2
	Shell	1.509E-2	4	1.509E-2	4	1.527E-2	5	





**Figure 2.29** FEA model of solid (a) and thin walled (b) beam cross section

**TABLE 2.15** Deviation from Eulerian beam equation result

Cross Section	10% Convergence		5% Convergence		1% Convergence	
	Solid	Shell	Solid	Shell	Solid	Shell
20x5	-2.3%	-1.9%	-1.5	-1.9%	-1.0%	-1.9%
20x10	-1.5%	-1.1%	-0.9	-1.1%	-0.6%	-1.1%
20x20	-0.6%	1.7%	1.4%	1.7%	1.4%	1.7%
20x20x2	11.8%	9.5	12.8%	9.5%	13.3%	13.2%
20x20x5	4.1%	13.2%	4.3%	13.2%	4.7%	14.6%

For the solid beam, both two- and three-dimensional elements predict the displacement of a cantilevered beam with respectable accuracy. Depending on the level of convergence, shell based FEA models run at 25% of the time required for the three-dimensional model. The thin walled beam, however, reveals a few surprises. First, the 2 mm thin cross section requires almost five times the computing time of the 5 mm thick cross section. Also, the predicted displacement deviates around 13% from the actual displacement for the thin section compared to less than 5% for the thick section. This leads to an important conclusion: three-dimensional elements aren't well suited for sections that have a small thickness-to-width ratio. Should a model require these elements nevertheless, caution is necessary when sizing the elements. As a rule of thumb, sections with a small thickness-to-width

ratio need to have significantly smaller element sizes than specified by default settings found in many software packages.

The 2D elements also show some noticeable deviation from the exact solution. Of interest is that the result for the thinner section is closer to the displacement predicted by the Eulerian beam equation than the thicker section. This is generally true for shell elements and is due to the way these elements are created. As mentioned in Section 2.4.4, midsurfaces which are the basis of these elements, are created by compressing opposed surfaces. The thinner the cross section, the closer the location of the midsurface will be to that of the actual surfaces, giving the model a better accuracy. For shell elements to be acceptably accurate, the ratio between width to thickness should be 20 or better.

### **STG Bridge**

To further demonstrate the differences between two- and three-dimensional elements, two FEA models based on these elements of the STG 5-axis tool and cutter grinder are analyzed and examined for the result and runtime (Figure 2.30). The geometry of both models is identical and the default settings for sizing the elements has been used. To show the effects of convergence levels, a moderate 5% was set for one run and then subsequently decreased to a rigorous 1% level. The model has both of its supports fully constrained so as to simulate the bolted-on connection to the base of the machine. The surfaces to which the bearing blocks are mounted have a load attached which is equivalent to a cutting force of 1000 N acting at the tool tip in the direction of the Z-axis.

Because the force acts right in the center of the model parallel to the Z-axis with no component in the X-direction, further time saving could have come from using the symmetry of the model. This is a method whereby a symmetric model is cut at the symmetry line and the created surface is constrained accordingly. Because only half of the model needs to be analyzed, computing time is reduced by 50%. However, this method only works when both the geometry of the model and all applied loads and constraints exhibit the same symmetry.

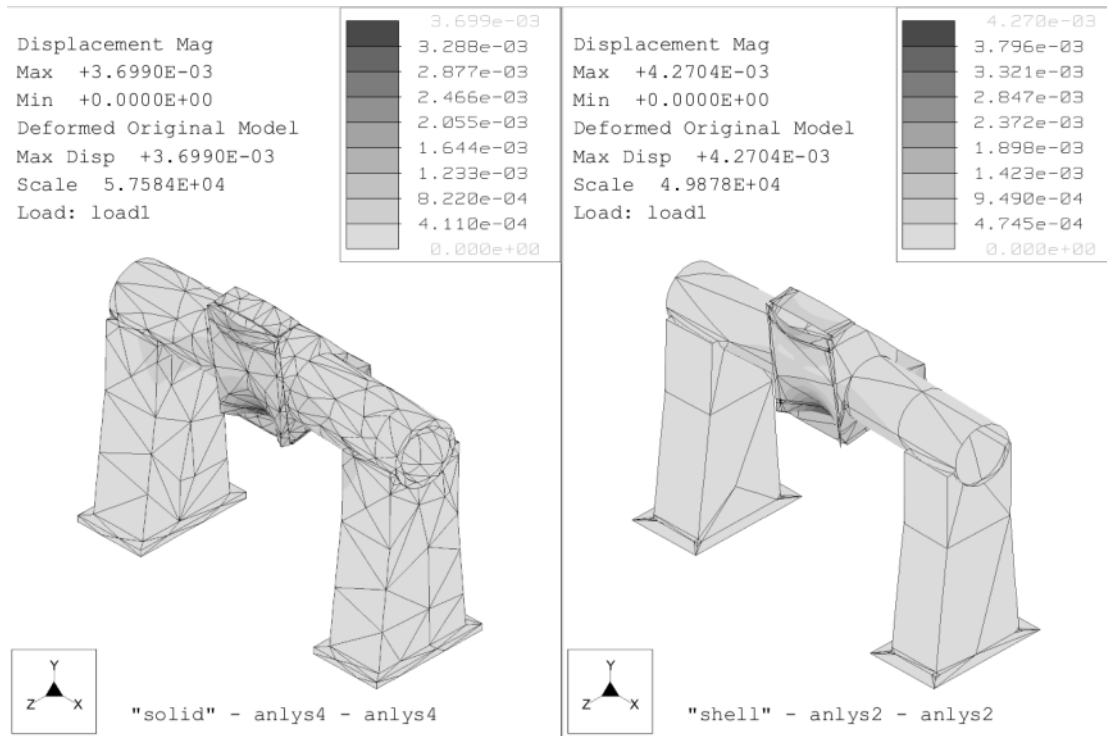


Figure 2.30 STG bridge modeled as solids (a) and shells (b)

TABLE 2.16 STG bridge modeled with shell and solid elements

	5% Convergence		1% Convergence	
	Solid	Shell	Solid	Shell
Maximum Displacement [mm]	3.65E-3	4.24E-3	3.65E-3	4.25E-3
Rotation of mounting surface [rad]	1.78E-6	1.94E-6	1.79E-6	1.98E-6
Runtime [min]	150	3.5	473	6.5

## **2.5 Conclusion**

Throughout this section, examples were used to illustrate one of the core elements of rapid machine design: the use of advanced engineering tools for generating and evaluating concepts for production equipment. A step by step selection process was introduced which is capable of reliably identifying the best of all concepts at hand. Although not specifically mentioned, the presented method of computer aided concept generation paired with a well structured evaluation process is applicable at every level of a design process, starting with the overall machine concept all the way down to the development of components and sub-components. The only difference with component concepts is the following: the overall machine concept has already set the realm of the component. Because a component is a subset of an entity, its degree of freedom as far as shape and functionality is concerned can only be a fraction of what was available for the overall design. In other words, it is of no use to develop concepts of components that are no match for the overall concept. If the overall design calls for a gantry, developing anything that is not shaped like a gantry is futile. Deviating from the design goal set by the selection of an overall concept will result in wasted time and effort.

# Chapter 3

## MANUFACTURING PRINCIPLES

The methodology of rapid machine design attempts to shorten design-to-manufacture time of production equipment by using advanced engineering tools such as CAD systems and finite elements in the conceptual design phase. This part of rapid machine design has been discussed in Chapter 2 in great detail. Now it is time to present the remaining elements of this novel design approach starting with the machine structure.

### 3.1 Fabricated Structures

Traditionally, the base and other major components of a machine tool have been made of gray or nodular cast iron, which has the advantages of low cost and good damping, but the disadvantage of heavy weight. Casting is a net-shaping process whereby molten metal is poured into a mold, thereby assuming its shape upon solidification. In modern equipment design, lightweight structures are desirable because of ease of transportation, higher natural frequencies, and lower inertial forces of moving members [Kalpakjian]. Lightweight designs are a basic goal in rapid machine design and require fabrication processes such as mechanical fastening (bolts and nuts) of individual components and welding. A fabricated design consists of pre-cut stock materials such as plates, tubes, channels, and angles which are joined together to form the structure. Such stock items are available in a wide range of sizes and shapes and have some highly desirable mechanical properties such as formabil-

ity, machinability and weldability. Of special interest are round and rectangular tubes whose closed cross sections have a very high stiffness-to-weight ratio.

Polymer concrete is yet another type of material used to build structures. The process and characteristics are very similar to cast iron designs, requiring molds and time to cure. Compared to cast iron, polymer concrete structures have a better strength-to-weight ratio, thermal stability and damping capacity. As a recent development, profiled structures from aluminum are available that can easily be cut to length and joined through fasteners to form the desired structure. However, due to the excessive thermal expansion coefficient of aluminum and the limited strength of the joints, applications are generally limited to low force operations such as very light machining or assembly.

In rapid machine design, fabrication is the preferred technique because of the following key advantages:

- Low fixed costs make it highly suitable for low to medium production volume.
- Fabrication can easily be done in-house, making the need for outsourcing obsolete.
- Use of highly standardized materials ensures high availability and competitive prices.
- Fabrication equipment is rather inexpensive [Kalpakjian].
- Minimum tooling costs. Fabricated structures only need some form of fixturing which is universally applicable. No expensive molds are required.
- Minimum lead time. No proprietary tooling such as molds are required, shortening design-to-manufacture time.
- Great scalability. No re-tooling required when scaling the design to change available workvolume.
- High flexibility. Design changes are not impaired by existing tooling, making alterations inexpensive and easy to implement.
- Modular components can initially be fabricated separately and then joined whenever it is convenient.

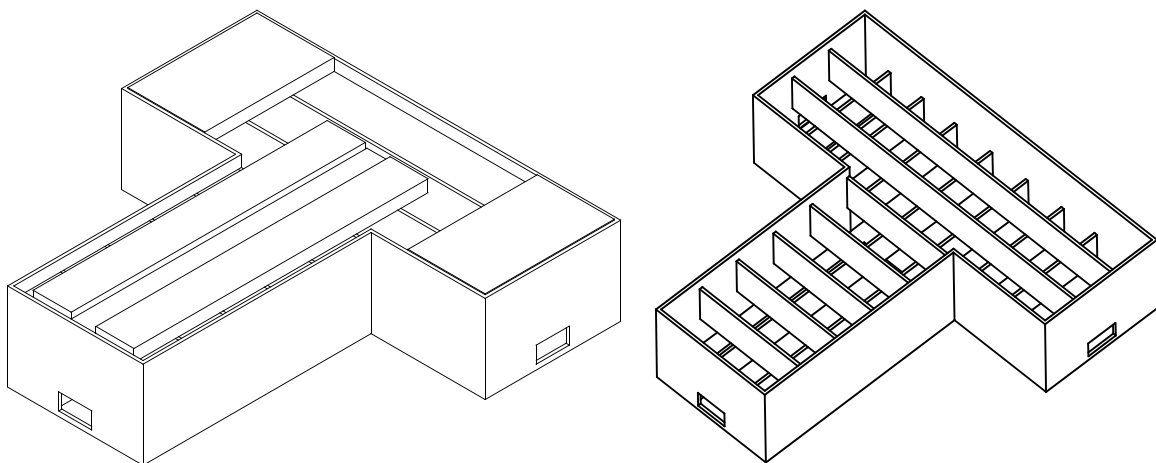
However, fabricated structures have also a few disadvantages associated. These include:

- Comparably high variable costs prohibit large production volumes.
- Structures generally need stress-relief either through thermal or vibrational relaxation.
- All welds should be reasonably accessible, imposing sometimes hard to meet design constraints.
- Fabricated structures have much less damping compared to cast-iron based designs, requiring other forms of damping such as constrained layer damping (see Section 4.5).

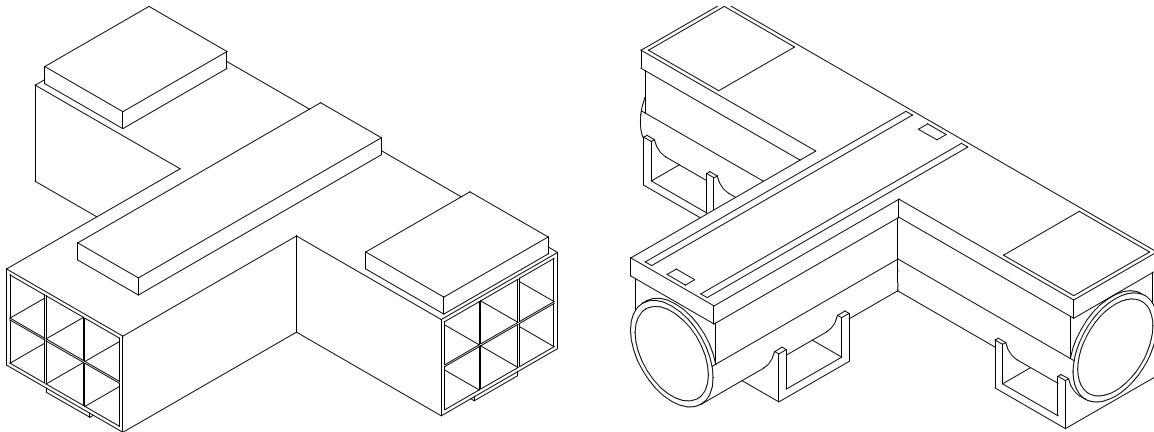
Despite the shortcomings listed above, designing and building a machine as a fabricated structure has the big advantage of a much lighter design with a substantially shorter lead-time compared to a cast design.

An example of a conventional box-type machine base is shown in Figure 3.1a. The pictured structure is fabricated by welding steel plates together to form a box. The base is strengthened by welding webbing to the inside of the box (Figure 3.1b). Additional stiffness and especially damping comes from concrete which is used to fill all cavities of the base.

Alternative designs are presented in Figure 3.2. The ShearDamper™ base shown in Figure 3.2a is an open box-type design with no webbing inside the base. Instead, all cavi-



**Figure 3.1** STG conventional box-type base design with concrete filling



**Figure 3.2** Box type base with ShearDampers™ and based on large diameter round tube

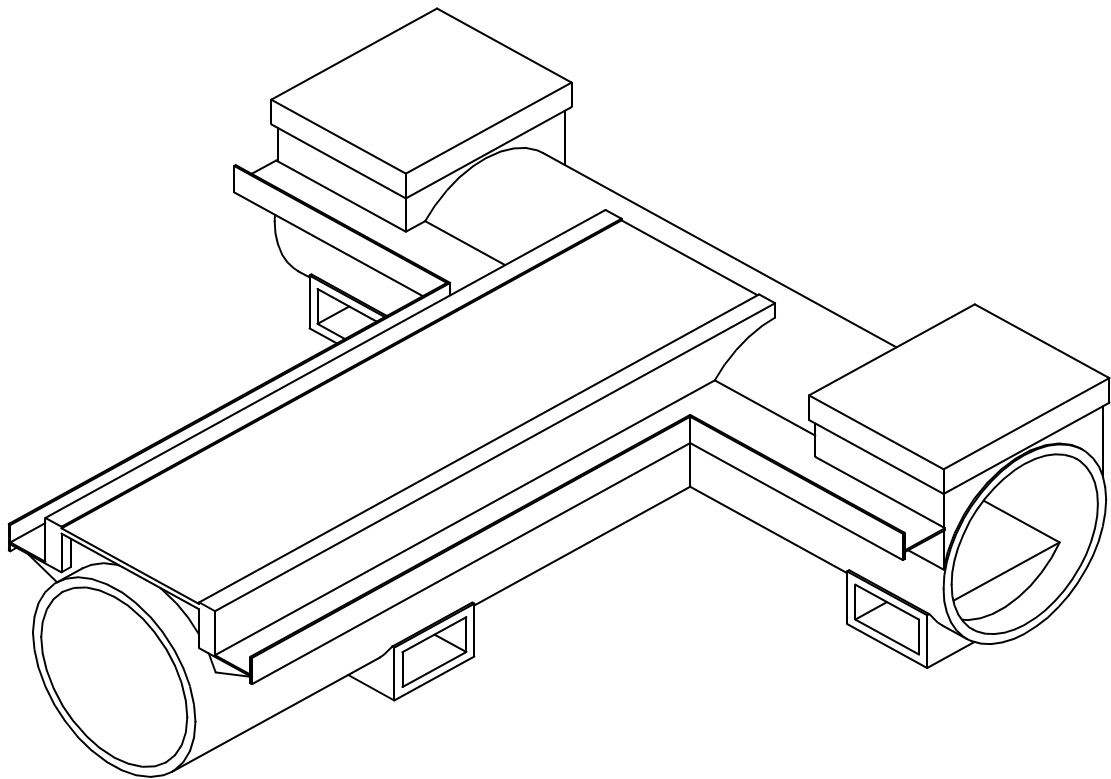
ties are filled with rectangular ShearDampers™<sup>1</sup> that add both stiffness and most of all damping to the structure. The novel base design in Figure 3.2b is primarily fabricated from two, large diameter tubes which are welded together to form the T-shaped base required for the STG. As discussed in Section 2.3.3 on page 44, round structures have significant advantages over rectangular designs in terms of stiffness and weight and led to a round tube based gantry design for the STG. For that same reason, the actual base of the STG, which is shown in Figure 3.3, is build from two round tubes as well, resulting in a lightweight yet remarkably stiff design.

At the core of the STG base are two 24 inch diameter tubes with a wall thickness of 1.5 inches. The back tube, which has the mounting surfaces of the bridge welded to its ends, is a continuous pipe of 80 inches in length. The front tube receives a circular cut along the face which is welded to the back tube. Shaped webbing is welded on top of the round base to form an interface between the flat top plate and the round surfaces of the base core.

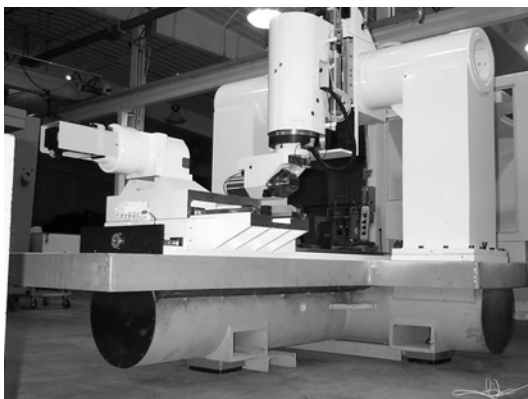
---

1. ShearDamper™ is a registered trademark of AESOP, Inc.





**Figure 3.3** Final base design for STG



**Figure 3.4** STG tubular base design

### 3.2 Kinematically Defined Machine Supports

A machine base, regardless of how light and stiff it might be, will elastically sag between supports from its own weight. While fabricated structures generally have a better strength-to-weight ratio than cast structures, the weight induced sag is an important issue nevertheless because it causes supposedly flat surfaces to warp. The traditional way of dealing with this symptom is the following: the machine base is milled and ground on a machining center large enough to hold the entire base. With the base evenly supported, all precision surfaces are machined to specification. Next, the base is put on its supports which are commonly located in the corners of the base and, depending on the overall length, sometimes even in between. Because the support is now localized and no longer uniform, the structure will sag, which is removed through scraping. Scraping is a manual finishing process whereby a thin layer of ink is spread over the surface of interest. Next, a straight master surface, usually granite, is put on top and rubbed against. The ink will wear off at the high spots but remain untouched at the low spots. Next, a scraper is used to remove all high spots and then the process is repeated until the surface is sufficiently flat. Due to its low forces, scraping is a tremendously accurate but also very time consuming process that requires very skilled workers.

In rapid machine design, the problem of sag is avoided altogether by two key measures: kinematically defined support and a specialized machining setup. A rigid body has six degrees of freedom, three translations and three rotations. No more than six spatially distributed points (constraints may not be in line) are required to fully constrain such a body, and these are referred to as kinematically defined constraints. The orientation of the body, because it is kinematically defined, is free of any ambiguity and the body will always assume the exact same position in space. For objects that need to be located on a non-frictionless surface such as the floor of a machine shop, three points of contact are enough for a complete constraint. The three spatially distributed points constrain one translational (vertical) and two rotational (pitch and roll) degrees of freedom. The remaining two translational (horizontal) and rotational (yaw) degrees of freedom are constrained through fric-

tion at the supports, provided that the forces parallel to the floor are smaller than the static friction forces. It should be noted that machine supports are unaffected by machining forces because they are not part of the structural loop. The only forces that affect the supports are external forces and inertial forces which are caused by vibration and moving members of the machine as they accelerate or decelerate.

Using a three-point support for machine structures preserves its integrity when it is moved, i.e. the structure does not undergo dimensional changes between setups. A surface will be just as flat and an edge just as straight as it was when the machine was assembled originally. This also holds while the machine is still in production at the manufacturer's plant and leads to the special machining setup mentioned at the beginning of this section. Rather than machining a machine base with uniform support using shims, the base is machined using its native three point support. Now the sag from its own weight is machined out initially and the geometry of the base does not change when it is put down from the machining center onto the floor.

### **3.3 Standard Machine Elements**

In an attempt to keep component cost and assembly time down, equipment designed according to the rapid machine design philosophy heavily relies on standard machine elements. The highly competitive market for these systems helps to keep costs down and quality up.

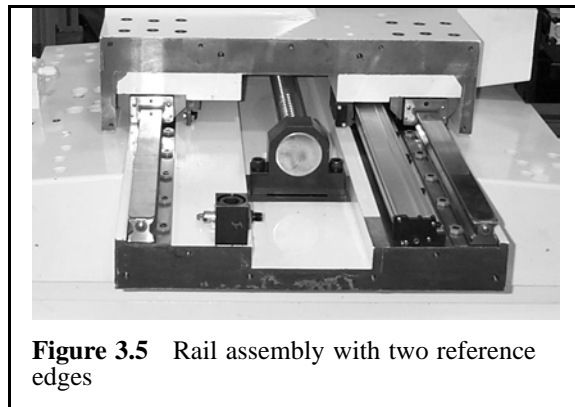
#### **3.3.1 Linear Rails**

The STG is equipped with a standard linear bearing system as offered by numerous suppliers such as NSK, THK, Schneeburger or Star Linear. Bearing trucks and rails are highly standardized and bolt compatible. While the actual bearing surfaces are proprietary, i.e. rails and trucks from different vendors cannot be mixed, the bolt compatibility of these systems allows to switch to a different supplier without the need for redesign.

Linear bearing systems that use rolling elements are known to have very little static friction, which makes them a good choice for applications where precise positioning is needed. Both ball and roller systems can be used; however, since balls make only point contact with the rails, they are prone to indentation when subject to sudden overload such as a machine crash. Rollers, on the other hand, make line contact and provide more safety against damage from overloading the system. While they tend to have slightly higher internal friction and can't sustain speeds as high as ball-based bearings, they usually are the better choice for machine tools that require high dynamic stiffness. Roller bearings, because of their slightly more complicated internal circulation mechanism, are more expensive than ball bearings. However, due to their higher load capacity, roller bearings can frequently be sized one size down from ball bearings, making roller systems only about 10% more expensive than their ball counterparts.

Linear bearing rails, even though their rated straightness might be in the order of a few microns, are not straight at all when they come out of the box. Instead, the rails have a reference edge on either one or sometimes even both sides that is used to straighten the rail as it is being tightened to the machine's structure. Common techniques include ground or scraped reference edges that are part of the structure against which the rails are being pushed by wedges or frequently spaced cam screws (see Figure 3.5).

High accuracy applications will use one reference edge for each rail, creating a highly overconstrained but accurate system. Less stringent applications will have only one rail being pushed against a straight edge. This rail is called the master rail and once fully tightened, the slave rail is being tightened at a position dictated by the master rail.



**Figure 3.5** Rail assembly with two reference edges

A recent development in precision machine assembly eliminates the use of a reference edge altogether. Instead, the profile of the rail is recorded and while the rail is tightened to the structure, wedges are used to bend the rail according to the measured profile.

The non-straightness of bearing rails and the consequence of having to straighten them as they are mounted to the structure, raises an important concern with fabricated structures: the local stiffness of the structure surrounding the bearing rails needs to be considerably higher than the stiffness of the rails. If this was not the case, and the structure's compliance was of the same order as the rail's compliance, the rail would actually warp the structure rather than being straightened by it. Consequently, the linear bearing system would not be as straight as rated by the bearing vendor, causing an increase of error due to non-straightness which has not been accounted for in the error-budget.

### **3.3.2 Ballscrews**

To convert the rotary motion of a motor into the linear motion needed by a machine axis, ballscrews are very often used. As a highly standardized component, ballscrews are available in a wide range of sizes from many different suppliers. Like the linear bearing market, competition among suppliers is intense, ensuring high quality and reliable availability at a very competitive price. And since all major components are standardized, switching to a different supplier once the machine is in production is not a problem at all. Ballscrews are the most often used solution for driving machine axes for the following reasons:

- Easy and reliable conversion from rotary to linear motion.
- Low friction losses through recirculating rolling elements within the ballscrew nut.
- Easy and reliable preload of the ballscrew nut through oversized rolling elements or preload through double-nut. This is done by the supplier according to specifications.
- Low maintenance when connected to automatic machine lubrication system.
- Excellent lifetime when properly protected from overloading.
- High rigidity when properly dimensioned.

- Built-in transmission ratio improves position accuracy and allows the use of inexpensive rotary encoders mounted to the end of the shaft.
- Built-in transmission ratio generates high forces with comparably small torques, limiting the required motor size.

The downsides of the design are:

- Ballscrews need to be protected from overloading through either a torque-limiting clutch or electronic torque limit circuitry to prevent indentation of the threaded surface.
- Ballscrews need to be covered to keep chips and grit off.
- Rigidity of the ballscrew assembly varies with the position of the nut along the length of the shaft.
- Frictional losses within the nut cause the shaft to heat up and expand thermally.
- Rotational speeds are limited by critical speed of the shaft.
- Torsional compliance of the screw leads to control errors.
- Heavy preload or internal cooling is needed to prevent thermal errors.

Some of the disadvantages listed above can be compensated for. Thermal expansion, for instance, can be limited through temperature controlling the screw, by having coolant run through the hollow shaft [Makino]. Mounting the rotary encoder on the non-driven end of the ballscrew eliminates errors as the screw is twisting under load [Slocum (a)] while using a linear encoder also eliminates errors from thermal expansion of the shaft. Altogether, ballscrews are very versatile and deservedly the most often used system to drive machine axes.

### **3.4 Replication**

In general, replication is a shaping process whereby a polymer is poured around a master feature, thereby assuming its shape accurately. The master feature is coated with a mold release and can be removed and reused once the polymer has cured. To minimize the effect of shrinkage, the polymer needs to have very low shrinkage and be applied as thin as possible. The thin layer also limits the amount of polymer used, and since the curing process

of most resins is exothermic, limits the amount of heat generated during the process which otherwise might distort the replicated feature.

### 3.4.1 Reference Edge

Using a straight edge it is possible to replicate the reference edge used to align machine elements such as linear rails. This eliminates the need for machining this particular feature, cutting down fabrication time and the need for machine tools big enough to hold the structure whose reference edge is to be created.

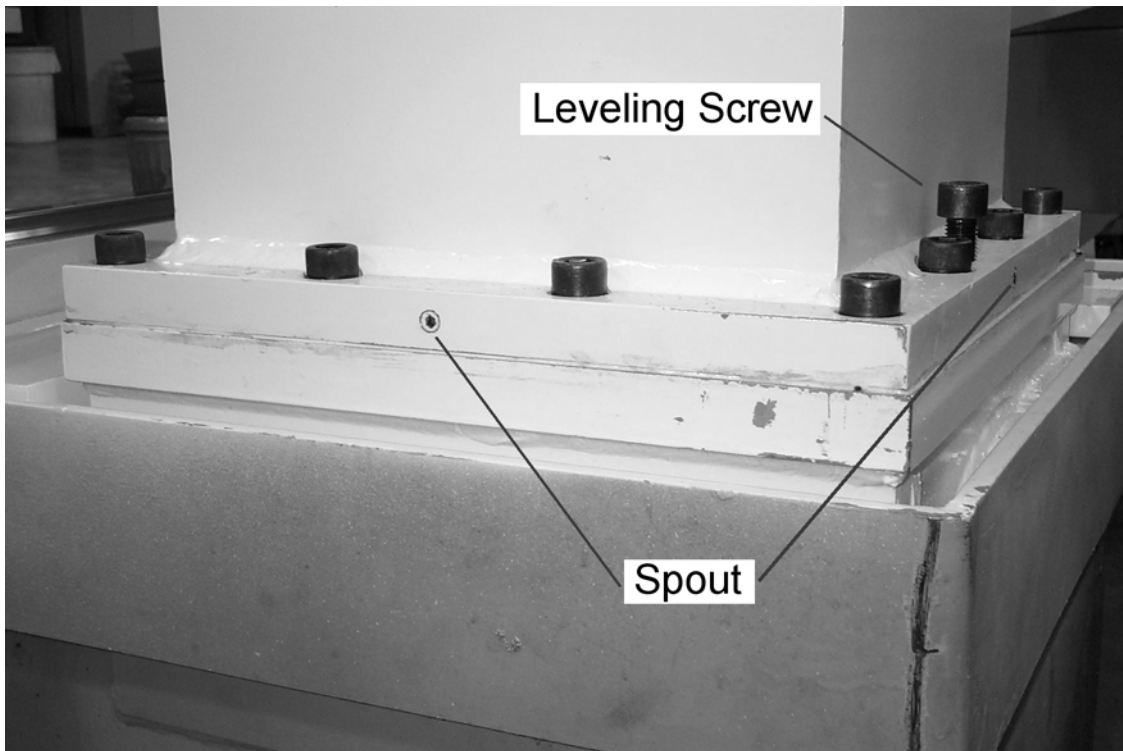
### 3.4.2 Replicated Joints

A tremendously useful application of replication is a technique whereby polymer is used to bridge gaps between machine components. This technique is used at the interface between base and bridge of the STG and is shown in Figure 3.6. The use of polymer eliminates the need for precision surfaces at the joint between the bridge and the



**Figure 3.6** STG bridge - base joint

base. Instead, the bridge is set upon an O-ring which is laid along the perimeter of the joint. The thickness of the ring is chosen such that a small gap ( $<1$  mm) exists within the joint. Next, the bridge is leveled and oriented using three leveling screws until the Y-axis is properly aligned with respect to the X- and Z-axis. Finally, polymer is injected through four spouts into each joint until the gap between the two mounting surfaces is completely filled (see Figure 3.7). Once the moglice has cured, the leveling screws are removed and the bolts around the joint tightened.



**Figure 3.7** Replication of mating surfaces

Replication of the joint surfaces has the following advantages that make it an important element of rapid machine design:

- Mounting surfaces need no particular precision, allowing the surfaces to be milled instead of ground or even scraped.
- The ability to easily align the bridge to the base allows the two components to be completely finished as separate components.
- Deformations of the base as a result of the weight of the bridge are automatically compensated for during the alignment process.
- Deformations of the bridge as a result of its own weight are automatically compensated for during the alignment process.
- The large distance between the leveling screws allows for a very fine alignment.



# Chapter 4

## DAMPING

The preceding chapters were mostly concerned with the static response of the machine to loads as they occur during machining. Now it is time to address the dynamic issues as well. Cutting forces have a static and a dynamic component with a wide range of excitation frequencies. If a structure becomes excited at or near its natural frequency, the responding amplitude can exceed the static deflection by several orders of magnitude. The result of this amplification will show up in the form of vibrations and may severely affect the performance of the design.

### 4.1 Mathematical Models

To gain some insight into the dynamics of a structure, it is useful to first examine the behavior of a single degree of freedom mass-spring system that has a dashpot attached. The equation of motion for such a system can be written as:

$$m\ddot{y} + c\dot{y} + ky = F(t) \quad (4.1)$$

where  $m$  denotes the mass and  $k$  the stiffness of the spring.

It is common to rewrite Eq. 4.1 in terms of its resonance frequency  $\omega_n = \sqrt{k/m}$  and damping factor  $\zeta = c/(2\sqrt{km})$  which then becomes

$$\ddot{y} + 2\zeta\omega_n\dot{y} + \omega_n^2y = \frac{F(t)}{m} \quad (4.2)$$

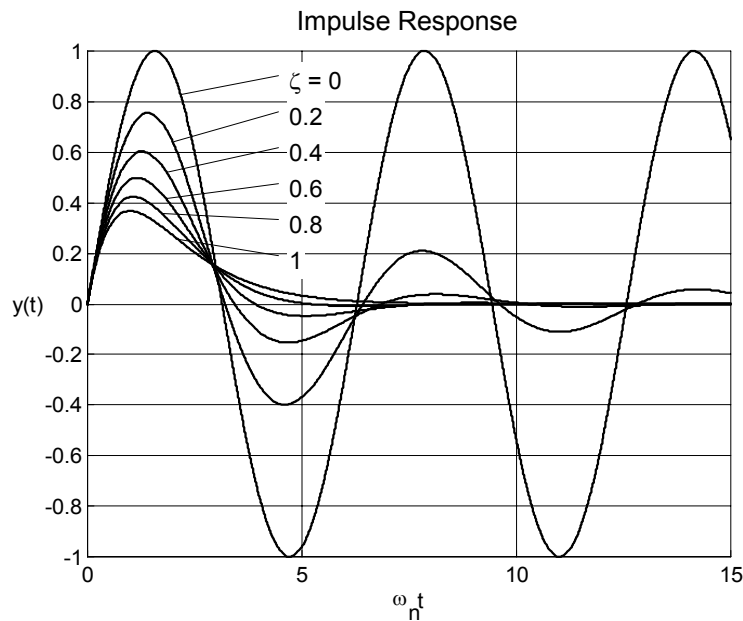
whose transfer function using a Laplace transformation can be written as:

$$H(s) = \frac{\omega_n^2}{s^2 + 2\zeta\omega_n s + \omega_n^2} \quad (4.3)$$

The response of such a system has three distinct solutions for  $0 < \zeta < 1$ ,  $\zeta = 1$  and  $\zeta > 1$ . The first solution is referred to as undercritically damped with a damping factor  $0 < \zeta < 1$  and is the most appropriate mathematical model to describe damping of mechanical systems. The response of such an underdamped system is [Franklin et al]:

$$y(t) = \frac{e^{-\zeta\omega_n t}}{\sqrt{1-\zeta^2}} \sin(\omega_d t) \quad \text{with} \quad \omega_d = \omega_n \sqrt{1-\zeta^2} \quad (4.4)$$

Figure 4.1 shows the response of a second order system with various damping factors. An undamped system ( $\zeta=0$ ) would have no means of dissipating its kinetic energy and would oscillate forever. Steel, for instance, has very little internal damping and can be modeled with a damping ratio of 0.0004 to 0.0007 [Slocum (a)].



**Figure 4.1** Response of a second order system to an impulse

The damping ratio  $\zeta$  determines how quickly the response decays and its effect is shown in Figure 4.2. For  $\zeta < 1$ , the response will oscillate around zero and eventually disappear. A critically damped system ( $\zeta = 1$ ) and an overdamped system ( $\zeta > 1$ ) would not have this kind of overshoot. Instead they would approach zero asymptotically. Setting the derivative of  $y(t)$  to zero, the rise time  $t_p$  can be calculated to:

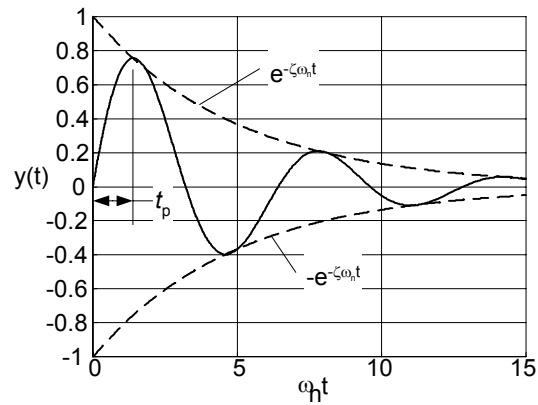
$$t_p = \frac{\pi}{\omega_d} \quad (4.5)$$

where  $\omega_d$  is the natural frequency of the damped system. Using the relation of Eq. 4.4, the damping ratio  $\zeta$  can be determined to be:

$$\zeta = \sqrt{1 - \left(\frac{\omega_d}{\omega_n}\right)^2} \quad (4.6)$$

The structure of a real machine is infinitely more complex than the simple mass-spring system described in Section 4.1 and does not follow the viscous damping model used to set up the equation of motion described in Eq. 4.1. A simplified approach to characterize the damping of such a system is the introduction of the loss factor  $\eta$ , which is determined by the ratio of the average energy dissipated per radian to the peak potential energy during a cycle [Nayfeh]. At resonance, the loss factor becomes  $2\eta$ . Damping can also be described by the quality factor  $Q$ , which is the amplification of the system vibrating at resonance and is calculated as the inverse of the loss factor  $\eta$ .

While real structures consist of a large number of spring-mass systems and therefore exhibit many resonance frequencies, Eq. 4.1 can still be used to illustrate the idea of max-

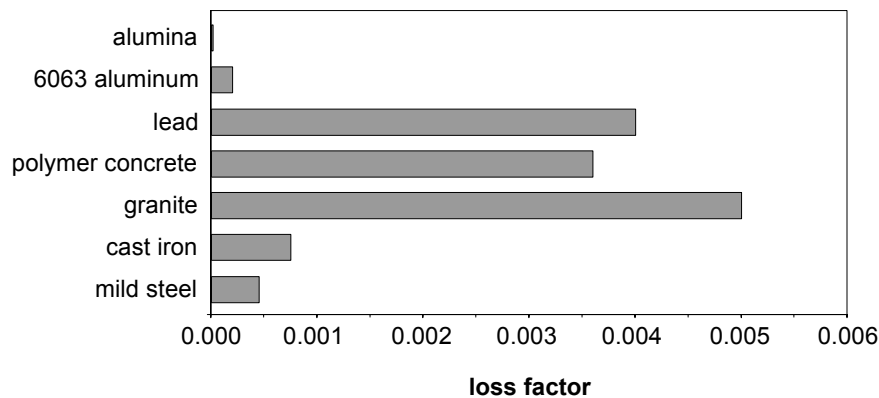


**Figure 4.2** Exponential envelope of second order system

imizing the system's stiffness while minimizing its mass to have a high, first natural frequency. Alternatively, disturbance frequencies may be much higher than the first mode, in which case higher but much less potent modes become excited. In machine dynamics, the lower modes are of particular interest because they tend to have the most energy.

## 4.2 Material Damping

All materials internally dissipate kinetic energy into heat through micro motion within their molecular or crystalline structure - the basic mechanism of material damping. Concrete, both cement and polymer-based, as well as cast iron are both known to have good internal damping and are therefore often used for machine tool structures. Filling structures with sand or lead pellets also dampens unwanted vibration and has recently been investigated in great detail by Bourinet et al (1999). However, the added weight from the granular material significantly lowers the natural frequency of the structure. The use of expanding concrete that adds both damping and stiffness is therefore preferable over filling cavities with sand.



**Figure 4.3** Typical loss factors of various materials [Lazan]

### 4.3 Damping in Bolted Joints and Bearings

Micro motion within a bolted joint also provides significant damping. The friction along dry joints dissipates energy and thus provides damping [Weck]. This type of damping is cumulative and therefore increases with the number of joints in a machine tool. Bearings are another source of damping and contact-less systems such as hydrostatic or hydrodynamic bearings are especially well suited for damping purposes because of the squeeze film damping that occurs between the very narrow gaps of the bearing surfaces. Ball bearings as well as roller bearings, especially in combination with grease-based lubrication, provide some damping also, though far less than sliding bearings.

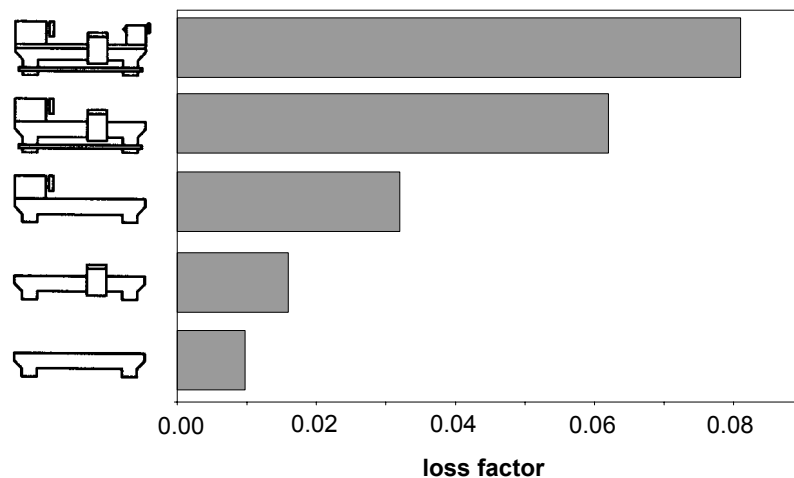


Figure 4.4 Damping at various stages of a machine assembly [Koenigsberger et al]

### 4.4 Active Damping

A rather complicated way of dampening vibrations uses a tuned mass damper that vibrates at the same frequency as the structure but with a 180 degree phase lag. The amplitude of the tuned mass damper is intended to cancel out the amplitude of the excitation frequency. In a machine tool with many different resonance frequencies and changing shape as axes move, setting up an active damping system would be a very complex task. In general,

active systems are used to isolate ultra-precise measuring systems from vibrations transmitted through the ground.

## **4.5 Constrained Layer Damping**

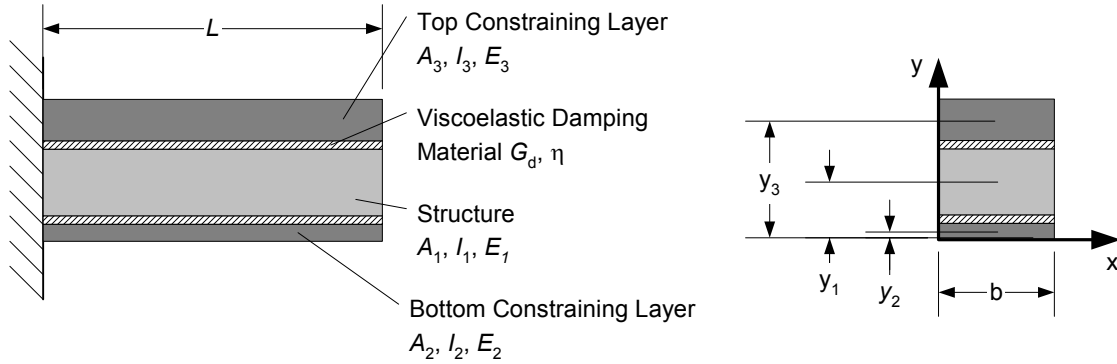
For a welded machine tool structure, the built-in damping as described in Chapter 4.2 and Chapter 4.3 generally proves insufficient for a good dynamic performance of the machine. Additional damping is necessary and can be achieved through a layer of special damping material squeezed within two layers of the structure. As the structure vibrates, the viscoelastic layer is subject to shear strain whose energy becomes dissipated into heat, thereby dampening vibration considerably [Slocum et al, Marsh et al].

### **4.5.1 Background**

The concept of constrained layer damping was first perceived by Plass (1957) and Ross, Ungar and Kerwin (1959) whose strain-energy approach for a three-layer plate under sinusoidal bending deflections became known as the RUK theory. The theory was later expanded to multiple constraining layers by DiTarantino et al (1965) and in 1970, Plunket and Lee introduced the use of discontinuous constraining layers. Internal damping designs and simplified analyses were first presented by Ruzicka (1961), Marsh et al (1996) and Slocum et al (1994). Constrained layer damping designs for torsional vibration of solid cross sections were investigated by Johnson and Woolf (1976) and Dewa (1989). Using Saint-Venants principle, Nayfeh (1998) studied torsional damping treatments for thin walled cross sections of arbitrary shape.

Recent studies focus mainly on active constrained layer damping (Park et al, 1999 and Chen et al, 1996) and report shear deformations higher than those generated by passive constrained layer dampers for cases where the ratio of longitudinal rigidity of the constraining layer to that of the base layer is less than unity.

### 4.5.2 Principle of Constrained Layer Damping



**Figure 4.5** Principal of constrained layer damping

While the performance of such a constrained layer in closed form can only be calculated for simple geometries, the equations presented are nevertheless suited for a qualitative comparison between different designs. As will be seen later, the most important design parameter when designing a constrained layer damping system is the stiffness ratio  $r$  (Eq. 4.8). It describes the ratio between the sum of the component's stiffness with respect to the system neutral axis and the sum of the component's stiffness with respect to their own neutral axis. The design goal will be to maximize this ratio in order to have maximum damping performance.

The location of the system neutral axis can be found through [Marsh, Hale]:

$$y_{\infty} = \frac{\sum y_i E_i A_i}{\sum E_i A_i} \quad (4.7)$$

The stiffness ratio  $r$  is defined as:

$$r = \frac{EI_{\infty} - EI_0}{EI_0} \quad (4.8)$$

where  $EI_0$  denotes the sum of all components' moments of inertia with respect to their own neutral axis:

$$EI_0 = \sum_i E_i I_i \quad (4.9)$$

and  $EI_\infty$  the sum of the components' stiffnesses with respect to the system neutral axis:

$$EI_\infty = EI_0 + \sum_i E_i A_i (y_i - y_\infty)^2 \quad (4.10)$$

For modal damping, the optimal damping parameter can be found to be:

$$\alpha_{opt} = \frac{1}{\sqrt{1 + \eta^2}} \quad (4.11)$$

and the actual damping parameter:

$$\alpha = \frac{G_d \sum_i \frac{b_i}{t_i} (y_i - y_1)^2}{\sum_i E_i A_i (y_i - y_\infty)^2} L_{eff}^2 \quad (4.12)$$

where the effective length is defined as:

$$L_{eff} \equiv \frac{\int_0^L \left( \frac{d\phi}{dx} - \frac{d\phi}{dx} \Big|_0 \right)^2 dx}{\int_0^L \left( \frac{d^2 \phi}{dx^2} \right)^2 dx} \quad (4.13)$$

The optimum damping sheet thickness can now be calculated to be:

$$t_{d,opt} = \frac{G_d L_{eff}^2}{\alpha_{opt} (EI_\infty - EI_0)} \sum_i b_i (y_i - y_1)^2 \quad (4.14)$$



the ratio of the static to the dynamic compliance is defined as:

$$Q = \frac{1 + (2 + r)\alpha + (1 + r)\alpha^2(1 + \eta^2)}{\eta r \alpha} \quad (4.15)$$

and the optimum compliance ratio using the optimum damping sheet thickness:

$$Q_{min} = \frac{1 + (2 + r)\alpha_{opt} + (1 + r)\alpha_{opt}^2(1 + \eta^2)}{\eta r \alpha_{opt}} \quad (4.16)$$

For simple Euler beams, the effective length can be found using basic mode shapes and boundary conditions:

**TABLE 4.1** Effective length of Eulerian beams with various end conditions [Hale]

<b>End Condition</b>	<b>Fundamental Mode Shape</b>	<b>Location of Zero Shear</b>	<b>Effective Length</b>
Fixed-Free	$\cosh\left(1.875\frac{x}{L}\right) - \cos\left(1.875\frac{x}{L}\right) - 0.734\left(\sinh\left(1.875\frac{x}{L}\right) - \sin\left(1.875\frac{x}{L}\right)\right)$	Fixed end	$0.613 L$
"	"	Free end	$0.314 L$
"	"	$0.4 L$	$0.229 L$
Pinned-Pinned	$\sin\left(\pi\frac{x}{L}\right)$	Center	$0.318 L$
Fixed-Fixed	$\cosh\left(4.73\frac{x}{L}\right) - \cos\left(4.73\frac{x}{L}\right) - 0.983\left(\sinh\left(4.73\frac{x}{L}\right) - \sin\left(4.73\frac{x}{L}\right)\right)$	Center	$0.158 L$
Free-Free	$\cosh\left(4.73\frac{x}{L}\right) + \cos\left(4.73\frac{x}{L}\right) - 0.983\left(\sinh\left(4.73\frac{x}{L}\right) + \sin\left(4.73\frac{x}{L}\right)\right)$	Center	$0.314 L$

### 4.5.3 The Split Tube Design

For tubular structures, constrained layer damping can be reasonably easy achieved with the split tube design (Figure 4.6 and Figure 4.8). Here, the constraining layers are created by cutting 8 slots starting from both ends of the tube until the cuts almost meet in the center of the tube. Next, a sheet of damping material (ISODAMP™ C-1002<sup>1</sup>) with adhesive on one side is

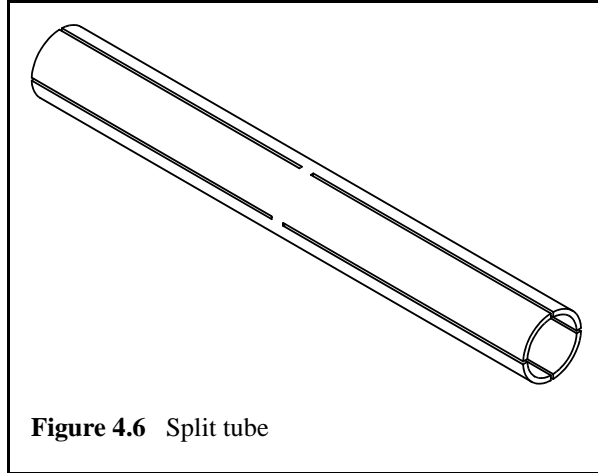


Figure 4.6 Split tube

wrapped around the split tube and the entire assembly inserted into the tubular machine structure. As the next step, the ends are sealed off with silicon and the gap between the damping layer and the outer structure is being filled with either epoxy or VibraDamp™<sup>2</sup>, a lower-cost alternative to epoxy which is essentially epoxy resin heavily filled with inert material. For gap sizes larger than 10 mm, cement grout can be used to minimize cost of the damper. The design parameters available to tune this constrained shear-layer damper

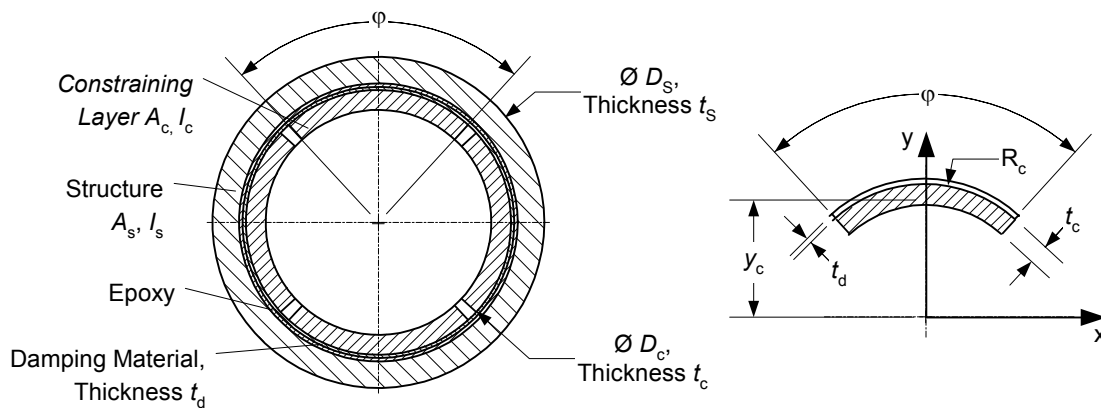


Figure 4.7 Split tube design parameters (a) and constrained layer parameters (b)

1. ISODAMP™ is a trademark licensed to AERO company
2. VibraDamp™ is a registered trademark of Philadelphia Resins



**Figure 4.8** ShearDamper™ based on split tube design in Star Cutter STG 5-axis grinder

system are shown in Figure 4.7. Of particular interest are a high first natural frequency and low dynamic compliance. While the outer structure’s dimensions are derived from the

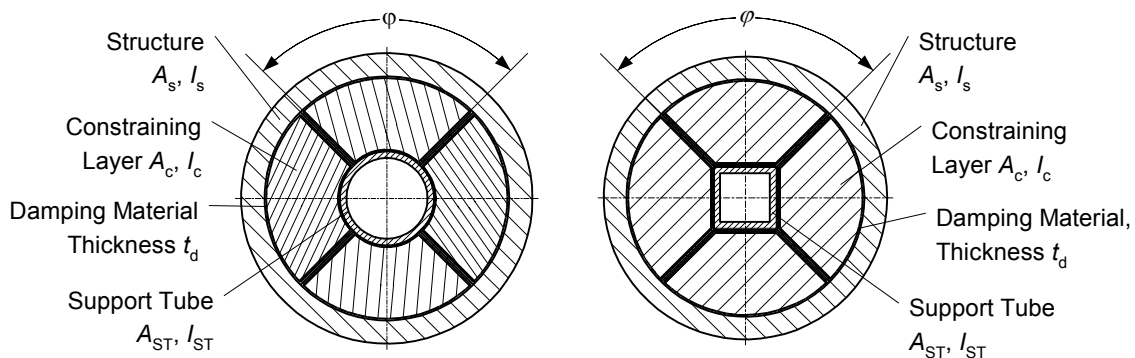
**TABLE 4.2** Constraining layer formulae for split tube

Property	Equation
area of constraining layer	$A_c = \frac{\widehat{\phi}}{2} (R_c^2 - (R_c - t_c)^2)$
constraining layer center of gravity	$y_c = \frac{4}{3} \frac{(R_c^3 - (R_c - t_c)^3) \sin \frac{\widehat{\phi}}{2}}{(R_c^2 - (R_c - t_c)^2) \widehat{\phi}}$
constraining layer moment of inertia with respect to system axis	$I_{c,x} = \frac{1}{8} (\widehat{\phi} + \sin \widehat{\phi}) (R_c^4 - (R_c - t_c)^4)$
constraining layer moment of inertia with respect to its own principal axis	$I_{c,0} = I_{c,x} - y_c^2 A_c$
damping layer center of gravity	$y_1 = \frac{4}{3} \frac{((R_c + t_d)^3 - R_c^3) \sin \frac{\widehat{\phi}}{2}}{((R_c + t_d)^2 - R_c^2) \widehat{\phi}}$
structure moment of inertia	$I_S = \frac{\pi}{64} (D_S^4 - (D_S - 2t_S)^4)$
$EI_0$	$EI_0 = E_S (2I_{c,0} + I_S)$
$EI_\infty$	$EI_\infty = E_S (2I_{c,x} + I_S)$

static requirements of the machine, the split tube's dimensions and the thickness of the damping layer need to be identified separately. The damping assembly of the Star Cutter STG 5-axis tool and cutter grinder, which is based on the ShearDamper<sup>TM1</sup> design, is shown in Figure 4.8.

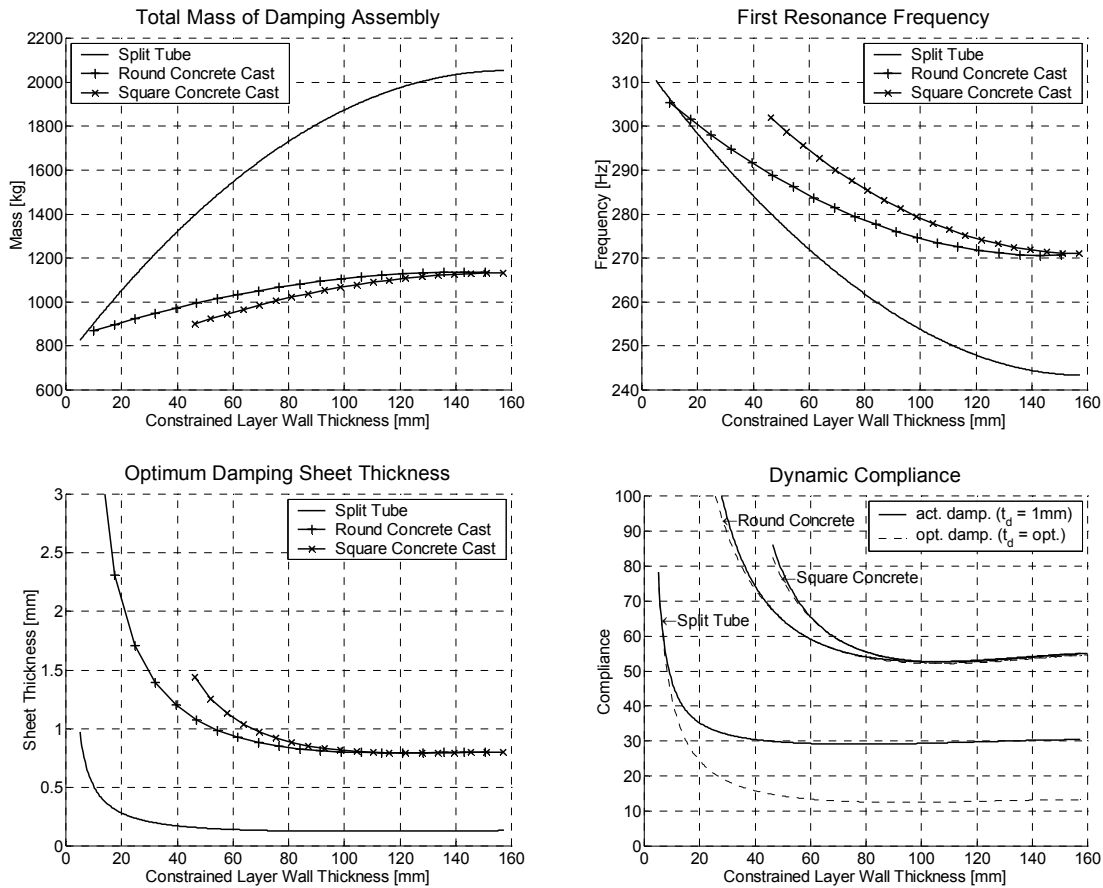
#### 4.5.4 Concrete Cast Damper

While the split tube design presented in the previous section offers good performance, due to its complex design it also adds significantly to the cost of the structure. Next, alternative designs are presented with the following idea: replace the split tube with less expensive structural materials and possibly increase the damping performance even further. Concrete, for instance, is very inexpensive and has a respectable amount of damping built-in. This new design would make use of “sausage-like” damping sheet enclosures which are inserted into the structural tube. The bottom ends are closed off and the center of this assembly is supported by a thin-walled tube. Finally, the four sausages are evenly filled with concrete with an expanding agent added. The added grout agent, which contains aluminum powder, oxidizes during the curing of the concrete, thereby producing little hydrogen bubbles. The gas causes the concrete to expand and counteracts its tendency to shrink during the curing. In fact, when dosed properly, the volume actually increases a bit, causing the damping material to be pressed against the inner diameter of the structural tube as



**Figure 4.9** Round (a) and square (b) concrete cast damper design

1. ShearDamper<sup>TM</sup> is registered trademark of AESOP, Inc.



**Figure 4.10** Round and square concrete cast vs. split tube

well as against the outer diameter of the central supporting tube. The pressure exerted will be large enough to create enough friction to keep the damping sheet from sliding along those two surfaces. If this wasn't the case, damping performance would not be as good as anticipated. The inner support tube can either be a round (Figure 4.9a) or a square tube (Figure 4.9b) and, provided that its stiffness is properly tuned to that of the concrete constraining layer, can add a significant amount of extra damping. Once the concrete is cured, the ends are cut off and the concrete is sealed with a layer of coating that prevents moisture from entering the system.

From the preliminary calculations shown in Figure 4.10 it can be seen that the concrete damper design does not reach the level of performance of the split tube despite having more damping layers available. This is due to the fact that the Young's modulus of con-

TABLE 4.3 Constraining layer formulae for concrete cast

	Round Core Concrete Cast	Square Core Concrete Cast
constraining layer area	$A_c = \frac{\widehat{\Phi}}{2} (R_c^2 - (R_c - t_c)^2)$	$A_c = \frac{\widehat{\Phi}}{2} R_c^2 - (R_c - t_c)^2 \tan \frac{\Phi}{2}$
constraining layer center of gravity	$y_c = \frac{4}{3} \frac{(R_c^3 - (R_c - t_c)^3) \sin \frac{\Phi}{2}}{(R_c^2 - (R_c - t_c)^2) \widehat{\Phi}}$	$y_c = \frac{2}{3} \frac{R_c^3 \sin \frac{\Phi}{2} - (R_c - t_c)^3 \tan \frac{\Phi}{2}}{\widehat{\Phi} R_c^2 - (R_c - t_c)^2 \tan \frac{\Phi}{2}}$
constraining layer moment of inertia with respect to system neutral axis	$I_{c,x} = \frac{1}{8} (\widehat{\Phi} + \sin \Phi) (R_c^4 - (R_c - t_c)^4)$	$I_{c,x} = \frac{1}{8} (\widehat{\Phi} + \sin \Phi) R_c^4 - \frac{1}{2} (R_c - t_c)^4 \tan \frac{\Phi}{2}$
constraining layer moment of inertia with respect to its own neutral axis	$I_{c,0} = I_{c,x} - y_c^2 A_c$	
structure moment of inertia	$I_S = \frac{\pi}{64} (D_S^4 - (D_S - 2t_s)^4)$	
support tube moment of inertia	$I_{ST} = \frac{\pi}{64} (D_{ST}^4 - (D_{ST} - 2t_{ST})^4)$	$I_{ST} = \frac{1}{12} (h_{ST}^4 - (h_{ST} - 2t_{ST})^4)$
$EI_0$	$EI_0 = 2E_c I_{c,0} + E_S (I_S + I_{ST})$	
$EI_\infty$	$EI_\infty = 2E_c I_{c,x} + E_S (I_S + I_{ST})$	
primary damping layer center of gravity	$y_1 = \frac{4}{3} \frac{(R_c + t_d)^3 - R_c^3}{(R_c + t_d)^2 - R_c^2} \widehat{\Phi} \sin \frac{\Phi}{2}$	
secondary damping layer center of gravity	$y_2 = \frac{4}{3} \frac{(R_c - t_c)^3 - (R_c - t_c - t_d)^3}{(R_c - t_c)^2 - (R_c - t_c - t_d)^2} \widehat{\Phi} \sin \frac{\Phi}{2}$	$y_2 = R_c - t_c$
tertiary damping layer center of gravity	$y_3 = \left(R_c - \frac{t_c}{2}\right) \cos \frac{\Phi}{2}$	$y_3 = \frac{1}{2} \left(R_c \left(1 + \cos \frac{\Phi}{2}\right) - t_c\right)$

crete is only about one third that of steel. The reduced stiffness causes the stiffness ratio  $r$  to decrease (Eq. 4.8), making the constraining layer more compliant than it should be. However, the above calculations do not account for the internal damping of the used materials. Instead, the results are purely based on the dissipation of energy within the viscoelastic layer. A more thorough study and even physical experiments will be required to fully assess the capabilities of concrete filled dampers. On the plus side, the concrete design is

much lighter than the split tube and though not as stiff, nevertheless has a significantly higher natural frequency. Using a  $15/1000$ " thick (0.381 mm) ISODAMP C-1002, which is the thinnest available thickness, the split tube achieves a damping factor  $Q$  of roughly 18 with a 60 mm thick inner tube. Such a design would weigh 1550 kg and have the first mode at 272 Hz. Assembled with its optimum thick damping sheet (0.75 mm), the round concrete cast (Figure 4.9a) would have its best  $Q$  at around 53 with a constrained layer thickness of 90 mm while weighing 450 kg less and having a slightly higher first resonance frequency than the split tube. The difference in weight gives an important cost indication: at roughly \$0.75 per pound of steel, the split tube will add about \$900 to the cost of the structure compared to about \$30 to 40 for the concrete.

### 4.5.5 Reinforced Concrete Cast Damper Design

What can be seen from Figure 4.10 is the need for matching the stiffness of the constraining layer to that of the structure to be damped. In the case of concrete, this cannot be achieved by concrete alone due to its significantly lower E-modulus compared to steel. To improve the damping, it is necessary to add stiffness to the constraining layers, which in the case of concrete can easily be done by adding inexpensive rebars (Figure 4.11). To investigate the effects of a single rebar, the equations of Table 4.3 need to be modified to accommodate the composite of steel and concrete (Table 4.4). As said before, the goal is to maximize the stiffness ratio  $r$  which can be achieved by pushing the constraining

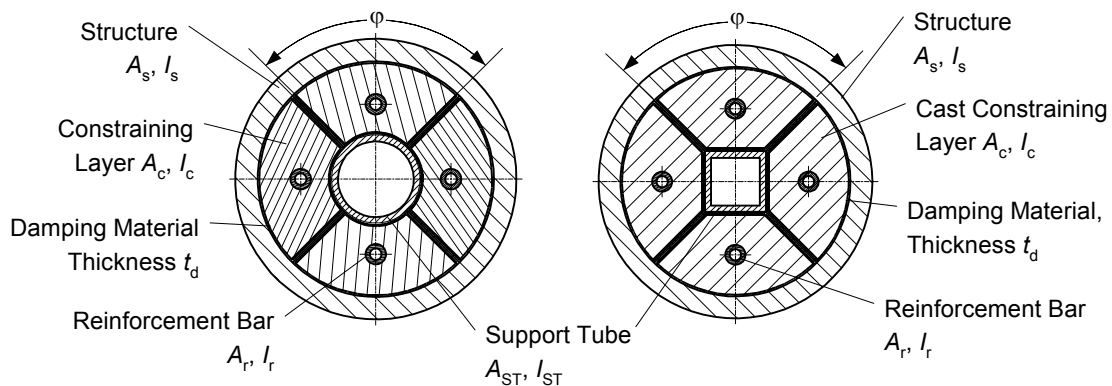


Figure 4.11 Reinforced round (a) and square (b) concrete cast design

layer's neutral axis away from the system neutral axis. Therefore, the distance  $R_b$  was set such that the rebar would have the greatest possible distance from the system neutral axis with only 5 mm concrete left to the outer radius of the constraining layer. A Matlab script was set up to compute mass, first natural frequency, optimal damping sheet thickness and dynamic compliance for designs with a single rebar of 0.5, 1, 1.5 and 2" diameter rebar.

TABLE 4.4 Constraining layer formulae

	Round Core Concrete with Single Rebar	Square Core Concrete with Single Rebar
$A_c$	$A_c = \frac{\widehat{\varphi}}{2} (R_c^2 - (R_c - t_c)^2) - \pi R_r^2$	$A_c = \frac{\widehat{\varphi}}{2} R_c^2 - (R_c - t_c)^2 \tan \frac{\widehat{\varphi}}{2} - \pi R_r^2$
$y_c$	$y_c = \frac{\frac{2}{3} (R_c^3 - (R_c - t_c)^3) \sin \frac{\widehat{\varphi}}{2} - R_b \pi R_r^2}{\frac{\widehat{\varphi}}{2} (R_c^2 - (R_c - t_c)^2) - \pi R_r^2}$	$y_c = \frac{\frac{2}{3} (R_c^3 \sin \frac{\widehat{\varphi}}{2} - (R_c - t_c)^3 \tan \frac{\widehat{\varphi}}{2}) - R_b \pi R_r^2}{\frac{\widehat{\varphi}}{2} R_c^2 - (R_c - t_c)^2 \tan \frac{\widehat{\varphi}}{2} - \pi R_r^2}$
$I_{c,x}$	$I_{c,x} = \frac{1}{8} (\widehat{\varphi} + \sin \widehat{\varphi}) (R_c^4 - (R_c - t_c)^4) - \left( \frac{\pi}{4} R_r^4 + R_b^2 \pi R_r^2 \right)$	$I_{c,x} = \frac{1}{8} (\widehat{\varphi} + \sin \widehat{\varphi}) R_c^4 - \frac{1}{2} (R_c - t_c)^4 \tan \frac{\widehat{\varphi}}{2} - \left( \frac{\pi}{4} R_r^4 + R_b^2 \pi R_r^2 \right)$
$I_{c,0}$	$I_{c,0} = I_{c,x} - y_c^2 A_c$	
$I_{r,x}$	$I_{r,x} = \frac{\pi}{4} (R_r^4 - (R_r - t_r)^4) + R_b^2 \pi (R_r^2 - (R_r - t_r)^2)$	
$I_{r,0}$	$I_{r,0} = \frac{\pi}{4} (R_r^4 - (R_r - t_r)^4)$	
$I_{ST}$	$I_{ST} = \frac{\pi}{64} (D_{ST}^4 - (D_{ST} - 2t_{ST})^4)$	$I_{ST} = \frac{1}{12} (h_{ST}^4 - (h_{ST} - 2t_{ST})^4)$
$EI_\infty$	$EI_\infty = 2E_c I_{c,x} + E_s (I_{r,x} + I_{ST} + I_S)$	
$EI_0$	$EI_0 = 2E_c I_{c,0} + E_s (I_{r,0} + I_{ST} + I_S)$	



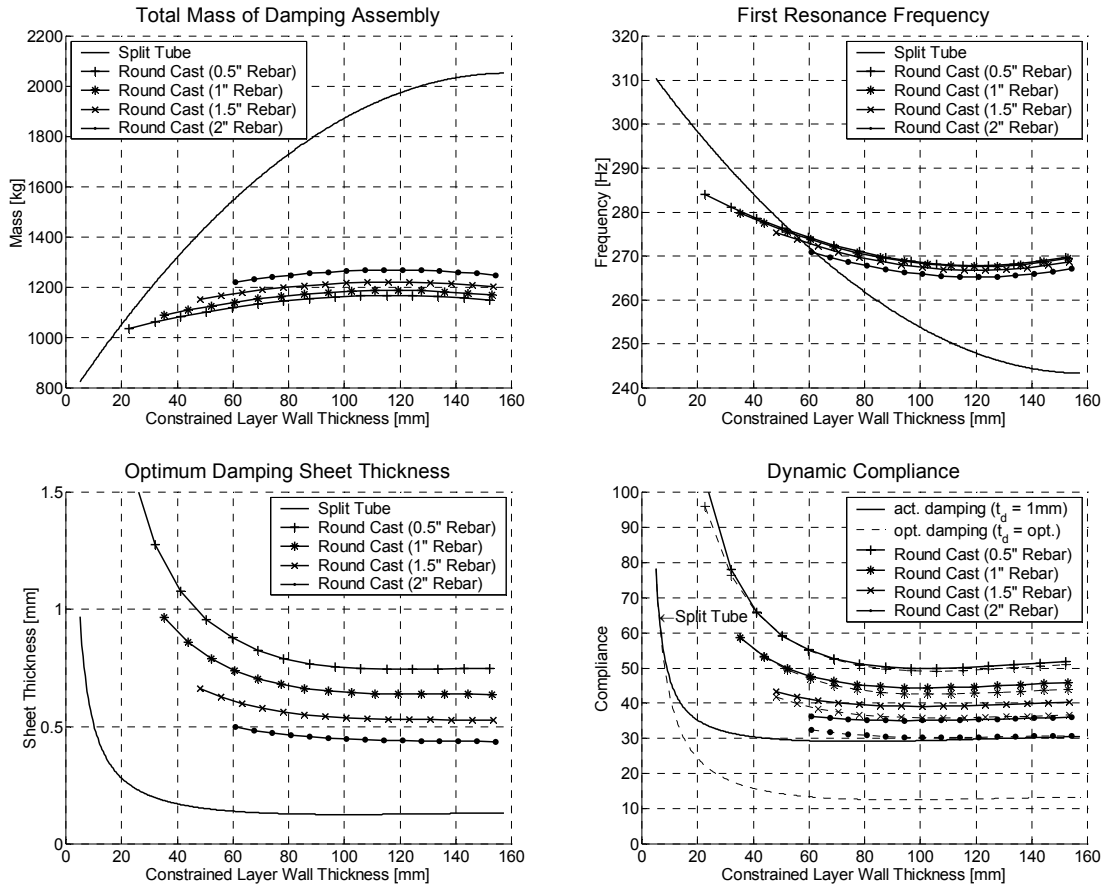


Figure 4.12 Round core concrete cast with single rebar vs. split tube

TABLE 4.5 Maximum damping factor for various concrete core designs

	Round Core Concrete Cast	Square Core Concrete Cast
no rebar	53	54
0.5"	50	53
1"	43	46
1.5"	36	37
2"	30	31

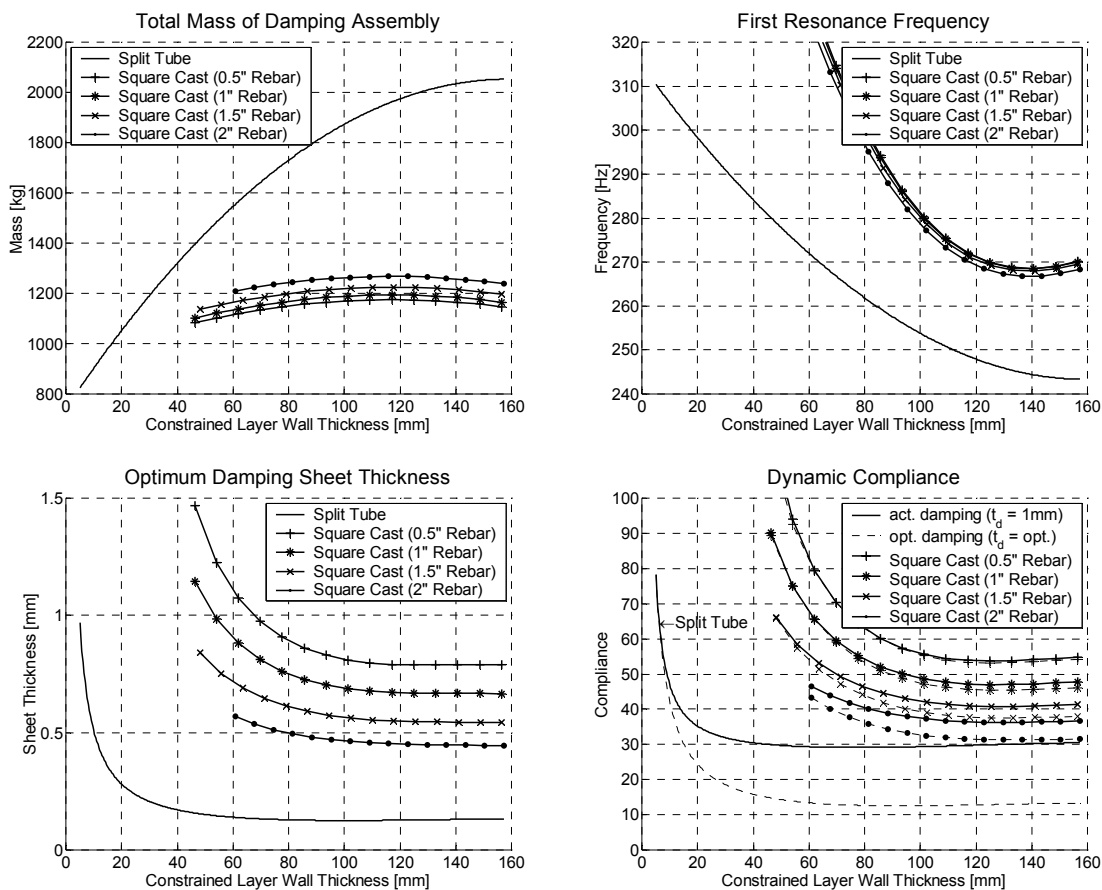
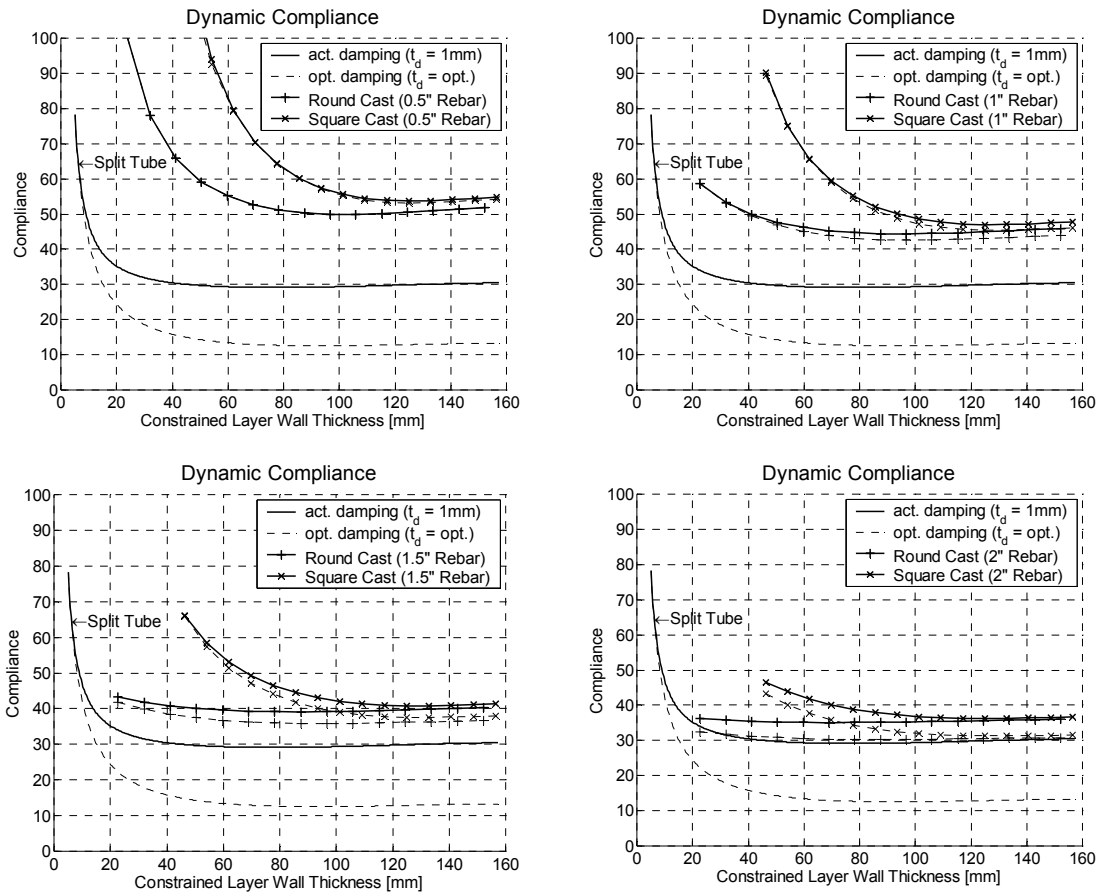


Figure 4.13 Square core concrete cast with single rebar vs. split tube

Table 4.5 gives an overview of the performance improvement shown in Figure 4.12 and Figure 4.13. This significant improvement is a result of an increased stiffness of the concrete/steel composite which leads to an improved stiffness ratio  $r$ . As a direct result, the dynamic compliance is lowered and more energy dissipated within the viscoelastic layer. Round tubes are generally more readily available than square tubes, so now would be a good time to find out if the square concrete cast has any significant advantages over the round design. Figure 4.14 presents a side by side comparison between the two designs in terms of their dynamic compliance.

The square core concrete design is not performing quite as well as the round core design because the stiffness ratio  $r$  is slightly smaller compared to the round concrete design. Given that the performance is slightly worse and the fact that square tubes are harder to

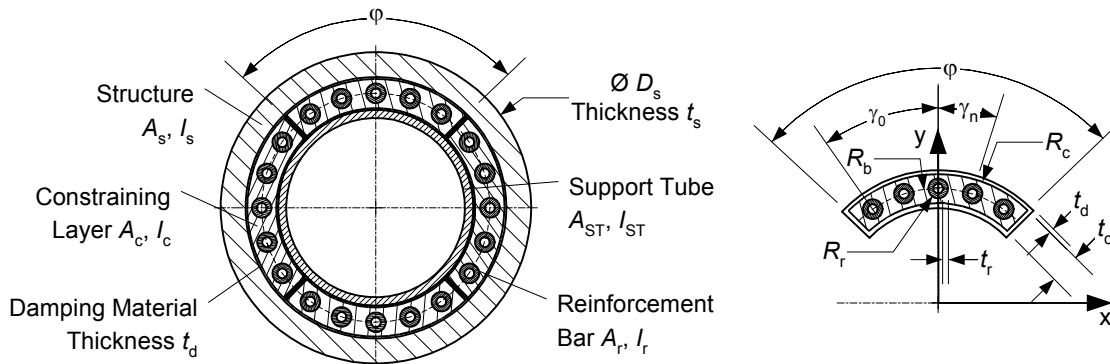


**Figure 4.14** Dynamic compliance of round core concrete cast vs. square core concrete cast

find than round ones, the square design will no longer be pursued. Instead, the focus will be on the round tube design and ways of increasing its performance even further. Motivated by the effects of single rebars, an alternative design using multiple, evenly spaced rebars will be investigated in the next section.

### 4.5.6 Round Core Concrete Cast with Multiple Reinforcement

Based on the findings in the previous section, a further improvement of the stiffness ratio  $r$  will be investigated by adding multiple rebars to the constraining layer. A Matlab script computes the maximum number of rebars at a given diameter (0.5, 1, 1.5 and 2") and minimum radial spacing (10 mm) and then varies the thickness of the constraining layer to calculate mass, frequency, and dynamic compliance properties based on these parameters.



**Figure 4.15** Round core concrete cast design with multiple rebars

As before, the rebar circle  $R_b$  was set to a maximum value in order to move the constraining layer neutral axis away from the system neutral axis. The general equations for such a steel/concrete matrix using multiple rebars are given in Table 4.7 while the Matlab script can be found in Appendix B.

As expected, constraining layers with multiple reinforcement exhibit a dramatically reduced dynamic compliance and therefore offer much better damping than all preceding concrete designs. The split tube, in order to have the lowest possible dynamic compliance, needs to have an extremely thin layer of damping material (0.15 mm). If such a thin layer is not available or too delicate to handle in a production environment, damping performance of the split tube will be very close to the predicted performance of multiple enforced concrete layers using reasonably sized damping sheets (0.5 to 1 mm). One can actually expect the composite layer to surpass the split tube when considering the material damping of the concrete itself. Further energy losses should result from micro motion between the concrete and the steel rebars, enhancing the damping of the system even further.

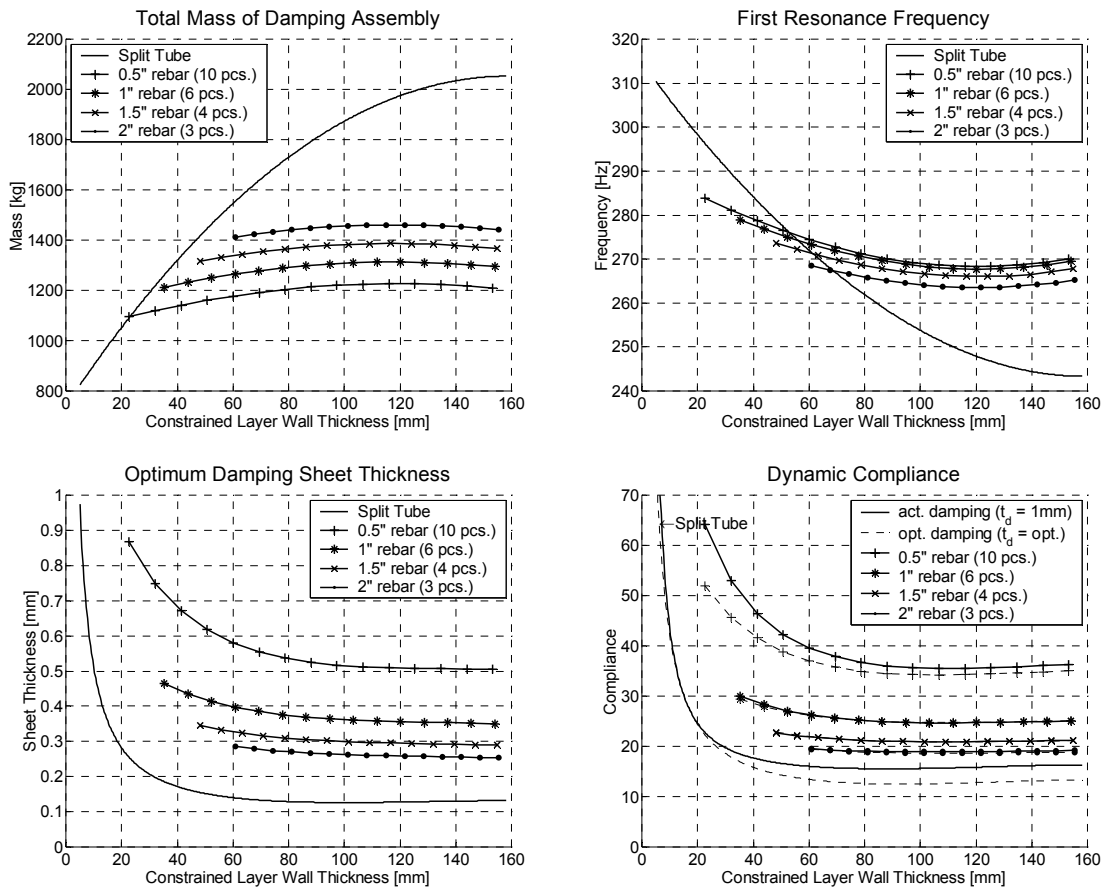


Figure 4.16 Split tube vs. round core concrete cast with multiple reinforcement

TABLE 4.6 Comparison of maximum achievable damping factor

	single rebar	multiple rebars
no rebar	53	53
0.5"	50	35
1"	43	25
1.5"	36	21
2"	30	18

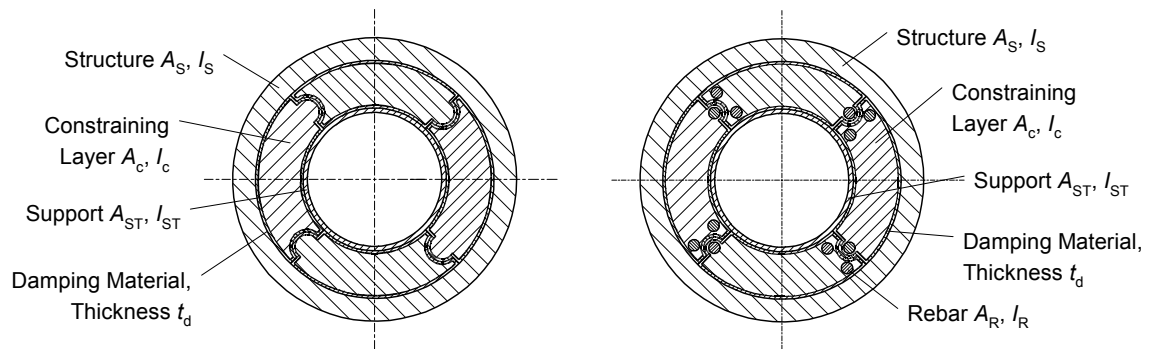
TABLE 4.7 Formulae for multiple reinforced constraining layer

<b>Round Core Concrete Cast with Multiple Rebars</b>	
$A_c$	$A_c = \frac{\phi}{2} (R_c^2 - (R_c - t_c)^2) - N\pi R_r^2$
$y_c$	$y_c = \frac{\frac{2}{3} (R_c^3 - (R_c - t_c)^3) \sin \frac{\phi}{2} - \sum_{n=0}^{N-1} R_b \cos(\gamma_0 + n\gamma_n) \pi R_r^2}{\frac{\phi}{2} (R_c^2 - (R_c - t_c)^2) - N\pi R_r^2}$
$I_{c,x}$	$I_{c,x} = \frac{1}{8} (\phi + \sin \phi) (R_c^4 - (R_c - t_c)^4) - \sum_{n=0}^{N-1} \frac{\pi}{4} R_r^4 + (R_b \cos(\gamma_0 + n\gamma_n))^2 \pi R_r^2$
$I_{c,0}$	$I_{c,0} = I_{c,x} - y_c^2 A_c$
$A_r$	$A_r = N\pi (R_r^2 - (R_r - t_r)^2)$
$y_r$	$y_r = \frac{\sum_{n=0}^{N-1} R_b \cos(\gamma_0 + n\gamma_n) \pi (R_r^2 - (R_r - t_r)^2)}{N\pi (R_r^2 - (R_r - t_r)^2)}$
$I_{r,x}$	$I_{r,x} = \sum_{n=0}^{N-1} \frac{\pi}{4} (R_r^4 - (R_r - t_r)^4) + (R_b \cos(\gamma_0 + n\gamma_n))^2 \pi (R_r^2 - (R_r - t_r)^2)$
$I_{r,0}$	$I_{r,0} = I_{r,x} - y_r^2 A_r$
$EI_\infty$	$EI_\infty = 2E_c I_{c,x} + E_s (I_{r,x} + I_{ST} + I_S)$
$EI_0$	$EI_0 = 2E_c I_{c,0} + E_s (I_{r,0} + I_{ST} + I_S)$

### 4.5.7 Concrete Cast with Interlocking Constraining Layers

It is possible to cast the constraining layers such that they interlock, similar to a jigsaw puzzle. This can be achieved by having the nozzle that fills the damping containers shaped like the final constraining layer. Alternatively, each nozzle can be mounted to plates that are shaped like the final constraining layers. By using four of these nozzles simultaneously and starting at the bottom of the damping containers, four similar shaped constraining layers are created that interlock similar to the design shown in Figure 4.17. Such a design is very likely to have even better damping performance and can very easily be fabricated.

Another possible way of achieving such an interlocked design would be to strategically place reinforcement bars near the joints such that the constraining layers assume the required shape to interlock.



**Figure 4.17** Concrete cast design with interlocking constraining layers





# Chapter 5

## DAMPING EXPERIMENTS

The concrete cast damper design presented in Section 4.5.4 has several advantages over steel-based constraining layers:

- Concrete has much better internal damping than steel.
- Concrete constraining layers are lighter than those made from steel, resulting in higher natural frequencies.
- The expanding concrete creates constraining layers that easily adapt to regular and irregular structural shapes.
- Concrete is significantly less expensive than steel constraining layers and the epoxy required to fill the gap between the structure and these layers.
- For structures that have only one side accessible, the split tube design has a potential leak problem at the bottom that may allow epoxy to end up outside the gap it is supposed to fill. With the concrete core cast, a sausage with a bottom can be used, thereby having a leak-proof seal inside the structure.
- Concrete cast dampers remove the need for finding an inner tube whose outer dimensions allow it to fit inside the structure AND having the appropriate wall thickness to achieve optimum damping.

In order to have a direct comparison between different damping designs, a set of experiments was conducted. The main objective of these experiments was an assessment of the damping characteristics and manufacturing issues of the various designs. The following experiments were performed:

- undamped structural tube.
- structural tube filled with sand.

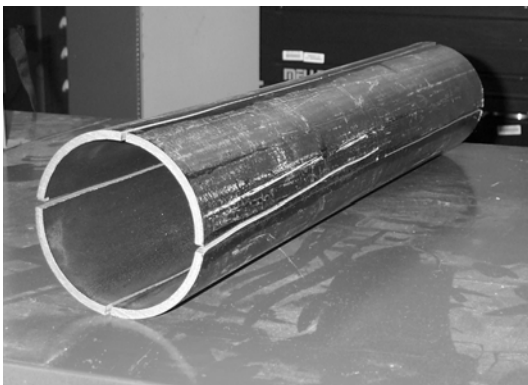
- structural tube filled with concrete.
- structural tube with split tube design.
- structural tube with concrete damper design (no rebar).
- structural tube with concrete damper design and 3 rebars per segment.

## 5.1 Building the Dampers

The two most generic criteria to evaluate a design are performance and economics. In this section, the manufacturability of damping designs, a subset of economics, is investigated. Together with material costs, expenses directly related to manufacturing greatly affect how economical a design solution will be to implement.

### 5.1.1 Split Tube

The constraining layer of the split tube design consists of a 4 inch pipe with 8 axial cuts. The theoretical design is built with four separate constraining layers but for manufacturing and handling reasons, the individual layers are kept together at the center of the split tube by having the eight axial cuts end shortly before they reach the center of the tube (Figure 5.1a). This simplifies fabricating the damper significantly because a single tube is much easier to locate than four separate, oddly shaped constraining layers. Next, the tube is wrapped with 0.381 mm thick ISODAMP<sup>TM</sup> C-1002 that has an adhesive applied on



**Figure 5.1** Split tube constraining layer, raw tube (a) and wrapped with ISODAMP<sup>TM</sup> C-1002 (b)

---

1. ISODAMP<sup>TM</sup> is a trademark licensed to AERO Industries



**Figure 5.2** Split tube, before (a) and after (b) epoxy filling

one side (Figure 5.1b). A fixture is used to locate the split tube in the center of the structural tube and the gap between the two tubes is filled with epoxy (Figure 5.2).

### 5.1.2 Concrete Core Damper

The damping material is supplied as sheets, so rectangles with a width equivalent to the perimeter of the sausages (plus some overlap) were cut out (Figure 5.3a) and a lap joint is used to form the dampers into tubes (Figure 5.3b). Neglecting edge effects and assuming that the thickness of the damping sheet is much smaller than the overall dimensions, the perimeter can be calculated to:

$$P = (D_S - 2t_S)\left(\frac{\pi}{4} + 1\right) + D_{ST}\left(\frac{\pi}{4} - 1\right) \quad (5.1)$$



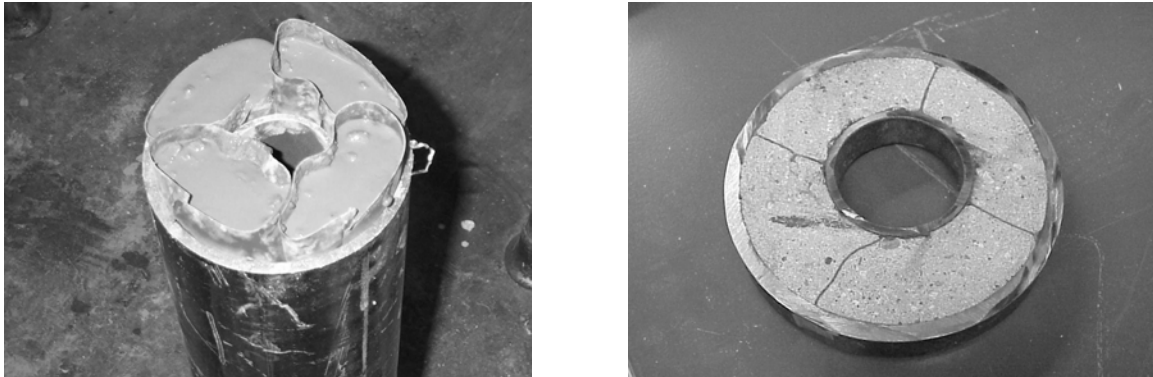
**Figure 5.3** Cutting the damping sheet (a) and forming the “damping sausage” with a lap joint



**Figure 5.4** Cast fixture (a) and closed of “damping sausages” (b)

For this experiment, a 2 inch pipe with a wall thickness of 0.154" was chosen as the support tube. Using Eq. 5.1, the perimeter of the sausages was calculated to be 8.43 inches. The length for the damping inserts was set to 30", making the sausages 6" longer than the structural tube. The excess length is used to close off the ends by rolling them around a cable tie a few times which is subsequently locked (Figure 5.4b). The structural tube is set on top of the cast fixture shown in Figure 5.4a and located at the outer diameter with a slightly oversized ring. The ends of all four sausages are pushed through the openings at the bottom of the fixture so that no end effects would affect the shape of the constraining layer at the bottom of the structural tube. The inner support tube is assembled next and the center peg of the fixture is locating this tube concentrically to the structural tube. Finally, the four sausages are filled evenly with concrete that has 1% Intraplast-N<sup>TM</sup><sup>1</sup> added to ensure that the concrete expands rather than shrinks as it cures. Because the damping sheet used is considerably less stiff in bending than it is in tension, the sausages should reliably assume their intended shapes. This includes the edges where the thin-walled sausages are bent to create the pie-like constraining layer shape. To assist the expanding concrete, the damping inserts should be filled slightly past the level of the structural tube. The end is then wrapped with plastic and sealed with tape to keep the hydrogen from escaping. Finally, a weight is applied to increase the pressure onto the concrete filling. After 36 hours, the concrete is fully cured and both ends are cut flush with the structural tube.

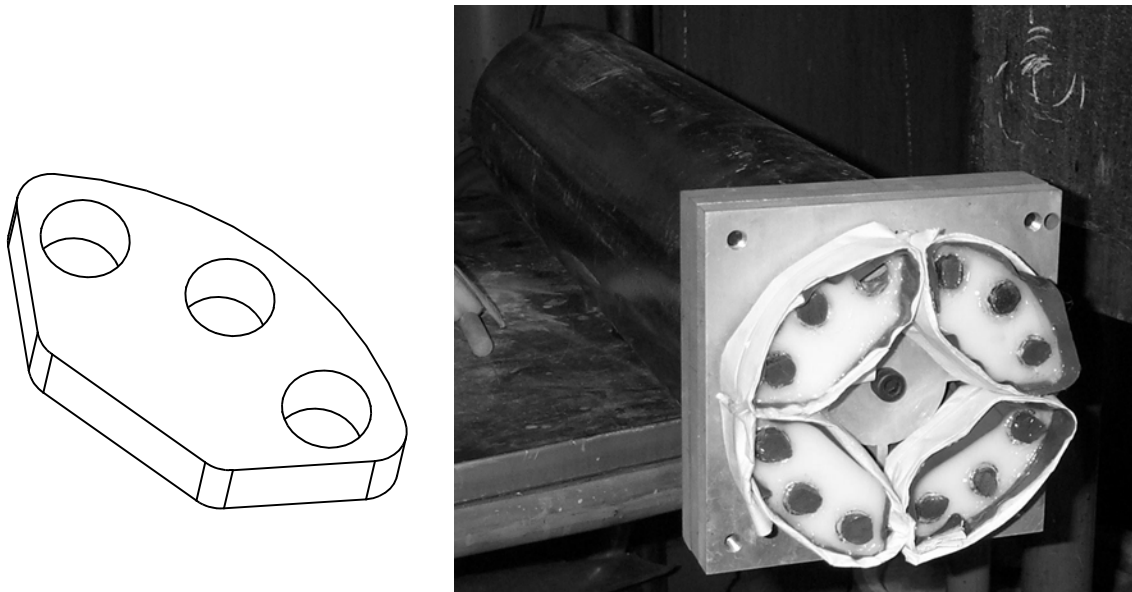
1. Intraplast-N<sup>TM</sup> is a registered trademark of Sika Corp.



**Figure 5.5** Finished concrete core cast (a) and a portion cut from the center of the damped tube (b)

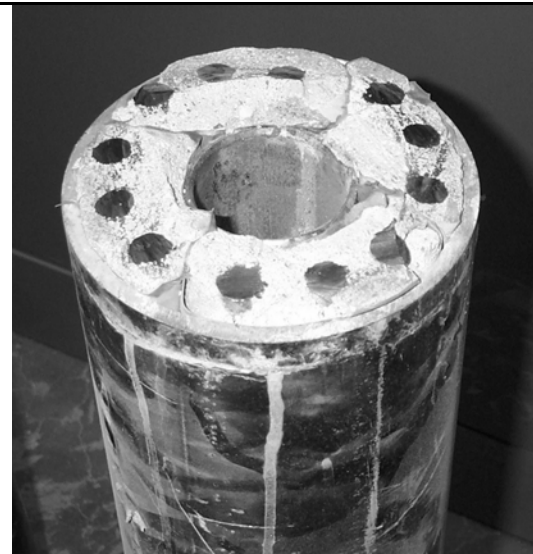
### 5.1.3 Concrete Core Cast with Reinforcement

Building the reinforced concrete core cast is very similar to the damper without rebars. The only difference comes from the need for locating the rebars inside the concrete core. For the purpose of sealing the sausages and locating the rebars, reusable fixture plates shown in Figure 5.6a have been designed. The three holes are used to hold and locate three rebars (see Figure 5.6b). The fixture plate's perimeter is chosen to be slightly larger than the perimeter of the sausage. The plate is inserted into the end of a sausage and a cable tie is wrapped around the sausage in order to tighten it against the fixture plate.



**Figure 5.6** Fixtures for concrete core cast with three rebars per core

This experimental design uses through-holes for the fixtures plate, and the gaps between the rebars and the holes were sealed off with a bead of hot glue. In production, blind holes would be advisable because they make this seal obsolete.



**Figure 5.7** Concrete Core Reinforced Damped Structure

#### 5.1.4 Concrete Mixture

The first set of experiments were conducted with a commercially available concrete mix. Such a mix typically contains one part cement, three parts sand, and four parts gravel. Following the instructions on the bag, water was added to the dry mix until the slurry had the right consistency. After thorough blending, the expanding agent was added and again mixed thoroughly. The slurry was rather thick and had to be scooped out of the container and pushed down the dampers. However, after the specimen had cured, large voids were found at the bottom of the sausage and the concrete was very porous and brittle, almost like lava. Obviously, the expanding grout wasn't mixed well enough, creating an inhomogenous slurry with localized high concentrations of Intraplast-N™. In addition, some of the gravel was rather large, almost half the characteristic size of the damper, making it very difficult to evenly fill the sausages. The bottom of the dampers were found to be full of defects because the thick slurry failed to fill all voids. This was especially true for the design with the three rebars, where the gaps between the rebars were in the order of gravel size.

The second set of experiments addressed these problems found during the initial experiments and used a different mix for the concrete. Rather than buying a concrete dry mix,

one part of Portland cement was dry mixed with two parts of sand. The amount of expanding agent was dosed to be exactly 1% of the cement's weight and was added dry to the cement and sand. This mixture was thoroughly mixed before adding just enough water to create a slurry that could be poured rather than scooped. The amount of water that is added to the mixture is quite crucial. Adding not enough water prevents the concrete from curing and is likely to create voids because of bad filling. Adding too much water causes the concrete to become porous, compromising its structural integrity and stiffness. During the experiments it was found that a concrete slurry, that was just about pourable, delivered the best results in terms of time required to fill the sausages and the achievable stiffness of the poured concrete core.

### 5.1.5 Material Cost

The material costs for the experiments conducted are given in Table 5.1. For the concrete core damping design without reinforcement, costs were 23.5% of the existing design. Adding the rebars causes a slight increase in cost to 28.8% of the steel-based damper.

**TABLE 5.1** Material cost

	<b>Split Tube</b>	<b>Concrete Cast</b>	<b>Reinforced Concrete Cast</b>
Pipe 4"	\$15.00		
Pipe 2"		\$6.50	\$6.50
C-1002-01/Plain		\$18.84	\$18.84
C-1002-02/PSA	\$12.08		
Epoxy	\$85.00		
Concrete		\$1	\$1
Rebars			\$6
<b>Total</b>	<b>\$112.08</b>	<b>\$26.34</b>	<b>\$32.34</b>
<b>Percentage</b>	<b>100%</b>	<b>23.5%</b>	<b>28.8%</b>

## 5.2 Experimental Setup

For the modal analysis, a Hewlett-Packard 35670A frequency analyzer was used (Figure 5.8). To simulate a free-free boundary condition, the tubes were elastically suspended at the nodal points for the first bending mode (Figure 5.9a). These points are at roughly 20% and 80% of the overall length. At a distance of 40 mm from the end, the accelerometer was glued to a flat spot on the outer tube's surface.

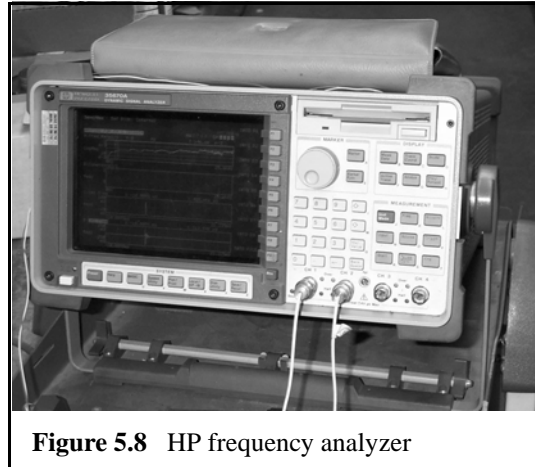


Figure 5.8 HP frequency analyzer

The structure was excited with an impact hammer right next to the sensor. Because of the expected high resonance frequencies, a metal tip was used in conjunction with the impact hammer to stimulate these high modes with an appropriate amount of energy. Using a Delrin tip, on the other hand, puts more energy into the system at a lower frequency, thereby stimulating lower modes. Consequently, the coherence between the input and the output signal was good between 500 Hz and 6.4 kHz, while below 500 Hz coherence was pretty bad. However, with the first bending mode predicted at 2 kHz, bad coherence in the lower frequency range is not a problem at all. Mapping of the results was achieved by having 16 such points distributed evenly along the perimeter of the structural tube (Figure 5.9b). The first bending mode, which is of particular interest in structural dynamics, was identified by

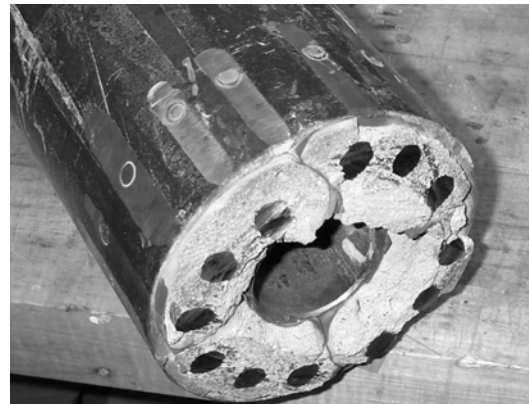


Figure 5.9 Free-free beam setup (a) and 16 measuring points



attaching a 3-axis accelerometer at 28 different locations along the length and perimeter of the tube. The signals from the impact hammer and the response signals from the transducer were recorded with the frequency analyzer and transformed from the time into the frequency domain using Fast Fourier transformations (FFT). For better results, each set was repeated ten times and averaged in the frequency domain. The transfer functions were analyzed with the Star System<sup>TM1</sup> software to identify the frequency of the first bending mode.

### 5.3 Damping Calculations

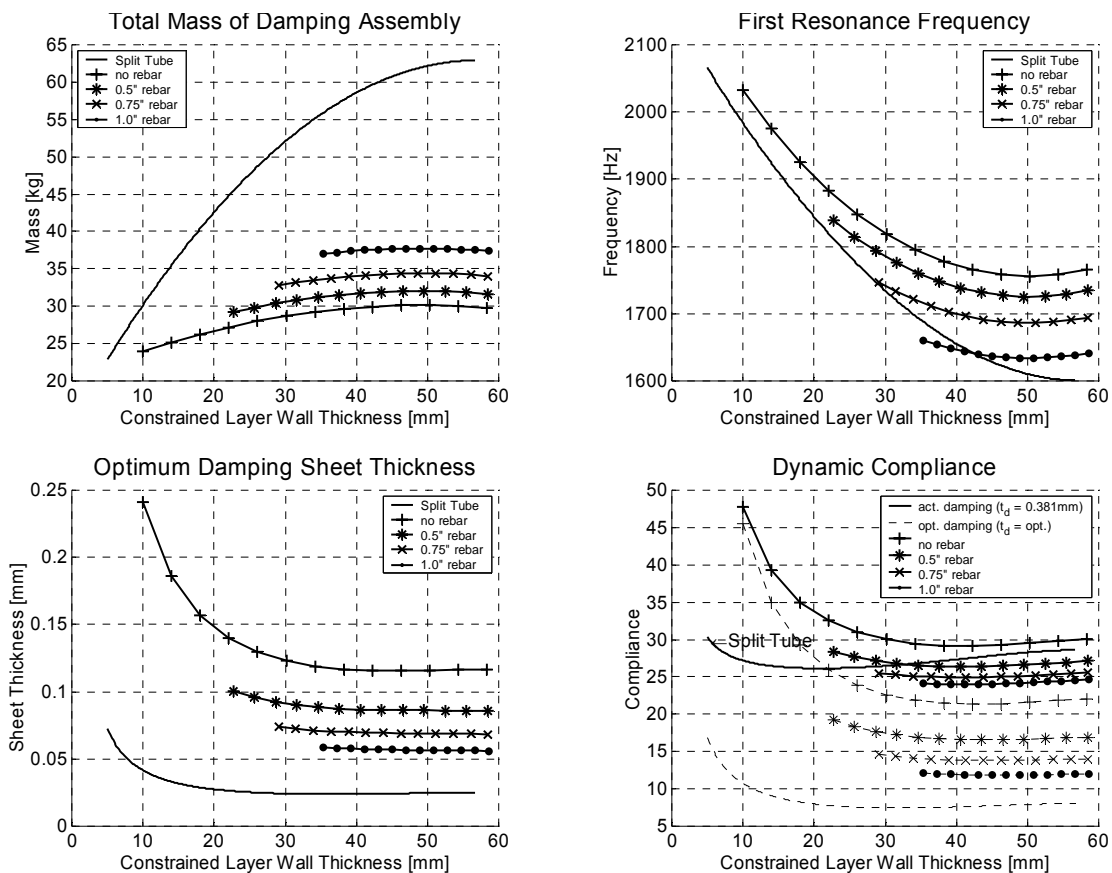
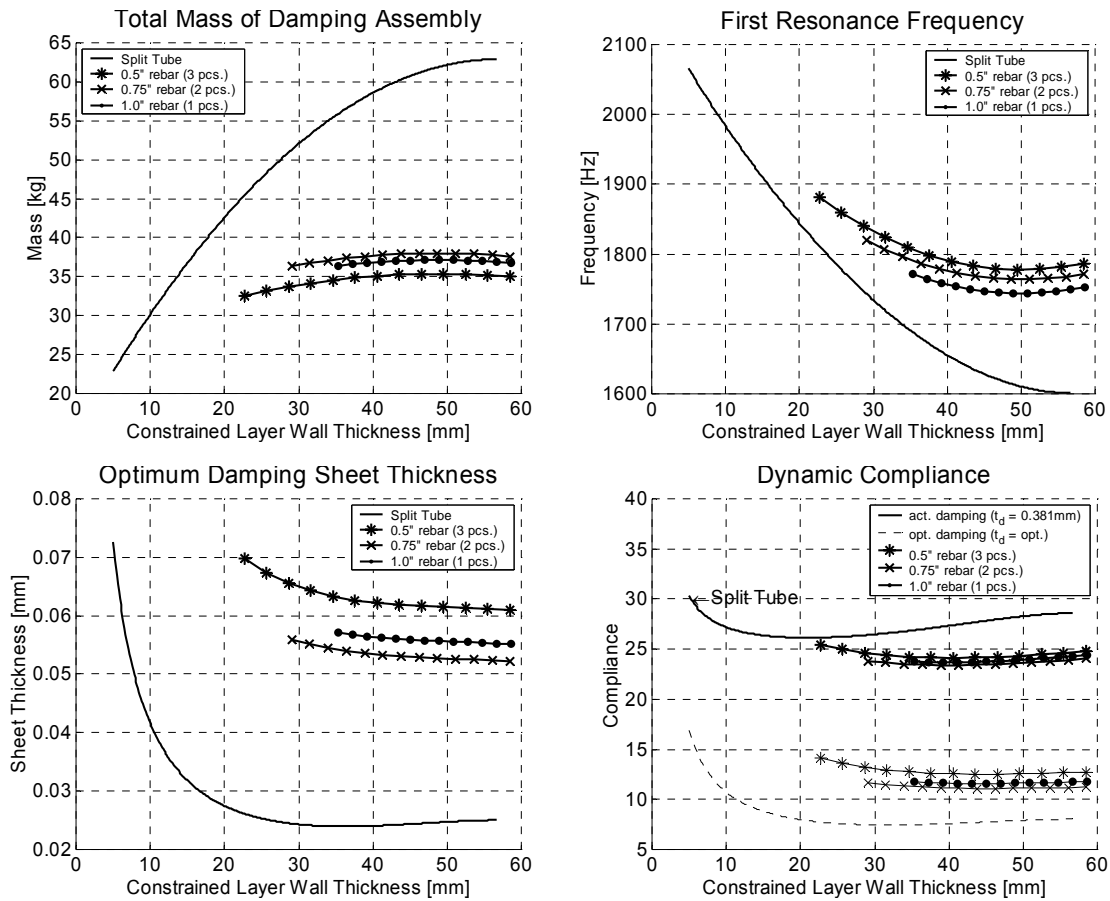


Figure 5.10 Predicted performance - split tube vs. concrete cast damper with single rebar

1. Star System<sup>TM</sup> is registered trademark of Spectral Dynamics



**Figure 5.11** Predicted performance - split tube vs. concrete cast design with multiple rebars

Using the analytical scheme presented in Section 4.5, a set of graphs was used to size the various damping designs in order to achieve maximum performance.

Based on Figure 5.11d, the pipe for the split tube constraining layer would ideally have a wall thickness of roughly 20 mm in order to achieve its maximum damping capability. However, no standard pipe was available with such dimensions. Instead, a 4" pipe with a wall thickness of 0.258" was used to constrain the viscoelastic layer. From Figure 5.11d, the dynamic compliance of such a system is predicted to be around 15. The outer dimension of the support tube for the concrete cast design was chosen such that the tube was applicable for all design variations and available as a standard pipe. Hence, the cast constraining layers were supported by a standard 2" pipe with a 0.154" wall thickness.

The resonance frequencies are predicted from the characteristic equation for a thin beam:

$$U(x) = C_1 \cos\left(\frac{\lambda x}{l}\right) + C_2 \sin\left(\frac{\lambda x}{l}\right) + C_3 \cosh\left(\frac{\lambda x}{l}\right) + C_4 \sinh\left(\frac{\lambda x}{l}\right) \quad (5.2)$$

A free-free beam has neither bending moments nor shear forces at its ends, and using the Euler-Bernoulli equation for a thin beam, the boundary conditions can be found to [Beitz et al]:

$$\begin{aligned} \text{bending moments: } & U''(x = 0) = 0 \text{ and } U''(x = l) = 0 \\ \text{shear forces: } & U'''(x = 0) = 0 \text{ and } U'''(x = l) = 0 \end{aligned} \quad (5.3)$$

Taking the derivatives of Eq. 5.2 and applying the boundary conditions found in Eq. 5.3, the characteristic frequency equation of such a beam can be calculated to (derivation in Section C.2 on page 204:

$$\cos \lambda \cosh \lambda = 1 \quad (5.4)$$

which has the following solutions:

**TABLE 5.2** Solutions of characteristic frequency equation

$\lambda_1$	$\lambda_2$	$\lambda_3$	$\lambda_4$
4.73	7.853	10.996	14.137

The modal frequencies for the bending beam can then be determined to be:

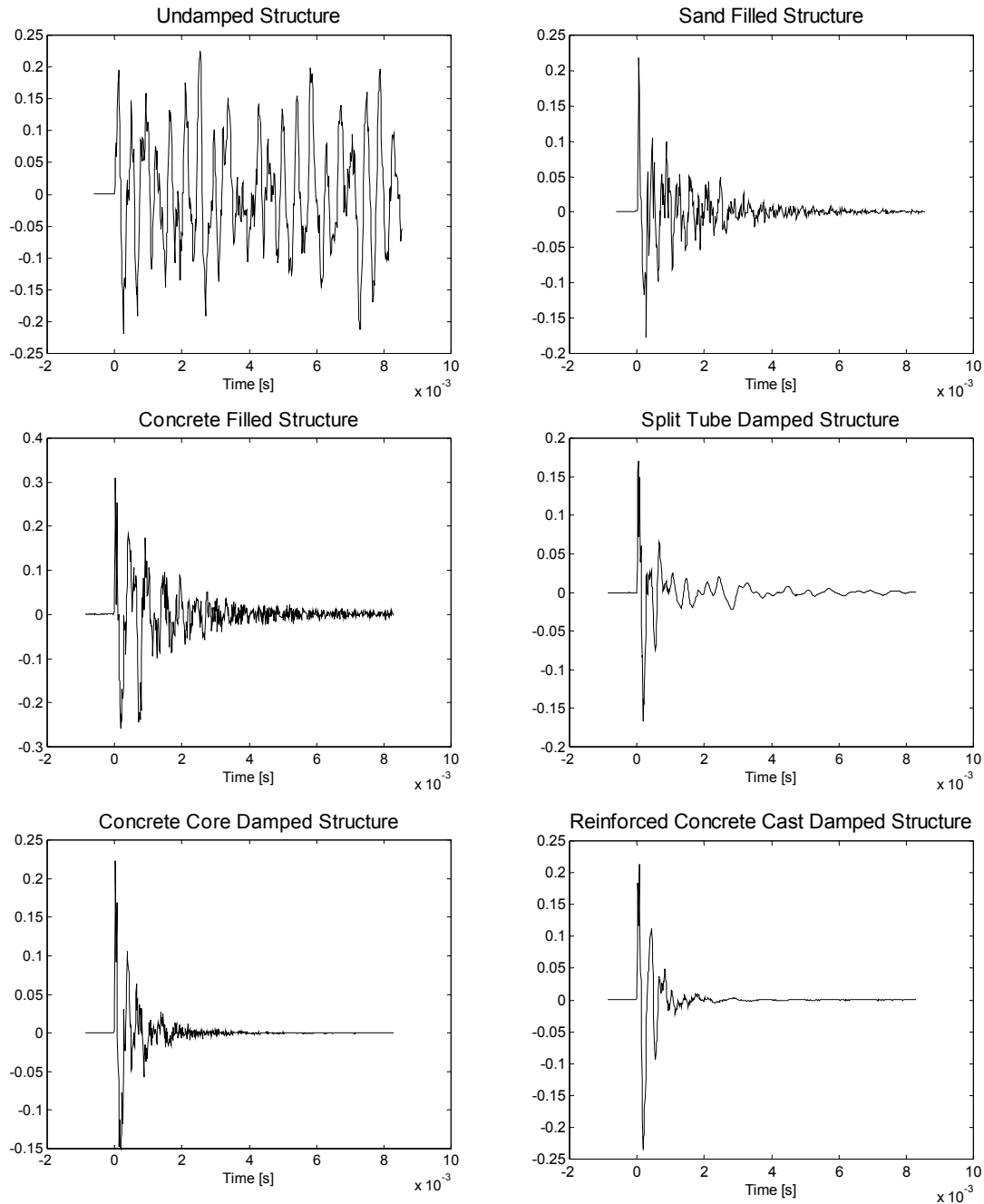
$$\omega_n = \frac{\lambda_n^2}{l^2} \sqrt{\frac{EI}{\rho A}} \quad (5.5)$$

## 5.4 Experimental Data

Exciting the free hanging damping assembly with the impact hammer and transforming the response and the impact signal from the time into the frequency domain, transfer functions for each damping design were recorded. A transfer function indicates the ratio of the response amplitude to the excitation amplitude over a frequency range. Resonance fre-

quencies show up as peaks because at these frequencies, the response is significantly larger than the excitation.

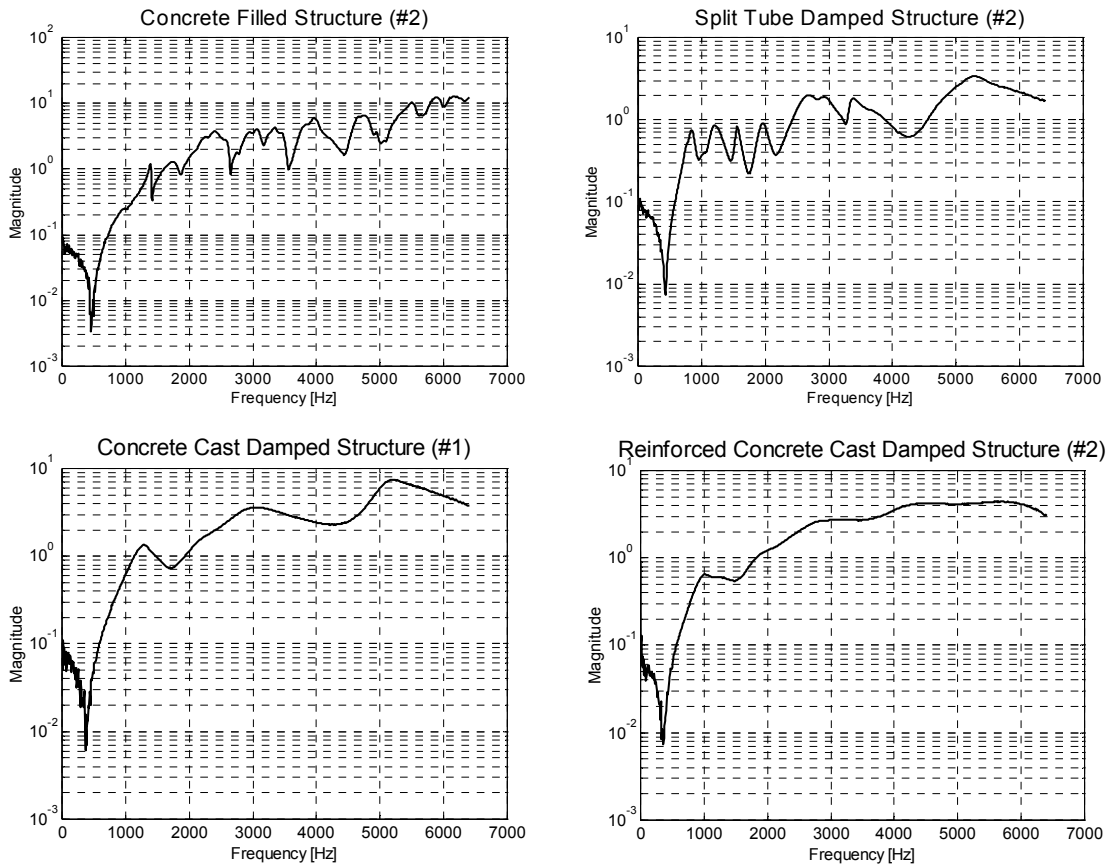
From the time response in Figure 5.12 it can already be seen that vibrations decay at different rates depending on the design of the damper. While the undamped tube rings like



**Figure 5.12** Time response of various damper

the liberty bell and shows no decay of the amplitude, both sand and concrete filled structures cause the amplitude of the vibration to decay rather quickly, indicating a substantial amount of damping. The time response of the split tube damped structure shows a similar behavior, suggesting that the damping is comparable to the sand and concrete filled tubes. The concrete cast dampers, however, exhibit a much improved behavior. The amplitudes of the vibration decay very quickly, much quicker than with any of the previous designs, indicating the presence of a substantially larger amount of structural damping.

For a quantitative assessment of the damping designs, the transfer functions obtained with the frequency analyzer were read into the Star System<sup>TM</sup><sup>1</sup> software, a vibration analysis package whose advanced curve fitting capabilities provide an easy means of determining



**Figure 5.13** Frequency response of damping designs

1. Star System<sup>TM</sup> is registered trademark of Spectral Dynamics

resonance frequencies and its associated damping factors. Figure 5.13 shows typical transfer functions.

The next step of the experiments is the identification of the bending modes. Because the damping assembly was rather short compared to its diameter, the bending modes don't readily show up in the transfer functions. Instead, a full modal analysis had to be performed by attaching a three-axis accelerometer at various locations on the outer tube and recording the frequency response with the analyzer. This three-dimensional data could then be analyzed with the Star System software to distinguish bending modes from other modes that occur in non-solid structures.

## 5.5 Test Results

The loss factors for the various damping designs at the first bending mode were calculated using the vibration analysis software. While the split tube damped design had a very distinct first bending mode, analyzing the concrete cast design was much harder. Consequently, the standard deviation for the split tubes was only 0.9% while the non-reinforced concrete damper's deviated roughly 2% and the reinforced design even 3.8%.

**TABLE 5.3** Predicted and actual performance of various damper designs

	<b>un-damped</b>	<b>sand filled</b>	<b>concrete filled</b>	<b>split tube</b>	<b>concrete no rebar</b>	<b>concrete 3x 0.5" rebar</b>
predicted mass [kg]	13.2	24.7	30.1	23	28.5	46
actual mass [kg]	13.1	24.1	29.8	22.8	28.1	45.5
1. predicted resonance frequency [Hz] (bending)	2286	1634	1720	1581	1503	1820
1. actual resonance frequency (bending)	N/A	N/A	N/A	1530	1260	1640
predicted loss factor	715	N/A	N/A	0.037	0.035	0.044
measured loss factor	N/A	N/A	N/A	0.055	0.145	0.3

## 5.6 Conclusion

The measured loss factor for the split tube damped structure is with 5.5% reasonably close to the predicted factor of 3.5%. This indicates that even though the closed form solution does not return the exact damping factors, the method is sufficiently accurate to do a first order layout of such a design. The concrete cast dampers, however, performed much better than predicted based on constrained layer damping theory. The design without any reinforcement topped the prediction by almost a factor of 3, providing an astonishing loss factor of 14.5% for the first bending mode. The reinforced design performed even better. With a measured modal loss factor of 30%, this design topped the prediction by a factor of more than 6.

Without a new set of experiments, no conclusive answer to the question as to why the concrete dampers performed so incredibly well, can be given. It can be speculated, that one or more of the following reasons may have contributed to this outstanding performance:

- Concrete adds material damping, an effect that was not included in the damping performance predictions.
- The pressure generated by the expanding concrete may have significantly squeezed the viscoelastic material, resulting in a thinner than expected damping layer. Because damping was limited by the lack of extremely thin damping sheets, performance may have improved as a direct result of the change in damping sheet thickness.
- Because the constraining layers are completely wrapped with viscoelastic material, more surface area is available where shear strain can occur.
- Unaccounted micro motion between concrete and rebars and/or damping sheet.
- Deviations from the ideal constraining layer shapes resulted in a jigsaw like interlocking between individual constraining layers. This effect is quite likely to enhance the damping performance as well.





# Chapter 6

## CASE STUDY - STG



**Figure 6.1** STG 5-axis tool and cutter grinder

The Star STG is a five-axis tool and cutter grinder designed for the manufacturing of end mills and similar shaped workpieces. The complex geometry of the workpieces requires the machine to have three linear and two rotary axes. The functional requirements (FR) for the machine are given in Table 6.1 as part of a comparison between the existing Star ATG, which is supposed to be replaced by the new design, and their most prominent competitors. Though not listed as part of the FR's, following the company's strategy, the new

machine had to include a few components of the existing machine such as the numerical controllers and the traction drive systems which is used to spin the two rotary axes. In accordance with the principle of rapid machine design, the STG had to be build from standard parts as much as possible.

**TABLE 6.1** Machine Specification Comparison

<b>Specification</b>	<b>Star ATG</b>	<b>Star STG</b>	<b>Walters MP</b>	<b>Walters HP</b>	<b>Anca RGX</b>	<b>Anca TGX</b>
-X- [mm]	213	350	470	660	390	460
-Y- [mm]	117	275	200	320	390	350
-Z- [mm]	292	700	350	490	380	760
-A- [deg]	360	360	360	360	360	360
-B- [deg]	90	±120	±200	±200	270	270
Max. Work Dia. [mm]	102	200	100	240	250	350
Max. Work Length [mm]	686	400	270	370	325	?
Work Holder Interface	∅63.5	HSK 63	ISO 50	ISO 50	ISO 50	ISO 50
Work Holder Clamp	No	Optional	Yes	Yes	No	Yes
Center Height w\ Table	89	165	130	145	?	?
Center Height wo\ Table	N/A	220	160	190	?	?
Auto Steady Rest	Opt.	Opt.	Opt.	Opt.	Opt.	Opt.
Spindle Power [kW]	6	21	7	18	8	18
Max Spindle Speed [1/ min]	5,275	8,000	9,500	8,500	10,000	8,000
Tool Interface	3" TPF	HSK 63F	?	?	ISO 30	HSK 50E
Max Wheel Dia. [mm]	150	220	150	200	?	200
Number of Spindles	1	1	2	2	2	1
Tool Changer	N/A	3	N/A	N/A	N/A	2
Wheel Truing Spindle	No	Opt.	Opt.	Opt.	No	Opt.
Wheel Probe	Opt.	Opt.	?	?	?	?
Software Simulation	No	Opt.	Opt.	Opt.	Opt.	Opt.
Rotary Encoders (A-B)	Opt.	Stand.	?	?	?	Stand.
Linear Encoders (X-Y- Z)	Stand.	Stand.	?	?	?	?
Intelli Dress System	No	Opt.	?	?	?	?
Auto Stick Feeder	No	Opt.	?	?	?	?
Price US Dollar	\$250k	?	\$200k	\$300k	\$185k	\$350k

This includes the use of standard linear rails instead of labor intensive box ways. Because the machine's functional requirement does not demand extremely high speeds and accelerations for the axes, the design will be equipped with ballscrews instead of highly dynamic but also very costly linear motor systems.

## **6.1 STG**

With a maximum projected workpiece size of 200 mm diameter and a maximum length of 400 mm, the machine using a 150 mm diameter grinding wheel, needs to have a X-axis travel of 350 mm, 275 mm travel for the Y-axis, and 700 mm travel for the Z-axis. Of especial importance are the two rotary axes and their orientation with respect to the endmill itself. The rotation of the A-axis is used to grind the cylindrical surface of the workpiece and therefore has to be continuous and along the endmill's axis of rotation. The B-axis needs to have a rotation of  $\pm 120^\circ$  in order to grind the round cutting edges of a ball endmill and must be orientated normal to the endmill's axis of rotation.

### 6.1.1 Overall Machine Concepts

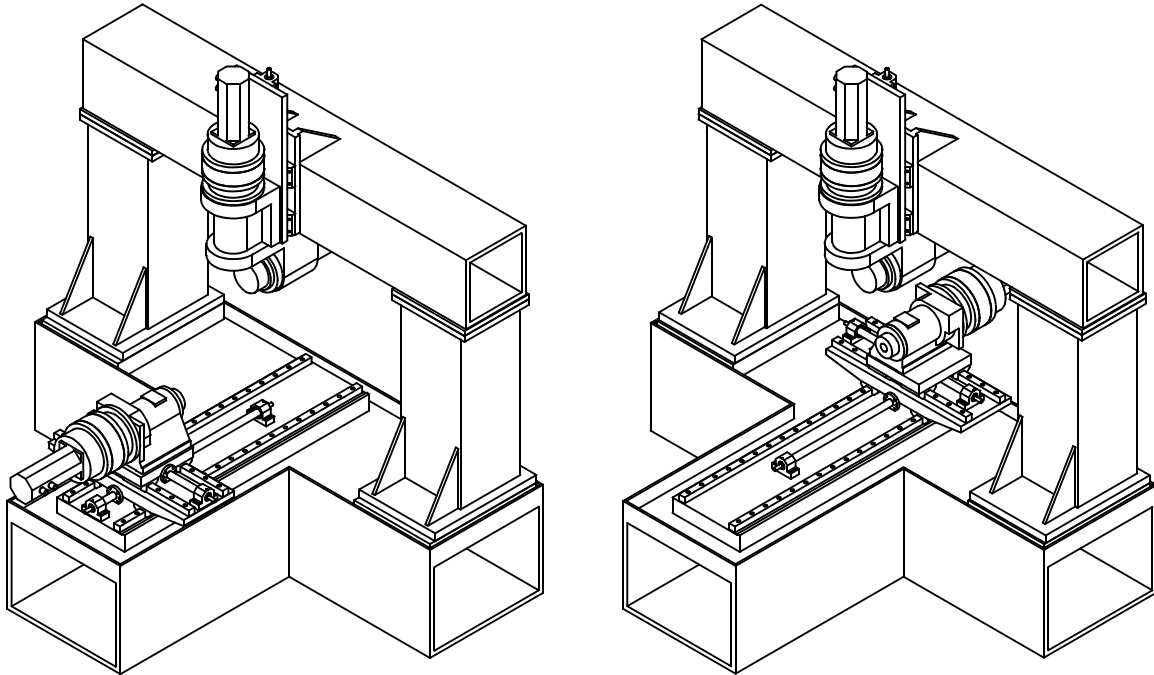


Figure 6.2 STG concepts #1 (a) and #2 (b)

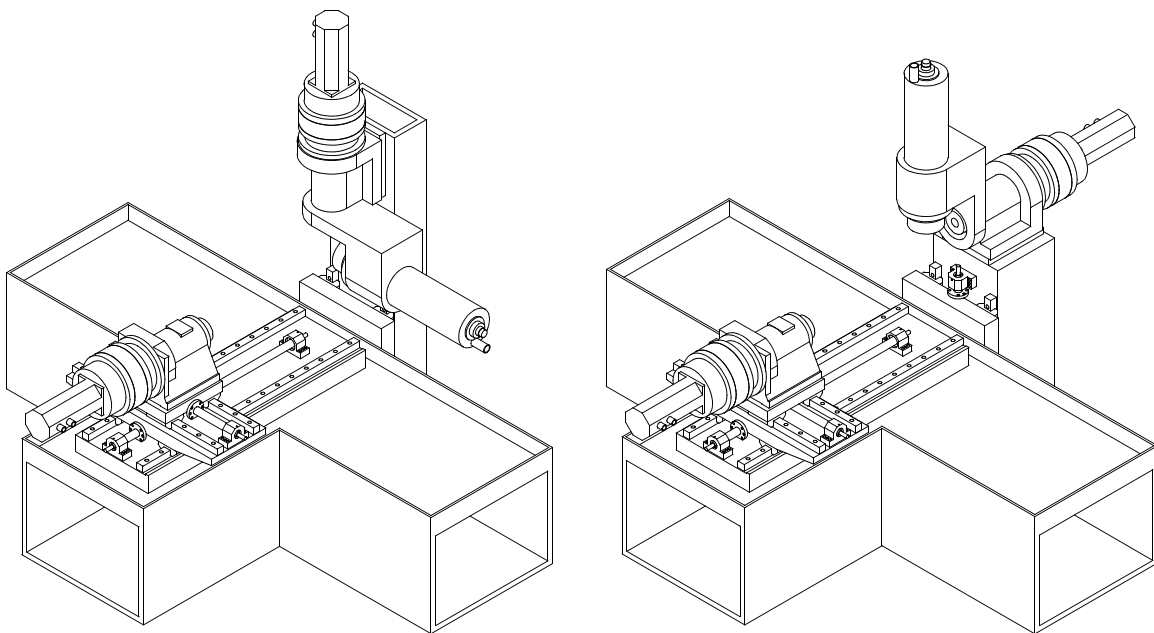
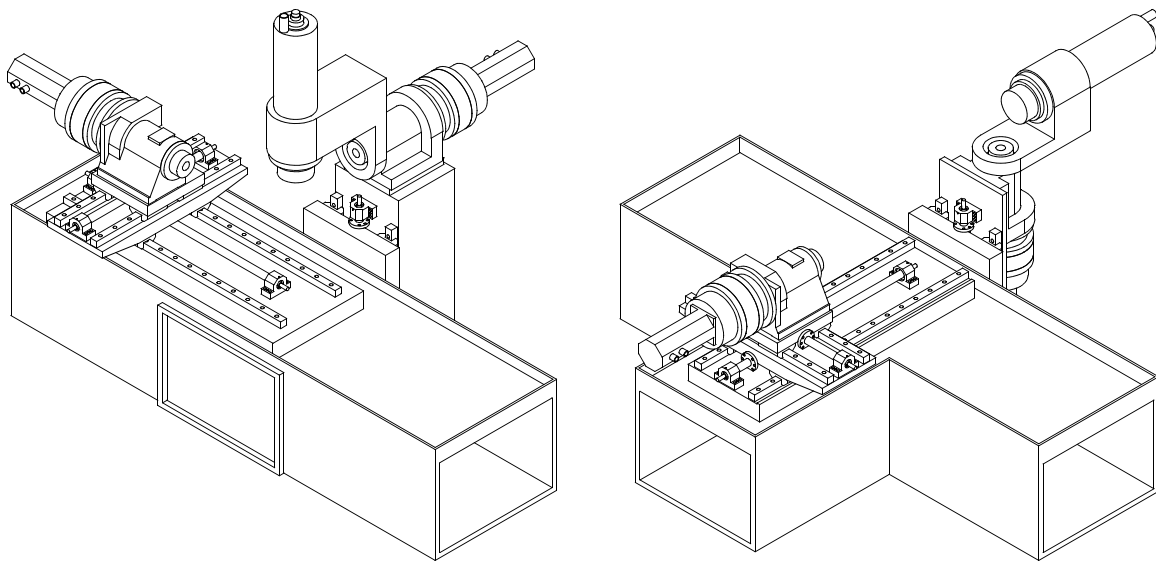
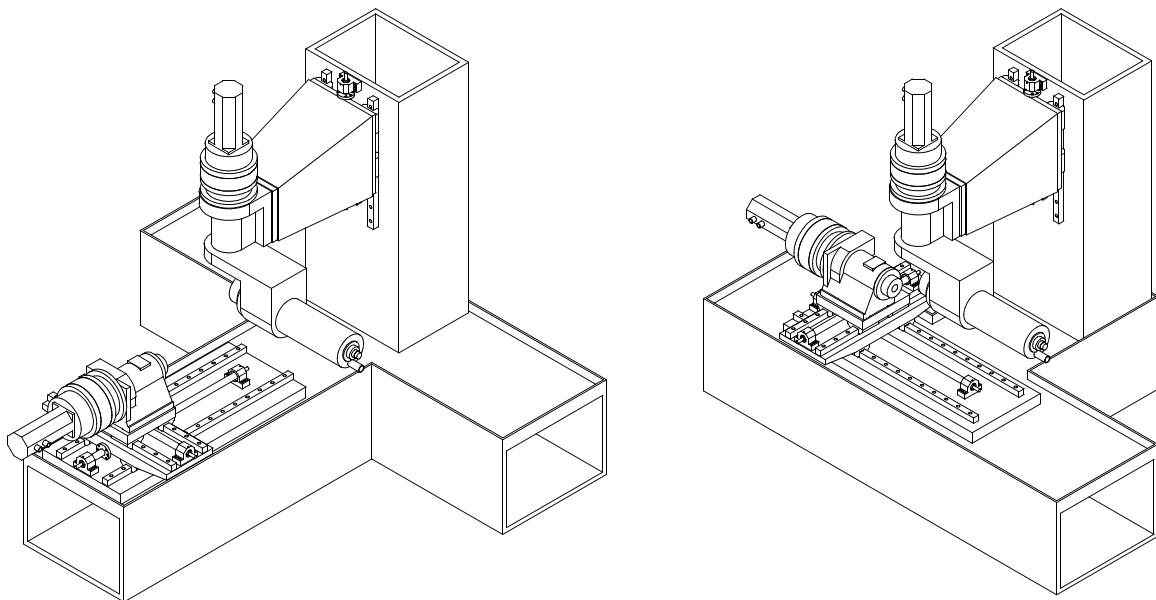


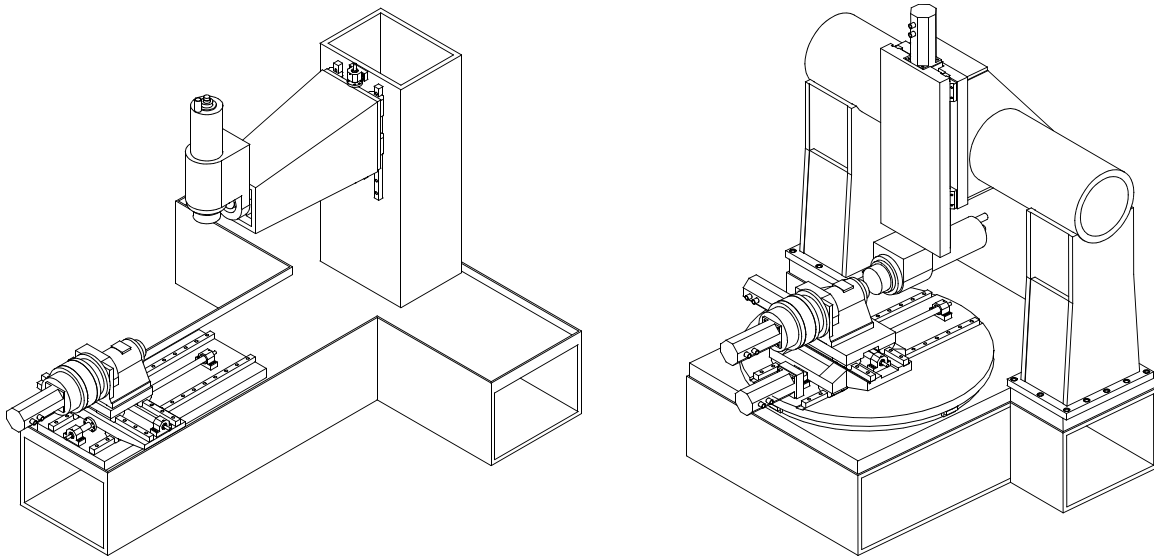
Figure 6.3 STG concepts #3 (a) and #4 (b)



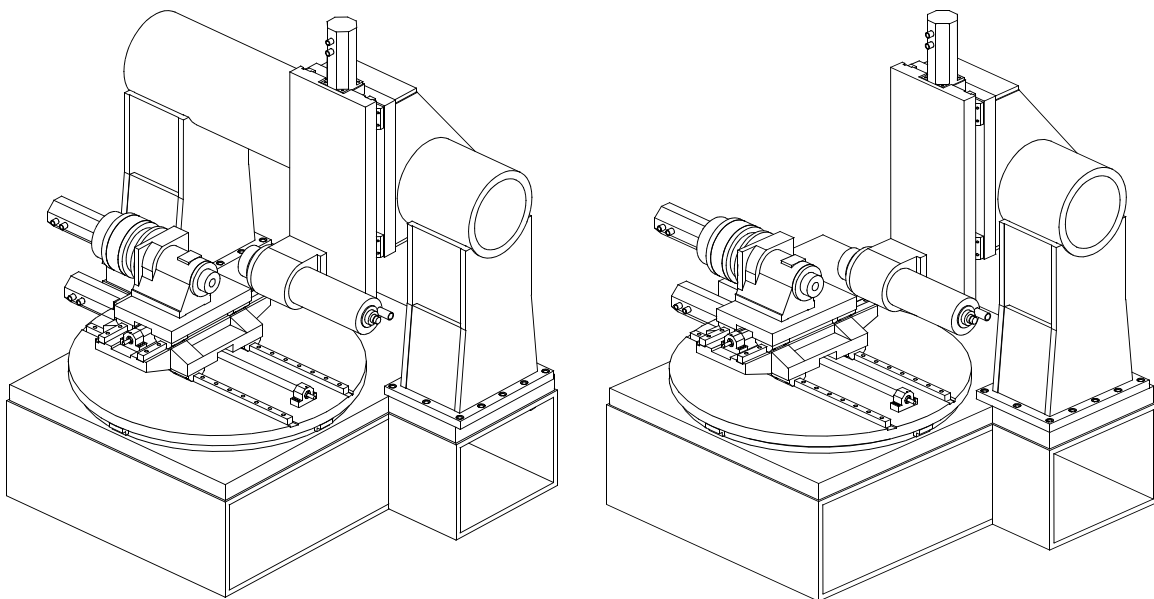
**Figure 6.4** STG concepts #5 (a) and #6 (b)



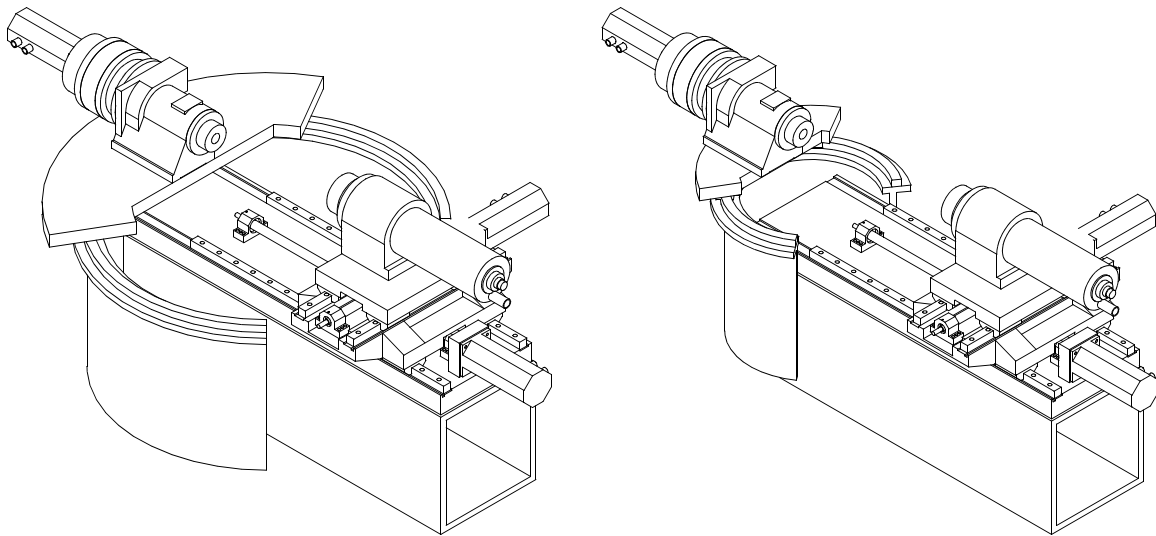
**Figure 6.5** STG concepts #7 (a) and #8 (b)



**Figure 6.6** STG concepts #9 (a) and #10 (b)



**Figure 6.7** STG concepts #11 (a) and #12 (b)



**Figure 6.8** STG concepts #13 (a) and #14 (b)

### **6.1.2 First Round Elimination - Fulfillment of Functional Requirements**

Applying the first set of criteria, concepts #3, #4, #5, and #9 become eliminated because their B-axes violate the functional requirement for grinding an endmill (Table 6.2). All four concepts fail to have either the B-axis normal to workpiece's rotational axis (# 4, #5, and #9) or the full  $\pm 120^\circ$  range of motion (#3). The remaining concepts satisfy the first criteria and are evaluated in Section 6.1.3 in more detail.

### **6.1.3 Second Round Elimination - Visual Inspection**

#### **Concept #1 and #2**

The two concepts are basically identical with the exception of the orientation of the Z-axis. Both are built as gantry-type machines, providing large workvolumes and good stiffness. Motion for all linear axes is provided by ballscrews and rotary motion is created through traction drives that have motors bolted on at the end. While with concept #1 the operator can conveniently reach the workpiece, concept #2 would force him to reach underneath the spindle. Also, concept #2 makes no use of the work space left of the spindle. Clearly concept #1 is better than #2 which will hereby be eliminated. The two most

**TABLE 6.2** Concept selection based on axis range of motion and orientation

Concept #	X-Axis	Y-Axis	Z-Axis	A-Axis	B-Axis
1	yes	yes	yes	yes	yes
2	yes	yes	yes	yes	yes
3	yes	yes	yes	yes	no
4	yes	yes	yes	yes	no
5	yes	yes	yes	yes	no
6	yes	yes	yes	yes	yes
7	yes	yes	yes	yes	yes
8	yes	yes	yes	yes	yes
9	yes	yes	yes	yes	no
10	yes	yes	yes	yes	yes
11	yes	yes	yes	yes	yes
12	yes	yes	yes	yes	yes
13	yes	yes	yes	yes	yes
14	yes	yes	yes	yes	yes

critical components are likely to be the gantry and the Y-axis. The gantry is subject to high torsional loads from the Y-axis which will cause it to twist and the Y-axis will experience substantial bending moments due to its rather long lever arm. In addition, the bearings of the Y-axis will have to take high normal loads when transmitting these bending moments to the gantry. As a result of these loads, deformations within the bearings will cause the Y-axis to rotate. Further rotation will come from the twist of the gantry, making this design prone to an effect commonly referred to as Abbe error. This effect, whereby an angular error manifests itself in a linear form via amplification by a lever arm is one of the dominant sources of error in a machine tool and its importance cannot be overstressed [Slocum (a), Bryan].



**Concept #6**

This variation has an unusual axis arrangement whereby the Y-axis becomes attached to the back-side of the base. Even though the orientation of the axes satisfies the functional requirement given in Table 6.1, the solution is not a very good one. The drive system of the Y-axis and the rotary mechanism of the B-axis push the grinding wheel too far away from the workpiece, rendering this variation basically useless. Through visual inspection it is hereby eliminated.

**Concept #7 and #8**

The following two variations have a series of characteristics in common. Both have the Y-axis mounted to a single, central upright and the B-axis suspended far enough away from the column to enable the spindle to rotate past it. The difference lies in the orientation of the Z-axis which for concept #7 is head-on to the Y-axis while concept #8 has is rotated by 90°, thereby decreasing the footprint of this variation considerably. Thus, concept #8 is more space efficient and therefore preferable to concept #7 which is eliminated from further evaluation. In Figure 6.5b, the most critical components of the design can be seen: the Y-axis. Because of the swept volume required by the spindle as it rotates driven by the B-axis, the Y-axis housing needs to be rather long. The structural loop of this arrangement is rather long and causes large bending moments within the Y-axis housing and the upright and as a result large normal forces on the Y-axis bearings. While the effect of the deformations within the upright and the Y-axis housing together with the compliance of the bearings can already be pretty substantial, it is being amplified by the large lever arm of the system, known as the Abbe error.

**Concept #10**

This variation attempts to limit Abbe errors found in concepts #6 by using a gantry to suspend the B-axis. Further stiffness enhancement results from using a circular bearing system (THK type HCR) underneath the rotary table instead of the ball bearings used inside the traction drive. The circular bearing system is built on a rail similar to linear bearings,

except it forms a circle rather than a straight [THK]. Because of the large diameter of this system, normal loads onto the bearing trucks are small, resulting in very small error motion from displacements within the bearings. The most critical component is probably going to be the Y-axis and its bearings as well as the gantry.

### **Concept #11**

This concept is a variation on #11 and has the spindle mounted higher on the Y-axis and rotated by  $90^\circ$ . The resulting reduction in lever arm between the tool and the Y-axis bearings minimizes the Abbe error of this axis compared to concept #10. The rotary tables of both designs are identical as are all linear axes. The smaller torsional loads onto the gantry and smaller moment loads on the Y-axis and its bearings make this variation preferable to concept #10.

### **Concept #12**

This variation has the left part of the gantry eliminated in an attempt to save material and labor costs. All other features are identical to concept #11. The most critical component will be the upright which has to take considerable moment and torsional loads.

### **Concept #13 and #14**

Both concepts attempt to combine the linear motion of the Y-axis with the rotary motion of the B-axis within a single component. The housing of the linear axis consists of a steel pipe which has a section cut out wide enough for the base slip in. On both sides of the opening, linear rails are mounted to connect the housing to the base. A third rail is mounted at the apex of the semi-circular weldment. A circular bearing system is bolted on top of the Y-axis and driven by a rack-and-pinion drive system. The design faces a couple of challenges: using three rails at the given spatial distribution creates a highly overconstrained system which will need multiple adjustments during the assembly. Furthermore, attaching the flat rails to the round surface of the tube will require complex adapters, making this solution rather costly. Also, the open section of the Y-axis causes the housing to lose a significant amount of stiffness compared to a closed section. Although the idea of

combining two axes in one housing might be appealing, the shown two concepts have too many difficulties associated to be viable options.

#### 6.1.4 Result of First and Second Round Elimination

Through visual inspection, several of the STG concepts were eliminated either because they failed to satisfy functional requirements or obvious difficulties in the design that were captured with other concepts. The remaining design solutions for the tool and cutter grinder are concepts #1, #8, #11, and #12 (Figure 6.9).

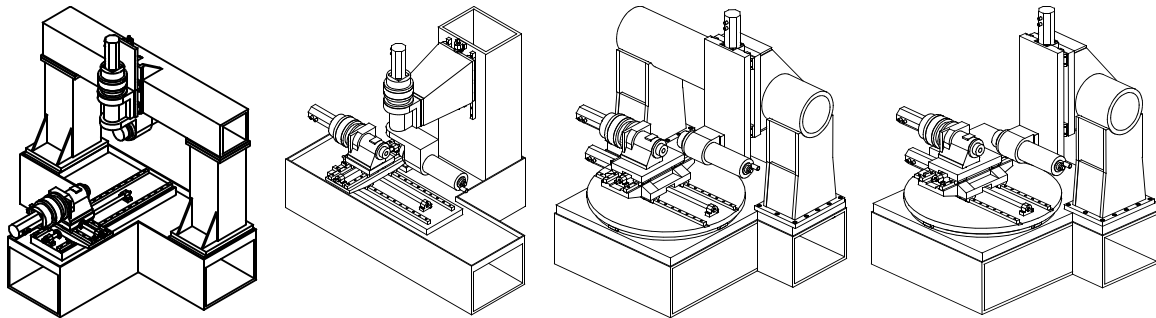
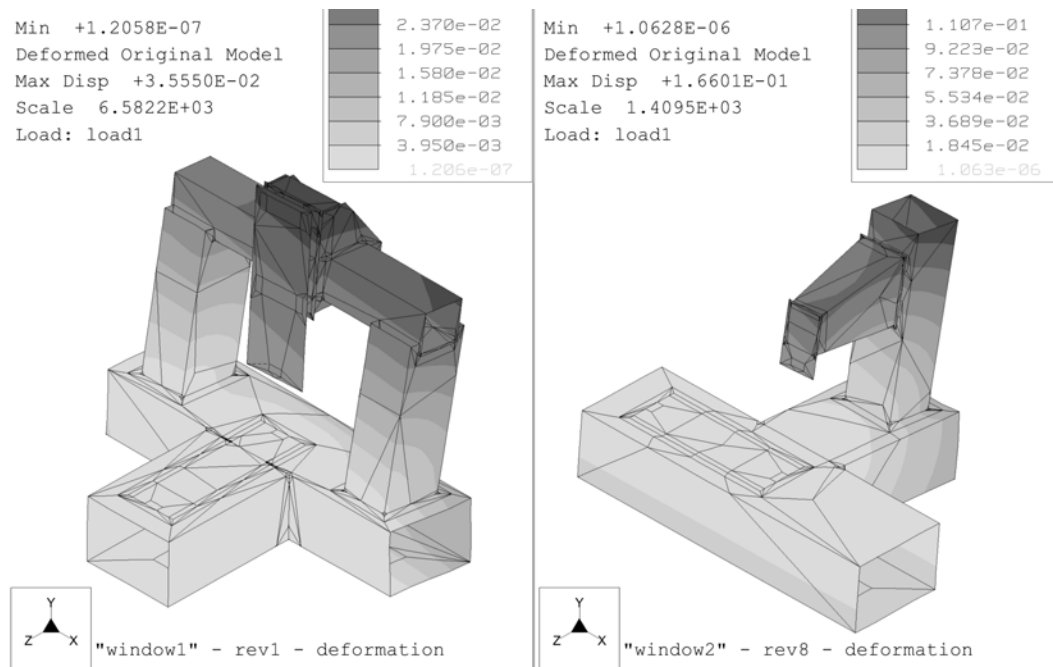


Figure 6.9 STG concepts remaining after first and second round elimination

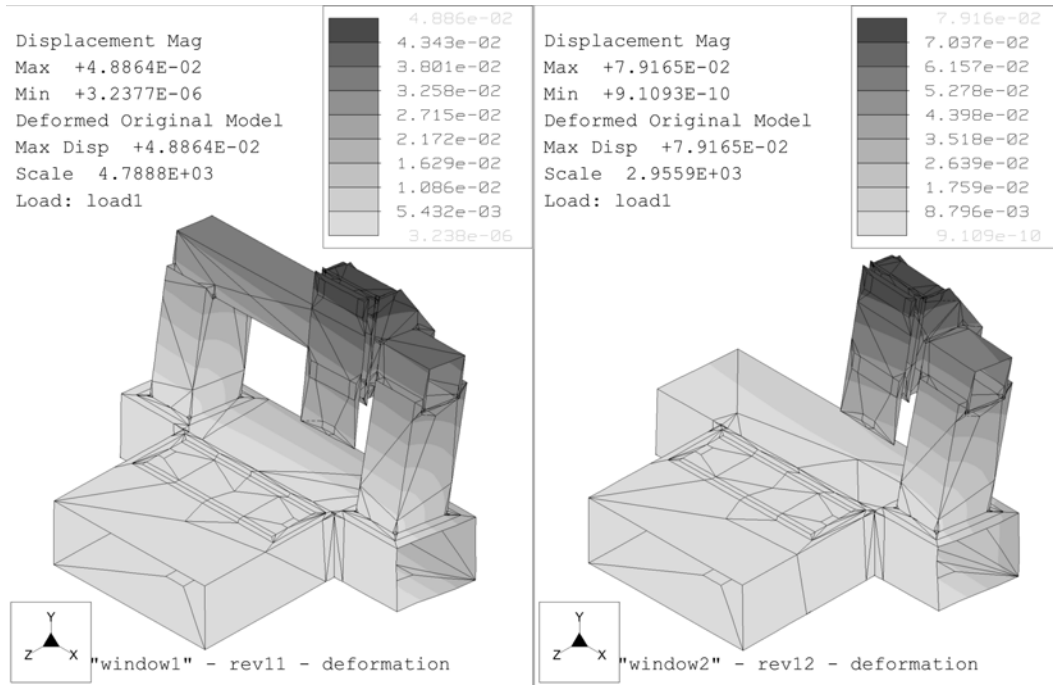
#### 6.1.5 Third Round Elimination - FEA Analysis

In Figure 6.9, four STG concepts that passed the first and second round elimination are shown. Shape and appearance of these remaining concepts is very different, which is why the visual inspection used in Section 6.1.3 cannot reliably be used for the final round selection. For instance, concept #11 and #12 are identical with the exception of the gantry, whose left support is omitted in concept #12. With the gantry being an open as opposed to a closed structure, the gantry of concept #12 is subject to additional bending and torsional loads, requiring the upright to be significantly more rigid than the columns used in concept #11. In order to have a quantitative rather than qualitative basis for the final concept selection, two sets of FEA analyses were performed on each design: static deformation and modal analysis.

For the purpose of selecting a concept, it is sufficient to know which concepts perform better than others, a conclusion which can be derived not only from absolute but also relative measures. In other words, at this point it is not necessary to know the absolute value of certain criteria. Instead, comparing performance criteria relative to each other is perfectly acceptable. For instance, the overall stiffness of the four concepts is one of the main criteria by which the design are selected. As discussed in Section 2.2.1, the structural loop of a design is defined as an assembly of springs in series and the Z- and X-axis are an important part of it. However, as can be seen in Figure 6.9, the assembly of the two axes is identical in all four concepts. While their compliance affects the absolute rigidity of all four concepts, their contribution to the overall compliance remains unchanged. As said earlier, comparing designs can be done using relative measures and it is therefore acceptable to neglect the effects of components that are identical in every of the designs to be compared. This allows a simplified setup of the models whereby the Z- and X-axis are omitted from the analysis because they are identical in every concept and their contribution to the overall compliance remains unchanged.



**Figure 6.10** Deformation of STG concept #1 (a) and concept #8 (b) with 1000 N applied in all three principal directions at tool tip



**Figure 6.11** Deformation of STG concept #11 (a) and concept #12 (b) with 1000 N applied in all three principal directions at tool tip

**TABLE 6.3** Comparison of STG concepts

Concept	$k_x$ [N/ $\mu\text{m}$ ]	$k_y$ [N/ $\mu\text{m}$ ]	$k_z$ [N/ $\mu\text{m}$ ]	1. mode [Hz]	weight [kg]
#1	72.0	277.9	64.2	15.0	4445
#8	19.6	17.6	17.7	21.8	2692
#11	122.3	540.5	56.2	12.5	4530
#12	63.1	82.0	40.2	13.0	3798

The FEA identifies concept #11 as the best design, followed by concept #1. This is a direct result of a shorter Y-axis made possible by rotating the spindle 90 degrees and mounting it closer to the bearings. In addition, the height gained by mounting the spindle higher up also allows the uprights to be shorter, resulting in a stiffer and lighter gantry. Both concepts have the potential to be a good solution to the given design problem.

Concept #12 is doing pretty well for a non-gantry setup, considering that the upright is identical to the ones used in concept #11. Optimizing this upright should make it possible to turn this concept into a viable design solution. Concept #8, on the other hand, suffers from the big bending moments that result from the long lever arm of the Y-axis. These bending moments not only deform the housing of this axis, they also induce huge loads onto the Y-axis bearings whose internal compliance causes the Y-axis to rotate. The rotational error of the bearing is translated to a substantial linear displacement at the tool tip, known as the Abbe error. This error is amplified further by the uprights as it twists under the torsional load from the Y-axis. Altogether, it would take an extremely stiff upright and Y-axis housing as well as extremely Y-axis bearings to bring this design even close to where the three other concepts are. It is therefore concluded, that concept #8 should not be pursued any further.

### **6.1.6 Final Round Elimination - Team Discussion**

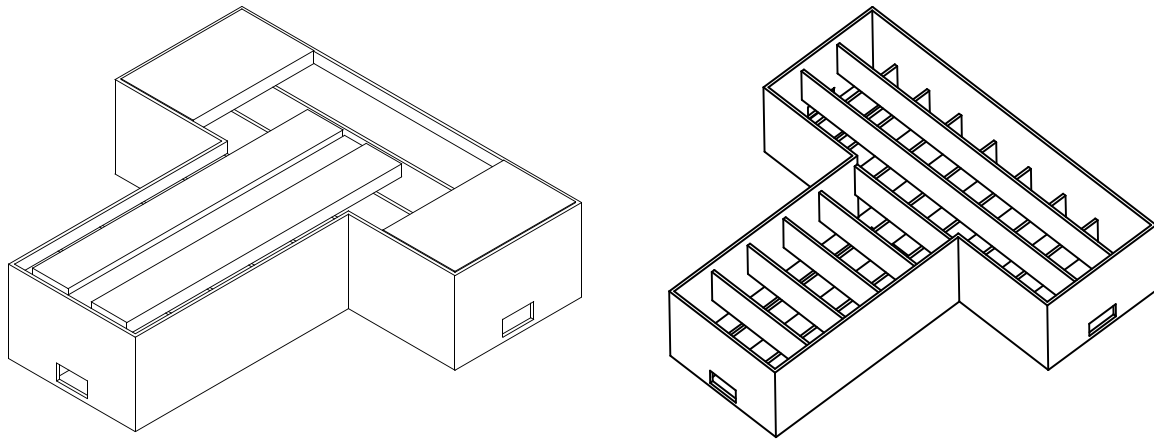
The FEA analysis performed in Section 6.1.5 identified three concepts that can potentially be turned into good design solutions, with concept #11 being the most promising design, followed by concept #1 and concept #12. While technically concept #11 would need the least additional effort to be optimized towards the final performance target, it was decided to select concept #1 as the design of choice. The reason behind this decision was an existing component of the old design that could be used for the B-axis utilized in concept #1. In fact, the drive system of the B-axis and the headstock are built from the same components, making this design quite modular. Concept #11 and #12, on the other hand, have a big round table with a highly specialized circular bearing system supporting it. The rotary inertia of such a table is substantial, requiring the drive system to handle large torques. In the end, concept #1 is a more compact design that can partly be built from existing components.

## **6.2 STG Base**

As the overall machine design, concept #1, a gantry type machine with a T-shaped base was chosen. In this section, fabricated design concepts for such a base are presented.

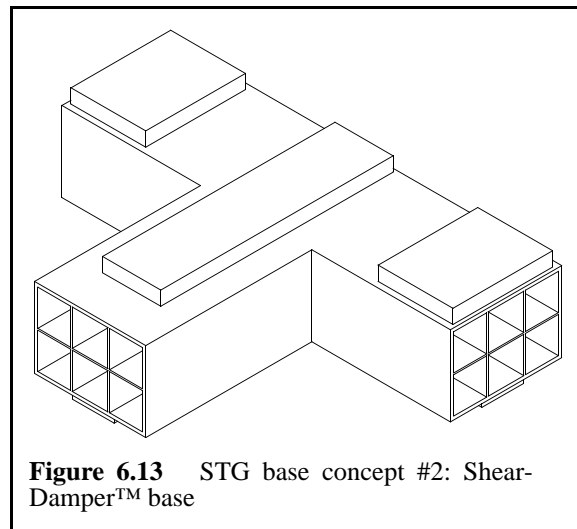
### **6.2.1 STG Base Concepts**

The first concept is a conventional box-type base with a T-shaped frame fabricated from steel plates (Figure 6.12). To stiffen up the structure, webbing is welded inside the base. The bottom remains open and is later used to fill all voids with concrete for additional stiffness and damping. The top has added, reasonably thick steel plates, that serve as mounting surfaces for the bridge and the Z-axis assembly.



**Figure 6.12** STG base concept #1: box-type (a) and shear layer damped base (b)

Alternatively, a similar shaped base could be used, but instead of using webbing and concrete, stiffness and damping would be enhanced by adding rectangular Shear-Dampers<sup>TM</sup><sup>1</sup>. The shear layer damped based is an open structure. i.e. the cross sections aren't closed off because the rectangular dampers are inserted through the openings after the basic frame is fabricated. The design faces a particular manufacturing



**Figure 6.13** STG base concept #2: Shear-Damper<sup>TM</sup> base

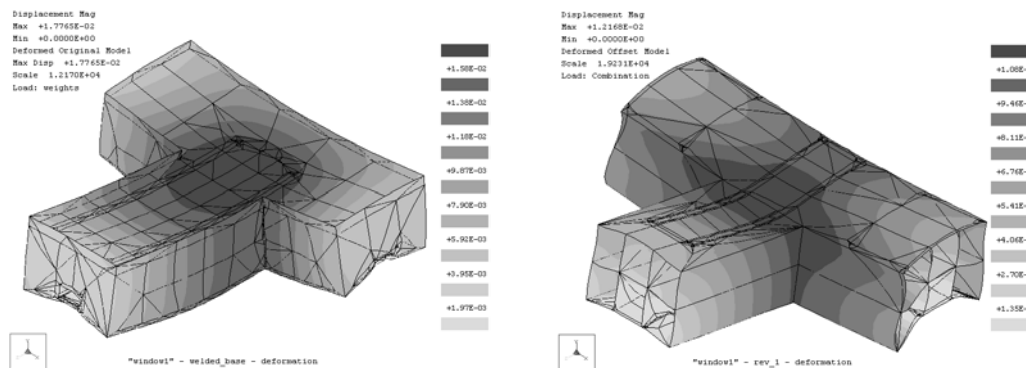
challenge in terms of sealing the shear dampers. As described in Section 4.5.3, the constraining layers, which are the rectangular tubes shown in Figure 6.13, are wrapped with a damping material, then inserted into the structure and all gaps are filled with epoxy. With the T-shaped base, only the rear part of the base has both sides accessible and the damping tubes can properly be sealed before pouring in the epoxy. The front part of the base is much harder to work with because only the front is readily accessible. The tubes have to be inserted into a blind hole, imposing considerable difficulties as far as sealing off the ends is concerned.

1. ShearDamper<sup>TM</sup> is a registered trademark of AESOP Inc.



In order to compare the performance of the two designs, a set of finite element analyses was performed. Using standard materials, issues such as modal frequencies and deformations from cutting forces and gravitational loads were investigated. The loads from the cutting forces were set up in a way that they simulate the forces and moments as they would occur in the real machine. This is a very important concept because forces that have an offset also create moment loads which often put more strain into a structure than the forces by themselves. These cutting loads were applied to the rail mounting surfaces and the interface between the base and bridge. Gravitational loads that simulate the weight of the base itself cause the shear damped base to deflect  $12\ \mu\text{m}$  while the box-type base sags  $18\ \mu\text{m}$  (Figure 6.14). In Section 3.2, kinematically defined machine supports are discussed and their major advantage is highlighted: sag-free machine setup if the reference surfaces are machined with the base fixtured using its native supports. This statement is true to a large extent but it is obvious that the method works best for structures that have sufficient stiffness and therefore limited sag to begin with. From this point of view, the shear damped base is preferable to the box-type base because it deforms less under its own weight than the box-type base does.

The second criteria are deformations from cutting loads. The shear damper base with its open cross section shows considerable twisting at the ends and the maximum deformations are  $1.9\ \mu\text{m}$ . The box-type base, on the other hand, has much more internal structural elements that improve torsional stiffness and only deflects  $0.5\ \mu\text{m}$ , 75% less compared to the alternative design. With an assumed cutting force of  $1000\ \text{N}$  applied in all three princi-



**Figure 6.14** Deformations due to gravity: box-type (a) and shear damped base (b)

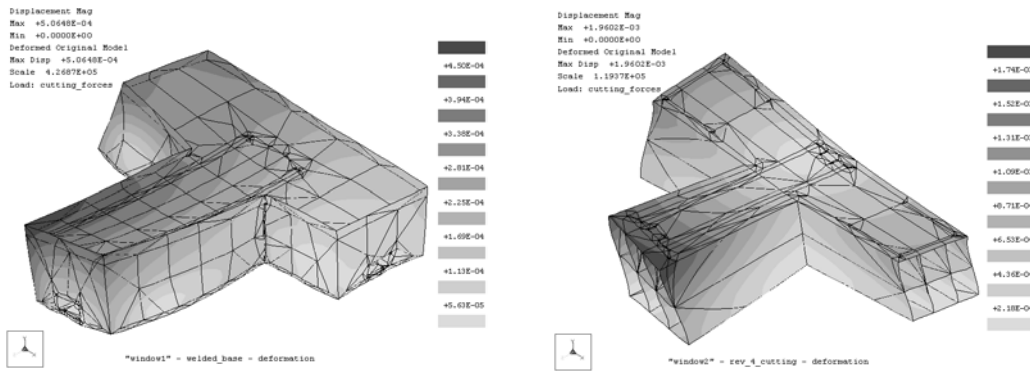


Figure 6.15 Deformations due to cutting force: box-type (a) and shear damped base (b)

pal directions, the stiffness for the box-type and the shear damped design comes out to be 3400 N/ $\mu\text{m}$  and 910 N/ $\mu\text{m}$ , respectively, making the conventional base shown in Figure 6.12a the preferred choice. It should be noted though, that the rigidity achieved by the shear damped base is about what is allocated to the base by the stiffness budget shown in Section 2.2.1. The third criteria for structures is the dynamic stiffness and the modal frequencies are used to express this characteristic. The box-type base has its first mode at 137.9 Hz and involves twist of the front part of the base. The second mode at 138.6 Hz

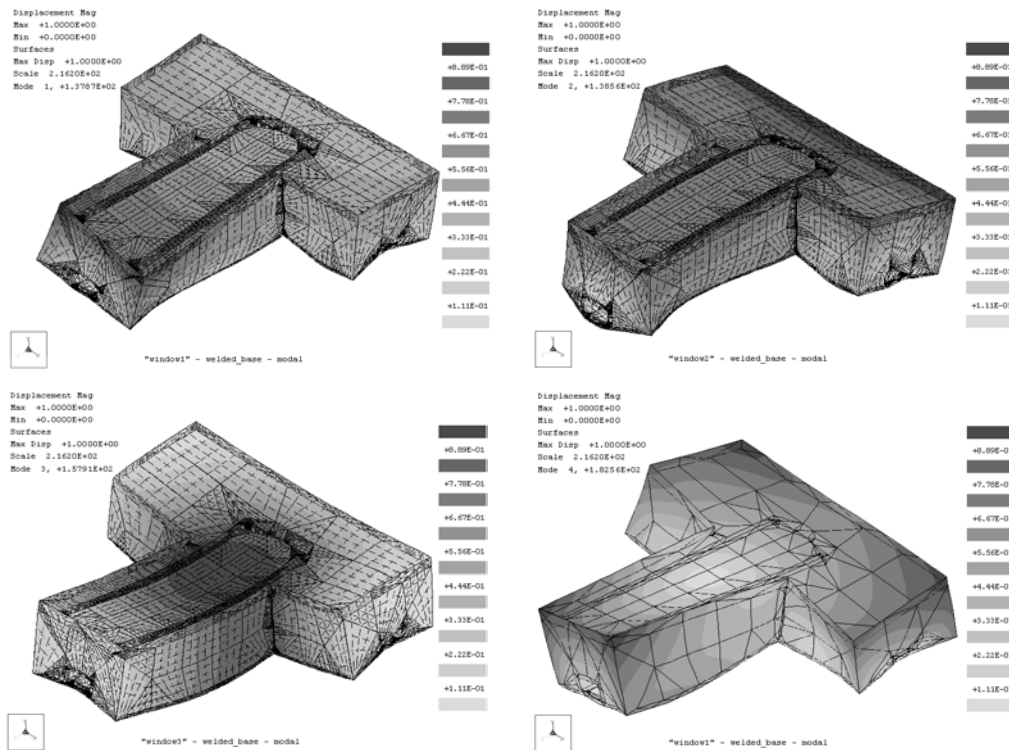
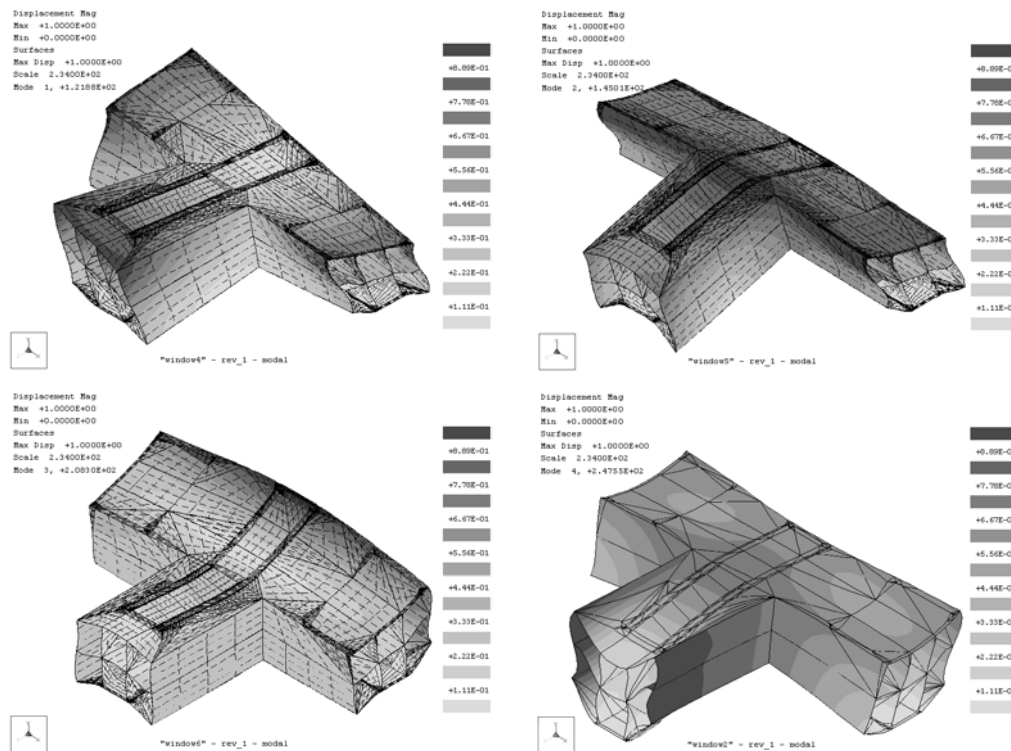


Figure 6.16 First to fourth mode of the box-type base



**Figure 6.17** First to fourth mode of shear damped base

also involves the front part but the resulting motion is a bending up and down bending motion. In the third mode, the entire base bulging up and down at a frequency of 158 Hz. As the fourth mode, the structure in its entirety is twisting at 183 Hz (Figure 6.16).

The shear damped base has its first mode at 122 Hz at which the entire structure is twisting about the Z-axis. The second mode at 145 Hz involves up and down bending of the front half of the base and the third mode at 208 Hz causes the structure to bulge in the center. Finally, the fourth mode exhibits shear motion at 234 Hz between the constrained bottom and the unconstrained top surface (Figure 6.17). From the modal as well as the static deformation analysis it can be seen, that the torsional compliance of the shear damped base is a big issue. The open structure acts like a shoe box without a lid: it twists very easily. Improvement would be the result of closing off the ends with some kind of a lid. However, this would have to involve mechanical fasteners because the viscoelastic damping material and the epoxy would not tolerate the high temperatures that occur during welding. Also, thermal stresses would induce strain and possibly warp the base. On the plus

side, the shear damper base with a total weight of 2390 kg is much lighter compared to the box-type base whose weight, not including the concrete, is 3150 kg. A better design would have a cross section with higher torsional stiffness while having the ends of the base open so that constrained layer damping element could be used to enhance dynamic stiffness.

In Section 2.3.3, the advantages of round cross sections versus square cross sections have been discussed in great detail with the following result: round cross sections have a better strength-to-weight ratio compared to square cross sections, provided that there is no space constraint. This restriction comes from the fact, that a round tube of equal stiffness occupies a larger envelope than a square tube with the same wall thickness.

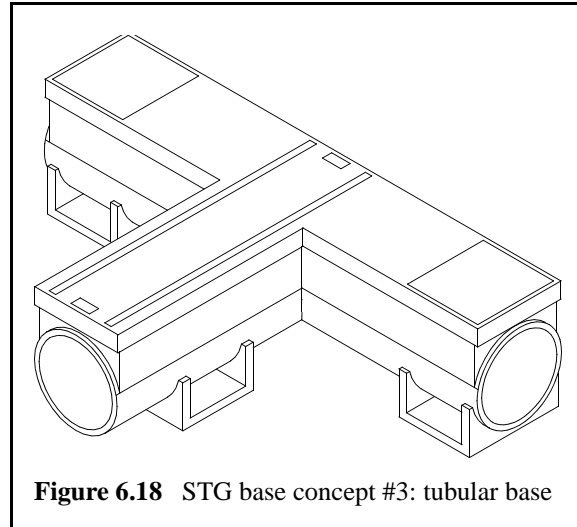


Figure 6.18 STG base concept #3: tubular base

It has also been discussed that round tubes are available in a wide range of sizes and wall thickness, allowing to select a standard round tube to form the “backbone” of a novel base design that consists of two round tubes with a flat plate welded on top (Figure 6.18). The interface between the round surfaces of the tubes and the flat surface of the top plate would be a t-shaped frame from 2 inch thick stock. The equivalent stiffness under cutting loads turns out to be in the order of 1970 N/ $\mu\text{m}$  but the thick T-shaped top plate adds a lot

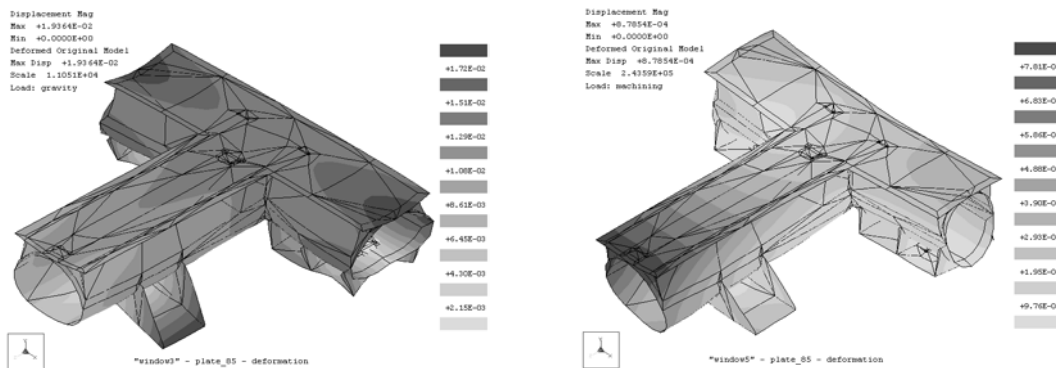


Figure 6.19 Round base subject to gravitational (a) and cutting loads (b)

of weight and makes the base rather heavy (3150 kg). As a direct result, deformations from gravitational loads are around  $19\ \mu\text{m}$  and the first mode occurs at 129 Hz.

## 6.2.2 Design Optimization

In Figure 6.19, the weak spots are the open cross sections and concept #4 (Figure 6.20) addresses this issue by welding a ring-shaped plate into the openings. The weight is reduced to 2878 kg by decreasing the thickness of the top plate to 50 mm. Gravity induced deflections drop to  $16\ \mu\text{m}$  while the stiffness in terms of cutting loads drops to  $1330\ \text{N}/\mu\text{m}$ . However, fabrication cost

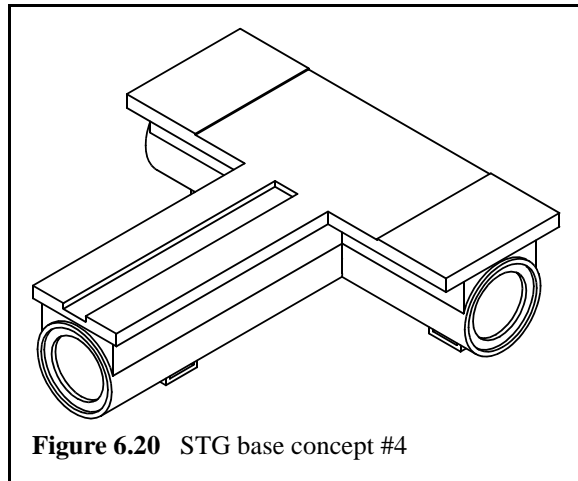


Figure 6.20 STG base concept #4

for the base were higher than anticipated, mostly caused by the 50 mm thick top plate which has to be welded from two separate steel plates.

A more radical design was developed next, whereby the cost raising plate was completely eliminated (Figure 6.21). Instead, 50 mm thick stock is welded directly onto the tubular base structure, providing mounting surfaces for the linear rails. Deformations from the base's own weight dropped to  $7.6\ \mu\text{m}$ , while deflections caused by cutting loads soared to  $11.9\ \mu\text{m}$ , which trans-

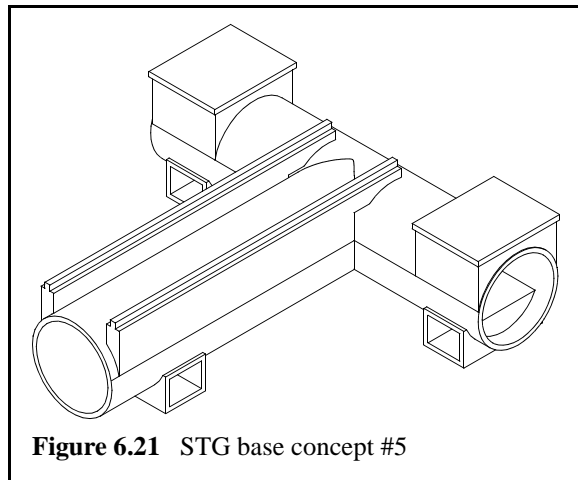
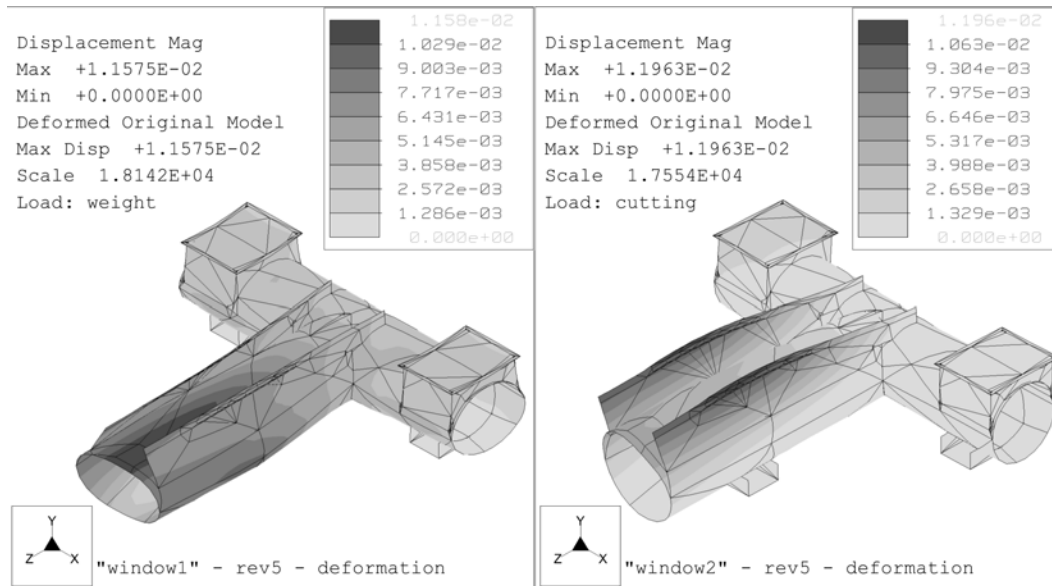


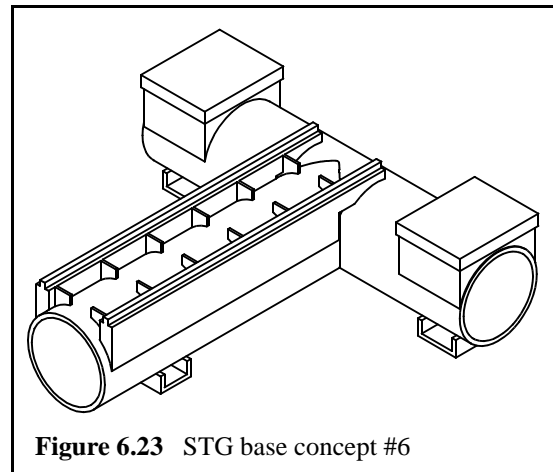
Figure 6.21 STG base concept #5

lates to a stiffness of only  $145\ \text{N}/\mu\text{m}$ , far less than what is allocated for the base. Most of the compliance can be attributed to the side rails which have to be sufficiently high to provide mounting space for the ballscrew. With less than 2000 kg, this base design is very lightweight and the first resonance frequency at 131 Hz isn't too bad either.



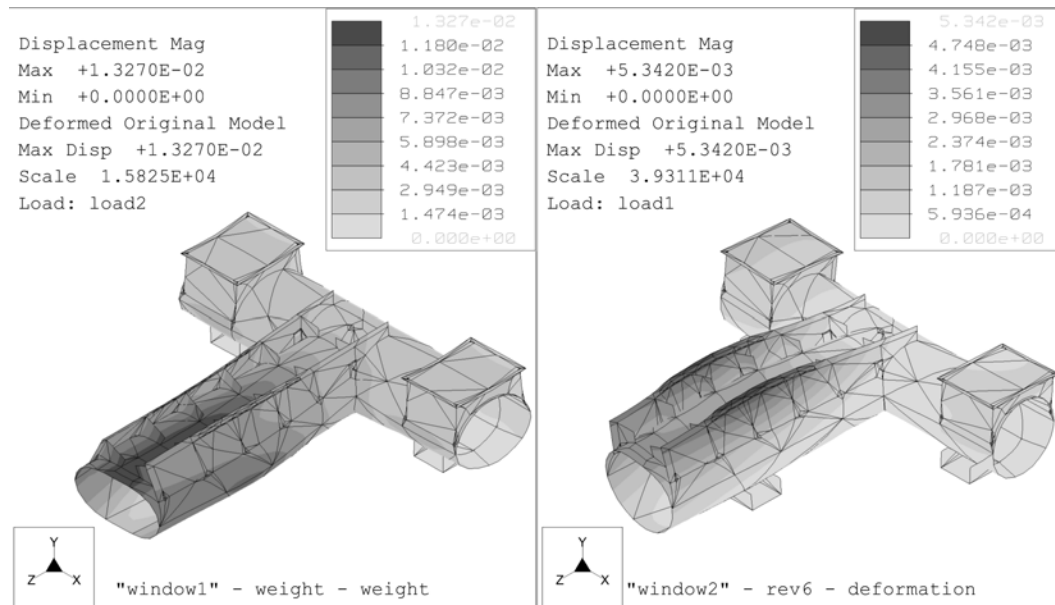
**Figure 6.22** STG base concept #5 - deformations from gravitational loads (a) and cutting forces (b)

In order to limit the deflections of the side rails, ribs were added as part of a new concept (Figure 6.23). The ribs noticeably enhance the rigidity of the side rails, allowing the base to deflect no more than 5.3  $\mu\text{m}$ , less than half of the previous concept. The first resonance frequency of this design is encountered at 144 Hz and the weight increases slightly to a total of 2014 kg. However, the



**Figure 6.23** STG base concept #6

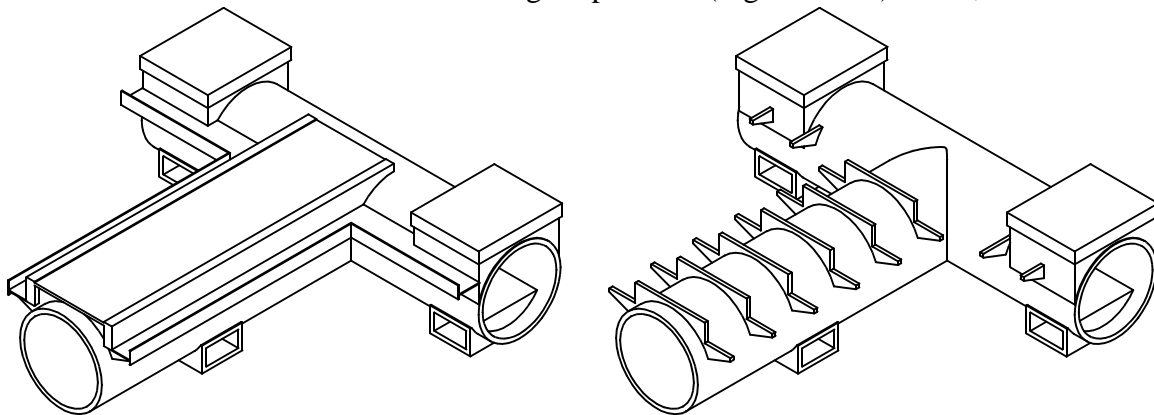
open structure with its various ribs make chip and coolant removal very difficult. For a good thermal budget, it is important to remove the heat generated by the cutting process as quickly as possible. Because most of the heat is contained within the chips, coolant is used to flush the removed material away from the structure and towards the filters, where the thermal energy can be dissipated into the environment. However, the ribs will trap a fair amount of coolant and chips and their heat is transferred into the structure, causing thermal errors that are hard to compensate. Further concerns involved an unlisted functional



**Figure 6.24** STG base concept #6 - deformation from gravitational loads (a) and cutting forces (b)

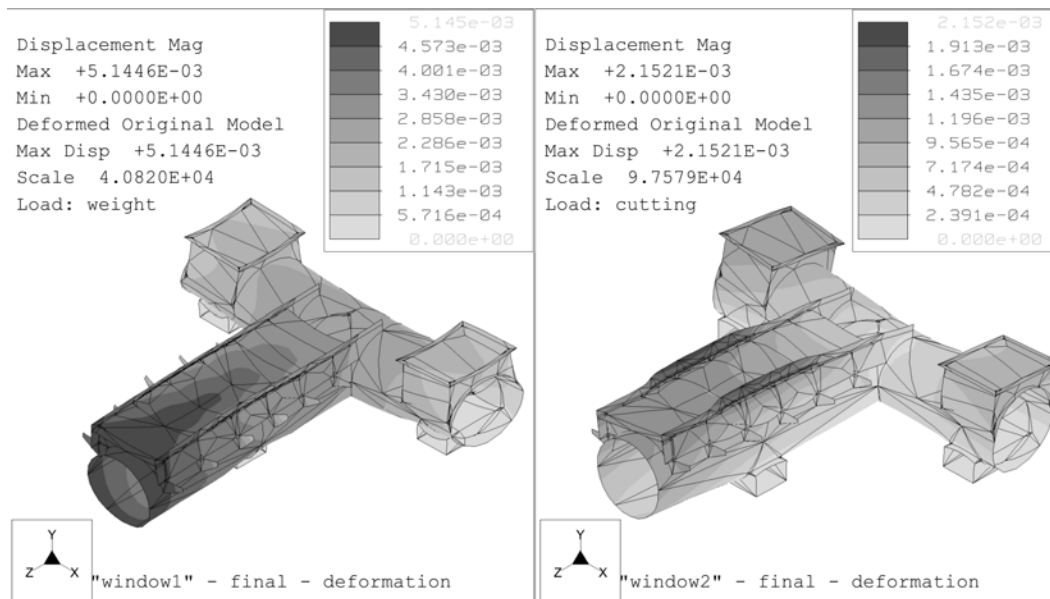
requirement that specifies the base to be 100% leak-proof as well as the need for an additional top plate to mount the ballscrews and the linear scales.

The final version is derived from concept #4 but avoids a big manufacturing challenge found in the original concept: welding the side rails directly onto the tubular structure. The weld would require the stock to be either bevelled or rounded at the bottom to mate with the round surface of the tube. The new concept uses “coat hanger” like ribs that are CNC plasma-cut from 3/4” plates. The round at the bottom mates perfectly with the underlying tubular structure and is welded on using skip welds (Figure 6.25b). Next, 50 mm thick



**Figure 6.25** STG base - final version (a) and without top plate, rails and gutter (b)

plates are welded to the sides of the hangers and are used to hold the linear rails for the Z-axis. A trough is created by welding on two 1/4" plates at a right angle, ensuring that the base is indeed 100% leak-proof. Finally, a 3/8" thick plate is welded on in between the rails, closing off the top cavities and serving as mounting surfaces for the ballscrews and the linear slide. This final design has its first resonance frequency at 178 Hz and weighs 2554 kg, significantly less than most of the previous concepts.

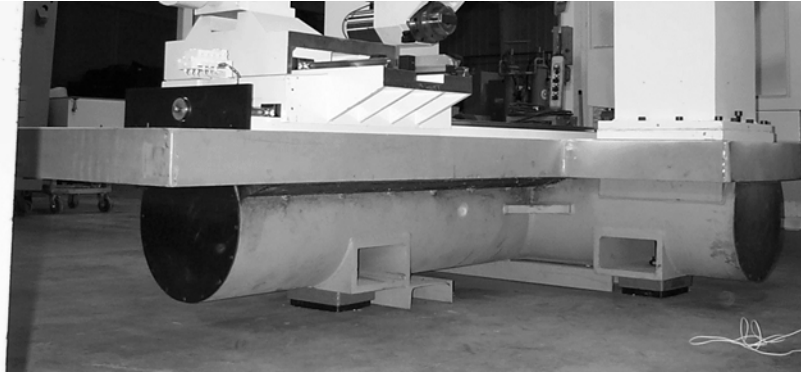


**Figure 6.26** STG final concept - deformations from gravitational loads (a) and cutting forces (b)

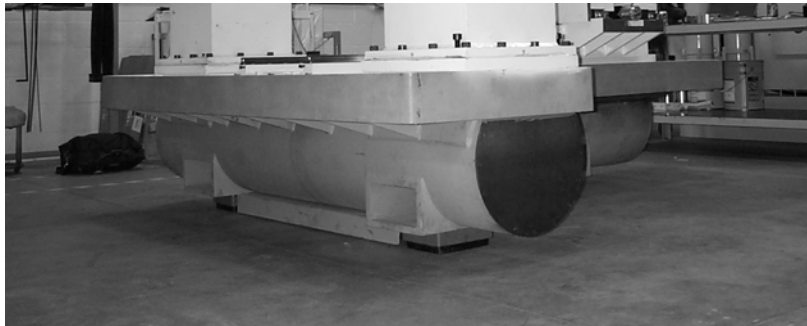
**TABLE 6.4** Comparison of STG base concepts

Concept	1	2	3	4	5	6	Final
max. deformation due to gravity [μm]	18	12	19	16	7.6	8.7	5.1
max. deformation due to cutting forces [μm]	0.5	1.9	0.9	1.3	11.9	5.3	2.0
equivalent stiffness [N/μm]	3400	910	1970	1330	145	326	866
1. mode	138	122	129	120	131	144	178
weight	3150	2390	3150	2880	1996	2014	2554





**Figure 6.27** STG base - front view



**Figure 6.28** STG base - rear view

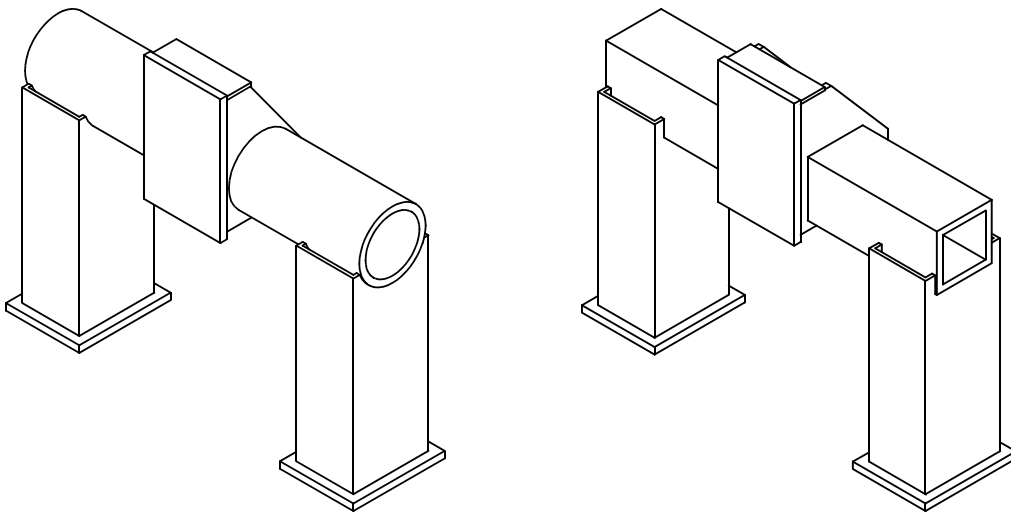
## **6.3 STG Gantry**

The gantry of the STG needs to hold two of the machine's axes: the Y- and the B-axis. The spacing between the two uprights is determined by the spindle's swept volume and should be kept as small as possible to limit the length of the connecting tube that is subject to torsion and bending. The basic shape of the gantry is already defined as part of the selected overall machine concept. In this section, concepts for the gantry are presented and evaluated in terms of their performance and economics.

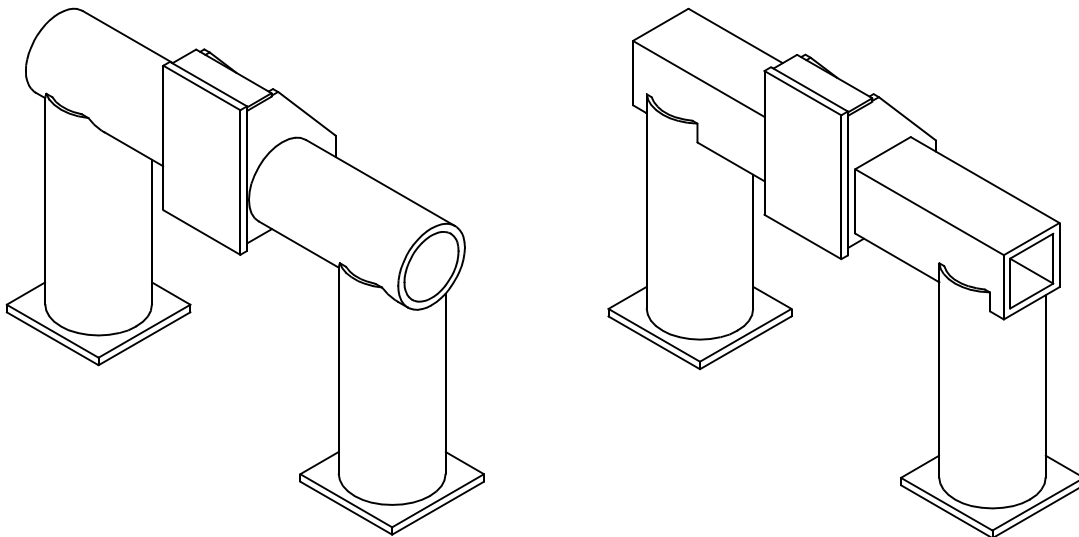
### **6.3.1 STG Gantry Concepts**

The first two concepts are built upon rectangular uprights that have the connecting tube welded on top. Concept #1 utilizes a round tube while concept #2 is built from a square

tube (Figure 6.29). Based on the findings regarding weight and stiffness of round versus square structures (Section 2.3.3 on page 44), the dimensions of the round tubes were chosen such that the bending stiffness of both designs is equal. Thus, both tubes have a wall thickness of 1.5 inches and while the round tube has a diameter of 16 inches, the square tube's width was set by Eq. 2.18 to be 13.4 inches. This should result in two structures of equal bending stiffness, with the round structure having 33% more torsional stiffness at 7% less weight.



**Figure 6.29** STG gantry concepts #1 (a) and #2 (b)



**Figure 6.30** STG gantry concepts #3 (a) and #4 (b)

It should be noted that the analysis whose model is shown in Figure 6.31 was set up in a very special way. The spindle was modeled from “stiff-stuff”, an idealized material with a Young’s modulus several orders of magnitude larger than that of steel but comparable density. This method allows a load to be applied at the point where it would occur in the real design. The extremely stiff spindle transmits the load through the bearings, which are modeled from springs (see also Section 2.4.3), into the gantry

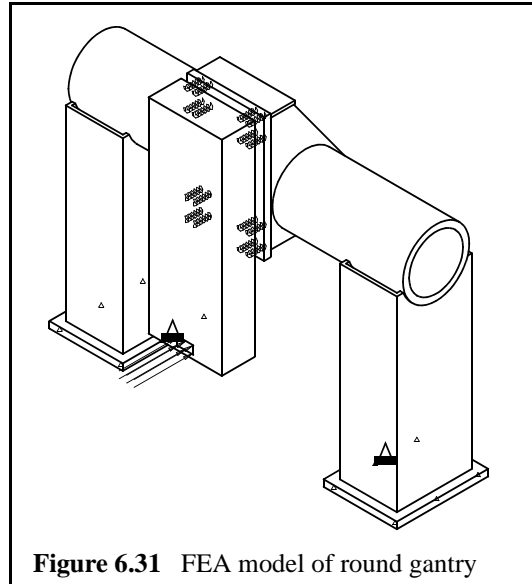


Figure 6.31 FEA model of round gantry

just like the real design would, creating very realistic load conditions. In return, the effects of deformations within the gantry get translated into linear displacements at the point of interest (tool tip) through the spindle, which does not contribute to these deformations itself due to its extremely large modulus of elasticity. The fringe plots showing the deformations of all four concepts are shown in Figure 6.32 and Figure 6.33.

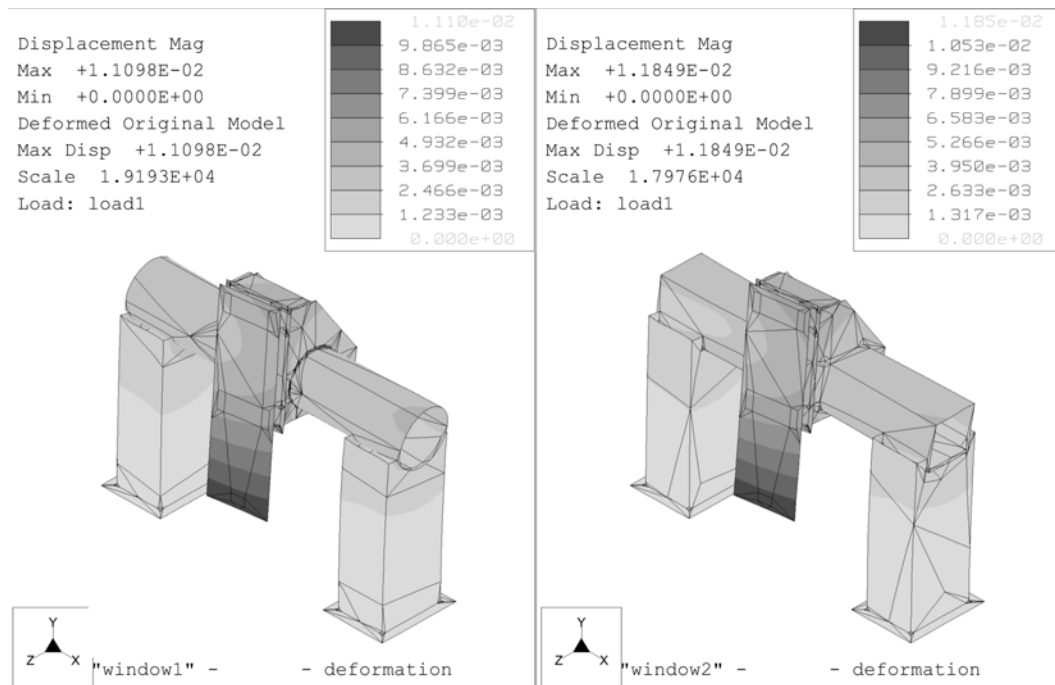
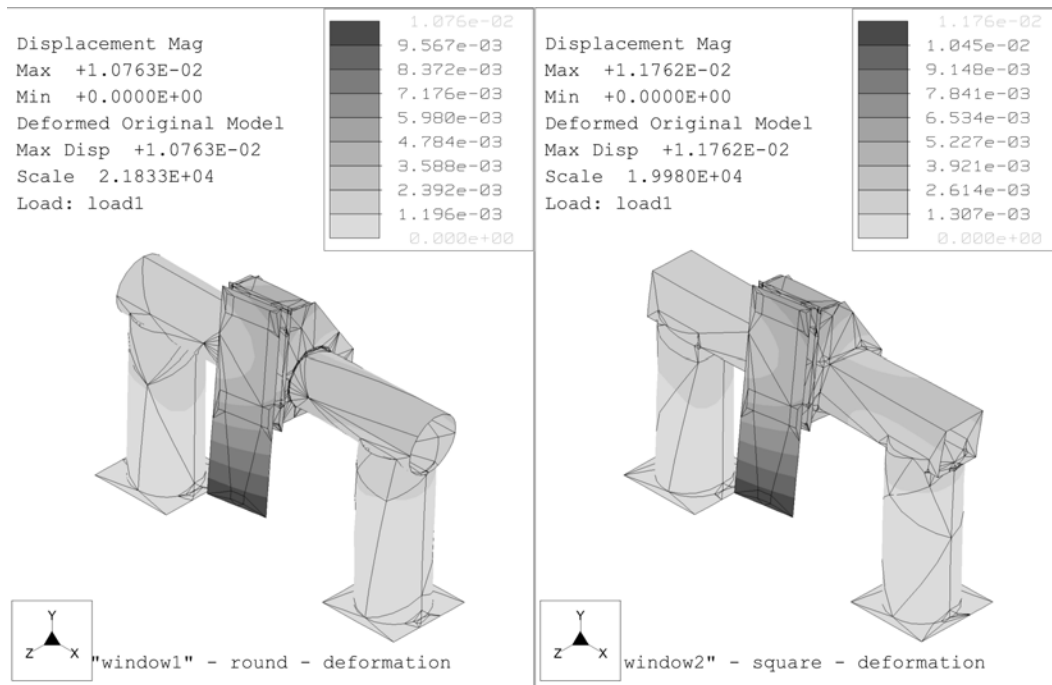


Figure 6.32 Deformation of STG gantry concept #1 (a) and #2 (b) to 1000 N load applied at the tool tip



**Figure 6.33** Deformation of STG gantry concept #3 (a) and #4 (b) to 1000 N load applied to tool tip

As can be seen from Table 6.5, the results of the finite element analysis pretty much agree with the first order approach developed in Section 2.3.3. The bending stiffness of concept #1 and concept #2 is virtually identical while the torsional stiffness of the round tube is 12% higher. Using the findings in Section 2.3.3, the increase in stiffness should have been around 33%, but this is for the tube alone. The bearings, which play an important role in this model, remained unchanged as did the uprights, limiting the increase in stiffness of the assembly.

**TABLE 6.5** Comparison of STG gantry concepts

	$k_x$ [N/ $\mu\text{m}$ ]	$k_y$ [N/ $\mu\text{m}$ ]	$k_z$ [N/ $\mu\text{m}$ ]	1. mode [Hz]	weight [kg]
Concept #1	132.9	404.4	131.9	83.9	1734
Concept #2	130.6	359.8	118.9	81.0	1776
Concept #3	150.8	386.1	126.8	73.5	1791
Concept #4	145.3	336.8	112.8	71.1	1837

Concept #3 and #4 don't perform quite as well as the designs with the rectangular uprights, especially in the torsional direction and modal frequencies. For a round tube to have equal bending stiffness compared to a square tube, the diameter of the structure needs to be larger by a factor of 1.19 (19%) compared to the width of square tube (see Section 2.3.3 on page 44). Therefore, in order to maintain the same space available for the spindle to rotate, the round uprights need to move outwards, making the connecting tube longer. The result is noticeable in the form of lower modal frequencies and increased torsional compliance.

It is therefore concluded, that gantry concept #1 with a round connecting tube and rectangular uprights are the best available design option. To save weight, the uprights can be tapered towards the top where bending moments from shear forces are minimal.



**Figure 6.34** STG gantry

## 6.4 STG Modal Analysis

As the STG was almost completely assembled, a modal analysis was conducted to identify the resonance frequencies of the machine and its modal damping factors. The modal points at which the accelerometer was attached are shown in Figure 6.35. The attached sensor measured the accelerations in the X-, Y-, and Z-direction at each of the modal points and the signal was transferred from the time into the frequency domain using Fourier transformations built into the attached frequency analyzer. For better averaging, the signal at each point was recorder ten times, transformed and averaged in the frequency domain. The excitation of the structures was done by creating an impulse with the impact hammer, whose signal was recorded and transformed as well. The ratio between the response and the excitation signal is called transfer functions and describes a structure's response to excitation.

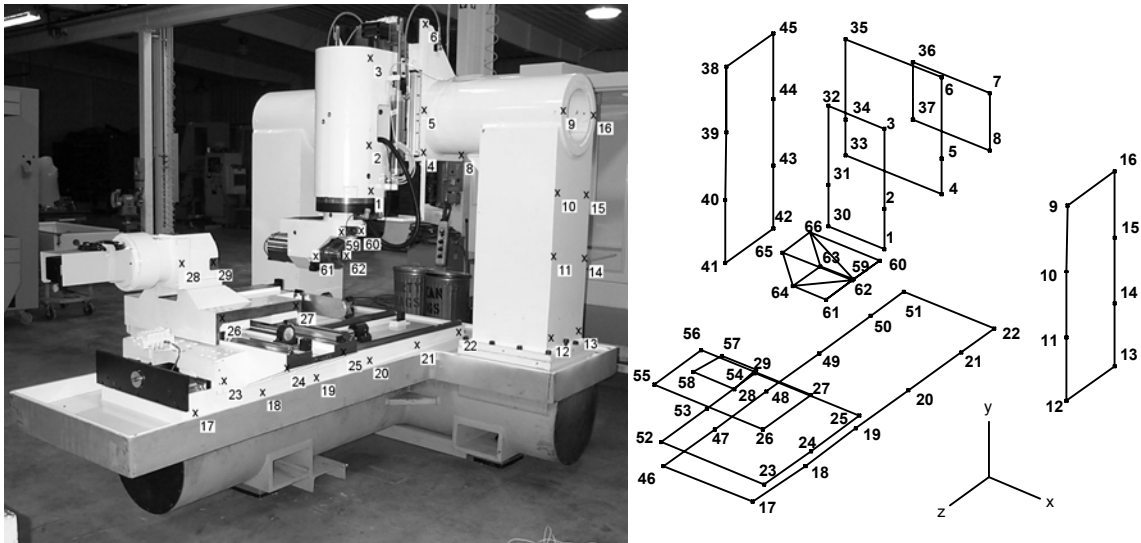
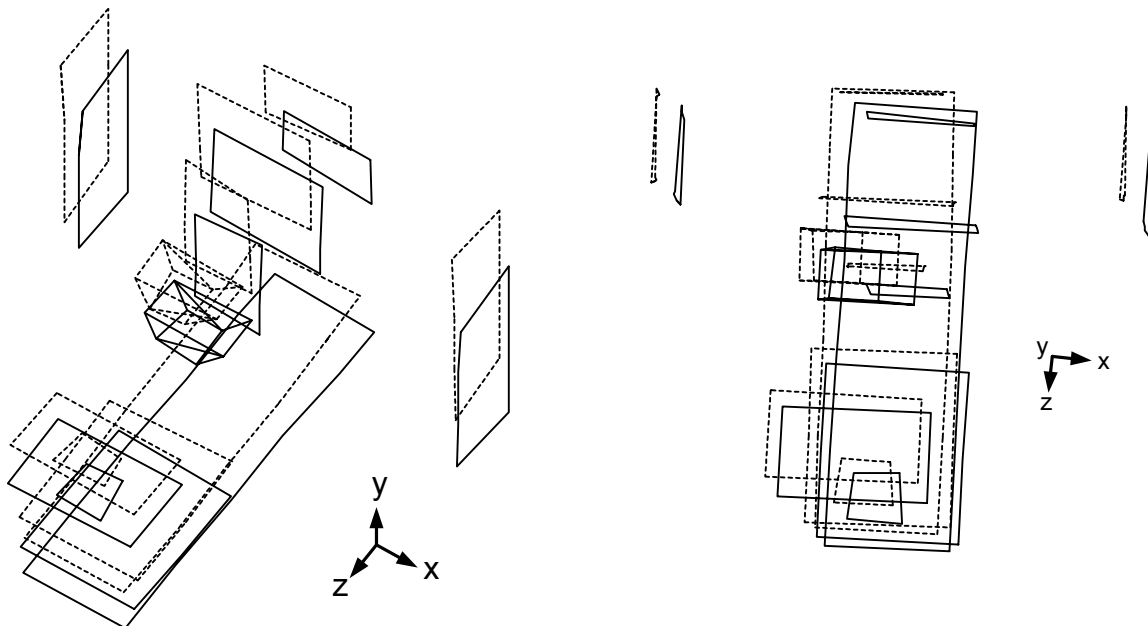


Figure 6.35 STG modal points

### 6.4.1 Rigid Body Modes

The base as it sits on its supports is not fully constrained like it would if it was bolted to the floor. Instead it just rests on its pads, allowing the base to rotate around its principal axes. These rotations show up in a modal as rigid body modes and their shapes are shown in Figure 6.36 to Figure 6.38. Because they are a result of unconstrained degrees of freedom, rigid body modes do not directly cause elastic deformation or stress in the structure [Crandall et al]. Thus, rigid body modes do not affect the accuracy of the machine, unless the frequency, at which these modes occur, are rather high. In this case, inertia effects may become noticeable and cause deformations within the structure if the frequencies of these rigid body modes become too high.

The first of these occurs at 5.8 Hz and is primarily translation of the machine in the horizontal plane. The second mode occurs at 6.5 Hz and is primarily rotation of the entire machine about the Y-axis. The next mode at 17.1 Hz corresponds to a rocking motion of the machine about a line in the xz plane.



**Figure 6.36** First rigid body mode, isometric (a) and top view (b)

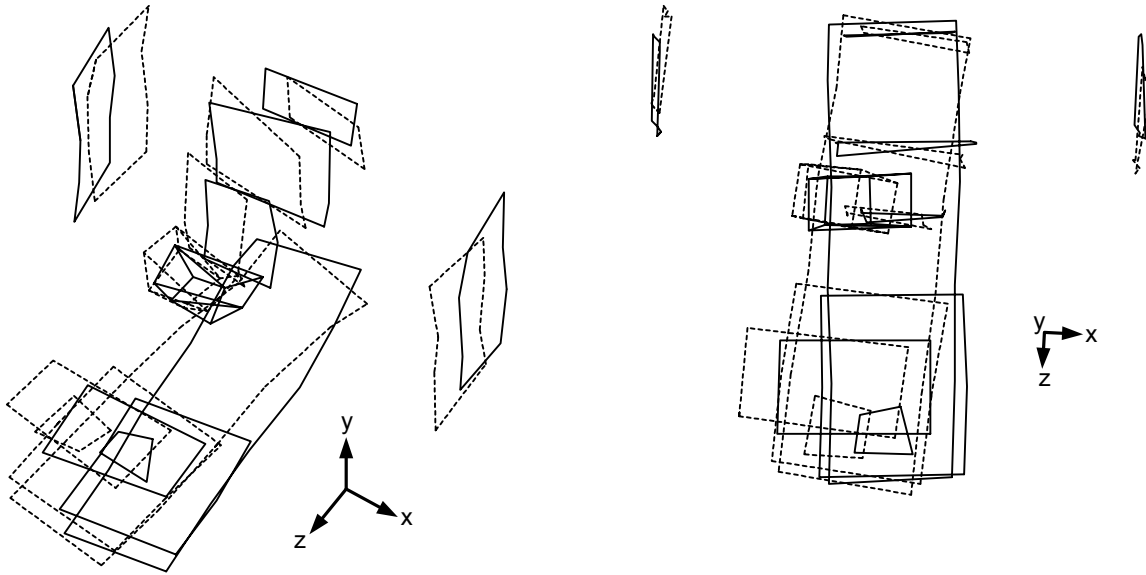


Figure 6.37 Second rigid body mode, isometric (a) and top view (b)

TABLE 6.6 Result of modal analysis

Mode	Frequency [Hz]	Damping [%]
1	5.8	3.73
2	6.4	3.65
3	17.1	3.66
4	18.5	1.05
5	70.0	2.16
6	100.9	5.58
7	114.3	4.38
8	159.6	0.74
9	161.8	0.54

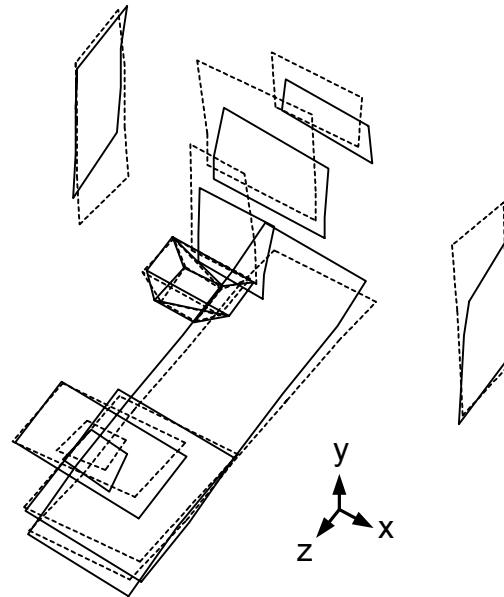


Figure 6.38 Third rigid body mode

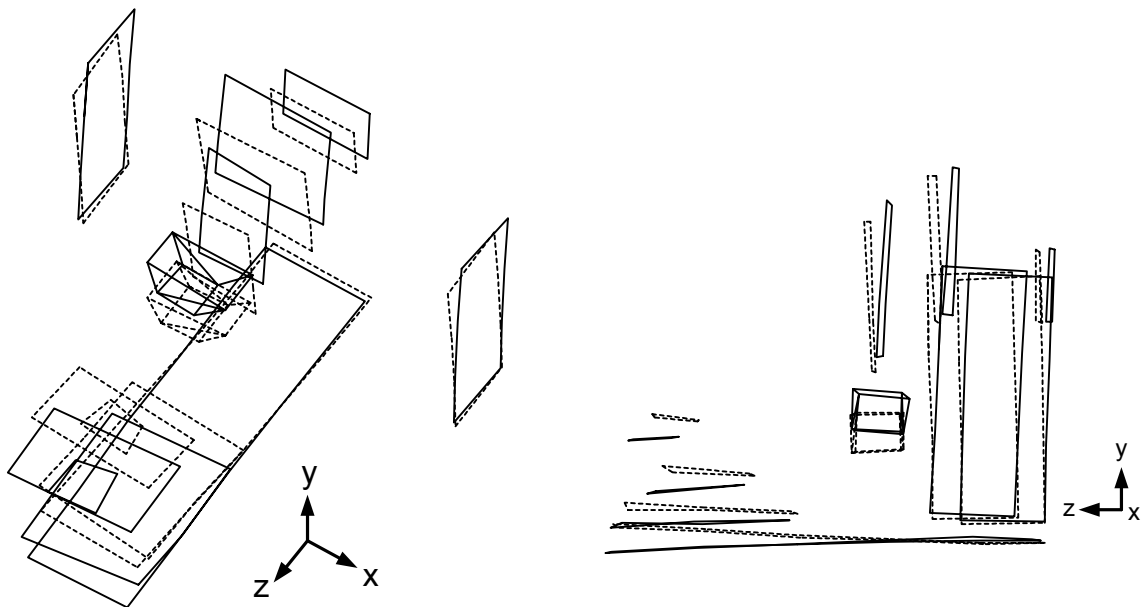


## 6.4.2 Actual Modes

Of all the modes given in Table 6.6, the first real mode of interest is mode number four and its shape is shown in Figure 6.39.

### First Mode

The first mode of the STG is purely a result of the base bending and twisting around the X-axis (Figure 6.39). At 18.5 Hz it is rather low and very close to the frequency servo systems typically control the position of an axis. With a modal damping factor of 1% it is only lightly damped, thus its amplitudes are quite significant. The compliance of the base is mostly a result of the twist that occurs within the rear base tube which holds the two uprights. This twist also induces considerable bending in the front base tube. As a result, both uprights are in phase and move back and forth, causing the bridge to rock back and forth as well, while the Z- and X-axis move up and down. The combined motion of the mode has its sensitive direction in the Y- and Z-direction. In order to increase the frequency of this mode, the compliance of the front base should be decreased by increasing the stiffness of the front supports. The stiffer support should limit the amplitude of the

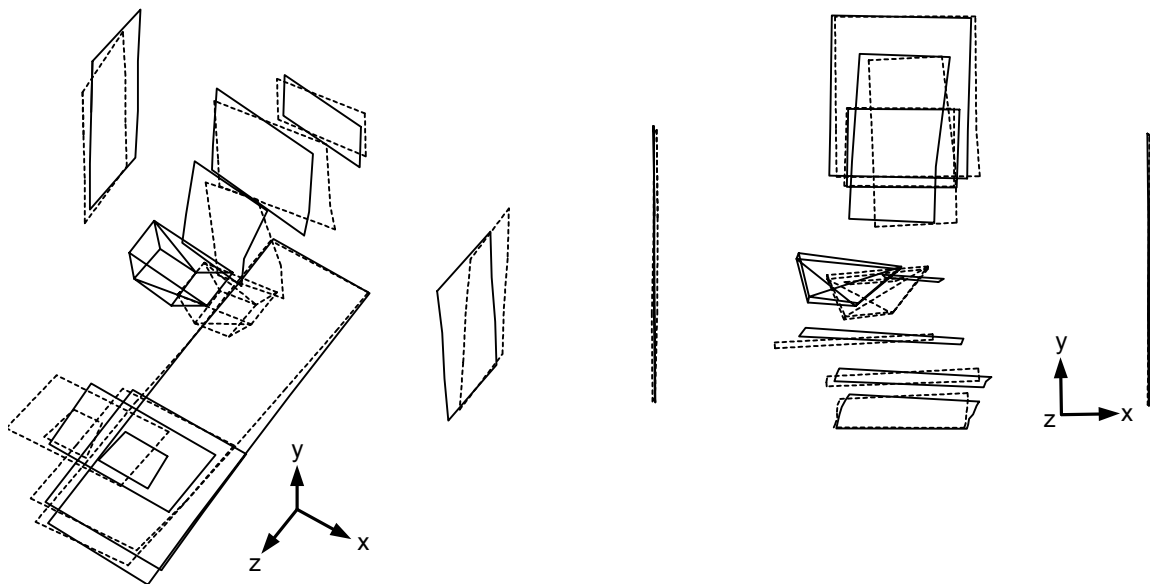


**Figure 6.39** STG first mode (18.5 Hz), isometric (a) and side view (b)

front part of the base as it going up and down. As a second measure, the base tubes should have more bending and torsional stiffness and the weight of the bridge should be decreased if possible. Damping should be increased by having a replicated constrained layer damper inside the base tubes.

### Second Mode

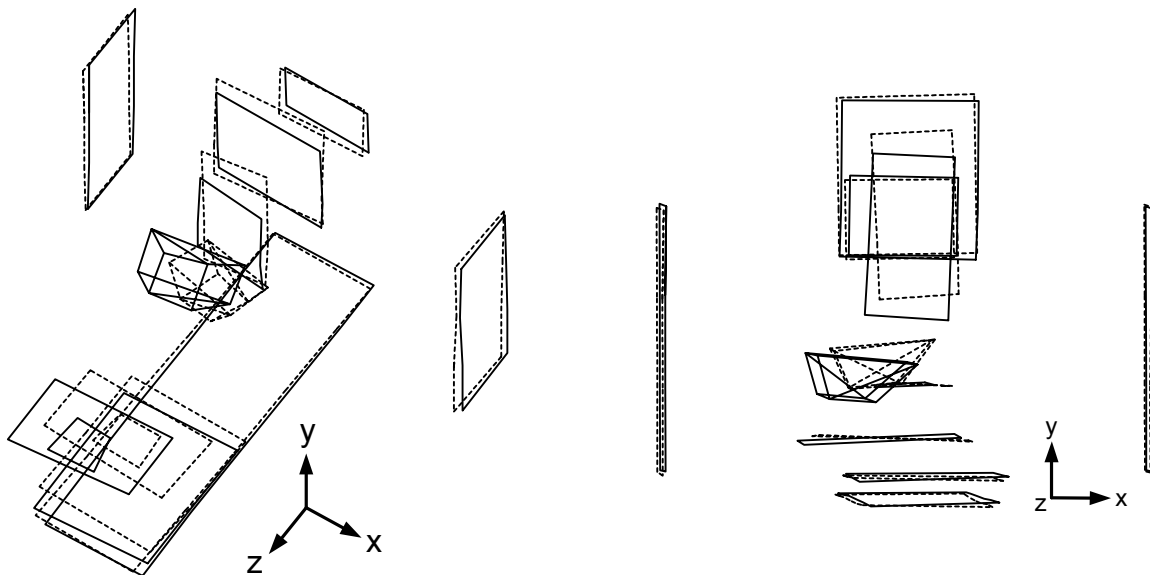
Mode number two is another twisting mode of the base that occurs at 70 Hz. Unlike the first mode, the left and right upright are out of phase, i.e. they move in opposite direction. This rotation causes the bridge to rotate around the Y-axis. The front base tube is twisting as well and is out of phase with respect to the rotation of the bridge. As can be seen from Figure 6.40a, the motions of the two rotations add because they move in opposite direction. The most significantly affected direction in terms of machine axes would be the X-axis. At 70 Hz, the frequency of this mode is nicely high and with a damping factor of more than 2% reasonably well damped. Improvement of this mode would result from increasing the torsional stiffness of the base tubes as well as decreasing the weight of the bridge.



**Figure 6.40** STG second mode (70.0 Hz), isometric (a) and front view (b)

### Third Mode

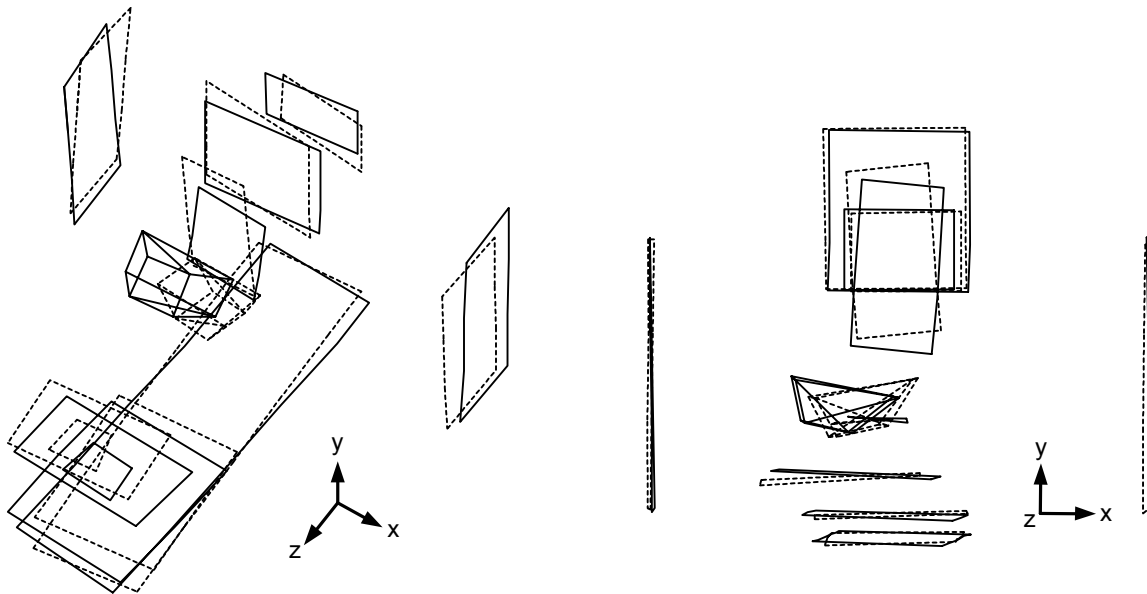
The effects of the third mode, which occurs at 100.9 Hz, can best be seen in Figure 6.41a. The wireframes for the base and bridge are basically identical, showing that neither one of these components participates at this frequency. Instead, all motion comes from the Y-axis as it moves up and down. The shape clearly shows which component of the Y-axis has its compliance at this modal frequency: the ballscrew assembly. The compliance either occurs within the ballscrew supports or the ballscrew itself. Because the ballscrew of this axis has one of its ends floating, compliance is most likely to be found within the screw. This mode is highly damped and most of system's energy is most likely dissipated within the linear bearings as a result of the static friction within the bearing. The friction within the pneumatic cylinders, that are used to counterbalance the weight of the Y-axis, also contribute to the damping. With a modal damping factor of 5.6%, it is well damped and should not affect the surface finish of the grinding operation, although it could potentially limit the servo gains of the Y-axis.



**Figure 6.41** STG third mode (100.9 Hz), isometric (a) and front view (b)

### Fourth Mode

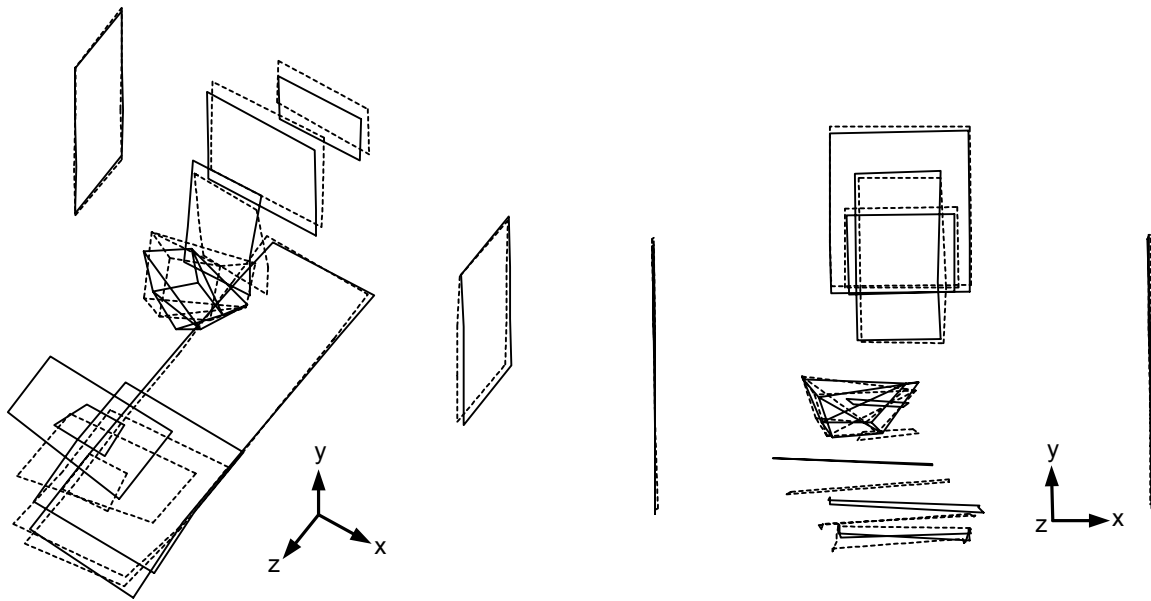
At 114.3 Hz, the machine exhibits its seventh mode, in which the bridge twists somewhat, but the deformation is concentrated in the Y-axis bearings. At this frequency both the Y and Z carriages tend to exhibit an out-of-phase yawing motion that results in an error in the X-direction.



**Figure 6.42** STG fourth mode (114.3 Hz), isometric (a) and front view (b)

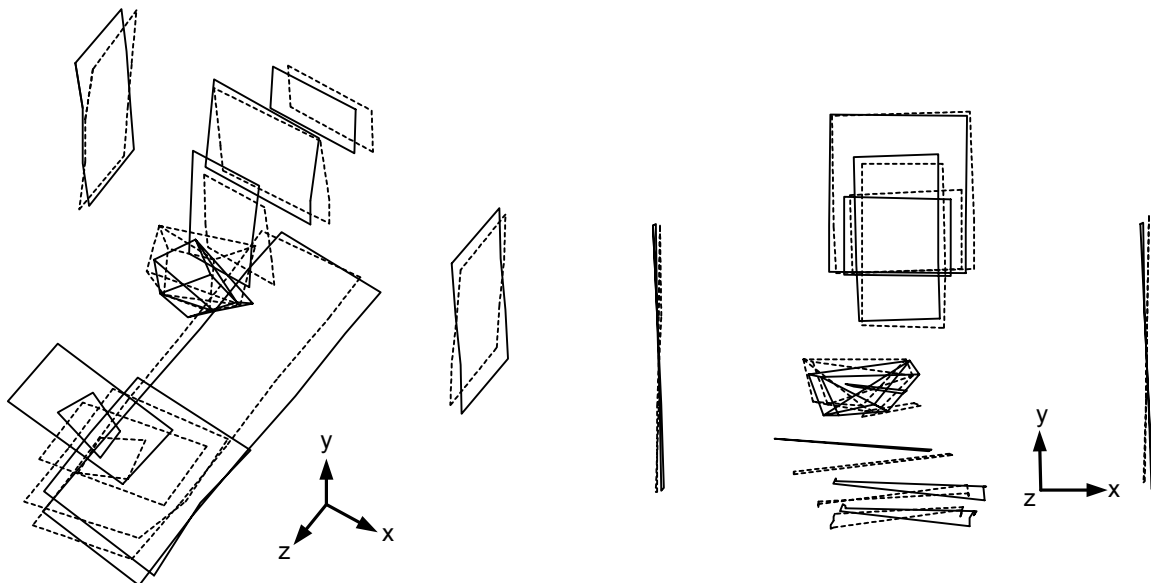
### Fifth Mode

All the motion caused by the fifth mode occurs in the bearings of the X- and Z-axis. Figure 6.43b clearly shows that the base and bridge are stationary while the X- and Z-slide move up and down with some additional rotation involved. The rotation are most likely caused by the X-slide which was offset 6 inches from the middle. At 159.6 Hz, this might be a mode which is becoming excited by the grinding process and with 0.7% damping it is not a terribly well damped mode. The damping in this case comes mostly from the bearing trucks, but since the motion is normal to the rail, static friction is small and little energy is being dissipated.



**Figure 6.43** STG fifth mode (159.6Hz), isometric (a) and front view (b)

### Sixth Mode



**Figure 6.44** STG sixth mode (161.8 Hz), isometric (a) and front view (b)

This mode consists primarily of a rolling motion of the base about the Z-axis accompanied by some stretching of the X-axis ballscrew or its support. It is also very lightly damped at 0.5%. This mode could be stiffened or damped by using a damped ballscrew support, or potentially by stiffening the portion of the base that extends in the X-direction against bending.

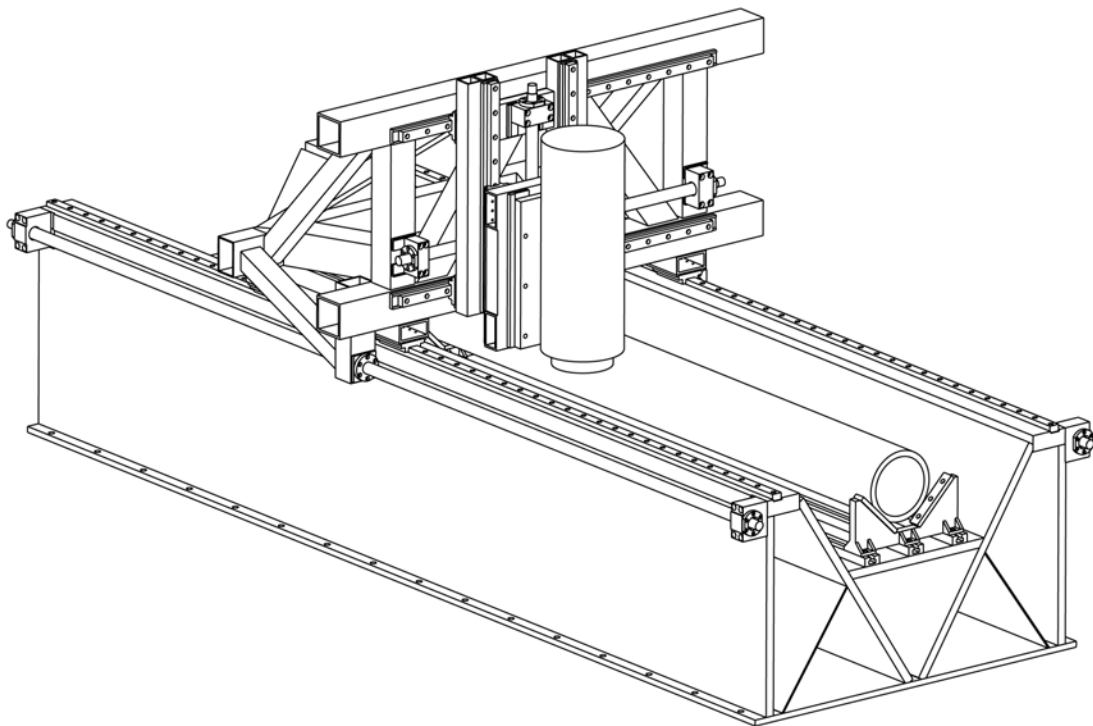
### **6.4.3 Recommendations**

The first three modes cause only small error motions, but are indicators of a structural compliance that plays a part in the lightly damped modes four and eight. There is a great deal of compliance in either the feet or the load path between the feet and the critical surfaces.

This compliance plays an important role in both the fourth mode, which occurs at 18.4 Hz and has only 1.1% damping, and in the eighth mode which occurs at 160 Hz and has only 0.7% damping. These modes have the greatest potential to be excited by either the feedback controllers or the grinding process and can probably be readily damped by introducing a suitable combination of replicant and viscoelastic material into the base near the feet.

# Chapter 7

## CASE STUDY - TUBEMILL



**Figure 7.1** The TubeMill

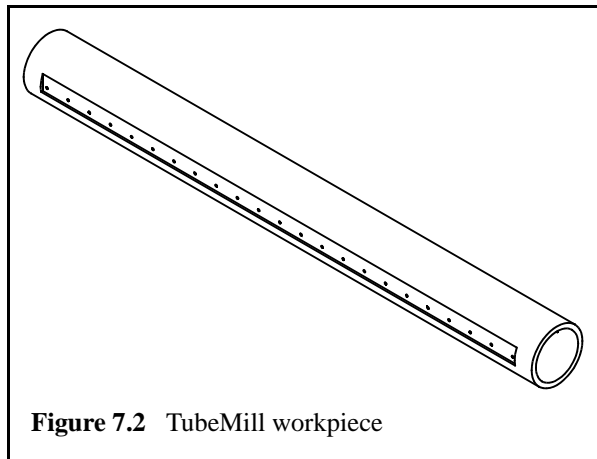
The TubeMill is a three-axis milling machine designed specifically for milling two particular features along a rather heavy, round tube (Figure 7.1). The functional requirements for this machine are given in Table 7.1.

**TABLE 7.1** Functional requirements for TubeMill

Functional Requirement	Design Parameter	Physics
Low cost	Keep design simple, use symmetry and replication techniques	Box beams
High accuracy	High quality components Error mapping? Minimize thermal drift using thermo-centric design Avoid or at least minimize Abbe errors	Center of mass coincident with center of stiffness
Fast delivery	Use off-the-shelf components and materials	
Mill 3 m long tube with 0.3 m outer diameter	Minimum work volume 3.25x0.6x0.4m	
Machine at least two tubes per day	High speed not required Manual tool change acceptable	Mass not too important
Easy machining setup with good repeatability	V-blocks	Deterministic fixturing
Easy chip removal	Use flat surfaces, tilt machine?	
Good ergonomics	Work pieces are heavy (530 kg), so make work area accessible for a crane	

## 7.1 Error Budget

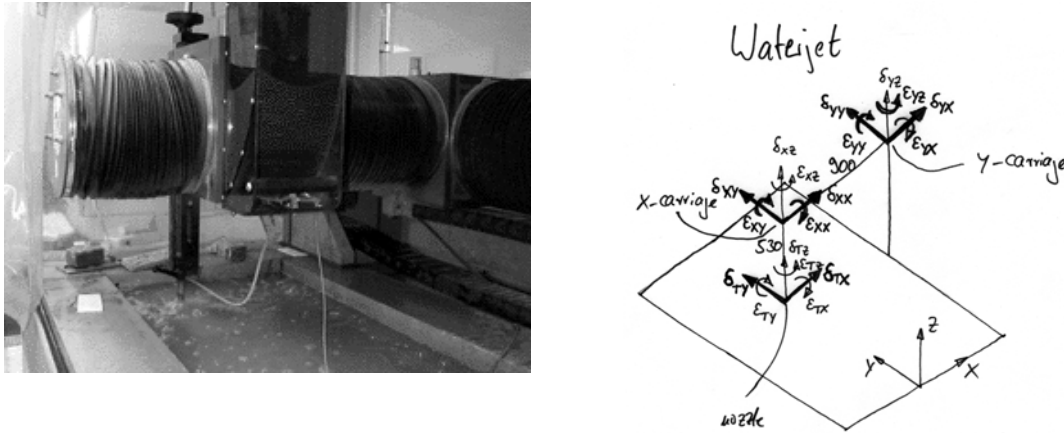
Figure 7.2 shows the workpiece and the main features which are to be machined on the TubeMill. The tube is part of the structure for a JetMachining Center®<sup>1</sup> and holds a pair of linear rails for the Y-axis carriage (Figure 7.3a). To save manufacturing cost, the mounting surfaces and reference edges for the rails have to be machined accurately enough to make

**Figure 7.2** TubeMill workpiece

subsequent grinding of these features obsolete. Also, the bolt holes for mounting the linear

1. JetMachining Center® is a registered trademark of OMAX Corp.

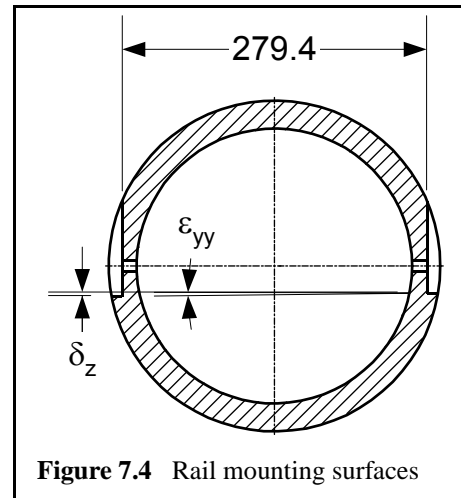




**Figure 7.3** JetMachining Center® (a) and its stick figure

rails have to be machined as well, although it is acceptable to change the fixturing after the rail mounting surfaces have been cut.

Using the stick figure shown in Figure 7.3b, the sensitive directions for the Y-carriage can be identified as the rotations  $\varepsilon_{yx}$  and  $\varepsilon_{yy}$  because the rather long lever of the Z-axis transforms these rotations into substantial linear motion at the nozzle. This error motion in the plane parallel to the workpiece is of great importance because it directly affects the accuracy of the machined parts. The vertical error of the Y-axis ( $\delta_{yz}$ ), on the other hand, only affects the height of the nozzle above the workpiece. Because of



**Figure 7.4** Rail mounting surfaces

the nature of the JetMachining Center® process, changes in height (the Z-direction) are basically of no consequence and therefore play no role in the error budget. It can therefore be concluded, that the absolute height of the reference edges shown in Figure 7.4 have no effect on the achievable accuracy of the JetMachining Center®. Of great importance, however, is the height of the two edges relative to each other ( $\delta_z$ ) because it is this difference in height that causes the  $\varepsilon_{yy}$  rotation of the Y-carriage. The linear tool tip displacement in the X-direction can be calculated to:

$$\begin{aligned}\delta_{T,x} &= \delta_{yx} + \varepsilon_{yy}530 \\ &= \left( \delta_{yx} + \delta_z \frac{530}{279.4} \right)\end{aligned}\quad (7.1)$$

The maximum allowable error in the X-direction due to the Abbe error of the Y-carriage is specified to not exceed 0.025 mm. Assuming that the straightness error of the rail is in the order of 0.015 mm, the maximum allowable height difference between the two reference edges  $\delta_z$  can then be calculated to:

$$\begin{aligned}\delta_{z,max} &= \frac{279.4}{530}(\delta_{T,max} - \delta_{yx}) \\ &= \frac{279.4}{530}(0.025\text{mm} - 0.015\text{mm}) = 0.005\text{mm}\end{aligned}\quad (7.2)$$

The result of the error budget is as follows: the TubeMill must be capable of milling two surfaces that have to be parallel to within 3  $\mu\text{m}$ , a challenging task given that the workvolume for this machine is more than 3 m long. Assuming zero slope boundary conditions at both ends of the tube, the sag for the workpiece due to its own weight can be calculated to [Gieck]:

$$\delta_{z,tube} = \frac{\rho_S g L^4 (D^2 - d^2)}{24E(D^4 - d^4)} = 8.5\mu\text{m}\quad (7.3)$$

Hence, the sag of the workpiece is already larger than the parallelism determined in the error budget. However, due to the nature of the JetMachining Center®, only the local parallelism has to be within the 3  $\mu\text{m}$  limit. The allowable overall parallelism can be significantly larger. Also, the tube is assembled with boundary conditions very similar to those encountered during machining. Therefore, the sag during machining will be very similar to the sag once the tube is assembled, resulting in a parallelism of the reference edges significantly better than the predicted 8.5  $\mu\text{m}$ .

## 7.2 Overall Machine Concepts

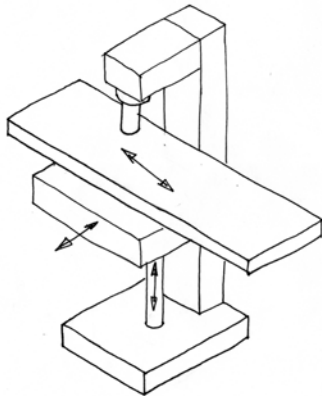


Figure 7.5 TubeMill concept 1-2

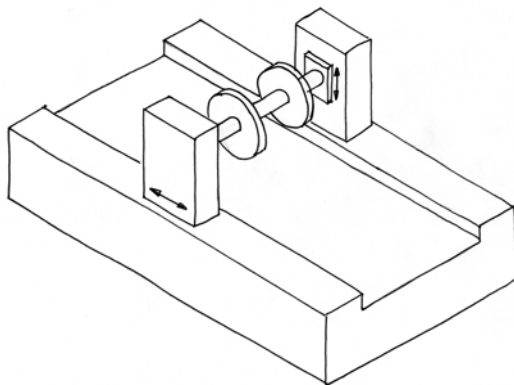
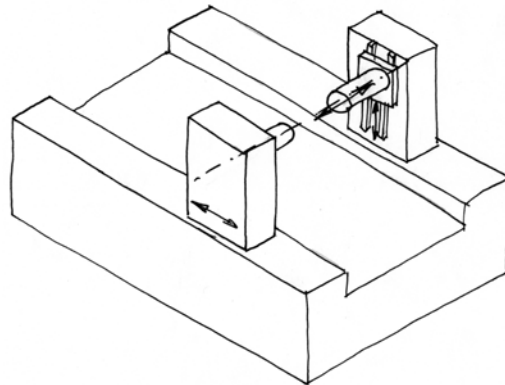


Figure 7.6 TubeMill concept 3-4

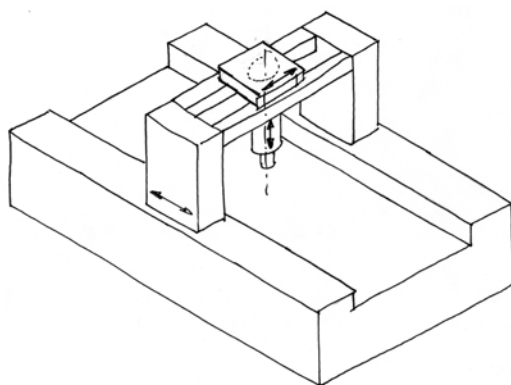
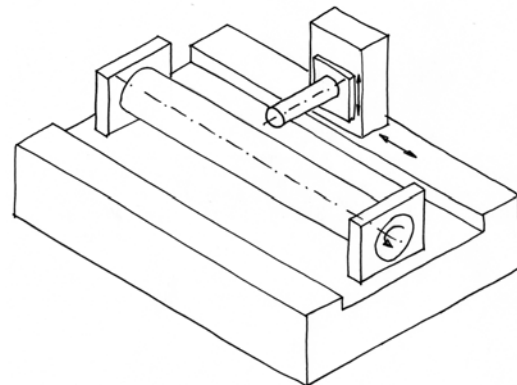
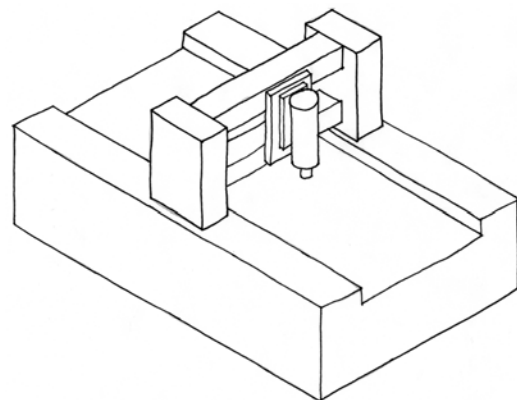


Figure 7.7 TubeMill concept 5-6



For the concept evaluation, a Pugh chart was used to identify the weaknesses and strengths of all designs.

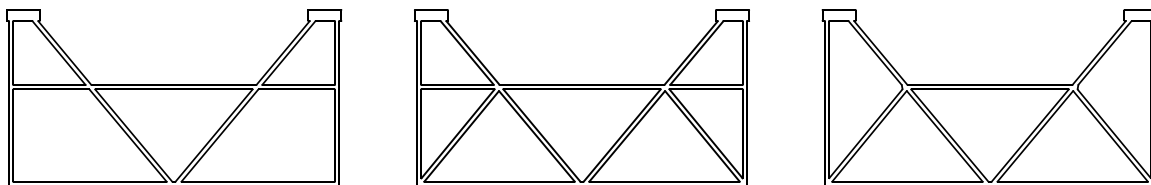
**TABLE 7.2** Pugh chart for TubeMill overall concept evaluation

	Design 1	Design 2	Design 3	Design 4	Design 5	Design 6
Low cost	0	0	-	-	0	0
High accuracy	0	-	-	--	+	+
High stiffness	0	-	0	-	0	++
Good repeatability	0	--	++	--	0	+
Scalability	0	+	++	+	++	++
Good dynamics	0	+	+	+	+	+
Ease of workpiece setup	0	++	++	++	++	++
Easy chip removal	0	0	0	0	0	0
Ability to drill and tap	0	++	--	++	0	0
<b>Total</b>	<b>0</b>	<b>2</b>	<b>3</b>	<b>0</b>	<b>6</b>	<b>9</b>

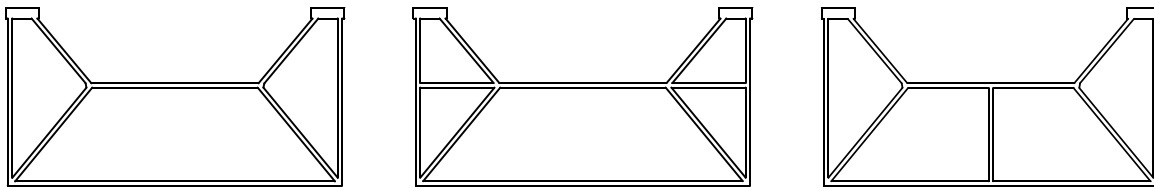
The Pugh chart shown in Table 7.2 identifies the design #6 as the best of all developed concepts.

### 7.3 Base Concepts

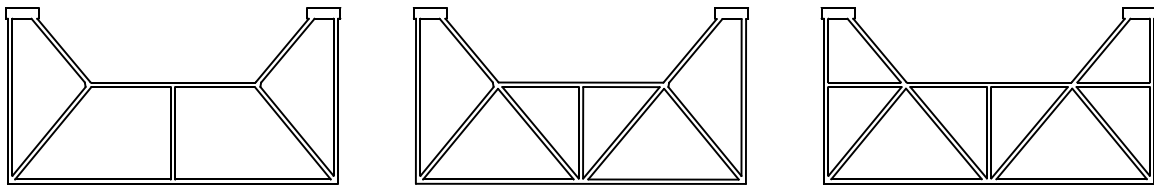
Based on the concept selection presented in Section 7.2, designs for the base of the Tube-Mill were created as fabricated structures.



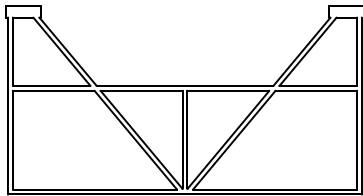
**Figure 7.8** TubeMill base concepts 1-3



**Figure 7.9** TubeMill base concepts 4-6



**Figure 7.10** TubeMill base concepts 7-9



**Figure 7.11** TubeMill base concepts 10

The concepts for the base of the TubeMill whose cross sections are shown in Figure 7.8 to Figure 7.11 are based on a truss design and are fabricated from steel plates. The thick plates at the top of the base serve as mounting surfaces for the linear rails and the ballscrews. The tub-like section in the middle will hold the workpiece.

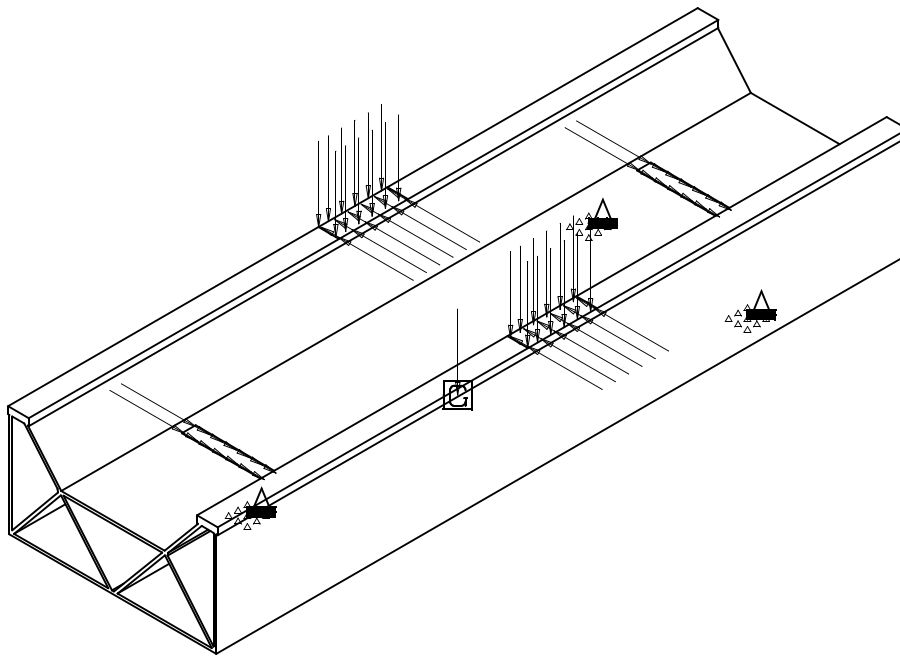
### 7.3.1 First Round Elimination - FEA Analysis

The concept selection process for this example is fully based on finite element analysis. For fast computing time, the models of the base were set up using shells which are a very reasonable idealization given that the base consists of plates with large length-to-thickness ratios (a detailed discussion on this technique can be found in Section 2.4.4).

## FEA Model

The model of the base includes the following features:

- Three point support to simulate real world support: no foundation necessary.
- Weight of gantry simulated as vertical surface load onto and applied at the worst case position - the center of the base.
- Cutting forces simulated as horizontal force acting on bearing surface and reaction force acting on mounting surface for v-block.
- Cutting force assumed to be 5000 N.
- Weight of gantry assumed to be 1500 kg.
- Length and thickness of each plate held constant.



**Figure 7.12** TubeMill base FEA model

Figure 7.15a shows a fringe plot of the deformations as they occur when the actio and reactio components of the cutting force are applied to the base. The maximum recorded displacement of this analysis is the basis for the calculation of the stiffness values pictured in Figure 7.13. The deformations as result of its own weight is presented in Figure 7.15b.

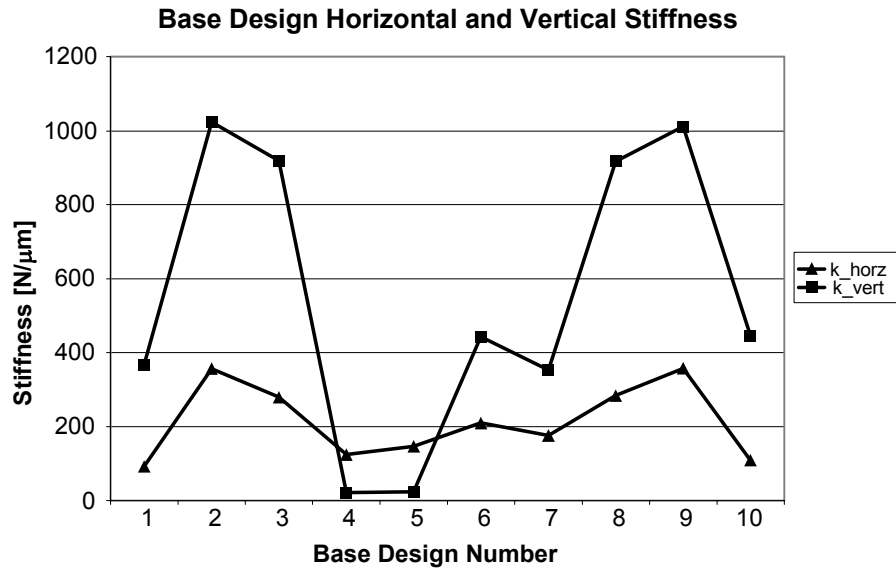


Figure 7.13 Horizontal and vertical stiffness of TubeMill base concepts

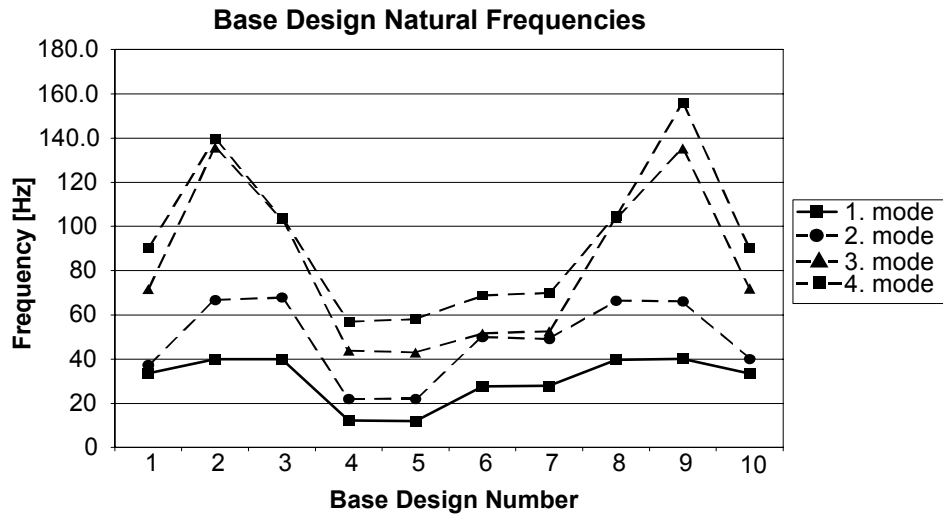


Figure 7.14 Resonance Frequencies of TubeMill base concepts

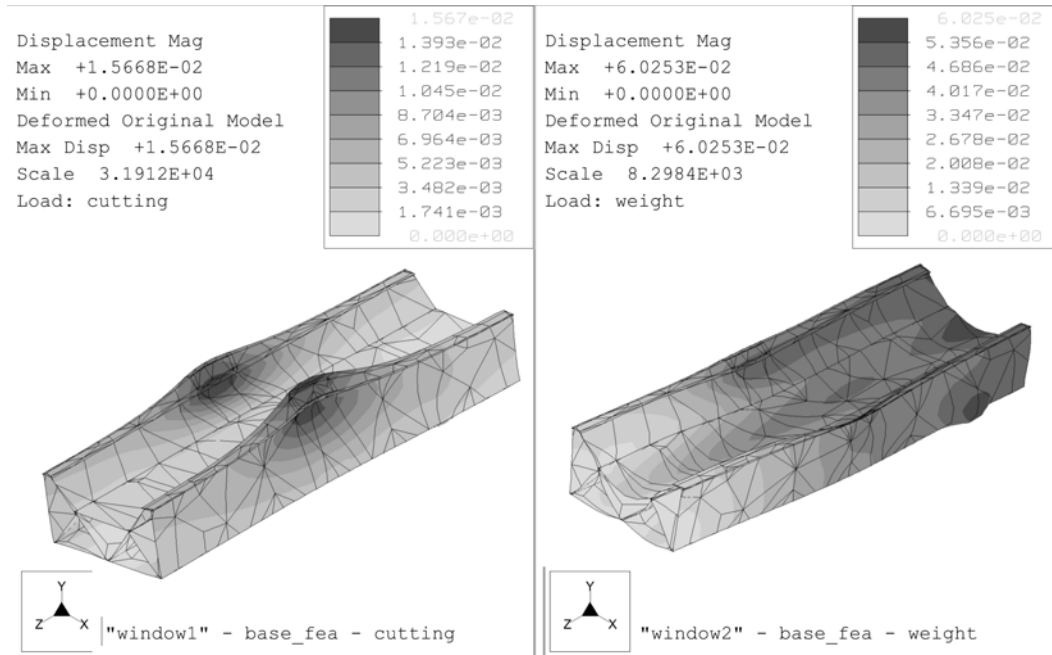


Figure 7.15 FEA fringe plots showing deformations from cutting loads (a) and weight (b)

**First Round Selection**

Looking at the FEA results shown in Figure 7.13 and Figure 7.14, only 4 designs offer promising stiffness and natural frequencies. These are concepts #2, 3, 8, and 9 (see Figure 7.16).

The analysis also reveals that the performances of concepts #2 and #9 are almost identical. This leads to the conclusion that the use of concept #9’s vertical center plate, which is the only difference between the two designs, cannot be justified. Hence, the design #9 is eliminated. Similarly, variations #3 and #8 are identical also, with the exception of the same

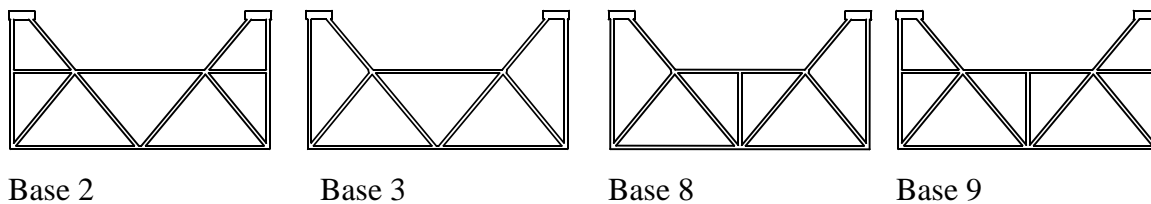


Figure 7.16 TubeMill concepts selected after first pass FEA analysis

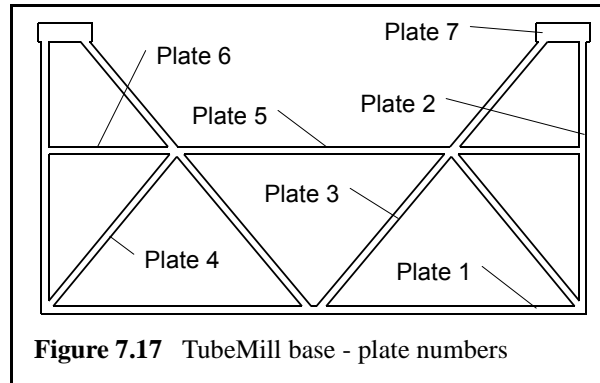


vertical plate. Again, stiffness and modal frequency for both designs are practically identical leading to the conclusion, that again the vertical center plate has no impact on the characteristic of the base. Hence, concept #8 is eliminated as well. The remaining two concepts are #2 and #3 which are evaluated in more detail in Section 7.3.2.

### **7.3.2 Second Pass Elimination - Global Sensitivity Study**

The general objective of a global sensitivity study is to identify parameters of a design that have the most impact on the design. For a design optimization, the parameter with the most influence is of special interest because tweaking that particular feature will have the most effect on the design. Knowing which parameters have little to no effect on a design is equally valuable, because it may lead to the elimination of these features altogether. A global sensitivity study is set up by replacing fixed values of dimensions with parameters. The value of always one particular parameter is varied within a preset range and the geometry automatically updated accordingly. Each update is followed by running an analysis and the results are tracked in form of a graph which shows the parameter's effect on key measures of a design such as stiffness, resonance frequency or whatever other measure is used to judge a design. Being a brute force method, the time required to run such an analysis is fairly substantial and increases linearly with the number of design parameters to be investigated. However, provided that the model is set up properly, no user intervention is required throughout the entire run. It is therefore possible to have such an analysis run overnight or over a weekend when it doesn't matter that the actual computing time is too long to be useful during regular hours. As said before, the model needs to be set up properly which is especially true if it is built from idealized elements such as shells. After setting up the parameters it is crucial to examine the geometry using the extreme values of the design parameters to verify that the updated model does not violate pre-requisites for these elements.

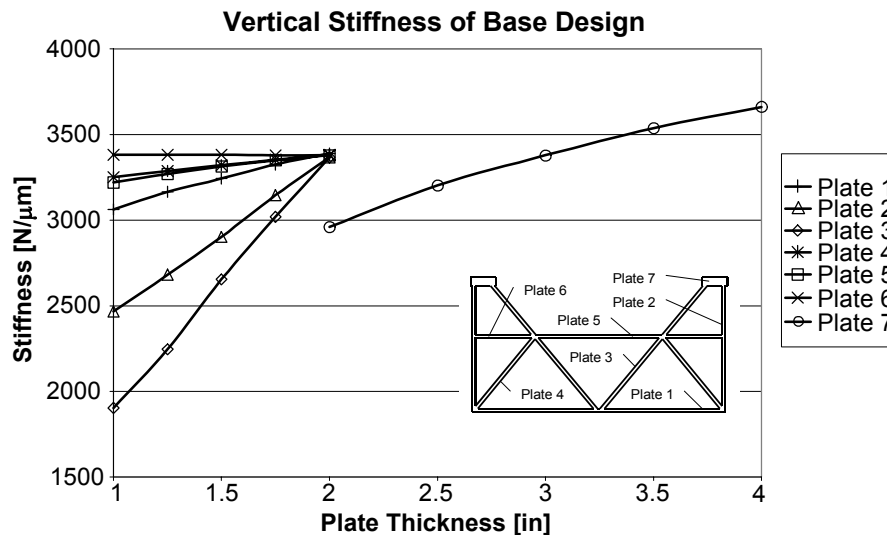
As can be seen in Figure 7.16, the two remaining concepts are very similar with concept #2 having one more plate than concept #1. The goal of the sensitivity study is to find out whether this plate (plate 6) is necessary and if it is, how thick should it be (see Figure 7.17). So in fact, this study is doing more than would



**Figure 7.17** TubeMill base - plate numbers

be required at this stage of the design. Not only is it a selection tool, it already optimizes the design, a process usually done later in the design. However, since the analysis doesn't require user intervention at all, it seems appropriate to combine these two design phases and extend the study to all plates involved. The setup is as follows:

- Thickness of plate 1 to 6 is varied in 4 steps from 1" to 2".
- Thickness of plate 7 is varied from 2" to 4".
- For plates whose thickness is held constant, a value of 2" is chosen.
- Length of plates remain unchanged.



**Figure 7.18** Result of global sensitivity study - vertical stiffness

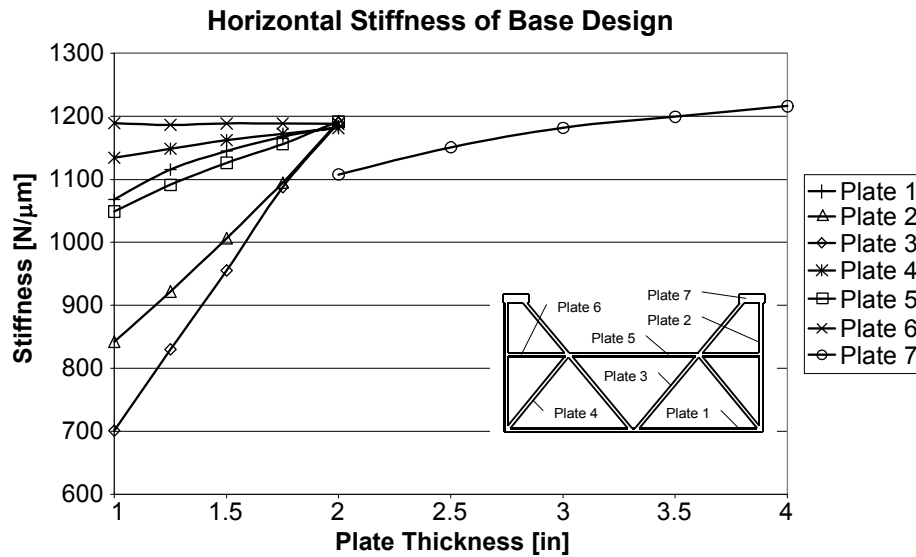


Figure 7.19 Result of global sensitivity study - horizontal stiffness

From the results shown in Figure 7.18 and Figure 7.19 it can be seen that plate #2 and #4 have the most influence on the base’s stiffness while plates #6 has no effect at all. This leads to the conclusion that plate #6 is not a crucial element of the truss that forms the base, favoring design #3 over design #2. As the best concept, base design #3 is chosen.

### 7.4 TubeMill Gantry Concepts

Following the overall machine concept selected in Section 7.2, a gantry type combination of Y- and Z-axis had to be designed. Like the base, the gantry was intended to be fabricated, however not from plates but standard sized square tubes. Being a moving component of the machine, the gantry has to be rather lightweight in order to limit inertia forces during acceleration and deceleration. Given the rather large spacing between the main bearings, a truss design that would stiffen up the gantry in the vertical direction seemed appropriate.

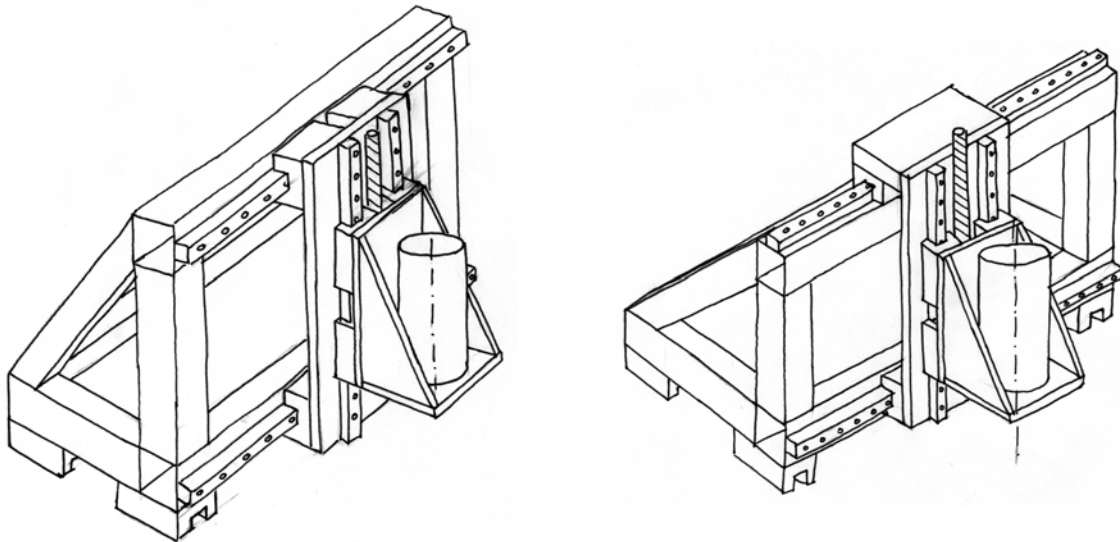


Figure 7.20 TubeMill overall gantry concept 1-2

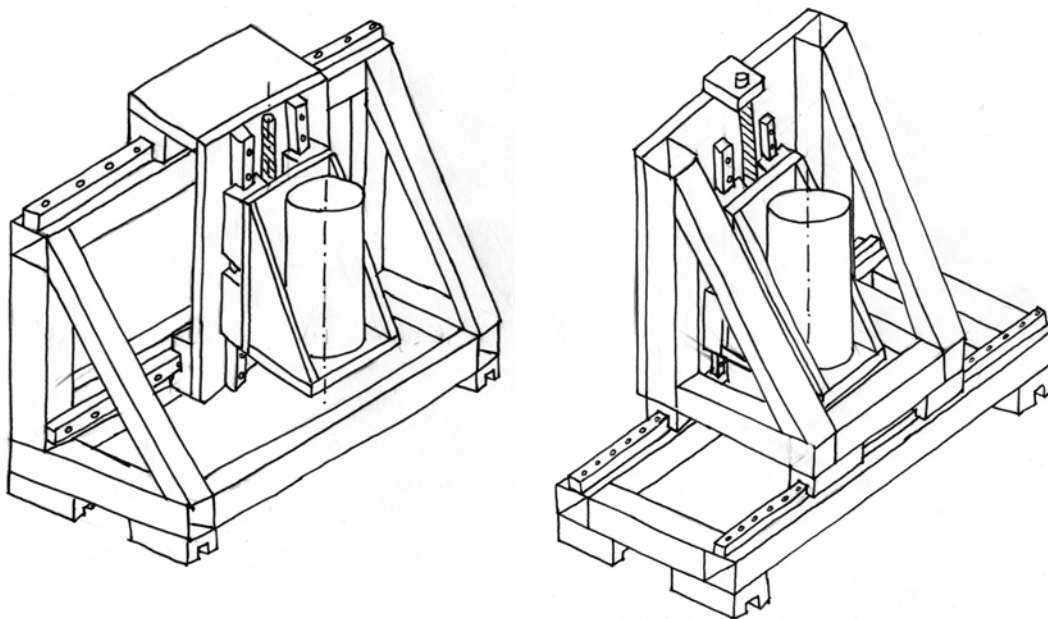
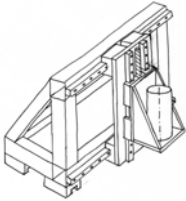
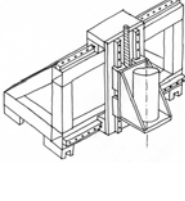
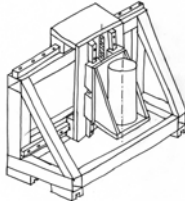
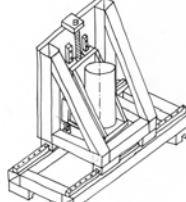
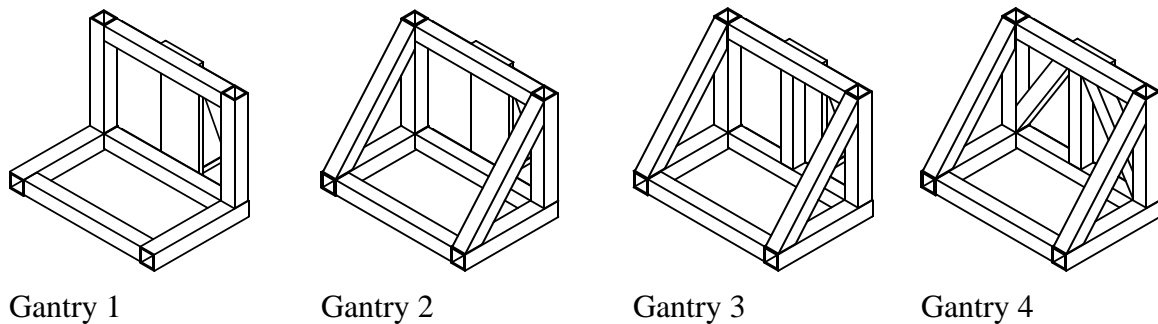


Figure 7.21 TubeMill overall gantry concept 3-4

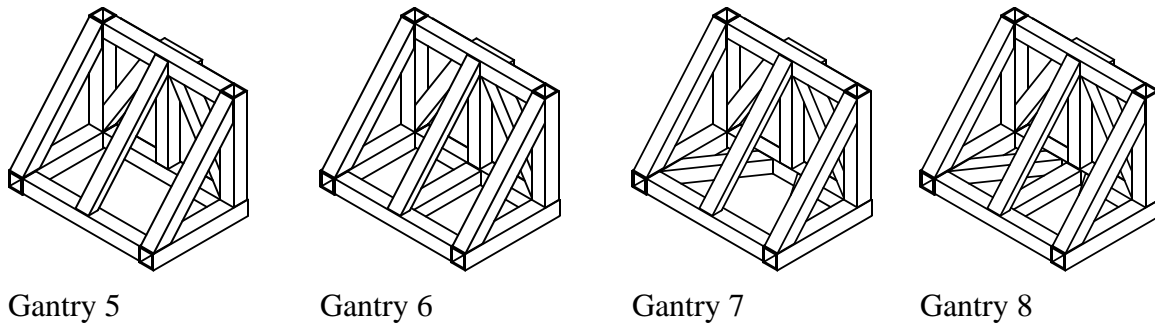
**TABLE 7.3** Pugh chart for TubeMill gantry selection

				
Low cost	0	-	-	0
High stiffness	0	-	0	--
Lightweight	0	0	0	+
Weldability	0	0	0	0
Machinability	0	0	--	--
Setup for manufacturing	0	--	--	--
<b>Total</b>	<b>0</b>	<b>-4</b>	<b>-5</b>	<b>-6</b>

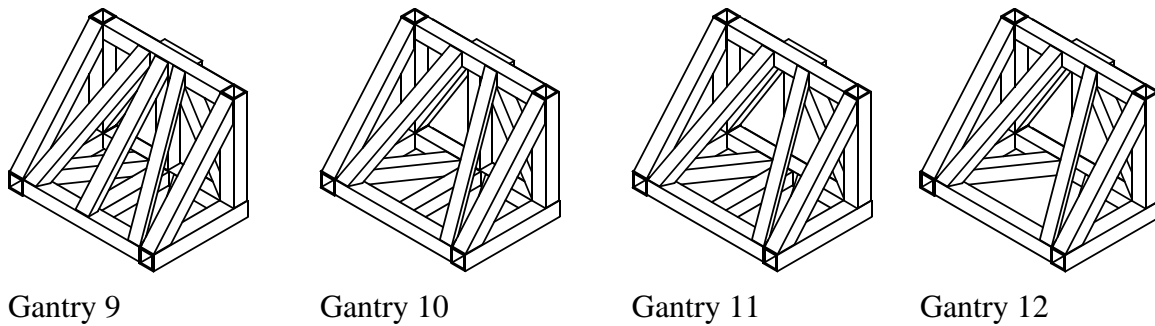
The best overall concept for the gantry turns out to be concept #1. Designs #2 and 3 have difficulties associated with manufacturing, especially #3 where one of the mounting surfaces for the linear rails is not accessible with a surface grinder. Concept #4, although the Y-carriage is composed of a truss, has a potential stiffness problem because the structure on which the carriage rides along is a simple bridge and not a truss.



**Figure 7.22** Gantry concepts 1 through 4



**Figure 7.23** Gantry concepts 5 through 8



**Figure 7.24** Gantry concepts 9 through 12

The model is built from shell elements, an idealization which is perfectly appropriate for the materials used. The mounting surfaces for the linear bearing trucks are used to fully constrain the model and a cutting force of 1000 N is applied to the mounting surface of the spindle in all three directions (see Figure 7.25). Even though idealizations are used to build the model, computing time is a bit too long in order to run the models during normal

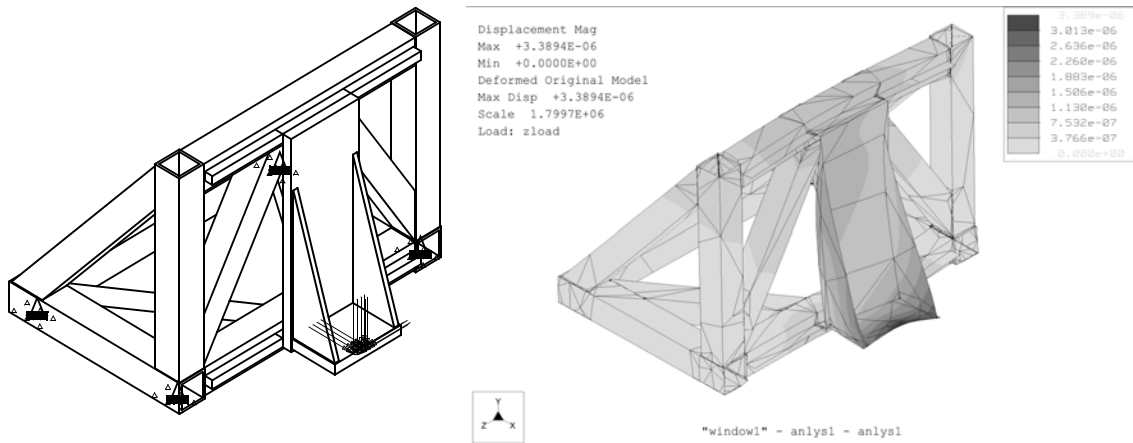


Figure 7.25 TubeMill Gantry: FEA model (a) and deformation fringe plot (b)

hours. In such a case, it is possible to define a series of analyses and have them run in a batch mode overnight or over a weekend.

In Figure 7.26 the numbering system for the structural beams is shown. Not numbered are the tubes that form the basic frame of the gantry which is coincident with concept #1. The stiffness values shown in Figure 7.27 were calculated using the ratio between the vectors of the cutting force and the displacement of the spindle mounting surface.

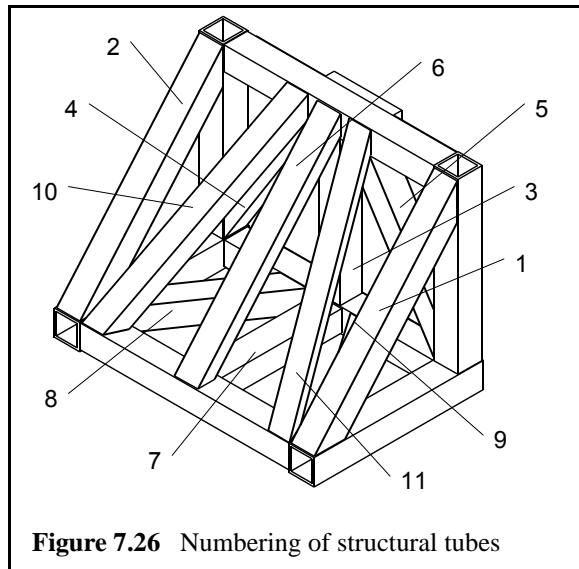


Figure 7.26 Numbering of structural tubes

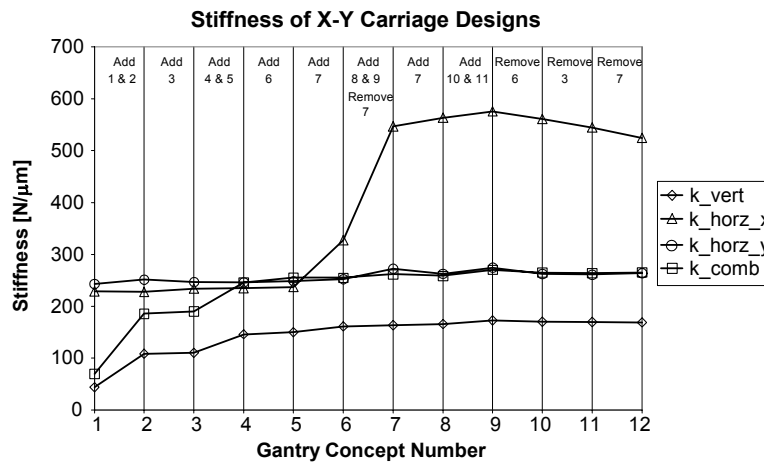


Figure 7.27 TubeMill gantry stiffness comparison

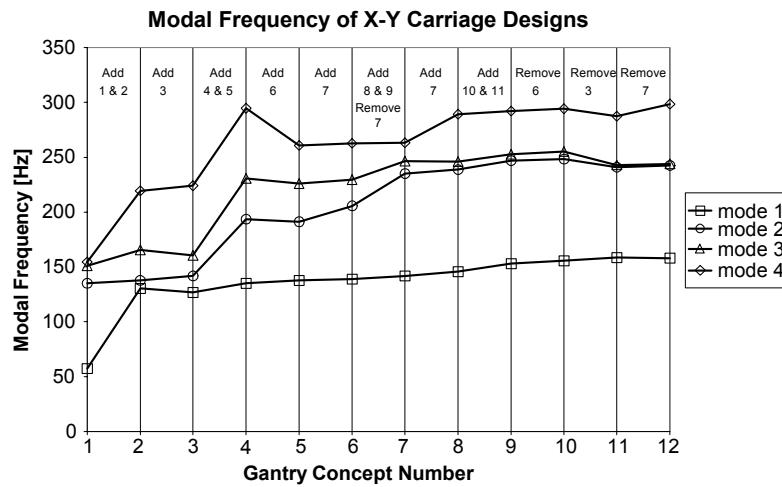


Figure 7.28 TubeMill gantry modal frequency comparison

From Figure 7.27 and Figure 7.28 the following can be derived:

- The horizontal stiffness is virtually unchanged throughout the entire series of analyses. It is therefore concluded that the compliance in the Y-direction is basically determined by the stiffness of the spindle mount.
- The addition of beams 1&2 greatly improves the vertical stiffness, boosting both the overall rigidity and the modal frequencies.
- Adding beam 3 has no effect on the stiffness of the gantry, causing a drop in modal frequency due to the added weight.



- Beams 4&5 substantially enhance the vertical stiffness, improving the gantry's overall stiffness and modal frequencies.
- The gantry stiffness is not affected by the addition of beam 6. Instead, modal frequencies drop as a result of the added weight.
- Beam 7 adds stiffness in the x-direction and raises the frequency of the second mode.
- Adding beams 8&9 boosts the vertical stiffness dramatically as well as the frequencies for the second and third mode.
- Beams 10&11 improve the overall stiffness and the frequencies for all modes.

From the above the following can be concluded:

- Structural elements #1, 2, 4, 5, 8, and 9 are the beams with the most impact on the gantry's static and dynamic stiffness.
- Beams #10&11 have more impact on the design than beam #7.
- Elements #3 and 6 do not affect the stiffness of the gantry. Instead, due to their additional weight, modal frequencies drop noticeably. Hence, these elements will not be used for the final design.

Based on the above findings it is concluded that design #12 offers the best compromise between performance, weight, and manufacturing costs, and will therefore be used as the final design for the TubeMill's gantry.

## 7.5 Design Optimization of Gantry

Having found the best design concept in Section 7.4, it is now time to optimize this concept in terms of finding an acceptable compromise between stiffness and weight. To find this best possible compromise, a design optimization study was set up that varied the cross section of every structural element within preset limits according to the availability of the materials. Table 7.4 shows the cross sections of the structural elements together with the resulting stiffness at the tool tip, modal frequencies, and weight. As the best compromise, gantry revision #16 was chosen with a stiffness at the tool tip of 322 N/ $\mu\text{m}$ , a first resonance frequency of 83 Hz and an overall weight of 810 kg.

TABLE 7.4 Result of design optimization for TubeMill gantry design #12

Rev	front beam	rear beam	1&2	4&5	8&9	10&11	k_tip [N/μm]	1. mode [Hz]	2. mode [Hz]	3. mode [Hz]	4. mode [Hz]	mass [lb]
1	5x5x0.5	5x5x0.5	4.5x4.5x0.5	5x5x0.5	4x4x0.5	2x2x0.25	448.0	104.4	126.8	165.1	205.5	2468
2	↓	↓	↓	↓	↓	2x2x0.12	433.4	98.7	127.1	164.6	203.3	2427
3	↓	↓	↓	↓	↓	2x2x0.095	432.1	96.6	127.3	164.5	203.4	2418
4	↓	↓	↓	↓	4x4x0.375	2x2x0.25	440.5	104.0	127.6	164.9	209.5	2435
5	↓	↓	↓	↓	4x4x0.25	↓	429.0	102.7	126.6	163.6	206.2	2399
6	↓	↓	↓	↓	4x4x0.12	↓	409.2	100.9	126.7	161.8	203.7	2359
7	↓	↓	↓	↓	4x4x0.083	↓	399.5	99.0	126.6	160.5	200.3	2347
8	↓	↓	↓	5x5x0.375	4x4x0.5	↓	435.8	104.6	126.9	165.1	201.4	2425
9	↓	↓	4.5x4.5x0.375	5x5x0.5	↓	↓	447.7	104.6	127.7	166.1	206.5	2428
10	↓	↓	4.5x4.5x0.25	↓	↓	↓	437.3	104.2	128.4	165.9	204.3	2384
11	↓	↓	4.5x4.5x0.12	↓	↓	↓	437.6	103.1	129.9	159.4	202.9	2336
12	↓	↓	4.5x4.5x0.083	↓	↓	↓	437.9	102.2	129.9	153.7	203.2	2321
13	↓	5x5x0.375	4.5x4.5x0.5	↓	↓	↓	447.7	101.9	125.8	161.8	202.3	2426
14	↓	5x4x0.188	3.5x3.5x0.125	5x3x0.188	5x4x0.188	2x2x0.095	372.7	84.3	127.3	147.1	185.0	1965
15	6x6x0.25	6x4x0.25	↓	↓	↓	↓	235.0	78.7	126.2	143.6	148.2	1675
16	6x6x0.375	↓	↓	↓	↓	↓	322.9	83.2	132.2	152.4	153.3	1780

# NOMENCLATURE

$\alpha$	thermal expansion coefficient [1/K]
$\delta$	linear error motion [m]
$\varepsilon$	rotational error motion [rad], efficiency
$\eta$	loss factor
$\varphi$	constraining layer angle [rad]
$\mu$	friction factor
$\lambda$	eigenvalue
$\mu$	friction factor
$\omega_e$	excitation frequency [rad/s]
$\omega_n$	natural frequency [rad/s]
$\rho$	density [kg/m <sup>3</sup> ]
$\zeta$	damping ratio
$A$	cross section [m <sup>2</sup> ]
$b$	width of gear [m]
$c$	damping factor [Ns/m]
$C_{dyn}$	dynamic load capacity [N]
$d$	diameter [m]
$d_S$	ball screw shaft diameter [m]
$d_W$	ball diameter [m]
$d_p$	pitch circle diameter [m]
$d_i$	inner diameter [m]
$E$	Young's modulus [Pa]
$F$	force [N]
$F_{A0}$	pre-load force [N]
$G$	shear modulus [Pa]
$h$	axial depth of cut [m]
$I, I_b$	area moment of inertia [m <sup>4</sup> ]
$I, I_t$	polar moment of inertia [m <sup>4</sup> ]
$J_{Rotor}$	polar moment of rotor #1 [kg*m <sup>2</sup> ]
$k$	stiffness [N/m]

$k_{\text{tot}}$	structural loop stiffness [N/m]
$lead$	pitch of ballscrew [m]
$L$	length [m]
$L_a$	ball screw mounting distance [m]
$Life$	lifetime [cycles]
$Life_h$	lifetime [hr]
$m$	mass [kg]
$n$	shaft and spindle speed [ $s^{-1}$ ]
$N$	number of rebars
$N_1$	number of teeth of gear #1
$N_2$	number of teeth of gear #2
$p$	pressure [Pa]
$P$	perimeter [m]
$preload$	preload of ball screw nut [%]
$q$	displacement vector
$Q$	dynamic compliance [mm/N], Load vector
$r$	radius [m]
$t$	time [s], wall thickness [m]
$t_{ac}$	acceleration time [s]
$T$	torque [Nm], temperature [K]
$U_m$	length of median [m]
$v_c$	cutting speed [m/s]
$v_{\text{max}}$	maximum speed [m/s]
$v_f$	feed rate [m/s]
$w$	width [m]

# REFERENCES

- [Arai et al] Arai, E. and Iwata, K., *Product Modeling System in Conceptual Design of Mechanical Products*, Robotics & Computer-Integrated Manufacturing, Vol. 9, No. 4-5, Aug-Oct, pp. 327-334, 1992.
- [Avalone et al] Avalone, E.A., Baumeister, Theodore, *Marks' Handbook for Mechanical Engineering*, 10th edition, McGraw-Hill, New York, 1996.
- [Bathe] Bathe, K.J., *Finite Element Procedures*, Prentice-Hall 1996.
- [Beitz et al] Beitz, W., Küttner, K.H., *Dubbel - Taschenbuch für den Maschinenbau*, 17. ed., Springer Verlag, Berlin, 1990.
- [Bjarnemo et al] Bjarnemo, R., Burman, A., and Anker, J.C., *Shortcomings of CAD Systems in Conceptual Design*, Current Topics in Computational Mechanics, American Society of Mechanical Engineers, Pressure Vessels and Piping Division (Publication) PVP, Vol. 305, pp. 227-232, 1995.
- [Bozzo et al] Bozzo, L.M., Barbat, A., and Torres, L., *Application of Qualitative Reasoning in Engineering*, Applied Artificial Intelligence, Vol. 12, No. 1, Jan-Feb, pp. 29-48, 1998.
- [Bourinet et al] Bourinet, J.M. and Le Houdec, D., *Dynamic Stiffness Analysis Of Damped Tubes Filled With Granular Materials*, Computers & Structures, Vol. 73, No. 1-5, Oct-Dec, pp. 395-406, 1999.
- [Bryan] Bryan, J.B., *The Abbe Principle Revisited - An Updated Interpretation*, Precision Engineering, Vol. 1, No. 3, pp. 129-132, 1989.
- [Burman et al] Burman, A. and Anker, J.C., *A Concept for a Finite Element Based Design Tool*, Advanced Computer Applications American Society of Mechanical Engineers, Pressure Vessels and Piping Division (Publication) PVP, Vol. 274, ASME, New York, pp. 103-112, 1994.
- [Chen et al] Chen, T., Baz, A., *Performance Characteristics of Active Constrained Layer Damping Versus Passive Constrained Layer Damping With Active Control*, Proceedings of SPIE - The International Society for Optical Engineering, Vol. 2715, pp. 256-268, 1996.
- [Craig] Craig, R.R., *Structural Dynamics - An Introduction to Computer Methods*, John Wiley & Sons, New York, 1981.
- [Crandall et al] Crandall, S.H., Dahl, N.C., Lardner, T.J., *An Introduction to the Mechan-*

- ics of Solids*, 2nd ed., McGraw-Hill, New York, 1978.
- [Crandall et al] Crandall, S.H., Karnopp, Dean C., Kurtz, E.F, Prodmore-Brown, David C., *Dynamics of Mechanical and Electromechanical Systems*, Krieger, Malabar, 1968.
- [Dewa] Dewa, H., *Torsional Stress Analysis and Vibration Damping of Three-Layered Rods*, JSME International Journal, Series I, Vol. 33, No. 2, pp. 152-159, 1989.
- [Dieter] Dieter, G.E, *Engineering Design. A Materials and Processing Approach*, McGraw-Hill, New York, 1983.
- [DiTarantino] DiTarantino, R.A., *Theory of Vibratory Bending for Elastic and Viscoelastic Layered Finite-Length Beams*, Journal of Applied Mechanics, Vol. 87, pp. 881-886, 1965.
- [Franklin et al] Franklin, G.F., Powell, D.J., Emami-Naeini, A., *Feedback Control of Dynamic Systems*, Third Edition, Addison Wesley, 1995.
- [Gieck] Gieck, K. and R., *Technische Formelsammlung*, 30. ed, Gieck Verlag, Germering, 1995.
- [Hale] Hale, L.C., *Principles and Techniques for Designing Precision Machines*, Ph.D. Thesis, Massachusetts Institute of Technology, Cambridge, 1999.
- [Harrington] Harrington, B.W., *Development of Software Tools for Automation and Acceleration of the Engineering Design Process*, IEEE Aerospace Applications Conference Proceedings, Vol. 4, pp. 265-275, 1998.
- [Horvath et al] Horvath, I., Thernesz, V., Bagoly, Z., *Conceptual Design With Functionally and Morphologically Parameterized Feature Objects*, Computers in Engineering ASME Database Symposium, ASME, New York, pp. 507-516, 1995.
- [Hsu et al] Hsu, W. and Woon, I.M.Y, *Current Research in the Conceptual Design of Mechanical Products*, Computer-Aided Design, Vol. 30, No. 5 Apr, pp. 377-389, 1998.
- [Johnson et al] Johnson, A.F. and Woolf, A., *Dynamic Torsion of a Two-Layer Viscoelastic Beam*, Journal of Sound and Vibration, Vol. 48, No. 2, pp. 251-263, 1976.
- [Kalpakjian] Kalpakjian, S., *Manufacturing Engineering and Technology*, Addison Wesley, p. 611, 1995.
- [Koenigsberger et al] Koenigsberger, F. and Tlusty, J., *Machine Tool Structures*, Pergamon Press, London, 1970.
- [Kronenberg] Kronenberg, M., *Machining Science and Application*, Pergamon Press,

pp. 203-316, 1966.

[Lazan] Lazan, B.J., *Damping of Materials and Members of Structural Mechanics*, Pergamon Press, London, 1968.

[Lipson et al] Lipson, H. and Shpitalni, M., *New Interface for Conceptual Design Based on Object Reconstruction From a Single Freehand Sketch*, *Cirp Annals*, Vol. 44, No. 1, pp. 133-136, 1995.

[Machinery's Handbook] *Machinery's Handbook*, 25th Edition, Industrial Press Inc., pp. 1042-1043, 1995.

[Makino] Makino Inc., *High Speed Machining*, Data Sheet for A55 Delta, <http://www.makino.com>, 1999.

[Marsh] Marsh, E.R., *An Integrated Approach to Structural Damping*, Ph.D. Thesis, Massachusetts Institute of Technology, Cambridge, 1994.

[Marsh et al] Marsh, E.R., Slocum, A.H., *Integrated Approach to Structural Damping*, *Precision Engineering Journal of the American Society for Precision Engineering*, Vol. 18, Apr-May, pp. 103-109, 1996.

[Nayfeh] Nayfeh, S.A., *Design and Application of Damped Machine Elements*, Ph.D. Thesis, Massachusetts Institute of Technology, Cambridge, 1998.

[Park et al] Park, C.H., and Baz, A., *Vibration Damping and Control Using Active Constrained Layer Damping: A Survey*, *Shock & Vibration Digest*. Vol. 31, No. 5, pp. 355-364, 1999.

[Pitarresi et al] Pitarresi, J.M. and Haller, K.A., *Air Layer Modeling for Air and Air-Vacuum Bearings*, *Journal of Manufacturing Science & Engineering, Transactions of the ASME*. Vol. 119, No. 3, Aug, pp. 388-392, 1997.

[Plass] Plass, H.J., *Damping Vibrations in Elastic Rods and Sandwich Structures by Incorporation of Additional Viscoelastic Material*, *Proceedings of Third Midwestern Conference on Solid Mechanics*, pp. 48-71, 1957.

[Plunkett et al] Plunkett, R., Lee, C.T., *Length Optimization for Constrained Viscoelastic Layer Damping*, *Journal of the Acoustic Society of America*, Vol. 48, No. 1, pp. 150-161, 1970.

[PTC] Parametric Technology Corporation, *Pro/MECHANICA Online Books*.

[Rasch] Rash, *Winkerverformungen von Linearlagern*, *Star Linear Systems*, 1995.

[Ross et al] Ross, D., Ungar, E., and Kerwin, E.M., *Damping of Plate Flexural Vibrations by Means of Viscoelastic Laminae*, *Structural Damping*, edited by Ruzicka, J.E.,

ASME, New York, 1959.

[Ruzicka] Ruzicka, J.E., *Damping Structural Resonances Using Viscoelastic Shear-Damping Mechanisms*, Journal of Engineering for Industry, Series B, Vol. 83, No. 4, pp. 414-424, 1961.

[Schorderet et al.] Schorderet, A. and Gmuer, T.C., *Solid to Shell Transition Finite Elements for Structural Dynamics Analysis*, Proceedings of the International Modal Analysis Conference - IMAC, Vol. 2, pp. 1091-1097, 1997.

[Shigley et al] Shigley, J.E., Mischke, C.R., *Standard Handbook of Machine Design*, 2. ed., McGraw-Hill, New York, 1996.

[Slocum (a)] Slocum, A.H., *Precision Machine Design*, Prentice Hall, New Jersey, 1992.

[Slocum (b)] Slocum, A.H., *Notes to 2.75 - Precision Machine Design*, Massachusetts Institute of Technology, Cambridge, 1998.

[Slocum et al] Slocum, A.H., Marsh, E.R., Smith, D.H., *New Daper Design for Machine Tool Structures: the Replicated Internal Viscous Damper*, Precision Engineering Journal of the American Society for Precision Engineering, Vol. 16, July, pp. 174-183, 1994.

[Smith] Smith, G.T., *Advanced Machining*, The Handbook of Cutting Technology, IFS Publication / Springer Verlag, p. 248, 1989.

[Star Linear] Star Linear Systems, *Ball Rail and Roller Rail Systems*, Product Catalog, 1998.

[THK] THK Co, Ltd., *Linear Motion Systems*, Catalog no. 200-1AE, Tokyo.

[van Dijk] van Dijk, C.G.C, *New Insights in Computer-Aided Conceptual Design*, Design Studies, Vol. 16, No. 1, January, pp. 62-80, 1995.

[Varela] Varela, F., *The Design of a Small and Inexpensive Abrasive Waterjet Cutter*, MSME Thesis, Massachusetts Institute of Technology, Cambridge, 1999.

[Wang et al] Wang, W.R. and Chang, C.N., *Dynamic Analysis and Design of a Machine Tool Spindle Bearing System*, Journal of Vibration & Acoustics - Transactions of the ASME, Vol. 116, No. 3, July, pp. 280-285, 1994.

[Weck] Weck, M., *Handbook of Machine Tools*, 4 vols., John Wiley & Sons, New York, 1984.

[Young] Young, W.C., *Roark's Formulas for Stress & Strain*, 6th ed. McGraw-Hill, New York, 1989.



# Appendix A

## DESIGN PRINCIPLES

### A.1 First Order Approach

Simplified area moment of inertia for thin walled round cross sections:

$$\begin{aligned} I_{b,rd} &= \frac{\pi}{64}(w_{rd}^4 - (w_{rd} - 2t)^4) \\ &= \frac{\pi}{64}(8w_{rd}^3t - 8w_{rd}^2t^2 - 16w_{rd}t^3 - 16t^4) \\ &= \frac{\pi}{8}w_{rd}^3t \quad \text{with } w_{rd} \gg t \end{aligned} \tag{A.1}$$

Simplified area moment of inertia for thin walled square cross sections:

$$\begin{aligned} I_{b,sq} &= \frac{1}{12}(w_{sq}^4 - (w_{sq} - 2t)^4) \\ &= \frac{1}{12}(8w_{sq}^3t - 8w_{sq}^2t^2 - 16w_{sq}t^3 - 16t^4) \\ &= \frac{2}{3}w_{sq}^3t \quad \text{with } w \gg t \end{aligned} \tag{A.2}$$

Polar moment of inertia for round cross section with large width-to-thickness ratio:

$$\begin{aligned} I_{t,rd} &= \frac{\pi}{4}\left(w_{rd} - \frac{t}{2}\right)^3 t \\ &= \frac{\pi}{4}\left(w_{rd}^3t - \frac{3}{2}w_{rd}^2t^2 + \frac{3}{4}w_{rd}t^3 - \frac{t^4}{8}\right) \\ &= \frac{\pi}{4}w_{rd}^3t \end{aligned} \tag{A.3}$$

Polar moment of inertia for square cross section with large width-to-thickness ratio:

$$\begin{aligned}
 I_{t, sq} &= \frac{\left(w_{sq} - \frac{t}{2}\right)^4}{w_{sq} - t} t & (A.4) \\
 &= \frac{w_{sq}^4 t - 2w_{sq}^3 t^2 - \frac{1}{2}w_{sq}^2 t^3 + \frac{1}{2}w_{sq} t^4 + \frac{t^5}{16}}{w_{sq} - t} \\
 &= \frac{w_{sq}^4 t}{w_{sq} - t} = w_{sq}^3 t
 \end{aligned}$$

Calculating the diameter of a round tube having the same weight and wall thickness  $t$  as a square tube with width  $w_{sq}$ :

with  $A_{rd} = A_{sq}$  follows: (A.5)

$$\begin{aligned}
 \frac{\pi}{4} \left( w_{rd}^2 - (w_{rd} - 2t)^2 \right) &= \left( w_{sq}^2 - (w_{sq} - 2t)^2 \right) \\
 \rightarrow w_{rd} &= \frac{4}{\pi} \left( w_{sq} + \left( \frac{\pi}{4} - 1 \right) t \right)
 \end{aligned}$$

## A.2 Pro/ENGINEER Relations for Generic Linear Rail Assembly

TABLE 7.5 Pro/ENGINEER relations to define a generic ball rail assembly size 25 to 55

1	cont. from 1	cont. from 2	cont. from 3	cont. from 4
IF size==25	IF size==35	IF size==45	IF size==55	S1=12.5
A2=23	A2=34	A2=45	A2=53	ENDIF
H2=23.55	H2=31.1	H2=39.1	H2=47.85	ENDIF
D=11	D=15	D=20	D=24	ENDIF
S5=7	S5=9	S5=14	S5=16	ENDIF
T1min=13	T1min=16	T1min=18	T1min=20	
T2=30	T2=40	T2=52.5	T2=60	D0:0=A2
N6=14.3	N6=19.4	N6=22.4	N6=28.7	D1:0=H2
A=70	A=100	A=120	A=140	N=floor((D2:0-2*T1min)/T2)
B=91	B=114	B=140	B=166.5	T1=(D2:0-N*T2)/2
H=36	H=48	H=60	H=70	
H1=30	H1=41	H1=51	H1=58	
E1=57	E1=82	E1=100	E1=116	
E2=45	E2=62	E2=80	E2=95	
E3=40	E3=52	E3=60	E3=70	
S1=6.8	S1=8.6	S1=10.5	S1=12.5	
else	else	else		

## A.3 Bearing Calculations

Kinetic energies:

$$T = \frac{1}{2}m\dot{x}^2 + \frac{1}{2}m\dot{y}^2 + \frac{1}{2}m\dot{z}^2 + \frac{1}{2}I_x\dot{\theta}_x^2 + \frac{1}{2}I_y\dot{\theta}_y^2 + \frac{1}{2}I_z\dot{\theta}_z^2 \tag{A.6}$$

Potential energies:

$$V = \frac{1}{2}k_{x_1}^2 + \sum_{i=1}^6 \frac{1}{2}k_{y_i}y_i^2 + \sum_{i=1}^6 \frac{1}{2}k_{z_i}z_i^2 \tag{A.7}$$

now write coordinates  $x_i$ ,  $y_i$  and  $z_i$  in terms of  $y$ ,  $z$ ,  $\theta_x$ ,  $\theta_y$ ,  $\theta_z$ :

$$\begin{aligned}
x_1 &= x + b_1 \theta_y & y_2 &= y + d_1 \theta_z & y_3 &= y + d_2 \theta_z \\
y_1 &= y & y_5 &= y - b_2 \theta_x + d_1 \theta_z & y_6 &= y - b_2 \theta_x + d_2 \theta_z \\
y_4 &= y - b_2 \theta_x & z_2 &= z - d_1 \theta_y & z_3 &= z - d_2 \theta_y \\
z_1 &= z & z_5 &= z - d_1 \theta_y & z_6 &= z - d_2 \theta_y \\
z_4 &= z & & & & 
\end{aligned} \tag{A.8}$$

now substitute A.8 into A.7

$$\begin{aligned}
V &= \frac{1}{2} k_x x^2 + k_x b_1 x \theta_y + 3k_y y^2 + 3k_z z^2 - 3k_y b_2 y \theta_x - 2k_z (d_1 + d_2) z \theta_y \\
&+ 2k_y (d_1 + d_2) y \theta_z - k_y b_2 (d_1 + d_2) \theta_x \theta_z + \frac{3}{2} k_y b_2^2 \theta_x^2 + \left( k_z (d_1^2 + d_2^2) + \frac{1}{2} k_x b_1^2 \right) \theta_y^2 \\
&+ k_y (d_1^2 + d_2^2) \theta_z^2
\end{aligned} \tag{A.9}$$

Setting up the equations of motion is done using Lagrange:

$$\frac{d}{dt} \left( \frac{\partial T}{\partial \dot{q}_i} \right) - \frac{\partial T}{\partial q} + \frac{\partial V}{\partial q_i} = Q_i \tag{A.10}$$

$$\begin{aligned}
m\ddot{x} + k_x x + k_x b_1 \theta_y &= F_x \\
m\ddot{y} + 6k_y y - 3k_y b_2 \theta_x + 2k_y (d_1 + d_2) \theta_z &= F_y \\
m\ddot{z} + 6k_z z - 2k_z (d_1 + d_2) \theta_y &= F_z \\
I_x \ddot{\theta}_x - 3k_y b_2 y + 3k_y b_2^2 \theta_x - k_y b_2 (d_1 + d_2) \theta_z &= M_x \\
I_y \ddot{\theta}_y + k_x b_1 x - 2k_z (d_1 + d_2) z + (2k_z (d_1^2 + d_2^2) + k_x b_1^2) \theta_y &= M_y \\
I_z \ddot{\theta}_z + 2k_y (d_1 + d_2) y - k_y b_2 (d_1 + d_2) \theta_x + 2k_y (d_1^2 + d_2^2) \theta_z &= M_z
\end{aligned} \tag{A.11}$$

In matrix form, these equations can be written as:

$$\begin{bmatrix} F_x \\ F_y \\ F_z \\ M_x \\ M_y \\ M_z \end{bmatrix} = \begin{bmatrix} m & 0 & 0 & 0 & 0 & 0 \\ 0 & m & 0 & 0 & 0 & 0 \\ 0 & 0 & m & 0 & 0 & 0 \\ 0 & 0 & 0 & I_x & 0 & 0 \\ 0 & 0 & 0 & 0 & I_y & 0 \\ 0 & 0 & 0 & 0 & 0 & I_z \end{bmatrix} \begin{bmatrix} \ddot{x} \\ \ddot{y} \\ \ddot{z} \\ \ddot{\theta}_x \\ \ddot{\theta}_y \\ \ddot{\theta}_z \end{bmatrix} \quad (\text{A.12})$$

$$+ \begin{bmatrix} k_x & 0 & 0 & 0 & k_x b_1 & 0 \\ 0 & 6k_y & 0 & -3k_y b_2 & 0 & 2k_y(d_1 + d_2) \\ 0 & 0 & 6k_z & 0 & -2k_z(d_1 + d_2) & 0 \\ 0 & -3k_y b_2 & 0 & 3k_y b_2^2 & 0 & -k_y b_2(d_1 + d_2) \\ k_x b_1 & 0 & -2k_z(d_1 + d_2) & 0 & 2k_z(d_1^2 + d_2^2) + k_x b_1^2 & 0 \\ 0 & 2k_y(d_1 + d_2) & 0 & -k_y b_2(d_1 + d_2) & 0 & 2k_y(d_1^2 + d_2^2) \end{bmatrix} \begin{bmatrix} x \\ y \\ z \\ \theta_x \\ \theta_y \\ \theta_z \end{bmatrix}$$

Or more general:

$$\vec{Q} = \vec{m}\ddot{\vec{q}} + \vec{K}\vec{q} \quad (\text{A.13})$$

For a quasi-static situation, the inertia terms become very small and can safely be neglected. This simplifies the equations to:

$$\vec{Q} = \vec{K}\vec{q} \quad (\text{A.14})$$

To find the linear and rotary displacements, A.14 needs to be solved for  $q$ : (A.15)

$$\vec{q} = \vec{K}^{-1}\vec{Q} \quad (\text{A.16})$$

where the inverse of the stiffness matrix  $K$  will be the compliance matrix  $C$ :

(A.17)

$$C = \frac{1}{d_1^2 + d_2^2 - d_1 d_2} \begin{bmatrix} \frac{4k_z(d_1^2 + d_2^2 - d_1 d_2) + 3k_x b_1^2}{4k_x k_z} & 0 & \frac{-(d_1 + d_2)b_1}{4k_z} & 0 & \frac{-3b_1}{4k_z} & 0 \\ 0 & \frac{5(d_1^2 + d_2^2) - 2d_1 d_2}{12k_y} & 0 & \frac{d_1^2 + d_2^2 - d_1 d_2}{3k_y b_2} & 0 & \frac{-(d_1 + d_2)}{4k_y} \\ \frac{-(d_1 + d_2)b_1}{4k_z} & 0 & \frac{d_1^2 + d_2^2}{4k_z} & 0 & \frac{d_1 + d_2}{4k_z} & 0 \\ 0 & \frac{d_1^2 + d_2^2 - d_1 d_2}{3k_y b_2} & 0 & \frac{2(d_1^2 + d_2^2 - d_1 d_2)}{3k_y b_2^2} & 0 & 0 \\ \frac{-3b_1}{4k_z} & 0 & \frac{d_1 + d_2}{4k_z} & 0 & \frac{3}{4k_z} & 0 \\ 0 & \frac{-(d_1 + d_2)}{4k_y} & 0 & 0 & 0 & \frac{3}{4k_y} \end{bmatrix}$$

## A.4 Ballscrew Calculations

Thermal expansion of ballscrew:

$$\Delta L_S = L_S \alpha_S \Delta T \quad (\text{A.18})$$

Hooke's Law for elastic spring:

$$F = kx \quad (\text{A.19})$$

$$= \frac{AE_S}{L_S} \Delta L_S$$

Combining A.18 and A.19 to calculate pre-stretch force for ballscrew:

$$F_{PL} = \alpha_S EA_S \Delta T \quad (\text{A.20})$$

# Appendix B

## DAMPING

### B.1 Moment of inertia for ring segment

In general:

$$I_x = \int_A y^2 dA = \iint y^2 dx dy \quad (\text{B.1})$$

here:

$$y = y(x) \quad \text{with} \quad \sqrt{r_c^2 - x^2} < y < \sqrt{R_c^2 - x^2}, \quad (0 < x < x_1) \quad (\text{B.2})$$

$$\frac{x \cos \alpha_c}{\sin \alpha_c} < y < \sqrt{R_c^2 - x^2}, \quad (x_1 < x < x_2) \quad (\text{B.3})$$

Using symmetry:

$$I_x = 2 \int_0^{x_1} \int_{\sqrt{r_c^2 - x^2}}^{\sqrt{R_c^2 - x^2}} y^2 dy dx + 2 \int_{x_1}^{x_2} \int_{\frac{x \cos \alpha_c}{\sin \alpha_c}}^{\sqrt{R_c^2 - x^2}} y^2 dy dx \quad (\text{B.4})$$

$$I_x = \frac{2}{3} \int_0^{x_1} (\sqrt{(R_c^2 - x^2)^3} - \sqrt{(r_c^2 - x^2)^3}) dx + \frac{2}{3} \int_{x_1}^{x_2} \left( \sqrt{(R_c^2 - x^2)^3} - \left( \frac{x \cos \alpha_c}{\sin \alpha_c} \right)^3 \right) dx \quad (\text{B.5})$$

using:

$$\int \sqrt{(a^2 - x^2)^3} dx = \frac{1}{4} \left( x \sqrt{(a^2 - x^2)^3} + \frac{3a^2 x}{2} \sqrt{a^2 - x^2} + \frac{3a^4}{2} \operatorname{asin} \frac{x}{a} \right) \quad (\text{B.6})$$

it follows:

$$\begin{aligned}
I_x = & \frac{1}{6} \left( x_1 \sqrt{(R_c^2 - x_1^2)^3} + \frac{3R_c^2 x_1}{2} \sqrt{R_c^2 - x_1^2} + \frac{3R_c^4}{2} \operatorname{asin} \frac{x_1}{R_c} \right) \\
& - \frac{1}{6} \left( x_1 \sqrt{(r_c^2 - x_1^2)^3} + \frac{3r_c^2 x_1}{2} \sqrt{r_c^2 - x_1^2} + \frac{3r_c^4}{2} \operatorname{asin} \frac{x_1}{r_c} \right) \\
& + \frac{1}{6} \left( x_2 \sqrt{(R_c^2 - x_2^2)^3} + \frac{3R_c^2 x_2}{2} \sqrt{R_c^2 - x_2^2} + \frac{3R_c^4}{2} \operatorname{asin} \frac{x_2}{R_c} \right) \\
& - \frac{1}{6} \left( x_1 \sqrt{(R_c^2 - x_1^2)^3} + \frac{3R_c^2 x_1}{2} \sqrt{R_c^2 - x_1^2} + \frac{3R_c^4}{2} \operatorname{asin} \frac{x_1}{R_c} \right) \\
& - \frac{1}{6} \frac{\cos^3 \alpha_c}{\sin^3 \alpha_c} (x_2^4 - x_1^4)
\end{aligned} \tag{B.7}$$

which simplifies to:

$$\begin{aligned}
I_x = & \frac{1}{6} \left( x_2 \sqrt{(R_c^2 - x_2^2)^3} + \frac{3R_c^2 x_2}{2} \sqrt{R_c^2 - x_2^2} + \frac{3R_c^4}{2} \operatorname{asin} \frac{x_2}{R_c} \right) \\
& - \left( x_1 \sqrt{(r_c^2 - x_1^2)^3} - \frac{3r_c^2 x_1}{2} \sqrt{r_c^2 - x_1^2} - \frac{3r_c^4}{2} \operatorname{asin} \frac{x_1}{r_c} - \frac{\cos^3 \alpha_c}{\sin^3 \alpha_c} (x_2^4 - x_1^4) \right)
\end{aligned} \tag{B.8}$$

using:

$$x_1 = r_c \sin \alpha_c \text{ and } x_2 = R_c \sin \alpha_c \tag{B.9}$$

it follows:

$$\begin{aligned}
I_x = & \left( R_c \sin \alpha_c \sqrt{(R_c^2 - (R_c \sin \alpha_c)^2)^3} + \frac{3R_c^3 \sin \alpha_c}{2} \sqrt{R_c^2 - (R_c \sin \alpha_c)^2} \right. \\
& + \frac{3R_c^4}{2} \operatorname{asin} \frac{R_c \sin \alpha_c}{R_c} - r_c \sin \alpha_c \sqrt{(r_c^2 - (r_c \sin \alpha_c)^2)^3} \\
& - \frac{3r_c^3 \sin \alpha_c}{2} \sqrt{r_c^2 - (r_c \sin \alpha_c)^2} - \frac{3r_c^4}{2} \operatorname{asin} \frac{r_c \sin \alpha_c}{r_c} \\
& \left. - \frac{\cos^3 \alpha_c}{\sin^3 \alpha_c} ((R_c \sin \alpha_c)^4 - (r_c \sin \alpha_c)^4) \right) \frac{1}{6}
\end{aligned} \tag{B.10}$$

which can be simplified to:



$$\begin{aligned}
 I_x = & \frac{1}{6} \left( R_c^4 \sin \alpha_c \sqrt{(1 - \sin^2 \alpha_c)^3} + \frac{3R_c^4 \sin \alpha_c}{2} \sqrt{1 - \sin^2 \alpha_c} + \frac{3R_c^4}{2} \text{asin}(\sin \alpha_c) \right) \quad (\text{B.11}) \\
 & - r_c^4 \sin \alpha_c \sqrt{(1 - \sin^2 \alpha_c)^3} - \frac{3r_c^4 \sin \alpha_c}{2} \sqrt{1 - \sin^2 \alpha_c} - \frac{3r_c^4}{2} \text{asin}(\sin \alpha_c) \\
 & - (\cos^3 \alpha_c \sin \alpha_c)(R_c^4 - r_c^4)
 \end{aligned}$$

which can be further simplified to:

$$\begin{aligned}
 I_x = & \frac{1}{6} \left( R_c^4 \sin \alpha_c \cos^3 \alpha_c + \frac{3R_c^4 \sin \alpha_c \cos \alpha_c}{2} + \frac{3R_c^4 \alpha_c}{2} \right) \quad (\text{B.12}) \\
 & - r_c^4 \sin \alpha_c \cos^3 \alpha_c - \frac{3r_c^4 \sin \alpha_c \cos \alpha_c}{2} - \frac{3r_c^4 \alpha_c}{2} \\
 & - (\cos^3 \alpha_c \sin \alpha_c)(R_c^4 - r_c^4)
 \end{aligned}$$

it now follows:

$$I_x = \frac{1}{6} \left( \frac{3R_c^4 \sin \alpha_c \cos \alpha_c}{2} + \frac{3R_c^4 \alpha_c}{2} - \frac{3r_c^4 \sin \alpha_c \cos \alpha_c}{2} - \frac{3r_c^4 \alpha_c}{2} \right) \quad (\text{B.13})$$

and now:

$$I_x = \left( \frac{1}{4} \sin \alpha_c \cos \alpha_c + \frac{1}{4} \alpha \right) (R_c^4 - r_c^4) \quad (\text{B.14})$$

$$I_x = \frac{1}{8} (\varphi + \sin \varphi) (R_c^4 - (R_c - t_c)^4) \quad (\text{B.15})$$

Next we need the center of gravity of this segment which can be calculated to be:

$$y_c = \frac{4R_c^3 - (R_c - t_c)^3 \sin \frac{\varphi}{2}}{3R_c^2 - (R_c - t_c)^2} \widehat{\varphi} \quad (\text{B.16})$$

and also the area which comes out to be:

$$A_c = \frac{\varphi}{2} (R_c^2 - (R_c - t_c)^2) \quad (\text{B.17})$$

The moment of inertia of the segment itself can be found to be:

$$I_{c0} = \frac{1}{8}(\varphi + \sin \varphi)(R_c^4 - (R_c - t_c)^4) - \frac{\left(\frac{4}{3}(R_c^3 - (R_c - t_c)^3) \sin \frac{\varphi}{2}\right)^2}{\frac{\varphi}{2}(R_c^2 - (R_c - t_c)^2)} \quad (\text{B.18})$$

# Appendix C

## DAMPING EXPERIMENTS

### C.1 Matlab source code

```
%5in constrained layer damping experiments
%ST -Split Tube
%RC - Round Concrete Cast
%RCSE - Round Concrete Cast with Single Rebar
%RCME Round Concrete Cast with Multiple Rebars

clear all
L=0.6096;%length of tube
Ds=0.1401064;%structural tube outer diameter
ts=0.0065532;%structural tube wall thickness
Es=2e11;% Young's modulus of steel
Ec=3.5e10; % Young's modulus of concrete
Ee=2.32e9;% Young's modulus
rho_s=7850; %density of steel
rho_c=2195; %density of concrete
rho_e=1185;%density of epoxy
Gv=9e5; % shear modulus of damping material
mode_shape=0.314;%mode shape factor for free-free boundary condition
lambda=4.73;%solution for first mode of a free-free beam
phi=0.98*pi/2;%angle of constraining layer
L_eff=L*mode_shape;%effective length for Eulerian beam
resolution=400;%number of steps between minimum and maximum constrained layer wall thickness
i=1:resolution;% vector to increase wall thickness incrementally
j=1:4;% vector to increase rebar diameter incrementally

%Structural Tube
Is=pi/64*(Ds^4-(Ds-2*ts)^4);% moment of inertia
As=pi/4*(Ds^2-(Ds-2*ts)^2);%area of structural tube
ms=As*rho_s;%mass of structural tube per unit length

%Split Tube
eta_ST=1;%loss factor of damping sheet
D_ST=0.1143;%outer diameter of constraining layer
```

```

R_ST=D_ST/2;% outer radius of constraining layer
t_ST=.000381;% thickness of damping sheet
tc_ST_min=0.005;% minimum thickness of constraining layer
tc_ST_max=R_ST-t_ST;% maximum thickness of constraining layer
al_opt_ST=1/sqrt(1+eta_ST^2);
y_ST=4/3*((Ds/2-ts)^3-(Ds/2-ts-t_ST)^3)*sin(phi/2)/((Ds/2-ts)^2-(Ds/2-ts-t_ST)^2)/phi;% center of gravity of damping layer
Ae=pi/4*((Ds-2*ts)^2-(D_ST+2*t_ST)^2);% area of epoxy
Ie=pi/64*((Ds-2*ts)^4-(D_ST+2*t_ST)^4);% moment of inertia of epoxy

ST(1,i)=tc_ST_min+(tc_ST_max-tc_ST_min)/resolution*(i-1);% wall thickness of constraining layer
ST(2,i)=phi/2*(R_ST^2-(R_ST-ST(1,i)).^2);% area of constraining layer
ST(3,i)=2/3*(R_ST^3-(R_ST-ST(1,i)).^3)*sin(phi/2)/ST(2,i);% center of gravity of constraining layer
ST(4,i)=1/8*(phi+sin(phi))*(R_ST^4-(R_ST-ST(1,i)).^4);% moment of inertia of top constr. layer around system x-axis
ST(5,i)=ST(4,i)-ST(3,i).^2.*ST(2,i);% moment of inertia of top constraining layer around its principal x-axis
ST(6,i)=1/8*(phi-sin(phi))*(R_ST^4-(R_ST-ST(1,i)).^4);% moment of inertia of side constraining layer around system and principal x-axis
ST(7,i)=2*Es*(ST(4,i)+ST(6,i))+Es*Is+Ee*Ie;% stiffness of all constraining layers plus structural tube
ST(8,i)=4*ST(2,i)*rho_s+ms+rho_e*Ae;% total mass per unit length
ST(9,i)=ST(8,i)*L;% total mass
ST(10,i)=1/(2*pi)*(lambda/L)^2*sqrt(ST(7,i)/ST(8,i));% first natural frequency of assembly
ST(11,i)=2*ST(4,i)*Es+Is*Es;% EI_inf
ST(12,i)=2*ST(5,i)*Es+Is*Es;% EI_0
ST(13,i)=Gv*2*(Ds/2-ts)*phi*y_ST^2*L_eff^2/t_ST/(ST(11,i)-ST(12,i));% damping factor alpha
ST(14,i)=Gv*2*(Ds/2-ts)*phi*y_ST^2/(al_opt_ST*(ST(11,i)-ST(12,i)))*L_eff^2;% optimum damping sheet thickness t_opt
ST(15,i)=(ST(11,i)/ST(12,i))-1;% stiffness ratio r
ST(16,i)=(1+(2+ST(15,i)).*ST(13,i)+(1+ST(15,i)).*ST(13,i).^2*(1+eta_ST^2))./(eta_ST.*ST(15,i).*ST(13,i));% actual damping
ST(17,i)=(1+(2+ST(15,i))*al_opt_ST+(1+ST(15,i))*al_opt_ST^2*(1+eta_ST^2))./(eta_ST.*ST(15,i).*al_opt_ST);% optimum damping using optimum damping sheet thickness

% Round Concrete Cast
t_RST=0.0039116;% wall thickness of round support tube
eta_RC=1;% loss factor of damping sheet
t_RC=.000381;% thickness of damping sheet
D_RC=Ds-2*ts-2*t_RC;% outer diameter of constraining layer
R_RC=D_RC/2;% outer radius of constraining layer
tc_RC_min=0.01;% minimum thickness of constraining layer
tc_RC_max=R_RC-t_RC-t_RST;% maximum thickness of constraining layer
al_opt_RC=1/sqrt(1+eta_RC^2);
y_RC1=4/3*((Ds/2-ts)^3-(Ds/2-ts-t_RC)^3)*sin(phi/2)/((Ds/2-ts)^2-(Ds/2-ts-t_RC)^2)/phi;% center of gravity of damping layer

RC(1,i)=tc_RC_min+(tc_RC_max-tc_RC_min)/resolution*(i-1);% wall thickness of constraining layer
RC(2,i)=R_RC-RC(1,i)-t_RC;% radius of support tube
RC(3,i)=4/3*(RC(2,i)+t_RC).^3-RC(2,i).^3)*sin(phi/2)/(((RC(2,i)+t_RC).^2-RC(2,i).^2)*phi);% center of gravity of secondary damping layer
RC(4,i)=pi*(RC(2,i).^2-(RC(2,i)-t_RST).^2);% area of supporting tube
RC(5,i)=pi/4*(RC(2,i).^4-(RC(2,i)-t_RST).^4);% stiffness of supporting tube

```

```

RC(6,i)=phi/2*(R_RC^2-(R_RC-RC(1,i)).^2);%area of constraining layer
RC(7,i)=2/3*(R_RC^3-(R_RC-RC(1,i)).^3)*sin(phi/2)/RC(6,i);%center of gravity of constraining layer
RC(8,i)=1/8*(phi+sin(phi))*(R_RC^4-(R_RC-RC(1,i)).^4);%moment of inertia of top constraining layer
around system x-axis
RC(9,i)=RC(8,i)-RC(7,i).^2.*RC(6,i);%moment of inertia of top constr. layer around its principal x-axis
RC(10,i)=1/8*(phi-sin(phi))*(R_RC^4-(R_RC-RC(1,i)).^4);%moment of inertia of side constraining layer
around system and principal x-axis
RC(11,i)=2*Ec*(RC(8,i)+RC(10,i))+Es*Is+Es*RC(5,i);%stiffness of all constraining layers plus structural
tube plus support tube
RC(12,i)=4*RC(6,i)*rho_c+ms+RC(4,i)*rho_s;%total mass per unit length
RC(13,i)=RC(12,i)*L;%total mass of damping assembly
RC(14,i)=1/(2*pi)*(lambda/L)^2*sqrt(RC(11,i)/RC(12,i));%first natural frequency of assembly
RC(15,i)=2*RC(8,i)*Ec+Is*Es+RC(5,i)*Es;%EI_inf
RC(16,i)=2*RC(9,i)*Ec+Is*Es+RC(5,i)*Es;%EI_0
RC(17,i)=(R_RC-RC(1,i)/2)*cos(phi/2);%center of gravity of side damping layers
RC(18,i)=Gv*(2*(Ds/2-
ts)*phi*y_RC1^2+4*RC(1,i).*RC(17,i).^2+(RC(2,i)+t_RC)*phi.*RC(3,i).^2)*L_eff^2/t_RC./(RC(15,i)-
RC(16,i));%damping factor alpha
RC(19,i)=Gv*(2*(Ds/2-ts)*phi*y_RC1^2+4*RC(1,i).*RC(17,i).^2+(RC(2,i)+t_RC)*phi.*RC(3,i).^2)/
(al_opt_RC*(RC(15,i)-RC(16,i))*L_eff^2;%optimum damping sheet thickness t_opt
RC(20,i)=(RC(15,i)/RC(16,i))-1;%stiffness ratio r
RC(21,i)=(1+(2+RC(20,i)).*RC(18,i)+(1+RC(20,i)).*RC(18,i).^2*(1+eta_RC^2))./
(eta_RC.*RC(20,i).*RC(18,i));%actual damping
RC(22,i)=(1+(2+RC(20,i))*al_opt_RC+(1+RC(20,i))*al_opt_RC^2*(1+eta_RC^2))./
(eta_RC*RC(20,i)*al_opt_RC);%optimum damping using optimum damping sheet thickness

```

%Round Concrete Cast with Single Rebar

```

t_RST=0.0039116;% wall thickness of support tube
eta_RCSE=1;%loss factor of damping sheet
t_RCSE=.000381;%thickness of damping sheet
D_RCSE=Ds-2*ts-2*t_RCSE;%outer diameter of constraining layer
R_RCSE=D_RCSE/2;%outer radius of constraining layer
tc_RCSE_max=R_RCSE-t_RCSE-t_RST;%maximum thickness of constraining layer
al_opt_RCSE=1/sqrt(1+eta_RCSE^2);
y_RCSE=4/3*((Ds/2-ts)^3-(Ds/2-ts-t_RCSE)^3)*sin(phi/2)/((Ds/2-ts)^2-(Ds/2-ts-t_RCSE)^2)/phi;%center
of gravity of damping layer

```

R\_R\_RCSE(1,1)=0.5/2\*25.4/1000;% VECTOR radius of Rebar

R\_R\_RCSE(1,2)=0.75/2\*25.4/1000;% VECTOR radius of Rebar

R\_R\_RCSE(1,3)=1/2\*25.4/1000;% VECTOR radius of Rebar

for p=1:3

tc\_RCSE\_min(1,p)=2\*R\_R\_RCSE(1,p)+0.01;% VECTOR minimum thickness of constraining layer

R\_B\_RCSE(1,p)=R\_RCSE-R\_R\_RCSE(1,p)-0.005;% VECTOR location of Rebar

t\_R\_RCSE(1,p)=R\_R\_RCSE(1,p); % VECTOR wall thickness of Rebar

for o=1:resolution

RCSE(1,o,p)=tc\_RCSE\_min(1,p)+(tc\_RCSE\_max-tc\_RCSE\_min(1,p))/resolution\*(o-1);% wall thick-  
ness of constraining layer

RCSE(2,o,p)=R\_RCSE-RCSE(1,o,p)-t\_RCSE;% outer radius of supporting tube

RCSE(3,o,p)=4/3\*((RCSE(2,o,p)+t\_RCSE).^3-RCSE(2,o,p).^3)\*sin(phi/2)/  
(((RCSE(2,o,p)+t\_RCSE).^2-RCSE(2,o,p).^2)\*phi);%center of gravity of secondary damping layer

```

RCSE(4,o,p)=pi*(RCSE(2,o,p).^2-(RCSE(2,o,p)-t_RST).^2);%area of supporting tube
RCSE(5,o,p)=pi/4*(RCSE(2,o,p).^4-(RCSE(2,o,p)-t_RST).^4);%stiffness of supporting tube
RCSE(6,o,p)=phi/2*(R_RCSE^2-(R_RCSE-RCSE(1,o,p))^2-pi*R_R_RCSE(1,p)^2);%area of concrete
constraining layer
RCSE(7,o,p)=(2/3*(R_RCSE^3-(R_RCSE-RCSE(1,o,p))^3)*sin(phi/2)-
R_B_RCSE(1,p)*pi*R_R_RCSE(1,p)^2)/RCSE(6,o,p);%center of gravity of concrete constraining layer
RCSE(8,o,p)=1/8*(phi+sin(phi))*(R_RCSE^4-(R_RCSE-RCSE(1,o,p))^4)-(pi/
4*R_R_RCSE(1,p)^4+R_B_RCSE(1,p)^2*pi*R_R_RCSE(1,p)^2);%moment of inertia of top concrete
constraining layer around system x-axis
RCSE(9,o,p)=RCSE(8,o,p)-RCSE(7,o,p)^2*RCSE(6,o,p);%moment of inertia of top concrete constrain-
ing layer around its principal x-axis
RCSE(10,o,p)=1/8*(phi-sin(phi))*(R_RCSE^4-(R_RCSE-RCSE(1,o,p))^4)-(pi/4*R_R_RCSE(1,p)^4);
%moment of inertia of side constraining layer around system and principal x-axis
RCSE(11,o,p)=pi*(R_R_RCSE(1,p)^2-(R_R_RCSE(1,p)-t_R_RCSE(1,p))^2); %area of Rebar
RCSE(12,o,p)=R_B_RCSE(1,p);%center of gravity of Rebar
RCSE(13,o,p)=pi/4*(R_R_RCSE(1,p)^4-(R_R_RCSE(1,p)-
t_R_RCSE(1,p))^4)+R_B_RCSE(1,p)^2*pi*(R_R_RCSE(1,p)^2-(R_R_RCSE(1,p)-t_R_RCSE(1,p))^2);
%moment of inertia of top Rebar with respect to system axis
RCSE(14,o,p)=RCSE(13,o,p)-RCSE(12,o,p)^2*RCSE(11,o,p);%moment of inertia of top layer Rebar
with respect to its principal axis
RCSE(15,o,p)=pi/4*(R_R_RCSE(1,p)^4-(R_R_RCSE(1,p)-t_R_RCSE(1,p))^4);%moment of inertia of
side layer Rebar with respect to system and principal axis

RCSE(16,o,p)=2*Ec*(RCSE(8,o,p)+RCSE(10,o,p))+Es*(RCSE(13,o,p)+RCSE(15,o,p)+RCSE(5,o,p))+Es
*Is;%stiffness of all constraining layers plus structural tube
RCSE(17,o,p)=4*RCSE(6,o,p)*rho_c+(RCSE(4,o,p)+4*RCSE(11,o,p))*rho_s+ms;%total mass per unit
length
RCSE(18,o,p)=RCSE(17,o,p)*L;%total mass
RCSE(19,o,p)=1/(2*pi)*(lambda/L)^2*sqrt(RCSE(16,o,p)/RCSE(17,o,p));%first natural frequency of
assembly
RCSE(20,o,p)=2*RCSE(8,o,p)*Ec+2*RCSE(13,o,p)*Es+Is*Es+RCSE(5,o,p)*Es;%EI_inf
RCSE(21,o,p)=2*RCSE(9,o,p)*Ec+2*RCSE(14,o,p)*Es+Is*Es+RCSE(5,o,p)*Es;%EI_0
RCSE(22,o,p)=(R_RCSE-RCSE(1,o,p)/2)*cos(phi/2);%center of gravity of side damping layers
RCSE(23,o,p)=Gv*(2*(Ds/2-
ts)*phi*y_RCSE^2+4*RCSE(1,o,p).*RCSE(22,o,p).^2+(RCSE(2,o,p)+t_RCSE)*phi.*RCSE(3,o,p).^2)*L_
eff^2/t_RCSE/(RCSE(20,o,p)-RCSE(21,o,p));%damping factor alpha
RCSE(24,o,p)=Gv*(2*(Ds/2-
ts)*phi*y_RCSE^2+4*RCSE(1,o,p).*RCSE(22,o,p).^2+(RCSE(2,o,p)+t_RCSE)*phi.*RCSE(3,o,p).^2)/
(al_opt_RCSE*(RCSE(20,o,p)-RCSE(21,o,p)))*L_eff^2;%optimum damping sheet thickness t_opt
RCSE(25,o,p)=(RCSE(20,o,p)/RCSE(21,o,p))-1;%stiffness ratio r

RCSE(26,o,p)=(1+(2+RCSE(25,o,p))*RCSE(23,o,p)+(1+RCSE(25,o,p))*RCSE(23,o,p)^2*(1+eta_RCSE^
2))/(eta_RCSE*RCSE(25,o,p)*RCSE(23,o,p));%actual damping

RCSE(27,o,p)=(1+(2+RCSE(25,o,p))*al_opt_RCSE+(1+RCSE(25,o,p))*al_opt_RCSE^2*(1+eta_RCSE^2
))/(eta_RCSE*RCSE(25,o,p)*al_opt_RCSE);%optimum damping using optimum damping sheet thickness
end
end

%round concrete cast with multiple rebars
t_RST=0.0039116;% wall thickness of supporting tube

```

```

eta_RCME=1;%loss factor of damping sheet
t_RCME=.000381;%thickness of damping sheet
D_RCME=Ds-2*ts-2*t_RCME;%outer diameter of constraining layer
R_RCME=D_RCME/2;%outer radius of constraining layer
tc_RCME_max=R_RCME-t_RCME-t_RST;%maximum thickness of constraining layer
al_opt_RCME=1/sqrt(1+eta_RCME^2);
y_RCME=4/3*((Ds/2-ts)^3-(Ds/2-ts-t_RCME)^3)*sin(phi/2)/((Ds/2-ts)^2-(Ds/2-ts-t_RCME)^2)/phi;%center
of gravity of damping layer

R_R_RCME(1,1)=0.5/2*25.4/1000;%0.5" rebar
R_R_RCME(1,2)=0.75/2*25.4/1000;%0.75" rebar
R_R_RCME(1,3)=1/2*25.4/1000;%1" rebar
for p=1:3
    tc_RCME_min(1,p)=2*R_R_RCME(1,p)+0.01;% VECTOR minimum thickness of constraining layer
    R_B_RCME(1,p)=R_RCME-R_R_RCME(1,p)-0.005;% VECTOR location of rebar
    t_R_RCME(1,p)=R_R_RCME(1,p); % VECTOR wall thickness of rebar
    t_rad=0.01;%minimum radial spacing of rebars

    for o=1:resolution
        RCME(1,o,p)=tc_RCME_min(1,p)+(tc_RCME_max-tc_RCME_min(1,p))/resolution*(o-1);% wall
thickness of constraining layer
        RCME(2,o,p)=fix(phi*R_B_RCME(1,p)/(2*R_R_RCME(1,p)+t_rad));%number of rebars
        RCME(3,o,p)=phi/2*(1/RCME(2,o,p)-1);%gamma_0
        RCME(4,o,p)=phi/RCME(2,o,p);%gamma_n
        Ac=0;
        yc=0;
        Ix=0;
        Iy=0;
        for n=0:RCME(2,o,p)-1
            Ac=Ac+pi*(R_R_RCME(1,p)^2-(R_R_RCME(1,p)-t_R_RCME(1,p))^2);
            yc=yc+R_B_RCME(1,p)*cos(RCME(3,o,p)+n*RCME(4,o,p))*pi*(R_R_RCME(1,p)^2-
(R_R_RCME(1,p)-t_R_RCME(1,p))^2);
            Ix=Ix+pi/4*(R_R_RCME(1,p)^4-(R_R_RCME(1,p)-
t_R_RCME(1,p))^4)+(R_B_RCME(1,p)*cos(RCME(3,o,p)+n*RCME(4,o,p)))^2*pi*(R_R_RCME(1,p)^2-
(R_R_RCME(1,p)-t_R_RCME(1,p))^2);%moment of inertia
            Iy=Iy+pi/4*(R_R_RCME(1,p)^4-(R_R_RCME(1,p)-
t_R_RCME(1,p))^4)+(R_B_RCME(1,p)*sin(RCME(3,o,p)+n*RCME(4,o,p)))^2*pi*(R_R_RCME(1,p)^2-
(R_R_RCME(1,p)-t_R_RCME(1,p))^2);
        end
        RCME(5,o,p)=R_RCME-RCME(1,o,p)-t_RCME; %outer diameter of supporting tube
        RCME(6,o,p)=4/3*((RCME(5,o,p)+t_RCME)^3-RCME(5,o,p)^3)*sin(phi/2)/
(((RCME(5,o,p)+t_RCME)^2-RCME(5,o,p)^2)*phi);%center of gravity of secondary damping layer
        RCME(7,o,p)=pi*(RCME(5,o,p)^2-(RCME(5,o,p)-t_RST)^2);%area of supporting tube
        RCME(8,o,p)=pi/4*(RCME(5,o,p)^4-(RCME(5,o,p)-t_RST)^4);%stiffness of supporting tube
        RCME(9,o,p)=phi/2*(R_RCME^2-(R_RCME-RCME(1,o,p))^2)-Ac;%area of concrete constr. layer
        RCME(10,o,p)=(2/3*(R_RCME^3-(R_RCME-RCME(1,o,p))^3)*sin(phi/2)-yc)/RCME(9,o,p);%center
of gravity of concrete constraining layer
        RCME(11,o,p)=1/8*(phi+sin(phi))*(R_RCME^4-(R_RCME-RCME(1,o,p))^4)-Ix;%moment of inertia
of top concrete constraining layer around system x-axis
        RCME(12,o,p)=RCME(11,o,p)-RCME(10,o,p)^2*RCME(9,o,p);%moment of inertia of top concrete
constraining layer around its principal x-axis

```

```

RCME(13,o,p)=1/8*(phi-sin(phi))*(R_RCME^4-(R_RCME-RCME(1,o,p))^4)-Iy;% moment of inertia
of side constraining layer around system and principal x-axis
RCME(14,o,p)=Ac; %area of rebar
RCME(15,o,p)=yc/Ac;%center of gravity of rebar
RCME(16,o,p)=Ix;%moment of inertia of top rebar with respect to system axis
RCME(17,o,p)=RCME(16,o,p)-RCME(15,o,p)^2*RCME(14,o,p);%moment of inertia of top layer rebar
with respect to its principal axis
RCME(18,o,p)=Iy;%moment of inertia of side layer rebar with respect to system and principal axis

RCME(19,o,p)=2*Ec*(RCME(11,o,p)+RCME(13,o,p))+2*Es*(RCME(16,o,p)+RCME(18,o,p))+RCME(8,
o,p)*Es+Es*Is;%stiffness of all constraining layers plus structural tube
RCME(20,o,p)=4*RCME(9,o,p)*rho_c+(RCME(7,o,p)+4*RCME(14,o,p))*rho_s+ms;%total mass per
unit length
RCME(21,o,p)=RCME(20,o,p)*L;%total mass
RCME(22,o,p)=1/(2*pi)*(lambda/L)^2*sqrt(RCME(19,o,p)/RCME(20,o,p));%first modey of assembly
RCME(23,o,p)=2*RCME(11,o,p)*Ec+2*RCME(16,o,p)*Es+Is*Es+RCME(8,o,p)*Es;%EI_inf
RCME(24,o,p)=2*RCME(12,o,p)*Ec+2*RCME(17,o,p)*Es+Is*Es+RCME(8,o,p)*Es;%EI_0
RCME(25,o,p)=(R_RCME-RCME(1,o,p)/2)*cos(phi/2);%center of gravity of side damping layers
RCME(26,o,p)=Gv*(2*(Ds/2-
ts)*phi*y_RCME^2+4*RCME(1,o,p)*RCME(25,o,p)^2+(RCME(5,o,p)+t_RCME)*phi*RCME(6,o,p)^2)*
L_eff^2/(t_RCME*(RCME(23,o,p)-RCME(24,o,p)));%damping factor alpha
RCME(27,o,p)=Gv*(2*(Ds/2-
ts)*phi*y_RCME^2+4*RCME(1,o,p)*RCME(25,o,p)^2+(RCME(5,o,p)+t_RCME)*phi*RCME(6,o,p)^2)*
L_eff^2/(al_opt_RCME*(RCME(23,o,p)-RCME(24,o,p)));%optimum damping sheet thickness t_opt
RCME(28,o,p)=(RCME(23,o,p)/RCME(24,o,p))-1;%stiffness ratio r

RCME(29,o,p)=(1+(2+RCME(28,o,p))*RCME(26,o,p)+(1+RCME(28,o,p))*RCME(26,o,p)^2*(1+eta_RC
ME^2))/(eta_RCME*RCME(28,o,p)*RCME(26,o,p));%actual damping

RCME(30,o,p)=(1+(2+RCME(28,o,p))*al_opt_RCME+(1+RCME(28,o,p))*al_opt_RCME^2*(1+eta_RC
ME^2))/(eta_RCME*RCME(28,o,p)*al_opt_RCME);%opt. damping using opt. damping sheet thickness
end
end

```

## C.2 Damping Calculations

$$U(x) = C_1 \cos\left(\frac{\lambda x}{l}\right) + C_2 \sin\left(\frac{\lambda x}{l}\right) + C_3 \cosh\left(\frac{\lambda x}{l}\right) + C_4 \sinh\left(\frac{\lambda x}{l}\right) \quad (C.1)$$

$$U'(x) = -C_1 \frac{\lambda}{l} \sin\left(\frac{\lambda x}{l}\right) + C_2 \frac{\lambda}{l} \cos\left(\frac{\lambda x}{l}\right) + C_3 \frac{\lambda}{l} \sinh\left(\frac{\lambda x}{l}\right) + C_4 \frac{\lambda}{l} \cosh\left(\frac{\lambda x}{l}\right) \quad (C.2)$$

$$U''(x) = -C_1 \left(\frac{\lambda}{l}\right)^2 \cos\left(\frac{\lambda x}{l}\right) - C_2 \left(\frac{\lambda}{l}\right)^2 \sin\left(\frac{\lambda x}{l}\right) + C_3 \left(\frac{\lambda}{l}\right)^2 \cosh\left(\frac{\lambda x}{l}\right) + C_4 \left(\frac{\lambda}{l}\right)^2 \sinh\left(\frac{\lambda x}{l}\right)$$

$$U'''(x) = C_1 \left(\frac{\lambda}{l}\right)^3 \sin\left(\frac{\lambda x}{l}\right) - C_2 \left(\frac{\lambda}{l}\right)^3 \cos\left(\frac{\lambda x}{l}\right) + C_3 \left(\frac{\lambda}{l}\right)^3 \sinh\left(\frac{\lambda x}{l}\right) + C_4 \left(\frac{\lambda}{l}\right)^3 \cosh\left(\frac{\lambda x}{l}\right)$$

Applying the boundary conditions:



$$U''(x=0) = 0: \quad -C_1\left(\frac{\lambda}{l}\right)^2 + C_3\left(\frac{\lambda}{l}\right)^2 = 0 \quad (\text{C.3})$$

$$U''(x=l) = 0: \quad -C_1\left(\frac{\lambda}{l}\right)^2 \cos\lambda - C_2\left(\frac{\lambda}{l}\right)^2 \sin\lambda + C_3\left(\frac{\lambda}{l}\right)^2 \cosh\lambda + C_4\left(\frac{\lambda}{l}\right)^2 \sinh\lambda = 0$$

$$U'''(x=0) = 0: \quad -C_2\left(\frac{\lambda}{l}\right)^3 + C_4\left(\frac{\lambda}{l}\right)^3 = 0$$

$$U'''(x=l) = 0: \quad C_1\left(\frac{\lambda}{l}\right)^3 \sin\lambda - C_2\left(\frac{\lambda}{l}\right)^3 \cos\lambda + C_3\left(\frac{\lambda}{l}\right)^3 \sinh\lambda + C_4\left(\frac{\lambda}{l}\right)^3 \cosh\lambda = 0$$

It now follows:

$$\begin{aligned} C_2 &= C_4 \quad \text{and} \quad C_1 = C_3 & (\text{C.4}) \\ C_1 \sin\lambda - (C_2 \cos\lambda + C_3 \sinh\lambda + C_4 \cosh\lambda) &= 0 \\ -C_1 \cos\lambda - C_2 \sin\lambda + C_3 \cosh\lambda + C_4 \sinh\lambda &= 0 \end{aligned}$$

Solving the above system of equations leads to:

$$C_2(1 - \cos\lambda \cosh\lambda) = 0 \quad (\text{C.5})$$

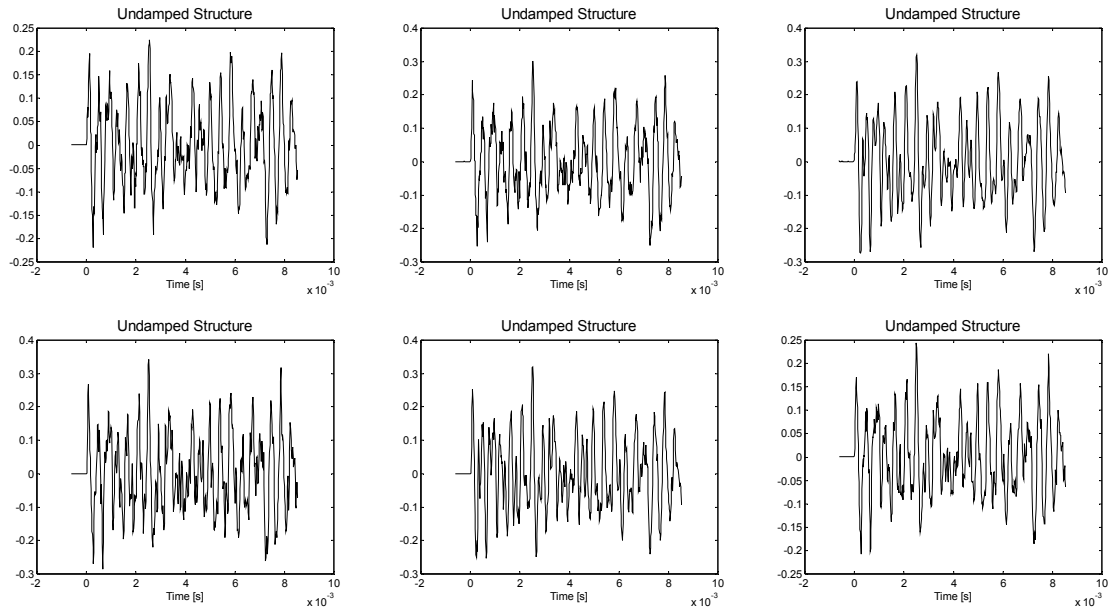
C.5 has the following non-trivial solution:

$$\cos\lambda \cosh\lambda = 1 \quad (\text{C.6})$$

which is known as the characteristic frequency equation of a free-free beam.

## C.3 Results

### C.3.1 Undamped Structure



Time response of undamped structure

### C.3.2 Sand Filled Structure

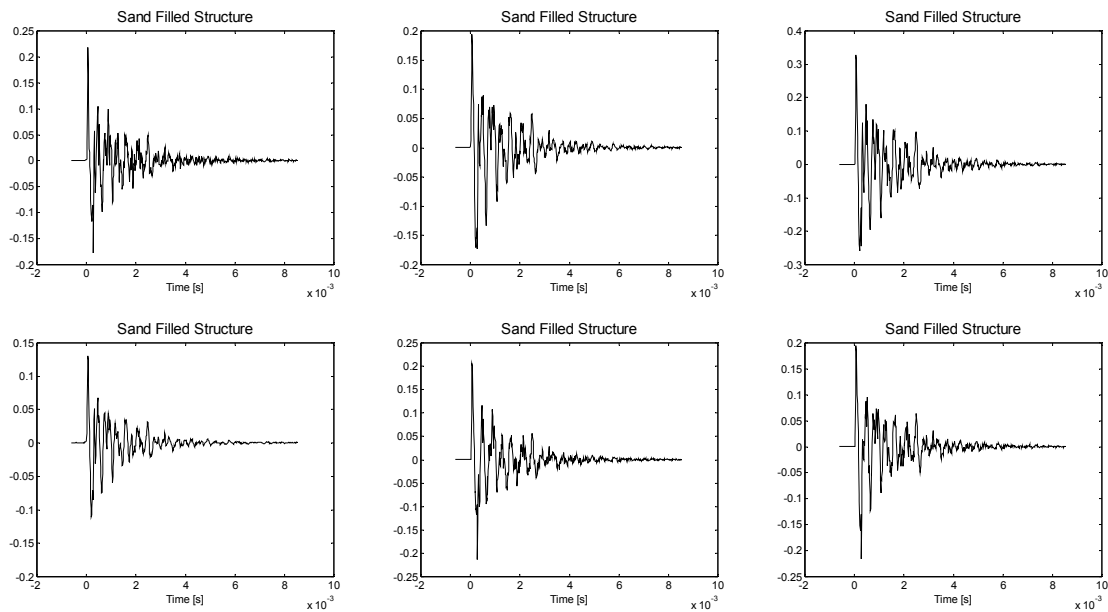


Figure C.1 Time response of sand filled structures

### C.3.3 Concrete Filled Structure

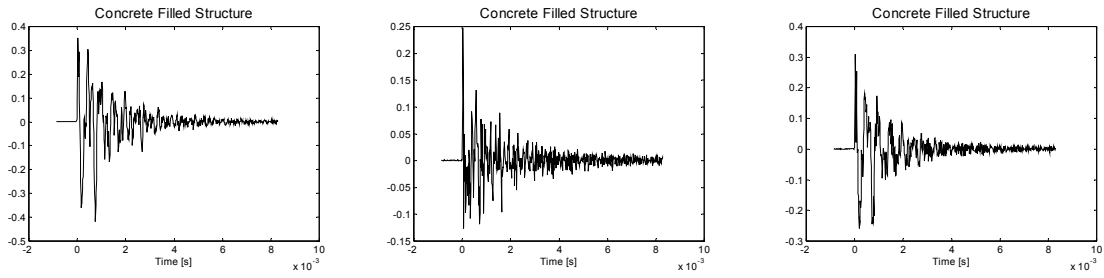


Figure C.2 Time Response of concrete filled structure

### C.3.4 Split Tube Damped Structure

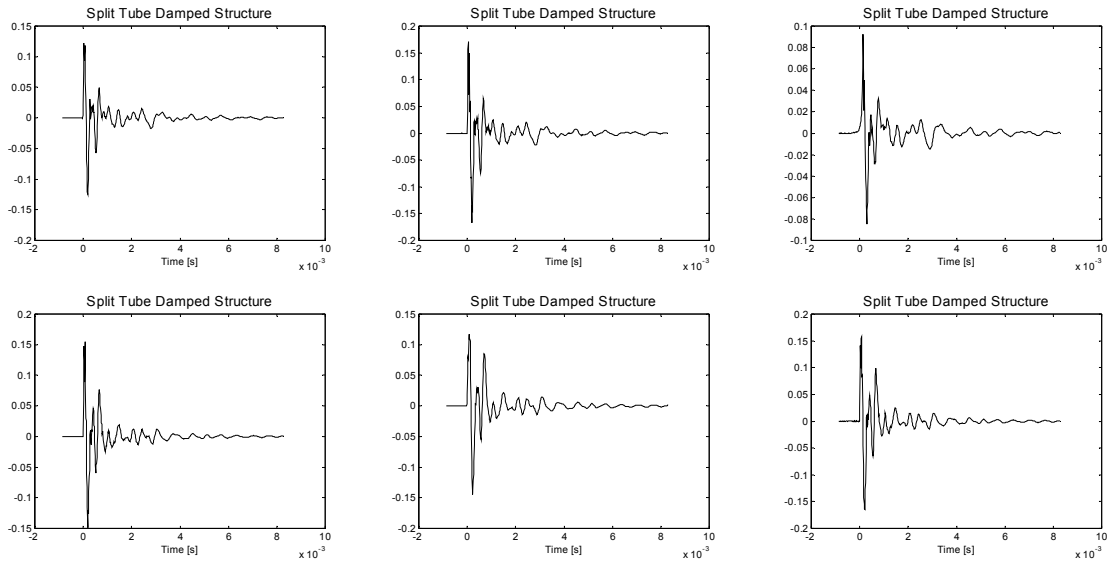

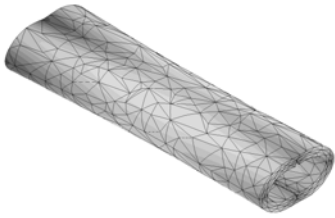
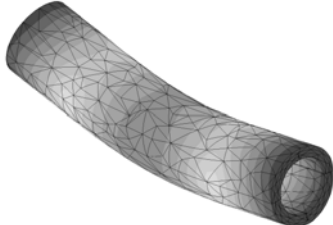
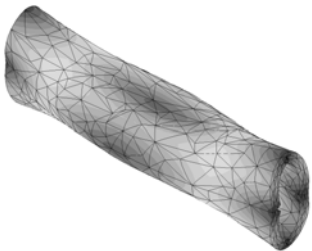
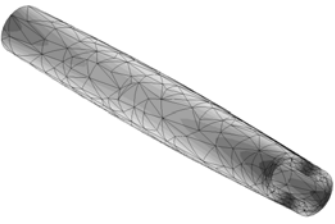
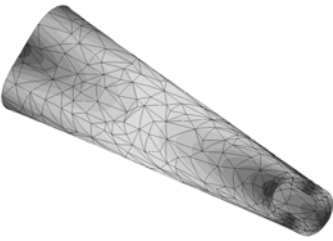
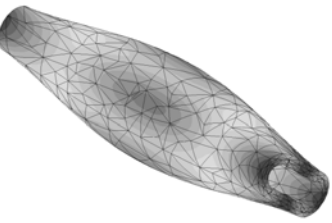
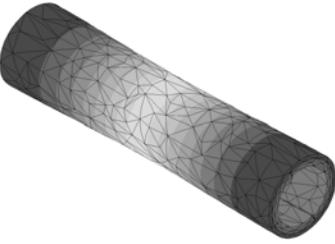
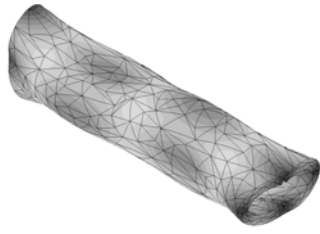
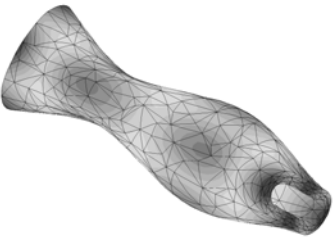
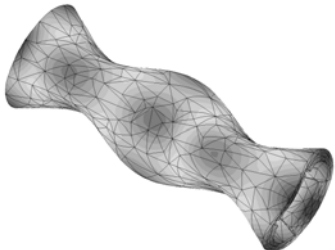
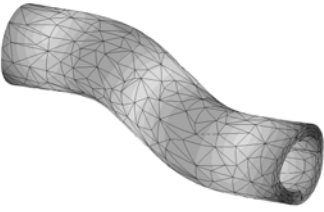
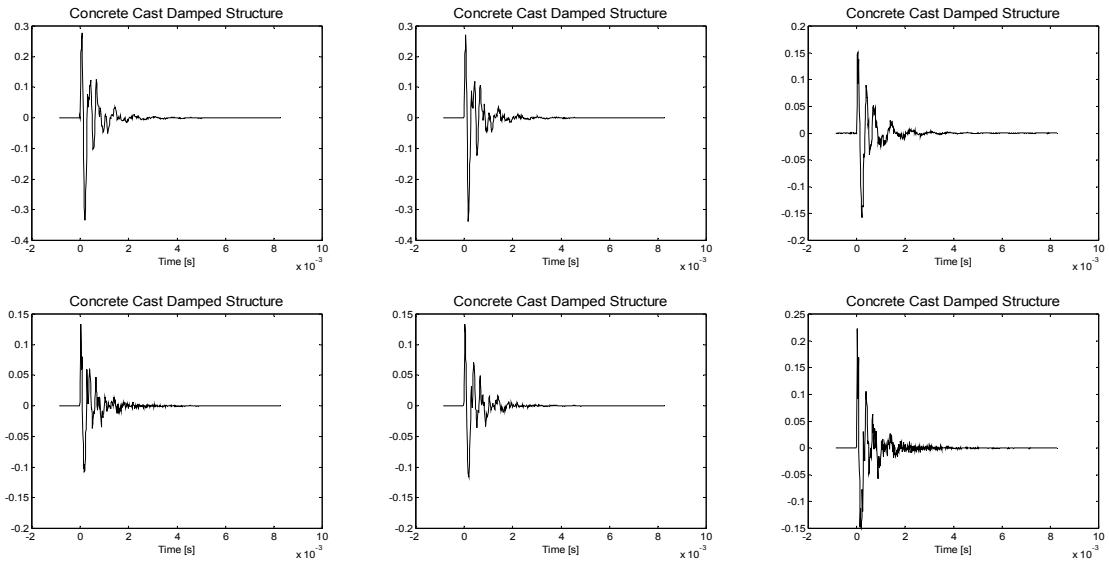


Figure C.3 Time response of split tube damped structure

**TABLE 7.6** Free-free vibration of split tube predicted by finite element analysis

 <p>1. Mode - 1212 Hz</p>	 <p>2. Mode - 1220 Hz</p>	 <p>3. Mode - 1582 Hz</p>
 <p>4. Mode - 1682 Hz</p>	 <p>5. Mode - 1917 Hz</p>	 <p>6. Mode - 1926 Hz</p>
 <p>7. Mode - 2059 Hz</p>	 <p>8. Mode - 2219 Hz</p>	 <p>9. Mode - 2406 Hz</p>
 <p>10. Mode - 2510 Hz</p>	 <p>11. Mode - 3232 Hz</p>	 <p>12. Mode - 3242 Hz</p>

### C.3.5 Concrete Cast Damped Structure



### C.3.6 Reinforced Concrete Cast Damped Structure

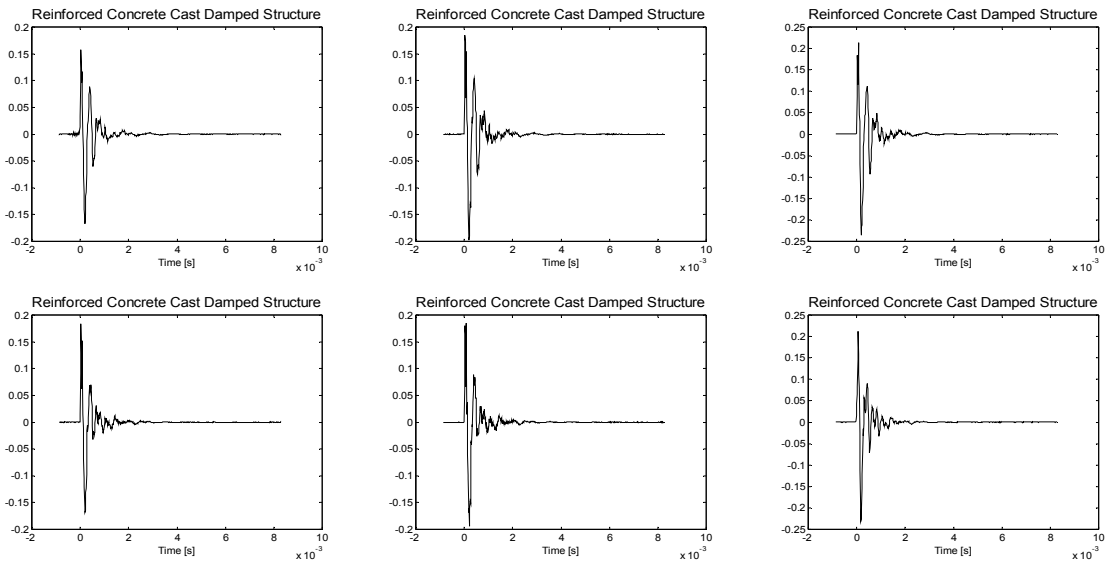


Figure C.4 Time Response of concrete core reinforced damped structure

TABLE 7.7 Damping results - split tube damped structure

Point	X		Y		Z	
	Frequency	$\zeta$	Frequency	$\zeta$	Frequency	$\zeta$
2	1530	1.59	1530	2.95	1520	2.79
3	1530	1.7	1530	3.29	1530	2.65
4	1530	1.77	1530	2.63	1530	2.93
5	1540	1.93	1530	2.89		
6	1540	1.91	1530	3.2	1530	2.86
7	1520	1.83	1520	3.73	1530	2.96
8	1530	1.44	1530	3.06	1530	2.96
9	1530	2.14	1530	2.9	1530	1.88
10	1530	2.73	1540	2.92	1530	1.85
11	1530	1.55	1540	2.9	1540	1.66
12	1540	2.07	1530	2.83	1540	2.12
13	1550	2.54	1540	2.75	1540	1.65
14	1540	1.82	1530	3.03	1540	1.48
15	1540	1.62	1530	2.86	1540	1.6
16	1540	1.34	1530	3.22	1530	2.93
17	1540	1.58	1530	3.16	1530	3.02
18	1550	1.91	1540	2.85	1530	3.05
19	1550	1.85	1530	3.12	1530	3.55
20	1550	1.81	1540	3.06	1540	2.98
21	1540	1.65	1540	2.96	1540	2.9
22	1540	1.74	1540	2.77	1530	2.77
23			1540	2.7	1550	1.78
24			1540	2.75	1530	2.69
25	1530	1.77	1540	2.83	1540	2.11
26	1550	2.11	1540	2.79	1530	2.97
27	1540	2.04	1540	2.82	1540	2.02
28	1540	1.96	1540	3.08	1530	1.45
29	1520	1.26	1540	2.85	1530	1.72

TABLE 7.8 Damping results - concrete cast structure

Point	X		Y		Z	
	Frequency	$\zeta$	Frequency	$\zeta$	Frequency	$\zeta$
2	1270	9.27	1260	7.21	1260	8.03
3			1270	8.03	1270	6.03
4	1280	4.6			1280	8.43
5	1260	5.98	1260	6.14		
6	1260	6.14	1280	6.72	1260	7.13
7					1260	7.09
8			1260	6.35	1260	6.64
9			1260	7.01	1260	8.38
10			1260	6.51		
11			1270	8.38		
12			1270	7.72		
13			1260	9.54		
14			1270	6.28		
15			1270	7.24		
16			1260	7.62	1260	7.33
17			1260	6.22	1270	6.69
18			1270	4.17	1260	7.08
19	1260	5.4	1270	6.42		
20			1270	5.95		
21					1260	5.28
22	1260	5.72			1260	6.27
23			1250	9.79	1270	7.64
24			1250	8.45		
25			1270	6.77		
26			1270	7.06		
27			1270	7.11		
28			1270	7.8		
29			1270	7.32		

**TABLE 7.9** Damping results - reinforced concrete cast structure

Point	X		Y		Z	
	Frequency	$\zeta$	Frequency	$\zeta$	Frequency	$\zeta$
2						
3						
4						
5						
6			1640	15.4		
7			1630	15.94	1630	11.66
8						
9						
10						
11						
12						
13	1640	16.68				
14			1640	15.28		
15						
16					1640	8.93
17						
18						
19						
20						
21						
22						
23						
24						
25						
26						
27						
28						
29						